Targeting LasB in *Pseudomonas aeruginosa*: A Multifaceted Antivirulence Strategy for Lung Infections

Dissertation

zur Erlangung des akademischen Grades

des Doktors der Naturwissenschaften

der Naturwissenschaftlich-Technischen Fakultät

der Universität des Saarlandes

von

Roya Shafiei

Saarbrücken

2025

Tag des Kolloquiums:	06.02.2026
Dekan:	Prof. Dr.-Ing. Dirk Bähre
Berichterstatter:	Prof. Dr. Anna K. H. Hirsch Prof. Dr. Claus-Michael Lehr
Vorsitz:	Prof. Dr. Martin Empting
Akad. Mitglied:	Dr. Christian Schütz

Die vorliegende Arbeit wurde von Januar 2022 bis März 2025 unter Anleitung von Frau Prof. Dr. Anna K. H. Hirsch in der Fachrichtung Pharmazie der Naturwissenschaftlich-Technischen Fakultät der Universität des Saarlandes sowie am Helmholtz-Institut für Pharmazeutische Forschung Saarland (HIPS) – Abteilung Wirkstoffdesign und Optimierung – angefertigt.

Table of Contents

Abstract

Pseudomonas aeruginosa is a major cause of pulmonary infections, particularly in hospitals and patients with chronic respiratory diseases. Its intrinsic and acquired antibiotic resistance, along with numerous virulence factors, make it an important contributor to the global antimicrobial resistance (AMR) crisis. As conventional antibiotics lose effectiveness, antivirulence therapies that target pathogenic mechanisms rather than bacterial viability are promising alternatives that limit resistance development and preserve the host microbiota.

This thesis examines elastase (LasB), a metalloprotease secreted by *P. aeruginosa* that disrupts lung barriers, modulates immune responses, and damages tissue. Using human lung epithelial models, we show that LasB degrades junctional proteins such as E-cadherin and Claudin-4, increasing epithelial permeability and vulnerability to infection. It also suppresses immune signaling by reducing GM-CSF, G-CSF and by altering MAPK and FGF pathways. Phosphonate-based LasB inhibitors reversed these effects, maintaining barrier integrity, partly restoring cytokine levels, and enhancing antibiotic activity.

We further quantified *lasB* expression in clinical isolates and demonstrated that dual LasB/LecA inhibitors protect lung cells from virulence-induced damage without cytotoxicity. Together, these findings elucidate LasB-driven lung pathogenesis and support antivirulence strategies as promising adjuncts to antibiotics in combating AMR

.

Zusammenfassung

Pseudomonas aeruginosa zählt zu den häufigsten Erregern von Lungeninfektionen, insbesondere in Krankenhäusern und bei Patienten mit chronischen Atemwegserkrankungen. Ihre intrinsische und erworbene Antibiotikaresistenz sowie zahlreiche Virulenzfaktoren machen sie zu einem zentralen Treiber der globalen antimikrobiellen Resistenz (AMR)-Krise. Da konventionelle Antibiotika an Wirksamkeit verlieren, gewinnen Antivirulenz-Therapien, die pathogene Mechanismen statt bakterieller Lebensfähigkeit bekämpfen, an Bedeutung, da sie Resistenzentwicklung begrenzen und die Mikrobiota erhalten.

Diese Arbeit untersucht die Elastase (LasB), eine von *P. aeruginosa* sezernierte Metalloprotease, die Lungenbarrieren stört, Immunreaktionen moduliert und Gewebe schädigt. In humanen Lungenepithelmodellen zeigen wir, dass LasB junktionale Proteine wie E-Cadherin und Claudin-4 abbaut, epitheliale Permeabilität erhöht und Infektanfälligkeit steigert. LasB unterdrückt Immunsignale durch Reduktion von GM-CSF, G-CSF und Modulation der MAPK-/FGF-Signalwege. Phosphonatbasierte LasB-Inhibitoren kehrten diese Effekte um, erhielten Barriereintegrität, stellten Zytokinspiegel teilweise wieder her und verstärkten Antibiotikawirkung.

Wir quantifizierten *lasB*-Expression in klinischen Isolaten und zeigten, dass duale LasB/LecA-Inhibitoren Lungenepithelzellen ohne Zytotoxizität vor virulenzinduziertem Schaden schützen. Diese Befunde klären die LasB-vermittelte Lungenpathogenese auf und unterstützen Antivirulenz-Strategien als Ergänzung zu Antibiotika zur Bekämpfung von AMR.

1 Introduction

1.1 Antimicrobial resistance

Antimicrobial resistance (AMR) has evolved into a pressing global health crisis with multidrug-resistant (MDR) bacterial pathogens causing untreatable infections that claim over 1.27 million lives annually worldwide.[1] The development of resistance is primarily driven by genetic mutations and the overuse of conventional antibiotics, which accelerate the selection and spread of resistant strains.[2] The severity of AMR development and its consequences is comparable to that of cancer, highlighting the urgent need for comprehensive strategies to combat this issue.[3] Additionally, AMR already imposes substantial economic and social burdens, with projections indicating that it could lead to up to 10 million deaths and a staggering global economic cost of $100 trillion by 2050.[4]

Understanding the mechanisms of AMR is crucial for developing effective countermeasures. This involves recognizing the complex interplay between genetic factors, antibiotic misuse, and environmental influences. For instance, studies have shown that the misuse of antibiotics in agriculture and healthcare settings contributes significantly to the emergence and dissemination of resistant pathogens.[5] Furthermore, the lack of new antibiotic discoveries exacerbates the problem as existing drugs become less effective against evolving resistant strains.[6]

To address this growing threat, researchers are exploring innovative approaches such as developing novel anti-infectives, creating vaccines targeting resistant pathogens, and implementing combination therapies.[7] Moreover, there is an increasing focus on understanding the evolutionary dynamics of resistance in bacteria to develop more effective strategies for combating AMR.[8]

1.2 Mechanisms of resistance development

Antibiotic resistance emerged almost simultaneously with the clinical introduction of antimicrobial therapies, with documented cases of resistance appearing as early as the 1940s during initial penicillin use.[9] This evolutionary phenomenon persists today, driven by selective pressures that favor bacterial survival through diverse molecular strategies. Bacteria develop resistance to antibacterials through four main mechanisms. These include the utilization of efflux pumps, modifications of antibiotic target site, the enzymatic degradation of antibacterial agents, and alterations in the cell membrane's permeability (Figure 1).[10]

Bacteria develop resistance mechanisms primarily through efflux pumps, which actively expel antimicrobial agents before they reach intracellular targets. This process is exemplified by multidrug-resistant *Pseudomonas aeruginosa* and *Staphylococcus aureus*.[11,12] These transmembrane protein complexes, such as the acridine resistance complex A and B – toluene resistance outer membrane channel (AcrAB-TolC) system in Gram-negative bacteria, reduce drug accumulation and compromise therapeutic efficacy — a major hurdle in antibiotic development.[13]

Another critical mechanism involves the modification of drug targets. Bacterial genomes acquire mutations that alter drug-binding sites, as seen in penicillin-binding protein (PBP)

mutations conferring β-lactam resistance in *Streptococcus pneumoniae*.[14,15] Enzymatic alterations, including ribosomal methylases in aminoglycoside-resistant Enterobacteriaceae, further disrupt drug–target interactions.[16]

Enzymatic degradation is another prevalent resistance strategy. Hydrolytic enzymes like β-lactamases inactivate antibiotics by cleaving critical molecular structures. Over 2,000 variants of these enzymes have evolved, with extended-spectrum β-lactamases (ESBLs) rendering cephalosporins ineffective in pathogens like *Klebsiella pneumoniae*.[15–18] These mechanisms are rooted in ancient microbial ecosystems, as evidenced by β-lactamase genes identified in 30,000-year-old permafrost samples.

To complement these strategies, bacteria can limit drug uptake by reducing the permeability of the bacterial cell membrane, preventing antibiotics from entering the cell.[10] Gram-negative bacteria, for instance, have an outer membrane that acts as a barrier to many antibiotics, limiting their entry through porin channels. Changes in porin expression or mutations can further impede drug uptake, as seen in Enterobacteriaceae, which reduce porin numbers to resist carbapenems.[19]

The persistence and diversification of resistance determinants underscore the urgent need for innovative therapeutic strategies that bypass conventional targets. Understanding these resistance pathways is critical for designing next-generation antimicrobials.

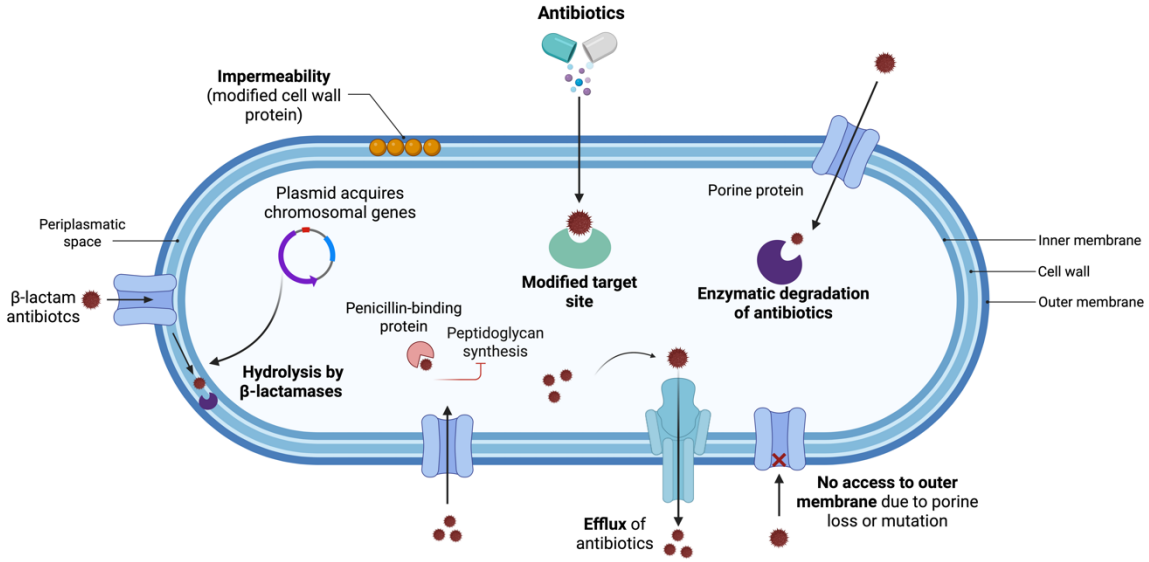

Figure 1: Mechanisms of antimicrobial resistance (AMR) in Gram-negative bacteria. Bacteria resist antibiotics through efflux pumps, target-site modification, enzymatic inactivation, and reduced membrane permeability, each limiting drug effectiveness and contributing to persistent resistance. Figure was created with **Biorender.com**.

1.3 Novel therapies to combat bacterial infections

Treating bacterial infections caused by MDR pathogens has become a critical challenge in modern healthcare, as conventional antibiotics increasingly fail to combat these evolving threats.[20–22] Among the most formidable culprits are the ESKAPE pathogens (*Enterococcus*

faecium, *S. aureus*, *K. pneumoniae*, *Acinetobacter baumannii*, *P. aeruginosa*, and *Enterobacter* species), which account for a disproportionate share of hospital-acquired infections and are linked to high mortality rates due to their pan-resistant profiles.[20,23] Addressing this challenge necessitates a paradigm shift in how we approach bacterial infections. Here, we will delve deeper into some of these innovative strategies, exploring their potential, challenges, and future directions in combating the global threat of AMR.

1.3.1 Antivirulence therapies

Antivirulence therapy represents a promising alternative to traditional antibiotics by focusing on neutralizing bacterial pathogenicity rather than killing bacteria or inhibiting their growth.[24,25] This approach reduces selective pressure for resistance development and preserves beneficial microbiota, addressing two critical limitations of conventional antimicrobials.[26] Key targets include bacterial toxins, biofilm formation, quorum sensing (QS) systems, and adhesins, which are essential for colonization, immune evasion, and disease progression (Figure 2).[27,28]

Toxins are prime targets due to their direct role in host damage. For example, inhibitors of anthrax toxin receptor binding, such as soluble receptor analogs or monoclonal antibodies, block *Bacillus anthracis* lethality in animal models.[29] Similarly, bezlotoxumab, an FDA-approved antivirulence agent, targets the toxin B (TcdB) in *Clostridioides difficile* infections.[30] Biofilm formation is targeted by disrupting the extracellular matrix or bacterial adhesion. It enhances antibiotic tolerance through physical barriers and metabolic adaptations.[31,32] Myrtenol, a plant-derived compound, inhibits *Acinetobacter baumannii* biofilm formation by suppressing extracellular polysaccharide synthesis and adhesion-related genes.[32] In *P. aeruginosa*, matrix-degrading enzymes or small molecules interfere with biofilm integrity, reducing chronic-infection persistence.[31] QS is disrupted by molecules that interfere with bacterial signaling pathways. QS inhibitors block autoinducer molecules (*e.g.*, *N*-acyl homoserine lactones in Gram-negative bacteria), preventing coordinated virulence-factor expression.[33,34] Tea polyphenols suppress *P. aeruginosa* QS systems (las, rhl), reducing elastase (LasB) and pyocyanin production while weakening biofilm formation.[34] Adhesins, such as lectins and surface proteins, are inhibited to prevent bacterial colonization. In *P. aeruginosa*, LecA mediates host-cell adhesion through carbohydrate binding, and inhibitors like galactose analogs block this interaction.[35,36]

Despite its advantages, antivirulence therapy has limitations. Pathogens can still evolve resistance to these strategies, albeit at a slower rate compared to traditional antibiotics.[37,38] Additionally, antivirulence drugs may not be effective as monotherapy in immunocompromised patients since their activity depends on host-mediated bacterial clearance rather than direct virulence attenuation.[27] Notably, combining antivirulence drugs with antibiotics has shown synergistic effects, restoring growth inhibition in antibiotic-resistant clones and even reversing resistance in some cases.[39] However, further research is needed to elucidate resistance mechanisms and optimize combination regimens for clinical use.

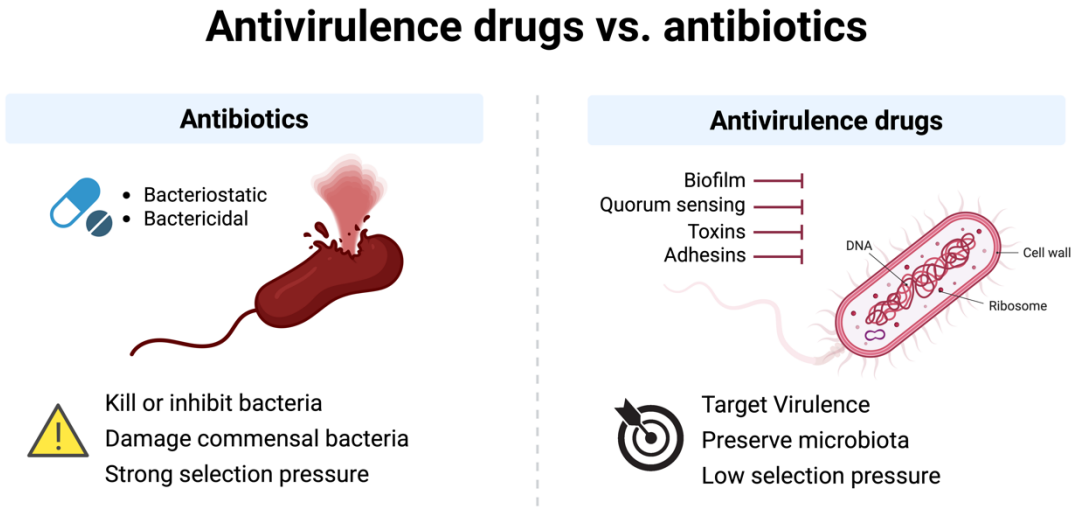

Figure 2: Comparison of antibiotics and antivirulence drugs. Antibiotic therapies target essential bacterial functions for growth or survival, while antivirulence therapies neutralize pathogenicity factors such as toxins, biofilm, quorum sensing, and adhesins, thereby preserving beneficial microbiota and reducing resistance selection pressure. Figure was created with **Biorender.com**.

1.3.2 Phage-based therapies

Bacteriophage (phage) therapy leverages viruses that specifically infect and lyse bacterial cells, offering a promising alternative to traditional antibiotics.[40] During a lytic infection cycle, phages attach to bacterial receptors, inject their genetic material, replicate within the bacterium, and ultimately lyse the host cell, releasing new phage particles.[41,42] This self-amplifying mechanism makes phages potentially more efficient than antibiotics, which do not replicate within the host.[42] For instance, a novel murine model demonstrated the efficacy of phage therapy against chronic *P. aeruginosa* lung infections, including in biofilm-associated cystic-fibrosis (CF) environments.[43] These findings underscore the potential of phage therapy for treating recalcitrant chronic infections.

Phage therapy offers high specificity, targeting only pathogenic bacteria while sparing beneficial microbiota, and is effective against antibiotic-resistant strains, making it a promising alternative to traditional antibiotics.[44] Nevertheless, it faces challenges such as bacterial resistance and immune system interactions.[45] Personalized phage cocktails tailored to specific bacterial strains complicate regulatory approval, while bacteria can evolve resistance by altering surface receptors or clustered regularly interspaced short palindromic repeats – CRISPR-associated proteins (CRISPR-Cas systems), although resistance rates are generally lower than with antibiotics.[46,47] Additionally, phages may trigger immune responses, reducing efficacy or causing inflammation in immunocompromised patients.[48–51] Current research focuses on combining phages with antibiotics or CRISPR-engineered phages to enhance efficacy and mitigate resistance risks.[52–55]

1.3.3 CRISPR-Cas-based antimicrobials

The CRISPR-Cas system, a naturally occurring bacterial defense mechanism, safeguards against foreign genetic elements by capturing and storing short sequences of invading DNA or

RNA. When the same genetic material is encountered again, the system identifies and degrades it, providing a robust immune response.[56] Researchers have harnessed this system to selectively target and disrupt bacterial genomes, offering a groundbreaking approach to combating infections, particularly those caused by antibiotic-resistant pathogens.[57] For instance, previous works have shown that introducing CRISPR sequences designed to target antibiotic resistance genes can lead to the elimination of recipient bacterial cells. This highlights the potential of engineered CRISPR systems to specifically target and neutralize pathogens by disrupting critical resistance or virulence genes.[58]

The CRISPR-Cas system offers several advantages, including high specificity, adaptability, and the ability to target multiple genes simultaneously.[59,60] However, challenges such as off-target effects, delivery mechanisms, and the evolution of CRISPR-resistant bacteria must be addressed to fully harness its potential.[61,62] Future prospects include refining CRISPR-based tools for precision antimicrobial therapy, developing CRISPR-based diagnostics, and exploring its role in modulating bacterial communities.[63,64] Continued research into CRISPR mechanisms and applications could revolutionize the fight against AMR and other infectious diseases, paving the way for more effective and targeted treatments.

1.3.4 Antimicrobial peptides (AMPs)

Antimicrobial peptides (AMPs) are naturally produced by a wide range of living organisms and are considered promising alternatives to traditional antimicrobial agents due to their broad-spectrum activity and potential to combat AMR.[65,66] These peptides are integral components of the innate immune system, primarily exerting their antibacterial effects by targeting bacterial cell membranes. They disrupt membrane permeability and structural integrity, leading to cell-structure damage.[67,68]

The therapeutic potential of AMPs is significant, as demonstrated by their ability to enhance the efficacy of existing antibiotics. For instance, combination therapy with the antimicrobial peptide DP7 has been shown to overcome resistance to vancomycin and azithromycin in pathogens such as *S. aureus*, *P. aeruginosa*, and *E. coli.* This highlights their role in addressing MDR infections.[69]

Despite their potential, the cytotoxicity of AMPs toward host cells remains a challenge, limiting their widespread clinical application. This has prompted extensive research into designing structural analogs with optimized properties to reduce toxicity while maintaining antimicrobial efficacy.[67,70] Efforts to refine AMPs include modifying their amino acid sequences, enhancing selectivity for bacterial membranes, and exploring novel delivery systems to minimize off-target effects.[71,72]

1.3.5 Antibodies and antibody-antibiotic conjugates (AACs)

Antibodies and antibody-antibiotic conjugates (AACs) are emerging as innovative tools to combat bacterial infections, particularly in the face of rising antibiotic resistance. Obiltoxaximab, an FDA-approved monoclonal antibody (mAb), neutralizes *B. anthracis* toxins, offering a critical treatment for inhalational anthrax. Its approval under the FDA's Animal Rule highlights the potential of mAbs in addressing life-threatening bacterial infections, despite risks

like hypersensitivity.[73] AACs combine the specificity of antibodies with the potency of antibiotics, delivering targeted therapy to bacterial cells while minimizing off-target effects.[74,75] AACs can enhance antibiotic efficacy, especially against intracellular pathogens like methicillin-resistant *S. aureus* (MRSA), by releasing potent antibacterial components directly at the infection site.[76] This approach not only reduces drug dosage but also addresses challenges such as toxicity and resistance. However, further research is needed to optimize their clinical application and overcome limitations like manufacturing difficulties.[77,78]

1.3.6 Vaccines

Vaccination serves as a critical strategy in addressing AMR by preventing infections and reducing reliance on antibiotics. Unlike antibiotics, vaccines target pathogens with high specificity, minimizing selective pressure on non-target microbes and lowering the risk of resistance emergence.[79] Resistance to vaccines is exceptionally rare because they preemptively block pathogen colonization or eliminate infections before replication, denying opportunities for adaptive mutations.[80] This mechanism relies on priming the immune system to rapidly neutralize pathogens through antibody-mediated responses or cellular immunity, thereby preventing symptomatic disease or reducing its severity.[80]

The *Haemophilus influenzae* type b (Hib) conjugate vaccine exemplifies this success, demonstrating >95% efficacy in preventing invasive Hib disease after a primary series of 2–3 doses.[81] Similarly, pneumococcal conjugate vaccines (PCVs) have reduced invasive pneumococcal disease by more than 90% in children under five through direct serotype-specific protection and herd immunity. Post-vaccination surveillance reveals near-elimination of vaccine-targeted antibiotic-resistant pneumococcal strains in immunized populations.[82]

In summary, vaccines are vital in reducing antibiotic use by preventing infections. Their targeted protection, ability to reduce transmission, and role in limiting resistant strains make them essential tools in global AMR prevention strategies.[83,84]

1.4 Bacterial proteases as drug targets

In the context of developing novel antivirulence therapies, bacterial proteases have emerged as promising drug targets due to their crucial roles in pathogen survival and virulence. Bacterial proteases represent a diverse and essential class of enzymes involved in maintaining cellular homeostasis, facilitating stress responses, and contributing to pathogenic mechanisms.[85] Pathogenic bacteria, particularly opportunistic species, exploit proteolytic enzymes as critical virulence factors to support host colonization, evade immune defenses, promote tissue invasion, and induce host damage during infection.[86] Among these, bacterial matrix metalloproteases (MMPs) are of particular interest, as they selectively cleave a broad range of substrates, including cytokines, cell surface receptors, adhesion molecules, and even other proteases, underscoring their therapeutic potential.[87] Several bacterial pathogens produce such enzymes: *S. aureus* secretes aureolysin, a metalloprotease that modulates immune responses and activates downstream virulence pathways, while *C. perfringens* expresses alpha-toxin, a phospholipase with serine protease-like properties that disrupt host cell membranes.[88,89] Additionally, bacterial collagenases from *Clostridium* species are metalloproteases capable of degrading multiple

forms of collagen, contributing to tissue destruction in conditions such as gas gangrene and gastrointestinal diseases.[90,91]

Among secreted bacterial metalloproteases, one of the most extensively studied is LasB, produced by *P. aeruginosa*. This zinc-dependent protease exhibits broad substrate specificity, enabling it to degrade host structural proteins and immune mediators, thereby facilitating infection and immune evasion.[92,93] Given its central role in the virulence of *P. aeruginosa*, LasB has emerged as a particularly attractive target for the development of novel antimicrobial therapies.

1.4.1 Targeting Elastase (LasB) in *P. aeruginosa*

P. aeruginosa is a Gram-negative, MDR pathogen that poses a significant clinical challenge, particularly in hospital-acquired pneumonia (HAP), ventilator-associated pneumonia (VAP), immunocompromised individuals, and patients with CF.[94,95] Its pathogenic success is attributed to an extensive range of cell-associated and secreted virulence determinants that collectively contribute to host invasion, immune evasion, and tissue damage.[96] A hallmark of *P. aeruginosa* infections is its capacity to form dense, structured biofilms, which exhibit strong resistance to antibiotics and host immune mechanisms. This biofilm-mediated protection significantly impairs bacterial clearance and fosters persistent, chronic infections.[97,98] Among the regulatory systems contributing to its virulence, QS plays a pivotal role. QS enables population-wide coordination of gene expression in response to cell density, orchestrating a wide range of behaviors including biofilm development, immune modulation, swarming motility, and the production of virulence factors.[96,99,100] In addition, *P. aeruginosa* utilizes a suite of specialized secretion systems to deliver an array of toxins and degradative enzymes directly into host tissues, facilitating colonization and immune subversion.[96,101]

Among these secreted factors, LasB is a major zinc-dependent metalloprotease exported via the type II secretion system (T2SS) and represents a key virulence component of *P. aeruginosa*.[102–104] LasB exerts broad pathogenic effects, including tissue invasion, degradation of structural matrix proteins, and interference with immune signaling. It facilitates immune evasion and promotes the establishment and maintenance of biofilms by modifying the local host environment.[104,105] LasB is the most abundantly secreted protease by *P. aeruginosa*, targeting vital structural components such as elastin, collagen, and laminin, leading to substantial tissue degradation.[106–108] Additionally, it impairs host defense by proteolytically degrading immunoglobulins IgG and IgA, as well as key cytokines including IL-6 and IL-8, thereby suppressing both innate and adaptive immune responses.[109–112]

Studies have confirmed that LasB contributes significantly to both acute and chronic pulmonary infections. In acute infection models, LasB induces the activation of IL-1β through a non-canonical, inflammasome-independent pathway, provoking a strong neutrophilic inflammatory response and consequent pulmonary damage.[113] In chronic infections — particularly in the context of CF — LasB supports bacterial persistence by degrading critical immune mediators such as IL-6, undermining immune surveillance and promoting long-term colonization. These effects have been validated in murine models.[114,115] Interestingly, during the course of chronic infection, *P. aeruginosa* exhibits adaptive phenotypic changes, including the downregulation

of *lasB* expression. This likely represents an evolutionary strategy to minimize immune detection and preserve a stable ecological niche within the host lung.[115]

Given its multifaceted role in tissue destruction, immune interference, and biofilm development, LasB stands out as a central virulence factor and a promising target for therapeutic antivirulence strategies.

1.4.2 The role of LasB in the disruption of respiratory barrier function

The pulmonary epithelium serves as a critical barrier that initiates the lung's response to both infectious and non-infectious challenges.[116] It is the body's first point of contact with inhaled substances and plays a vital role in protecting the lungs and maintaining normal respiratory function.[117] This protective function relies on the integrity of tight junctions (TJs) and adherens junctions (AJs), which regulate paracellular transport and preserve cell–cell interactions.[118] In chronic respiratory diseases such as chronic obstructive pulmonary disease (COPD) and CF, these junctional structures are frequently compromised, contributing to increased susceptibility to infection and inflammation.[119]

P. aeruginosa is a major cause of nosocomial infections and relies on a range of secreted virulence factors including LasB to establish infection, compromise host barrier integrity, and modulate immune response (Figure 3).[120,121] For systemic spread, *P. aeruginosa* must breach epithelial and endothelial barriers, a process in which LasB is critically involved. Studies have shown that LasB directly degrades essential junctional proteins such as VE-cadherin and occludin, weakening intercellular cohesion and enhancing paracellular permeability.[121–123] This proteolytic activity disrupts not only the structural integrity of cell–cell junctions but also the functional barrier that prevents bacterial dissemination. In the airway epithelium, LasB contributes further to barrier dysfunction by targeting Claudin-1 and Claudin-4 in nasal epithelial cells, leading to transient disassembly of tight junctions.[124] Moreover, LasB has been associated with the delocalization of key junctional proteins including occludin and zonula occludens-1 (ZO-1) in airway epithelial cells, although the exact pathways driving this redistribution are not yet fully understood.[125] These findings collectively underscore the role of LasB in promoting epithelial-barrier breakdown, a critical step in the pathogenesis and systemic spread of *P. aeruginosa*.

Despite growing evidence implicating LasB in epithelial-barrier disruption, the precise mechanisms by which it contributes to lung-disease progression remain insufficiently defined. Most current findings stem from isolated *in vitro* models or non-pulmonary systems, limiting our understanding of its role in the complex lung micro-environment. Advancing this knowledge is crucial for informing the development of antivirulence strategies that target LasB activity, with the aim of preserving epithelial integrity and preventing *P. aeruginosa* dissemination.

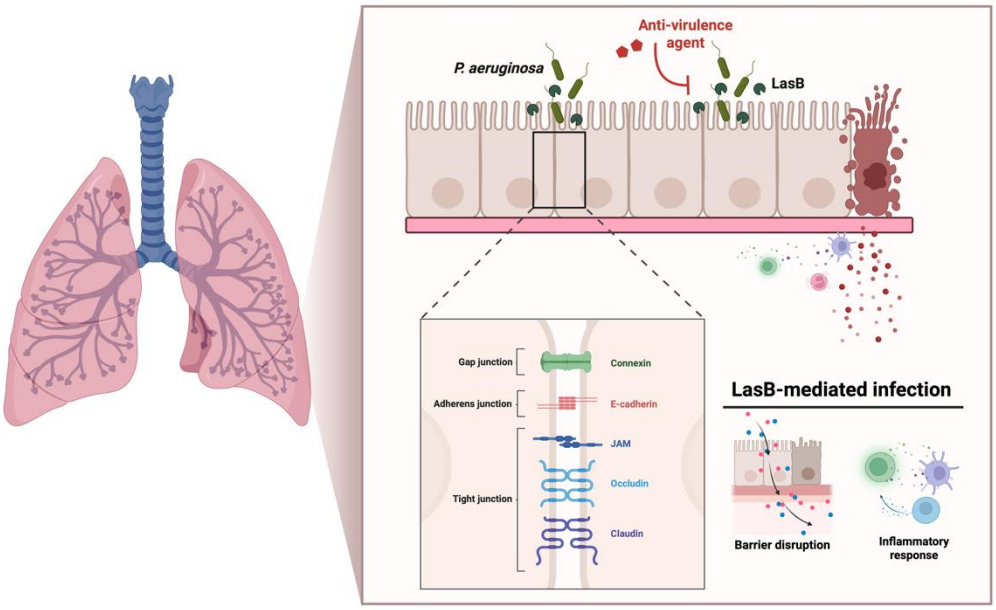

Figure 3: Role of LasB in epithelial barrier disruption and immune modulation. LasB degrades essential junctional proteins, weakening intercellular cohesion and increasing paracellular permeability. These actions compromise both structural and functional barriers, facilitating bacterial dissemination of *Pseudomonas aeruginosa*. Additionally, LasB modulates immune response, further promoting infection and systemic spread. Figure was created with **Biorender.com**.

1.4.3 Targeting LasB: Known inhibitors and therapeutic potential

The high abundance of LasB in the *P. aeruginosa* secretome and its broad spectrum of toxic effects on host-tissue integrity and immune function have positioned this zinc-dependent metalloprotease as a promising target for antivirulence therapy.[93] Most current approaches to inhibiting LasB focus on neutralizing its catalytic activity through interaction with the active-site zinc ion, typically employing a zinc-binding group (ZBG) to coordinate the metal and block enzymatic function.[104] Several distinct classes of LasB inhibitors have been developed, each offering unique chemical scaffolds and biological profiles. The compounds discussed below represent some of the most extensively studied examples to date.

Phosphoramidons were among the first compounds identified to inhibit LasB. Originally isolated from *Streptomyces tanashiensis* and characterized as thermolysin inhibitors (with a K_i value of ~30 nM at physiological pH), these compounds also exhibit activity against LasB due to the structural and functional homology between thermolysin and LasB.[126]

Thiols, particularly mercaptoacetamide derivatives, have shown significant inhibitory activity against LasB as well as clostridial and bacillary collagenases. These compounds have demonstrated *in vivo* efficacy in *Galleria mellonella* infection models and exhibit strong selectivity over human MMPs.[127] A notable subclass — *N*-aryl mercaptoacetamides — has been reported to inhibit both metallo-β-lactamases (MBLs) and LasB, with low micromolar to submicromolar potency.[128]

Hydroxamates are another extensively studied class of ZBGs, known for their strong chelation of zinc. Initially developed as derivatives of phosphoramidon, some hydroxamates have shown

potent LasB inhibition with nanomolar-range K_i values.[104,129] More recently, a hydroxamic acid-based inhibitor developed by Kany *et al*. was found to reduce *P. aeruginosa* biofilm formation and, for the first time, decrease extracellular DNA (eDNA) release, suggesting broader effects on bacterial virulence mechanisms.[130]

Phosphonates represent a newer class of LasB inhibitors with promising drug-like properties. A systematic exploration of ZBGs identified phosphonic acid derivatives exhibiting nanomolar inhibitory activity against LasB, alongside favorable *in vitro* ADMET profiles and strong *in vivo* efficacy when administered via inhalation in a murine lung infection model.[109] Further optimization within this class yielded compounds that, in murine models of *P. aeruginosa* keratitis, enhanced the therapeutic efficacy of meropenem in combination therapy and modulated immune responses when administered as monotherapy.[131]

While these inhibitors illustrate the diversity of chemical strategies explored for LasB inhibition, none have yet progressed to clinical application. Common limitations include suboptimal *in vivo* efficacy, limited stability, and insufficient selectivity.[104] Nevertheless, ongoing efforts continue to refine these scaffolds and investigate combination strategies to enhance therapeutic potential. Importantly, further progress in this field depends not only on compound optimization but also on a deeper mechanistic understanding of the role of LasB in infection and host interaction. Comprehensive characterization of this target is essential to guide future drug discovery and translational development.

1.5 Aims of this Thesis

The global rise in AMR demands novel therapeutic strategies that go beyond traditional antibiotics.[1] Antivirulence approaches — which aim to disarm bacterial pathogenicity without directly affecting viability — offer a promising avenue to circumvent resistance development while preserving host microbiota.[132,133] One clinically relevant antivirulence target is LasB, a zinc-dependent metalloprotease secreted by *P. aeruginosa*, which plays a multifaceted role in tissue damage, immune evasion, and disease progression, especially in lung infections.[92,93,109,130]

Although several small-molecule inhibitors have been developed to neutralize LasB activity, comparatively fewer studies have focused on elucidating the mechanistic impact of LasB on host–pathogen interactions in physiologically relevant lung models. A deeper understanding of the biological functions of LasB, particularly in the lung micro-environment, is critical for advancing therapeutic development and evaluating the translational potential of LasB-targeting strategies.

This thesis aims to address this gap by employing a multidisciplinary approach to investigate the biological effects of LasB across a range of experimental systems. It is structured into three chapters, each contributing to the overarching goal of validating LasB as a therapeutic target and exploring tools to evaluate its inhibition.

Chapter A focuses on dissecting the cellular and molecular mechanisms by which LasB disrupts the lung epithelial barrier. We established a transwell-based *in vitro* system using Calu-3 (bronchial) and Arlo (alveolar) epithelial cells to model distinct anatomical regions of the human lung. This comparative study was designed to investigate whether LasB exerts

differential effects across epithelial subtypes, recognizing that epithelial tissue-specific responses may influence disease progression and therapeutic response.

We assessed early-stage barrier disruption using non-invasive measurements of transepithelial electrical resistance (TEER) and paracellular permeability. These functional assays were complemented by molecular analyses of junctional-protein integrity including E-cadherin, using both confocal microscopy and Western blotting. Further, we investigated the immune-modulatory effects of LasB by quantifying transcriptional changes in a range of inflammatory and homeostatic cytokines, including *TNF*, *IL6*, *CSF*s, and others. Whole-transcriptome analysis revealed alterations in pathways relevant to lung defense and repair, including mitogen-activated protein kinase (MAPK) and fibroblast growth factor (FGF) signaling, and highlighted potential targets such as Claudin-4, whose expression was validated at both transcript and protein levels.

Chapter B expands the therapeutic evaluation of LasB by addressing its expression across clinical *P. aeruginosa* isolates. As part of a broader pharmacological study investigating the efficacy of newly developed LasB inhibitors, the strain used in a murine keratitis model had not been previously characterized for *lasB* expression.[131] To enable this, we established a qPCR-based assay for both relative and absolute quantification of *lasB* mRNA. The assay was applied to a panel of clinical isolates, including the keratitis strain, to determine the presence and variability of *lasB* expression. This approach not only validated the relevance of the tested strain for LasB-targeting interventions but also provided a standardized molecular tool to support future research and potential diagnostic applications in the context of strain-specific antivirulence strategies.

Chapter C builds on the therapeutic potential of LasB inhibition by evaluating a novel class of dual-acting inhibitors that target both LasB and LecA, a lectin involved in adhesion and biofilm formation during *P. aeruginosa* infections.[134] Using an A549 cell-based model, we evaluated the cytotoxicity and protective efficacy of three compounds — a LasB inhibitor, a LecA inhibitor, and a dual inhibitor — to determine whether the dual inhibitor outperforms the combination of the individual agents. Functional assays and fluorescence microscopy demonstrated that the dual inhibitor not only retained activity against LasB but also significantly reduced LecA-mediated effects, offering a promising approach for broader-spectrum antivirulence therapy.

Together, the three chapters of this thesis provide a comprehensive evaluation of LasB as a virulence factor — from mechanistic insights and biomarker discovery to therapeutic profiling and assay development. By integrating cellular models, gene and protein-level analyses, and pharmacological screening, this work aims to support the rational design of targeted interventions that could enhance treatment outcomes for *P. aeruginosa* lung infections in the era of antibiotic resistance.

1.6 References

1. Frieri, M., Kumar, K. & Boutin, A. Antibiotic resistance. *J Infect Public Health* **10**, 369–378 (2017).
2. Davies, J. & Davies, D. Origins and Evolution of Antibiotic Resistance. *Microbiology and Molecular Biology Reviews* **74**, 417–433 (2010).
3. Bush, K. *et al.* Tackling antibiotic resistance. *Nat Rev Microbiol* **9**, 894–896 (2011).
4. MacLean, R. C. & San Millan, A. The evolution of antibiotic resistance. *Science (1979)* **365**, 1082–1083 (2019).
5. Bo, L. *et al.* Combating antimicrobial resistance: the silent war. *Front Pharmacol* **15**, (2024).
6. Sharma, S. *et al.* Emerging challenges in antimicrobial resistance: implications for pathogenic microorganisms, novel antibiotics, and their impact on sustainability. *Front Microbiol* **15**, (2024).
7. Salam, Md. A. *et al.* Antimicrobial Resistance: A Growing Serious Threat for Global Public Health. *Healthcare* **11**, 1946 (2023).
8. Irfan, M., Almotiri, A. & AlZeyadi, Z. A. Antimicrobial Resistance and Its Drivers—A Review. *Antibiotics* **11**, 1362 (2022).
9. Wright, G. Mechanisms of resistance to antibiotics. *Curr Opin Chem Biol* **7**, 563–569 (2003).
10. Belay, W. Y. *et al.* Mechanism of antibacterial resistance, strategies and next-generation antimicrobials to contain antimicrobial resistance: a review. *Front Pharmacol* **15**, (2024).
11. Wise, R. A review of the mechanisms of action and resistance of antimicrobial agents. *Can Respir J* **6 Suppl A**, 20A–2A (1999).
12. Kapoor, G., Saigal, S. & Elongavan, A. Action and resistance mechanisms of antibiotics: A guide for clinicians. *J Anaesthesiol Clin Pharmacol* **33**, 300 (2017).
13. Peterson, E. & Kaur, P. Antibiotic Resistance Mechanisms in Bacteria: Relationships Between Resistance Determinants of Antibiotic Producers, Environmental Bacteria, and Clinical Pathogens. *Front Microbiol* **9**, (2018).
14. LAMBERT, P. Bacterial resistance to antibiotics: Modified target sites. *Adv Drug Deliv Rev* **57**, 1471–1485 (2005).
15. Dever, L. A. Mechanisms of Bacterial Resistance to Antibiotics. *Arch Intern Med* **151**, 886 (1991).
16. Reygaert, W. C. An overview of the antimicrobial resistance mechanisms of bacteria. *AIMS Microbiol* **4**, 482–501 (2018).
17. Darby, E. M. *et al.* Molecular mechanisms of antibiotic resistance revisited. *Nat Rev Microbiol* **21**, 280–295 (2023).
18. De Pascale, G. & Wright, G. D. Antibiotic Resistance by Enzyme Inactivation: From Mechanisms to Solutions. *ChemBioChem* **11**, 1325–1334 (2010).
19. Hunt, D. and O. S. Kates. A Brief History of Antimicrobial Resistance. *AMA J Ethics* **26**, E408-417 (2024).

20. Levy, S. B. & Marshall, B. Antibacterial resistance worldwide: causes, challenges and responses. *Nat Med* **10**, S122–S129 (2004).
21. Wang, C.-H., Hsieh, Y.-H., Powers, Z. M. & Kao, C.-Y. Defeating Antibiotic-Resistant Bacteria: Exploring Alternative Therapies for a Post-Antibiotic Era. *Int J Mol Sci* **21**, 1061 (2020).
22. Kumar, N. R., Balraj, T. A., Kempegowda, S. N. & Prashant, A. Multidrug-Resistant Sepsis: A Critical Healthcare Challenge. *Antibiotics* **13**, 46 (2024).
23. Chang, R. Y. K., Nang, S. C., Chan, H.-K. & Li, J. Novel antimicrobial agents for combating antibiotic-resistant bacteria. *Adv Drug Deliv Rev* **187**, 114378 (2022).
24. Cegelski, L., Marshall, G. R., Eldridge, G. R. & Hultgren, S. J. The biology and future prospects of antivirulence therapies. *Nat Rev Microbiol* **6**, 17–27 (2008).
25. Calvert, M. B., Jumde, V. R. & Titz, A. Pathoblockers or antivirulence drugs as a new option for the treatment of bacterial infections. *Beilstein Journal of Organic Chemistry* **14**, 2607–2617 (2018).
26. Maura, D., Ballok, A. E. & Rahme, L. G. Considerations and caveats in anti-virulence drug development. *Curr Opin Microbiol* **33**, 41–46 (2016).
27. Dehbanipour, R. & Ghalavand, Z. Anti-virulence therapeutic strategies against bacterial infections: recent advances. *Germs* **12**, 262–275 (2022).
28. Schütz, C. & Empting, M. Targeting the *Pseudomonas* quinolone signal quorum sensing system for the discovery of novel anti-infective pathoblockers. *Beilstein Journal of Organic Chemistry* **14**, 2627–2645 (2018).
29. Rasko, D. A. & Sperandio, V. Anti-virulence strategies to combat bacteria-mediated disease. *Nat Rev Drug Discov* **9**, 117–128 (2010).
30. Dickey, S. W., Cheung, G. Y. C. & Otto, M. Different drugs for bad bugs: antivirulence strategies in the age of antibiotic resistance. *Nat Rev Drug Discov* **16**, 457–471 (2017).
31. Bu, F. *et al.* Targeted Anti-Biofilm Therapy: Dissecting Targets in the Biofilm Life Cycle. *Pharmaceuticals (Basel)* **15**, (2022).
32. Selvaraj, A. *et al.* Antibiofilm and antivirulence efficacy of myrtenol enhances the antibiotic susceptibility of Acinetobacter baumannii. *Sci Rep* **10**, 21975 (2020).
33. BK, T. & MD, A. Targeting Quorum Sensing as a Next-Generation Approach to Bacterial Infections. *Open Access Journal of Microbiology & Biotechnology* **9**, 1–6 (2024).
34. Yin, H. *et al.* Tea polyphenols as an antivirulence compound Disrupt Quorum-Sensing Regulated Pathogenicity of Pseudomonas aeruginosa. *Sci Rep* **5**, 16158 (2015).
35. Cusumano, Z. T., Klein, R. D. & Hultgren, S. J. Innovative Solutions to Sticky Situations: Antiadhesive Strategies for Treating Bacterial Infections. *Microbiol Spectr* **4**, (2016).
36. Zahorska, E. *et al.* Neutralizing the Impact of the Virulence Factor LecA from *Pseudomonas aeruginosa* on Human Cells with New Glycomimetic Inhibitors. *Angewandte Chemie International Edition* **62**, (2023).
37. Lau, W. Y. V., Taylor, P. K., Brinkman, F. S. L. & Lee, A. H. Y. Pathogen-associated gene discovery workflows for novel antivirulence therapeutic development. *EBioMedicine* **88**, 104429 (2023).

38. Allen, R. C., Popat, R., Diggle, S. P. & Brown, S. P. Targeting virulence: can we make evolution-proof drugs? *Nat Rev Microbiol* **12**, 300–308 (2014).

39. Rezzoagli, C., Archetti, M., Mignot, I., Baumgartner, M. & Kümmerli, R. Combining antibiotics with antivirulence compounds can have synergistic effects and reverse selection for antibiotic resistance in Pseudomonas aeruginosa. *PLoS Biol* **18**, e3000805 (2020).

40. Gordillo Altamirano, F. L. & Barr, J. J. Phage Therapy in the Postantibiotic Era. *Clin Microbiol Rev* **32**, (2019).

41. Clokie, M. R. J., Millard, A. D., Letarov, A. V. & Heaphy, S. Phages in nature. *Bacteriophage* **1**, 31–45 (2011).

42. Kortright, K. E., Chan, B. K., Koff, J. L. & Turner, P. E. Phage Therapy: A Renewed Approach to Combat Antibiotic-Resistant Bacteria. *Cell Host Microbe* **25**, 219–232 (2019).

43. Waters, E. M. *et al.* Phage therapy is highly effective against chronic lung infections with *Pseudomonas aeruginosa*. *Thorax* **72**, 666–667 (2017).

44. Olawade, D. B. *et al.* Phage therapy: A targeted approach to overcoming antibiotic resistance. *Microb Pathog* **197**, 107088 (2024).

45. Abd-Allah, I. M., El-Housseiny, G. S., Yahia, I. S., Aboshanab, K. M. & Hassouna, N. A. Rekindling of a Masterful Precedent; Bacteriophage: Reappraisal and Future Pursuits. *Front Cell Infect Microbiol* **11**, (2021).

46. Mishra, V., Bankar, N., Tiwade, Y. & Ugemuge, S. How Phage Therapy Works, Its Advantages and Disadvantages: Mini Review. *J Pure Appl Microbiol* **18**, 177–184 (2024).

47. Caflisch, K. M., Suh, G. A. & Patel, R. Biological challenges of phage therapy and proposed solutions: a literature review. *Expert Rev Anti Infect Ther* **17**, 1011–1041 (2019).

48. Berkson, J. D. *et al.* Phage-specific immunity impairs efficacy of bacteriophage targeting Vancomycin Resistant Enterococcus in a murine model. *Nat Commun* **15**, 2993 (2024).

49. Souza, E. B. de, Pinto, A. R. & Fongaro, G. Bacteriophages as Potential Clinical Immune Modulators. *Microorganisms* **11**, 2222 (2023).

50. Podlacha, M. *et al.* Bacteriophage DNA induces an interrupted immune response during phage therapy in a chicken model. *Nat Commun* **15**, 2274 (2024).

51. Tang, M. *et al.* Host immunity involvement in the outcome of phage therapy against hypervirulent *Klebsiella pneumoniae* infections. *Antimicrob Agents Chemother* (2024) doi:10.1128/aac.01429-23.

52. Van Nieuwenhuyse, B. *et al.* Bacteriophage-antibiotic combination therapy against extensively drug-resistant Pseudomonas aeruginosa infection to allow liver transplantation in a toddler. *Nat Commun* **13**, 5725 (2022).

53. Stellfox, M. E. *et al.* Bacteriophage and antibiotic combination therapy for recurrent *Enterococcus faecium* bacteremia. *mBio* **15**, (2024).

54. Manohar, P. *et al.* Synergistic Effects of Phage–Antibiotic Combinations against *Citrobacter amalonaticus*. *ACS Infect Dis* **8**, 59–65 (2022).

55. Gencay, Y. E. *et al.* Engineered phage with antibacterial CRISPR–Cas selectively reduce E. coli burden in mice. *Nat Biotechnol* **42**, 265–274 (2024).

56. Pursey, E., Sünderhauf, D., Gaze, W. H., Westra, E. R. & van Houte, S. CRISPR-Cas antimicrobials: Challenges and future prospects. *PLoS Pathog* **14**, e1006990 (2018).

57. Duan, C., Cao, H., Zhang, L.-H. & Xu, Z. Harnessing the CRISPR-Cas Systems to Combat Antimicrobial Resistance. *Front Microbiol* **12**, (2021).

58. Bikard, D., Hatoum-Aslan, A., Mucida, D. & Marraffini, L. A. CRISPR Interference Can Prevent Natural Transformation and Virulence Acquisition during In Vivo Bacterial Infection. *Cell Host Microbe* **12**, 177–186 (2012).

59. Garneau, J. E. *et al.* The CRISPR/Cas bacterial immune system cleaves bacteriophage and plasmid DNA. *Nature* **468**, 67–71 (2010).

60. Walsh, R. M. & Hochedlinger, K. A variant CRISPR-Cas9 system adds versatility to genome engineering. *Proceedings of the National Academy of Sciences* **110**, 15514–15515 (2013).

61. Uribe, R. V. *et al.* Bacterial resistance to CRISPR-Cas antimicrobials. *Sci Rep* **11**, 17267 (2021).

62. Mayorga-Ramos, A., Zúñiga-Miranda, J., Carrera-Pacheco, S. E., Barba-Ostria, C. & Guamán, L. P. CRISPR-Cas-Based Antimicrobials: Design, Challenges, and Bacterial Mechanisms of Resistance. *ACS Infect Dis* **9**, 1283–1302 (2023).

63. Ahmed, M. *et al.* CRISPR-Cas Systems in the Fight Against Antimicrobial Resistance: Current Status, Potentials, and Future Directions. *Infect Drug Resist* **Volume 17**, 5229–5245 (2024).

64. Mayorga-Ramos, A., Zúñiga-Miranda, J., Carrera-Pacheco, S. E., Barba-Ostria, C. & Guamán, L. P. CRISPR-Cas-Based Antimicrobials: Design, Challenges, and Bacterial Mechanisms of Resistance. *ACS Infect Dis* **9**, 1283–1302 (2023).

65. Lewies, A., Du Plessis, L. H. & Wentzel, J. F. Antimicrobial Peptides: the Achilles' Heel of Antibiotic Resistance? *Probiotics Antimicrob Proteins* **11**, 370–381 (2019).

66. Lázár, V. *et al.* Antibiotic-resistant bacteria show widespread collateral sensitivity to antimicrobial peptides. *Nat Microbiol* **3**, 718–731 (2018).

67. Zharkova, M. S. *et al.* Application of Antimicrobial Peptides of the Innate Immune System in Combination With Conventional Antibiotics—A Novel Way to Combat Antibiotic Resistance? *Front Cell Infect Microbiol* **9**, (2019).

68. Browne, K. *et al.* A New Era of Antibiotics: The Clinical Potential of Antimicrobial Peptides. *Int J Mol Sci* **21**, 7047 (2020).

69. Wu, X. *et al.* Synergistic effects of antimicrobial peptide DP7 combined with antibiotics against multidrug-resistant bacteria. *Drug Des Devel Ther* **Volume11**, 939–946 (2017).

70. Min, K. H., Kim, K. H., Ki, M.-R. & Pack, S. P. Antimicrobial Peptides and Their Biomedical Applications: A Review. *Antibiotics* **13**, 794 (2024).

71. Talapko, J. *et al.* Antimicrobial Peptides-Mechanisms of Action, Antimicrobial Effects and Clinical Applications. *Antibiotics (Basel)* **11**, (2022).

72. Zhang, Q.-Y. *et al.* Antimicrobial peptides: mechanism of action, activity and clinical potential. *Mil Med Res* **8**, 48 (2021).

73. Greig, S. L. Obiltoxaximab: First Global Approval. *Drugs* **76**, 823–830 (2016).

74. Yu, L. *et al.* Antibody–Antimicrobial Conjugates for Combating Antibiotic Resistance. *Adv Healthc Mater* **12**, (2023).

75. Darbandi, A. *et al.* Antibody-Antibiotic Conjugates: A Comprehensive Review on Their Therapeutic Potentials Against BacterialInfections. *J Clin Lab Anal* **38**, e25071 (2024).

76. Lehar, S. M. *et al.* Novel antibody–antibiotic conjugate eliminates intracellular S. aureus. *Nature* **527**, 323–328 (2015).

77. Mariathasan, S. & Tan, M.-W. Antibody–Antibiotic Conjugates: A Novel Therapeutic Platform against Bacterial Infections. *Trends Mol Med* **23**, 135–149 (2017).

78. Cavaco, M., Castanho, M. A. R. B. & Neves, V. The Use of Antibody-Antibiotic Conjugates to Fight Bacterial Infections. *Front Microbiol* **13**, (2022).

79. Micoli, F., Bagnoli, F., Rappuoli, R. & Serruto, D. The role of vaccines in combatting antimicrobial resistance. *Nat Rev Microbiol* **19**, 287–302 (2021).

80. Buchy, P. *et al.* Impact of vaccines on antimicrobial resistance. *International Journal of Infectious Diseases* **90**, 188–196 (2020).

81. GRIFFITHS, U. K. *et al.* Dose-specific efficacy of *Haemophilus influenzae* type b conjugate vaccines: a systematic review and meta-analysis of controlled clinical trials. *Epidemiol Infect* **140**, 1343–1355 (2012).

82. Loo, J. D. *et al.* Systematic Review of the Effect of Pneumococcal Conjugate Vaccine Dosing Schedules on Prevention of Pneumonia. *Pediatric Infectious Disease Journal* **33**, S140–S151 (2014).

83. Jansen, K. U., Knirsch, C. & Anderson, A. S. The role of vaccines in preventing bacterial antimicrobial resistance. *Nat Med* **24**, 10–19 (2018).

84. Cohen, R., Cohen, J. F., Chalumeau, M. & Levy, C. Impact of pneumococcal conjugate vaccines for children in high- and non–high-income countries. *Expert Rev Vaccines* **16**, 625–640 (2017).

85. Culp, E. & Wright, G. D. Bacterial proteases, untapped antimicrobial drug targets. *J Antibiot (Tokyo)* **70**, 366–377 (2017).

86. Travis, J. & Potempa, J. Bacterial proteinases as targets for the development of second-generation antibiotics. *Biochimica et Biophysica Acta (BBA) - Protein Structure and Molecular Enzymology* **1477**, 35–50 (2000).

87. Vanlaere, I. & Libert, C. Matrix Metalloproteinases as Drug Targets in Infections Caused by Gram-Negative Bacteria and in Septic Shock. *Clin Microbiol Rev* **22**, 224–239 (2009).

88. Laarman, A. J. *et al.* Staphylococcus aureus Metalloprotease Aureolysin Cleaves Complement C3 To Mediate Immune Evasion. *The Journal of Immunology* **186**, 6445–6453 (2011).

89. Oda, M., Terao, Y., Sakurai, J. & Nagahama, M. Membrane-Binding Mechanism of Clostridium perfringens Alpha-Toxin. *Toxins (Basel)* **7**, 5268–5275 (2015).

90. Wu, S., Zhou, X., Jin, Z. & Cheng, H. Collagenases and their inhibitors: a review. *Collagen and Leather* **5**, 19 (2023).

91. Duarte, A. S., Correia, A. & Esteves, A. C. Bacterial collagenases – A review. *Crit Rev Microbiol* **42**, 106–126 (2016).

92. Cathcart, G. R. A. *et al.* Novel Inhibitors of the Pseudomonas aeruginosa Virulence Factor LasB: a Potential Therapeutic Approach for the Attenuation of Virulence Mechanisms in Pseudomonal Infection. *Antimicrob Agents Chemother* **55**, 2670–2678 (2011).

93. Everett, M. J. & Davies, D. T. Pseudomonas aeruginosa elastase (LasB) as a therapeutic target. *Drug Discov Today* **26**, 2108–2123 (2021).

94. Micek, S. T. *et al.* Pseudomonas aeruginosa Nosocomial Pneumonia: Impact of Pneumonia Classification. *Infect Control Hosp Epidemiol* **36**, 1190–1197 (2015).

95. Driscoll, J. A., Brody, S. L. & Kollef, M. H. The Epidemiology, Pathogenesis and Treatment of Pseudomonas aeruginosa Infections. *Drugs* **67**, 351–368 (2007).

96. Jurado-Martín, I., Sainz-Mejías, M. & McClean, S. Pseudomonas aeruginosa: An Audacious Pathogen with an Adaptable Arsenal of Virulence Factors. *Int J Mol Sci* **22**, 3128 (2021).

97. Lee, K. & Yoon, S. S. Pseudomonas aeruginosa Biofilm, a Programmed Bacterial Life for Fitness. *J Microbiol Biotechnol* **27**, 1053–1064 (2017).

98. Yan, S. & Wu, G. Can Biofilm Be Reversed Through Quorum Sensing in Pseudomonas aeruginosa? *Front Microbiol* **10**, (2019).

99. Lee, J. & Zhang, L. The hierarchy quorum sensing network in Pseudomonas aeruginosa. *Protein Cell* **6**, 26–41 (2015).

100. Kariminik, A., Baseri-Salehi, M. & Kheirkhah, B. Pseudomonas aeruginosa quorum sensing modulates immune responses: An updated review article. *Immunol Lett* **190**, 1–6 (2017).

101. Filloux, A. Protein Secretion Systems in Pseudomonas aeruginosa: An Essay on Diversity, Evolution, and Function. *Front Microbiol* **2**, (2011).

102. Bastaert, F. *et al.* Pseudomonas aeruginosa LasB Subverts Alveolar Macrophage Activity by Interfering With Bacterial Killing Through Downregulation of Innate Immune Defense, Reactive Oxygen Species Generation, and Complement Activation. *Front Immunol* **9**, (2018).

103. Everett, M. J. & Davies, D. T. Pseudomonas aeruginosa elastase (LasB) as a therapeutic target. *Drug Discov Today* **26**, 2108–2123 (2021).

104. Camberlein, V., Jézéquel, G., Haupenthal, J. & Hirsch, A. K. H. The Structures and Binding Modes of Small-Molecule Inhibitors of Pseudomonas aeruginosa Elastase LasB. *Antibiotics* **11**, 1060 (2022).

105. Kamath, S., Kapatral, V. & Chakrabarty, A. M. Cellular function of elastase in Pseudomonas aeruginosa: role in the cleavage of nucleoside diphosphate kinase and in alginate synthesis. *Mol Microbiol* **30**, 933–941 (1998).

106. Yang, J. *et al.* Mechanistic Insights into Elastin Degradation by Pseudolysin, the Major Virulence Factor of the Opportunistic Pathogen Pseudomonas aeruginosa. *Sci Rep* **5**, 9936 (2015).

107. Nagano, T. *et al. Downloaded from Iovs*. *Investigative Ophthalmology & Visual Science* vol. 42 (2001).

108. Heck, L. W., Morihara, K. & Abrahamson, D. R. Degradation of soluble laminin and depletion of tissue-associated basement membrane laminin by Pseudomonas aeruginosa elastase and alkaline protease. *Infect Immun* **54**, 149–153 (1986).

109. Konstantinović, J. *et al.* Inhibitors of the Elastase LasB for the Treatment of Pseudomonas aeruginosa Lung Infections. *ACS Cent Sci* **9**, 2205–2215 (2023).

110. Wretlind, B. & Pavlovskis, O. R. Pseudomonas aeruginosa Elastase and Its Role in Pseudomonas Infections. *Clinical Infectious Diseases* **5**, S998–S1004 (1983).

111. Saint-Criq, V. *et al. Pseudomonas aeruginosa* LasB protease impairs innate immunity in mice and humans by targeting a lung epithelial cystic fibrosis transmembrane regulator–IL-6–antimicrobial–repair pathway. *Thorax* **73**, 49–61 (2018).

112. Matheson, N. R., Potempa, J. & Travis, J. Interaction of a novel form of Pseudomonas aeruginosa alkaline protease (aeruginolysin) with interleukin-6 and interleukin-8. *Biol Chem* **387**, (2006).

113. Sun, J. *et al.* The Pseudomonas aeruginosa protease LasB directly activates IL-1β. *EBioMedicine* **60**, 102984 (2020).

114. Zhu, Y. *et al.* Clinical Strains of Pseudomonas aeruginosa Secrete LasB Elastase to Induce Hemorrhagic Diffuse Alveolar Damage in Mice. *J Inflamm Res* **Volume 14**, 3767–3780 (2021).

115. Cigana, C. *et al.* Pseudomonas aeruginosa Elastase Contributes to the Establishment of Chronic Lung Colonization and Modulates the Immune Response in a Murine Model. *Front Microbiol* **11**, (2021).

116. Brune, K., Frank, J., Schwingshackl, A., Finigan, J. & Sidhaye, V. K. Pulmonary epithelial barrier function: some new players and mechanisms. *American Journal of Physiology-Lung Cellular and Molecular Physiology* **308**, L731–L745 (2015).

117. Humlicek, A. L. *et al.* Paracellular Permeability Restricts Airway Epithelial Responses to Selectively Allow Activation by Mediators at the Basolateral Surface. *The Journal of Immunology* **178**, 6395–6403 (2007).

118. Pohl, C. *et al.* Barrier functions and paracellular integrity in human cell culture models of the proximal respiratory unit. *European Journal of Pharmaceutics and Biopharmaceutics* **72**, 339–349 (2009).

119. Carlier, F. M., de Fays, C. & Pilette, C. Epithelial Barrier Dysfunction in Chronic Respiratory Diseases. *Front Physiol* **12**, (2021).

120. Muggeo, A., Coraux, C. & Guillard, T. Current concepts on Pseudomonas aeruginosa interaction with human airway epithelium. *PLoS Pathog* **19**, e1011221 (2023).

121. Golovkine, G. *et al.* VE-Cadherin Cleavage by LasB Protease from Pseudomonas aeruginosa Facilitates Type III Secretion System Toxicity in Endothelial Cells. *PLoS Pathog* **10**, e1003939 (2014).

122. Berube, B. J., Rangel, S. M. & Hauser, A. R. Pseudomonas aeruginosa: breaking down barriers. *Curr Genet* **62**, 109–113 (2016).

123. Beaufort, N., Corvazier, E., Mlanaoindrou, S., de Bentzmann, S. & Pidard, D. Disruption of the Endothelial Barrier by Proteases from the Bacterial Pathogen Pseudomonas aeruginosa: Implication of Matrilysis and Receptor Cleavage. *PLoS One* **8**, e75708 (2013).

124. Nomura, K. *et al.* Pseudomonas aeruginosa elastase causes transient disruption of tight junctions and downregulation of PAR-2 in human nasal epithelial cells. *Respir Res* **15**, 21 (2014).

125. Clark, C. A., Thomas, L. K. & Azghani, A. O. Inhibition of Protein Kinase C Attenuates Pseudomonas aeruginosa Elastase–Induced Epithelial Barrier Disruption. *Am J Respir Cell Mol Biol* **45**, 1263–1271 (2011).

126. Poncz, L., Gerken, T. A., Dearborn, D. G., Grobelny, D. & Galardy, R. E. Inhibition of the elastase of Pseudomonas aeruginosa by N.alpha.-phosphoryl dipeptides and kinetics of spontaneous hydrolysis of the inhibitors. *Biochemistry* **23**, 2766–2772 (1984).

127. Kany, A. M. *et al.* Binding Mode Characterization and Early in Vivo Evaluation of Fragment-Like Thiols as Inhibitors of the Virulence Factor LasB from Pseudomonas aeruginosa. *ACS Infect Dis* **4**, 988–997 (2018).

128. Yahiaoui, S. *et al.* N-Aryl mercaptoacetamides as potential multi-target inhibitors of metallo-β-lactamases (MBLs) and the virulence factor LasB from Pseudomonas aeruginosa. *RSC Med Chem* **12**, 1698–1708 (2021).

129. Grobelny, D., Poncz, L. & Galardy, R. E. Inhibition of human skin fibroblast collagenase, thermolysin, and Pseudomonas aeruginosa elastase by peptide hydroxamic acids. *Biochemistry* **31**, 7152–7154 (1992).

130. Kany, A. M. *et al.* Tackling Pseudomonas aeruginosa Virulence by a Hydroxamic Acid-Based LasB Inhibitor. *ACS Chem Biol* **13**, 2449–2455 (2018).

131. Kiefer, A. F. *et al.* Dipeptidic Phosphonates: Potent Inhibitors of Pseudomonas aeruginosa Elastase B Showing Efficacy in a Murine Keratitis Model. *Advanced Science* **12**, (2025).

132. Schütz, C. & Empting, M. Targeting the Pseudomonas quinolone signal quorum sensing system for the discovery of novel anti-infective pathoblockers. *Beilstein Journal of Organic Chemistry* **14**, 2627–2645 (2018).

133. Calvert, M. B., Jumde, V. R. & Titz, A. Pathoblockers or antivirulence drugs as a new option for the treatment of bacterial infections. *Beilstein Journal of Organic Chemistry* **14**, 2607–2617 (2018).

134. Metelkina, O. *et al.* Dual inhibitors of Pseudomonas aeruginosa virulence factors LecA and LasB. *Chem Sci* **15**, 13333–13342 (2024).

2 Results

2.1 Chapter A

Exploring the Role of *Pseudomonas aeruginosa* Elastase in Lung Epithelial Barrier Dysfunction: Advancing Towards Antivirulence Therapies

Roya Shafiei‡, *Alaa Alhayek*‡, *Lukas Hiller, Lorenz Latta, Tobias Neu, Ahmad Aljohmani, Sahar Abdollahibiroun, Eva-Maria Schönborn, Daniela Yildiz, Nicole Schneider-Daum, Claus-Michael Lehr, Jörg Haupenthal, Anna K.H. Hirsch.*

‡ these authors contributed equally

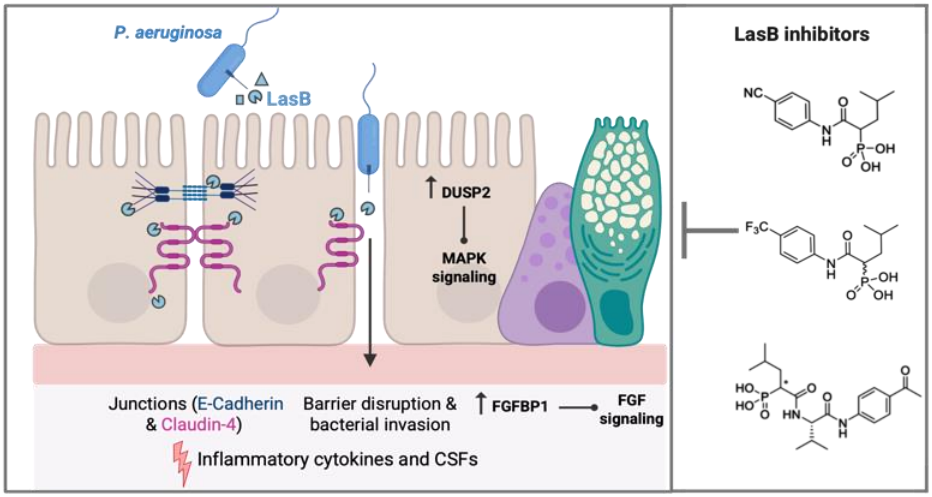

Manuscript submitted; under review for publication.

Abstract

Pseudomonas aeruginosa, a major cause of pulmonary infections, poses significant clinical challenges due to its virulence and rising antimicrobial resistance. This study highlights the role of LasB, a key virulence factor and elastase of *P. aeruginosa*, in disrupting the lung epithelial barrier. LasB cleaves the junctional protein E-cadherin, alters the localization of Claudin-4, and reducing levels of immunomodulatory cytokines including colony-stimulating factors GM-CSF and G-CSF. Using advanced bronchial and alveolar cell models, we demonstrate that LasB induces dose-dependent barrier damage in both systems. Transcriptomic analysis reveals widespread changes in gene expression, including upregulation of *DUSP2* and *FGFBP2*, genes associated with stress signaling and immune modulation. LasB inhibitors effectively mitigate barrier disruption and partially restore cytokine levels. In a living bacterial infection model, LasB inhibition synergizes with antibiotic treatment, enhancing bacterial clearance and preserving epithelial integrity. These findings establish LasB as a pivotal factor in *P. aeruginosa* pathogenesis and underscore the therapeutic potential of antivirulence strategies targeting LasB as promising adjuncts to conventional antibiotics.

Synopsis

LasB disrupts lung epithelial junctions and activates stress and immune evasion pathways; its inhibition restores barrier function and boosts antibiotic efficacy.

Keywords

Pseudomonas aeruginosa, LasB, Antivirulence therapies, Tight junctions, Colony stimulating factors, *DUSP2*, *FGFBP1*.

1. Introduction

The escalating problem of antimicrobial resistance (AMR) is one of the greatest challenges of global health, with *Pseudomonas aeruginosa* emerging as a major cause of antibiotic-resistant pulmonary infections.[1] This opportunistic pathogen poses a formidable threat due to its intrinsic virulence, diverse adaptation strategies, and ability to cause severe infections and high mortality even in the absence of antibiotic resistance.[2] Traditional antibiotics targeting bacterial viability are becoming increasingly ineffective against *P. aeruginosa*.[3] The ongoing rise in bacterial resistance, biofilm formation, and immune evasion mechanisms has rendered antibiotics less effective, leading to prolonged hospital stays, increased healthcare costs, and higher mortality rates.[4, 5] Consequently, there is an urgent need for resistance-agnostic therapeutic strategies that exert minimal selection pressure. Antivirulence strategies offer a promising alternative by disrupting bacterial pathogenic mechanisms rather than targeting viability, thereby reducing the risk of resistance while preserving the beneficial host microbiota.[6–8]

P. aeruginosa elastase (LasB) — secreted *via* the type II secretion system — plays a central role in pathogenicity.[9] This extracellular metalloprotease, known to degrade host structural proteins like elastin, collagen, and laminin, thereby facilitates tissue invasion and bacterial survival.[10–12] LasB also targets key immune components such as human immunoglobulins A and G, as well as pro-inflammatory cytokines like TNF, IL-1β, IFN-γ, and IL-6, exacerbating the infection severity.[13–17] Although the role of LasB in pathogenesis is well-studied, its precise mechanism in lung infections –

as well as how its inhibition might preserve the lung barrier and enhance antibiotic efficacy – remains poorly understood.

The lung epithelial barrier is crucial for protection against pathogens and environmental stressors.[18] Bronchial and alveolar epithelial cells — presented by the human lung adenocarcinoma cell line Calu-3 and the monoclonal human alveolar epithelial cell line Arlo, respectively — serve as physiological relevant in vitro models for studying lung infections.[19, 20] Calu-3 cells mimic key features of the bronchial epithelium in vivo, forming polarized monolayers with tight junctions — *e.g.,* Zonula Occludens-1 (ZO-1) and E-cadherin — and exhibiting transepithelial electrical resistance (TEER) values reaching ~300 Ω·cm² under air-liquid interface (ALI) culture conditions.[21, 22] In contrast, Arlo cells model the alveolar epithelium with high TEER values (up to ~3000 Ω·cm² under ALI conditions), which leads to improved barrier properties and mimicks the alveolar epithelium well in vivo.[23] Importantly, Arlo cells express genes relevant to barrier integrity and homeostasis, similar to primary human alveolar epithelial cells (hAEpC), offering a more physiologically relevant model for human-specific studies.[23] Models based on human cells and tissues are promising alternatives to animal experiments, allowing for the isolation of essential human biological processes and making them accessible in vitro.[23, 24] Together, these models of bronchial and alveolar epithelial cells provide a platform for investigating the impact of LasB on epithelial integrity and immune modulation.

This study aims to elucidate the biological impact of LasB on lung epithelium, focusing on its mechanisms of action at cellular and molecular levels. LasB disrupts junctional proteins like occludin and VE-cadherin, leading to increased permeability and barrier dysfunction.[10] This effect is observed not only in lung models but also in other epithelial systems such as the corneal epithelium, and in mouse models where LasB induces severe lung injury and diffuse alveolar damage.[25, 26] While LasB and antivirulence agents have been well studied in recent years, the need for physiologically relevant in vitro studies on lung cells that reflect the in vivo conditions remains high.[27–31] In particular, the role of LasB in immune modulation at the transcriptomic level remains to be investigated. Our research employs filter-based models in liquid-covered conditions (LCC) and transcriptomic analyses to investigate the effects of LasB on epithelial barriers, immune responses, and gene expression.

Our findings reveal a complex interplay of cellular responses, with LasB inducing diverse changes in gene expression patterns, particularly in pathways related to bacterial infection, cellular processes, and immune modulation, including FGF and MAPK signaling. These insights deepen our understanding of the molecular mechanisms underlying *P. aeruginosa* pathogenesis and highlight critical targets for therapeutic intervention. The identification of consistent gene expression patterns across experimental conditions advances diagnostic strategies by uncovering biomarkers to track disease progression and assess treatment efficacy, addressing a significant gap in evaluating antivirulence therapies in vivo and in clinical settings.[32, 33] By integrating functional assays, protein analyses, and transcriptomic studies, this study lays the groundwork for developing targeted therapies that synergize with antibiotics or immune modulators, offering a dual strategy to enhance bacterial clearance and preserve epithelial integrity in clinical settings.

2. Results and Discussion

2.1. LasB-Mediated Disruption of Epithelial Integrity and Immune Modulation in Bronchial and Alveolar Cells

Maintaining epithelial barrier integrity is critical for preventing microbial invasion and preserving lung function. In *P. aeruginosa* infections, the virulence factor LasB plays a key role in compromising this barrier by targeting junctional proteins, thereby undermining host defenses.[26, 34, 35] To assess the impact of LasB on lung epithelial integrity, we examined LasB-mediated changes in transepithelial electrical resistance (TEER), paracellular permeability to fluorescein sodium (FluNa), immune responses, and cleavage of the tight junction protein E-cadherin in bronchial Calu-3 and alveolar Arlo cells (Figure 1A). These complementary readouts provide a comprehensive view of barrier dynamics in cell models that closely resemble in vivo lung conditions. TEER and FluNa permeability are inversely related metrics of epithelial integrity, where higher TEER reflects a more intact barrier, while increased FluNa permeability reflects junctional disruption.[36–38]

LasB Effect on Calu-3 Cells: Disruption

In Calu-3 cells, exposure to bacterial supernatant (sn) from the wild-type (wt) LasB-producing *P. aeruginosa* strain PAO1 induced a concentration-dependent decrease in TEER, with up to a 77.9% reduction observed within 1h of exposure to 40% wt PAO1 sn, resulting in near-complete barrier loss by 7 h (Figure 1B). This decline was accompanied by a significant increase in FluNa permeability, confirming the compromised barrier function (Figure 1C). In contrast, sn from the LasB-deficient PAO1 mutant (Δ*lasB*) caused only moderate TEER reductions and minimal increases in FluNa permeability, with signs of partial recovery over time. This suggests that the absence of LasB mitigates junctional damage. Furthermore, clinical isolates NH57388A muc. and RP73, which express low levels of *lasB* (Figure S1) induced only limited changes in TEER and FluNa permeability, further supporting the central role of LasB in epithelial barrier disruption (Figure S2). [39, 40]

To determine the quantity of LasB required to disrupt the epithelial barrier, we treated Calu-3 cells with increasing concentrations of purified LasB. TEER measurements showed a clear, dose-dependent barrier-disrupting effect (Figure S3), with initial signs of disruption already evident at concentrations as low as 3 nM. Notably, the barrier disruption caused by 20% and 40% wt PAO1 sn was comparable to that induced by approximately 100 nM and 200 nM of purified LasB, respectively. This demonstrates that only a small amount of active LasB is needed to compromise barrier integrity, and even low levels present in clinical isolates can exert a potent disruptive effect. These findings underscore the clinical challenge that minimal quantities of LasB remain highly active and damaging to the lung epithelial barrier.

LasB Effect on Arlo Cells: Differential Resistance

Despite their inherently tighter barriers, Arlo cells also exhibited a concentration-dependent decline in TEER upon exposure to wt PAO1 sn, with reductions of up to 95.7% after 40% sn treatment, compared to the negative control cells (no sn) (Figure 1E). However, the extent of barrier disruption was less pronounced compared to Calu-3 cells, as reflected by a smaller increase in FluNa permeability (Figure 1F). This indicates that the inherently stronger barrier properties of Arlo cells provide partial resistance to LasB-mediated damage. In contrast, exposure to Δ*lasB* PAO1 sn resulted in sustained TEER and

minimal changes in FluNa permeability, suggesting that the absence of LasB preserves barrier function and may activate recovery mechanisms.

To confirm the non-invasive nature of the assay and rule out significant cell death during the 7 h exposure period, we measured lactate dehydrogenase (LDH) release. No significant differences in LDH levels were observed between treated and control groups in both cell types, indicating that LasB-mediated barrier disruption occurs independently of substantial death (Figure 1D, G). Importantly, these findings demonstrate that LasB can exert damaging effects even at low, non-cytotoxic concentrations, highlighting its ability to disrupt the epithelial barrier without inducing cell death.

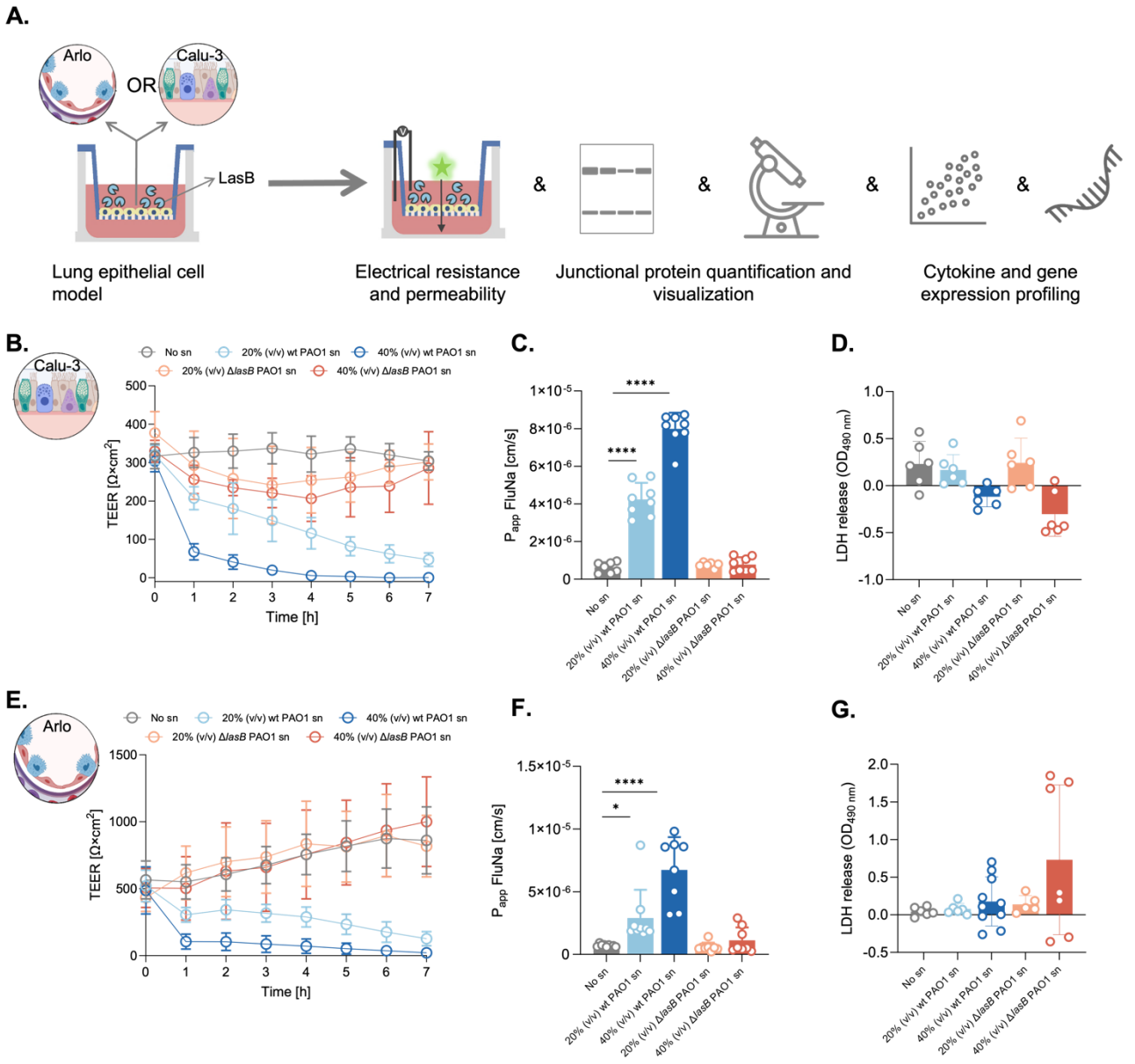

Figure 1: Experimental workflow and epithelial barrier disruption in Calu-3 and Arlo cells. (A) Overview of the experimental workflow. Calu-3 and Arlo cells were cultured on Transwell inserts until stable transepithelial electrical resistance (TEER) was achieved, followed by treatment with 20% and 40% (v/v) supernatants (sn) from *Pseudomonas aeruginosa* PAO1 wild-type (wt) and *lasB* knockout (Δ*lasB*) strains. Downstream analyses included TEER measurement, permeability of fluorescein sodium (FluNa), lactate dehydrogenase (LDH) release, junctional protein analysis, cytokine profiling, and gene expression. **(B–D)**

Barrier function in Calu-3 cells: **(B)** TEER, **(C)** FluNa permeability (P_{app}), and **(D)** LDH release under the indicated conditions. **(E–G)** Corresponding analyses in Arlo cells: **(E)** TEER, **(F)** FluNa permeability, and **(G)** LDH release. Data represent mean ± standard deviation (n = 3 independent experiments, each sample with 2 replicates within an experiment). Statistical analyses were performed using ordinary one-way ANOVA followed by Dunnett's multiple comparisons test comparing the mean value of each group with wt PAO1 sn (****$p \leq 0.0001$; ***$p \leq 0.001$; *$p \leq 0.05$).

Molecular Mechanisms of LasB-Mediated Barrier Disruption

To elucidate the molecular mechanisms underlying LasB-induced epithelial barrier disruption, we investigated the cleavage of the tight junction protein E-cadherin, a critical mediator of epithelial integrity.[41] We observed complex, cell-type-specific responses in E-cadherin dynamics in response to LasB exposure.

In Calu-3 cells, western blot analysis showed significant cleavage of E-cadherin upon exposure to wt PAO1 sn compared to Δ*lasB* PAO1 sn and no supernatant (no sn) control (Figure 2A, B). Interestingly, confocal laser scanning microscopy (CLSM) revealed a strong E-cadherin signal in wt PAO1 sn-treated Calu-3 cells, contrasting with weaker signals in control conditions (Figure 2C). This apparent discrepancy, coupled with the absence of significant changes in E-cadherin gene expression (Figure S4), suggests a post-translational response, possibly involving redistribution of existing E-cadherin to the cell surface, reduced protein turnover, or activation of a preexisting pool of E-cadherin as a compensatory response to junctional disruption. Notably, different antibodies were employed for western blot and CLSM due to compatibility constraints. Thus, partial cleavage of E-cadherin may abolish detection by western blot, while the CLSM antibody could still recognize intact epitopes, potentially accounting for the observed discrepancy.

In Arlo cells, western blot analysis showed only minor E-cadherin degradation following exposure to wt PAO1 supernatant, with no statistically significant differences between conditions (Figure 2D, E). While direct LasB effects appear limited, it is possible that in the presence of live bacteria, additional virulence mechanisms such as Type III Secretion System (T3SS) could facilitate epithelial disruption and enhance LasB accessibility to junctional targets. CLSM imaging showed weak E-cadherin signals across all conditions, with the appearance of punctate structures in wt PAO1 sn-treated cells (Figure 2F). These dots may represent cleaved E-cadherin fragments or indicate reorganization of E-cadherin in response to cellular stress. The less pronounced E-cadherin cleavage in Arlo cells compared to Calu-3 may reflect differences in E-cadherin expression, stability, or post-translational modifications, as well as Arlo cells' tighter junctions and higher TEER, which could limit LasB access to junctional proteins.[23] Additionally, Arlo cells may activate stress responses that reorganize or protect E-cadherin, and cell-type-specific differences in LasB susceptibility could further contribute to their relative resilience.

These findings highlight the differential responses of bronchial (Calu-3) and alveolar (Arlo) epithelial cells to LasB-induced stress, emphasizing the importance of post-translational mechanisms in maintaining epithelial barrier integrity. The cell type-specific responses underscore the complexity of host-pathogen interactions in *P. aeruginosa* infections and suggest that targeted therapeutic strategies may need to account for these tissue-specific differences to be most effective.

LasB Modulates Cytokine Expression and Cleavage to Suppress Immunity and Induce Tissue Damage

LasB degrades inflammatory cytokines that are essential for immune coordination during infection.[10, 42, 43] Our cytometric bead array (CBA) data revealed that challenging both lung cell types with wt PAO1 sn resulted in markedly reduced levels of IL-6 and TNF. This suggests that these cytokines may be degraded by the elastase (Figure 2G). LasB degradation of IL-6 is well characterized; the protease directly cleaves the cytokine, thereby suppressing immune signaling and epithelial repair pathways, as validated by protease-specific assays.[43, 44] While an earlier study suggest that *P. aeruginosa* elastase cleaves TNF, the specific contribution of LasB is unclear.[42] In our assay, TNF levels were significantly reduced in the presence of LasB, supporting the hypothesis that LasB contributes to its degradation during infection. Notably, cells challenged with Δ*lasB* PAO1 sn exhibited higher levels of most cytokines, except IL-1β, which showed slightly reduced activation compared to wt PAO1 sn-treated cells (Figure 2G). This suggests that LasB selectively modulates cytokine activity by suppressing certain mediators while promoting IL-1β maturation.[45, 46] Furthermore, these findings indicate that LasB-induced barrier disruption is primarily attributed to its proteolytic activity on junctional proteins rather than inflammatory processes, as it occurs independently of pro-inflammatory cytokine signaling.

Gene expression analyses revealed distinct patterns between Calu-3 and Arlo cells. Overall pro-inflammatory cytokine expression was significantly higher in Calu-3 cells. In these cells, wt PAO1 sn induced a stronger upregulation of *TNF*, *IL1A*, *IL1B*, and *CXCL8* compared to Δ*lasB* PAO1 sn, even though *TNF* and *IL6* were diminished at the protein level (Figure 2H). This discrepancy suggests transcriptional responses may compensate for LasB-associated reductions in cytokine protein abundance. The robust inflammatory response in Calu-3 cells aligns with their anatomical role as bronchial epithelial cells, which are evolutionarily primed to initiate immune signaling through cytokine/chemokine production and interaction with submucosal immune cells like macrophages and dendritic cells.[47, 48] This is supported by studies showing that Calu-3 cells actively secrete IL-6, CXCL8, and IL-10 during infection and thus, initiate inflammatory cascades.[49, 50]

In contrast, Arlo cells showed a different cytokine expression pattern (Figure 2H). *TNF* expression remained comparable between wt PAO1 sn and Δ*lasB* PAO1 sn, while *IL1A* was more upregulated in wt PAO1 sn-treated cells. Conversely, *CXCL8* and *IL1B* were more strongly upregulated in Δ*lasB* PAO1 sn-treated cells. These differences likely reflect cell line-specific properties, as different model systems can exhibit distinct immune-related responses, making it challenging to define clinically relevant pathways. Additionally, the more restrained inflammatory signaling observed in Arlo cells may be due in part to the absence of immune cells, such as alveolar macrophages, which are known to amplify cytokine responses in vivo.[51] Our findings are consistent with studies highlighting the crucial role of LasB in immune evasion, allowing chronic colonization.[43, 52] By reducing levels of cytokines such as IL-6 and simultaneously activating others like IL-1β, LasB creates a balanced environment that suppresses immunity while inducing localized tissue damage, potentially facilitating bacterial persistence.

To examine how LasB modulates anti-inflammatory signaling, we assessed the expression of *IL4*, *IL13*, *IL37*, and *TGFB1* in both cells. Most of these cytokines showed negligible expression, with *TGFB1* being the only one consistently expressed across all samples. However, exposure of cell to wt PAO1 sn did not alter *TGFB1* or any other tested anti-inflammatory cytokines, suggesting that its primary role is to modulate pro-inflammatory mediators rather than directly induce an anti-inflammatory response.

The impact of LasB extends beyond inflammatory cytokines and also includes colony-stimulating factors (CSFs), which are crucial for myeloid cell function.[53] Our data reveal that LasB induced a marked reduction in both GM-CSF (encoded by *CSF2*) and G-CSF (encoded by *CSF3*) levels in bronchial Calu-3 cells, suggesting that LasB may contribute to the degradation of these cytokines (Figure 2G). Notably, previous in vivo studies have reported reduced G-CSF levels as a consequence of LasB activity in mice, supporting our findings and

highlighting the relevance of this mechanism in disease models.[17] Interestingly, Calu-3 cells showed differential regulation of these CSFs when challenged with wt PAO1 sn versus Δ*lasB* PAO1 sn. *CSF2* upregulation was lower upon infection with Δ*lasB* PAO1 sn, while *CSF3* showed higher upregulation, suggesting that LasB promotes GM-CSF production but inhibits G-CSF at protein levels (Figure 2H). This complex modulation of CSFs by LasB aligns with its established role in immune evasion and early infection stages, particularly its higher activity in initial colonization. Additionally, LasB is able to diminish not only junctional proteins, but also various host immune factors.[43, 54] These results indicate a sophisticated mechanism by which *P. aeruginosa* manipulates the response of host myeloid cells and possibly influences the function of neutrophils and macrophages during the early phase of infection.[54, 55] Our findings underline the multifaceted role of LasB in the pathogenesis of *P. aeruginosa* and its potential as a therapeutic target to prevent initial colonization.[56]

The contrasting protein and gene expression profiles observed in our study underscore the complexity of host-pathogen interactions, where transcriptional responses may act to counterbalance protease activity. This dual mechanism provides insight into why Δ*lasB* strains, despite inducing stronger immune activation, exhibit reduced chronic colonization in vivo.[52, 57] Overall, these findings emphasize the importance of LasB as a therapeutic target in *P. aeruginosa* in early stages of infection, prompting further exploration of anti-virulence strategies targeting this multifaceted virulence factor.

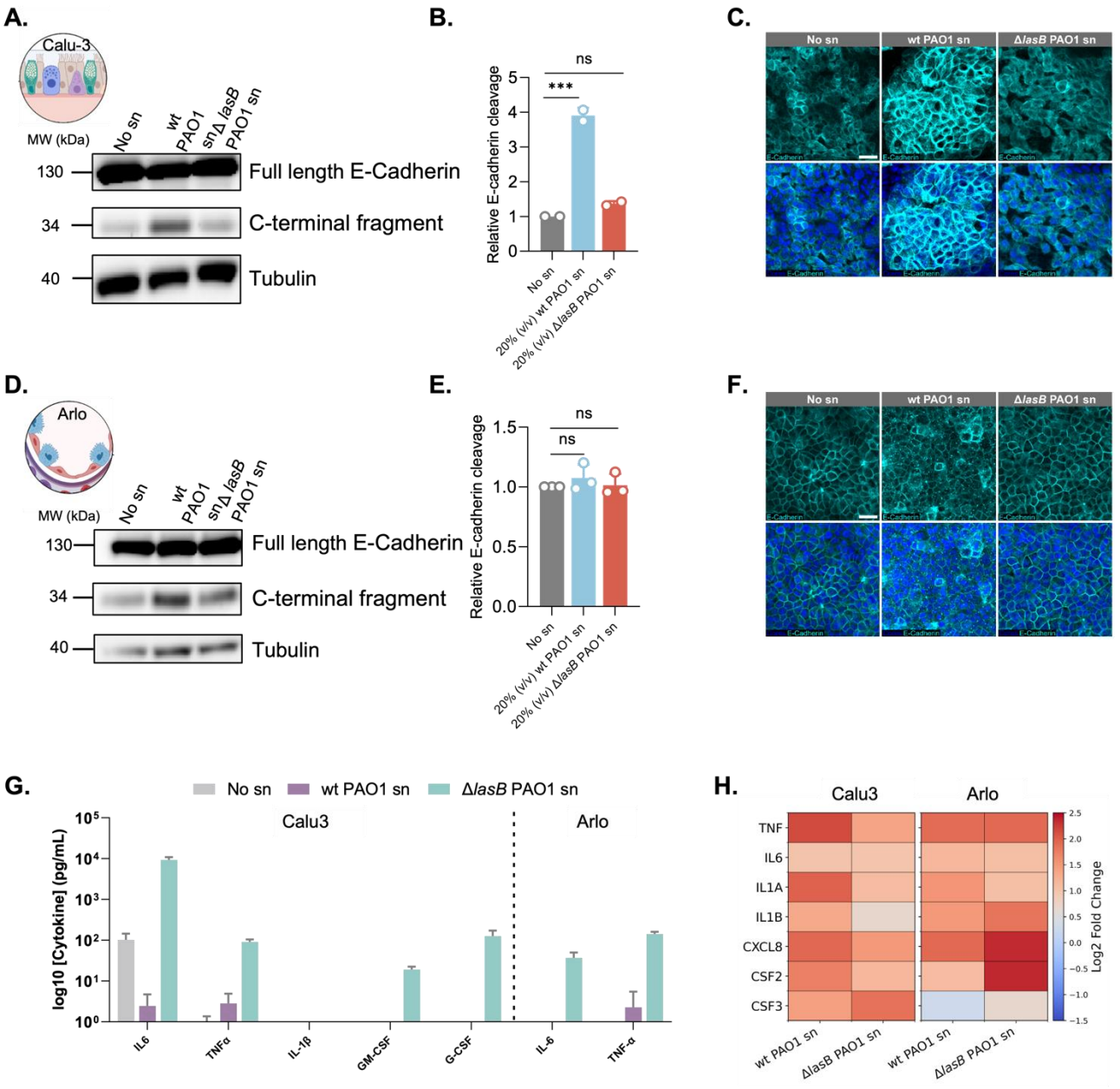

Figure 2: LasB-mediated cleavage of E-cadherin and modulation of inflammatory responses in bronchial and alveolar epithelial cells. (A, D) Western blot analysis of E-cadherin and C-terminal fragments in **(A)** Calu-3 and **(D)** Arlo cells treated with 20% (v/v) *Pseudomonas aeruginosa* wild-type (wt) PAO1 supernatant (sn), Δ*lasB* PAO1 sn, or no sn (control). **(B, E)** Quantification of E-cadherin cleavage relative to total E-cadherin levels. Data represent mean ± SD (n = 3). Statistical analyses were performed using one-way ANOVA with Dunnett's multiple comparisons test (***p ≤ 0.001; ns, not significant). **(C, F)** Confocal microscopy of E-cadherin (cyan) and DAPI (blue) in **(C)** Calu-3 and **(F)** Arlo cells. Scale bars: 25 µm. **(G)** Cytometric bead array (CBA) quantification of secreted inflammatory cytokines and colony-stimulating factors (CSFs) in bronchial Calu-3 (left) and alveolar Arlo (right) cells under healthy conditions, or following challenge with wild-type (wt) *Pseudomona aeruginosa* PAO1 supernatant (sn) or Δ*lasB* PAO1 sn. Data are presented as $\log_{10}$-transformed concentrations (pg/mL). **(H)** Gene expression profiles of key inflammatory mediators in bronchial Calu-3 (left) and alveolar Arlo (right) cells following exposure to wt PAO1 sn or Δ*lasB* PAO1 sn, displayed as $\log_2$ fold changes relative to healthy no sn controls. Values represent mean ± SD (n ≥ 3).

2.2. Inhibition of LasB-Induced Virulence: Restoring Epithelial Integrity

To evaluate the potential of antivirulence strategies in mitigating LasB-induced barrier dysfunction, we tested three recently published phosphonate-based LasB inhibitors (compounds **1** – **3**) (Table S1).[30, 58] These compounds have shown high efficacy in vivo and a favorable ADMET profile, highlighting their translational potential.

In Calu-3 cells, all three compounds significantly attenuated LasB-induced decrease in TEER at 100 µM. Compounds **1**, **2**, and **3** preserved TEER values at approximately 79.7%, 88.6%, and 95.4% of no sn control levels, respectively, compared to the drastic reduction to 14.1% observed in untreated wt PAO1 sn-challenged cells (Figure 3A). This protective effect was observed across all concentrations tested (*i.e.,* 10 and 1 µM), with a slight dose-dependency (Figure S5). Paracellular permeability assays using FluNa revealed that compound-treated cells treated with wt PAO1 sn exhibited permeability comparable to cells treated with Δ*lasB* PAO1 sn, indicating effective preservation of barrier integrity (Figure 3B). In Arlo cells, which have tighter junctions, the protective effect was more modest. TEER values were maintained at 53.6% with compound **1** and 40.4% with compounds **2** and **3** when challenged with wt PAO1 sn, compared to the severe reduction to 8.4% seen in untreated challenged cells (Figure 3F). While these compounds effectively enhanced epithelial barrier function in both cell types, their impact was more pronounced in Calu-3 cells. This difference likely reflects Arlo cells' stronger baseline barrier integrity, which may limit further improvements in TEER upon treatment. Nonetheless, significant reductions in paracellular permeability were still observed in both cell types following compound treatment, indicating effective restoration of barrier function even in cells with stronger junctions (Figure 3B, G). Notably, Arlo cells challenged with Δ*lasB* PAO1 sn showed progressive increases in TEER over time, suggesting engagement of compensatory mechanisms to restore barrier function in the absence of LasB (Figure 3F). Interestingly, Arlo cells in a healthy state also exhibited gradual TEER increases during prolonged culture. This likely reflects ongoing tight junction maturation *in vitro*, which may be amplified under Δ*lasB* PAO1 sn-treated conditions. Together, these findings underscore the crucial role of LasB in disrupting epithelial integrity during infection. To ensure specificity, we tested the compounds against Δ*lasB* PAO1 sn and assessed their potential cytotoxicity (Figure S6). Neither TEER nor permeability assays revealed any off-target effects or cytotoxicity, confirming that the observed preservation of barrier function was due to specific LasB inhibition (Figure S6). LDH release measurements further validated the non-invasive nature of the TEER assay and the absence of cell death (Figure S7).

Western blot analysis confirmed our previous observations, revealing more pronounced C-terminal fragment bands of E-cadherin in wt PAO1 sn treated Calu-3 cells compared to the negative control (no sn) and cells treated with Δ*lasB* PAO1 sn, indicative of LasB-mediated cleavage (Figure 3C). Treatment with each compound at 100 µM effectively inhibited this LasB-induced E-cadherin degradation with the resulting C-terminal fragment levels comparable to no sn and Δ*lasB* PAO1 sn controls. The quantification of E-cadherin cleavage further corroborated these findings, demonstrating that all compounds inhibited cleavage, with compound **3** showing the highest efficacy (Figure 3D). These results provide evidence that our compounds successfully mitigate LasB-induced E-cadherin degradation, thereby preserving epithelial barrier integrity. Arlo cells, on the other hand, did not show significant differences in E-cadherin cleavage upon compound treatment, which may be attributed to their inherently stronger barrier properties that make them less susceptible to LasB-mediated barrier

disruption (Figure S8). Consequently, the extent of E-cadherin cleavage in Arlo cells is limited, so the protective effect of the inhibitors is less pronounced and harder to detect compared to Calu-3 cells.

CLSM analysis of Calu-3 cells provided further insights into the protective effects of our inhibitors against LasB-induced E-cadherin degradation. CLSM imaging revealed that all tested compounds at 100 µM resulted in E-cadherin signal patterns more closely resembling those of healthy controls, in contrast to the altered distribution observed in wt PAO1 sn treated cells (Figure 3E, S9A). This indicates successful inhibition of LasB-mediated E-cadherin cleavage. Similarly, CLSM analysis of Arlo cells mirrored the findings from western blotting, as compound treatment did not produce notable changes in E-cadherin distribution compared to controls, consistent with the limited susceptibility of Arlo cells to LasB-mediated cleavage observed previously (Figure S9B). Control experiments confirmed that the compounds alone did not affect E-cadherin distribution in either of the cells (Figure S9C, D). Moreover, combination treatments with Δ*lasB* PAO1 sn and compounds showed no significant changes in E-cadherin localization, further supporting the specificity of the compounds in targeting LasB-mediated E-cadherin degradation (Figure S9E, F).

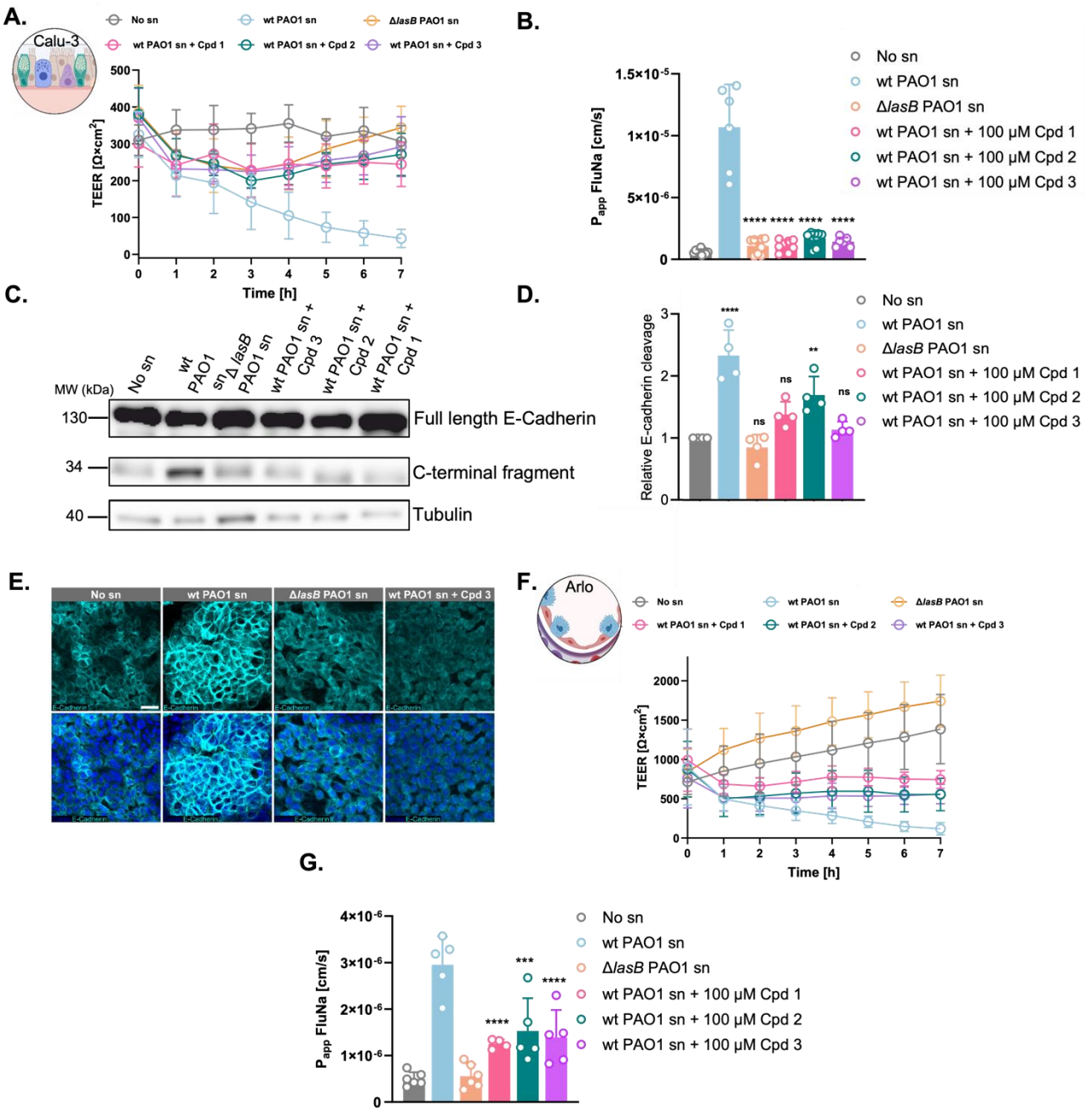

Figure 3: Pharmacological inhibition of LasB protects epithelial barrier function and prevents E-cadherin degradation. (A) Transepithelial electrical resistance (TEER) and **(B)** paracellular permeability (P_{app}) to fluorescent sodium (FluNa) in Calu-3 cells under healthy conditions or following challenge with wild-type (wt) *Pseudomonas aeruginosa* PAO1 supernatant (sn), Δ*lasB* PAO1 sn, or wt PAO1 sn with 100 µM of LasB inhibitors (**1–3**). **(C)** Western blot analysis of E-cadherin cleavage in Calu-3 cells across the same treatment groups, showing full-length and C-terminal fragment bands alongside tubulin as a loading control. **(D)** Relative quantification of E-cadherin cleavage in Calu-3 cells. Data represent mean ± SD (n = 3). Statistical analysis was performed using one-way ANOVA with Dunnett's multiple comparisons test. (****$p < 0.0001$; **$p < 0.01$; ns, not significant) FluNa permeability in Arlo cells under identical conditions. **(E)** CLSM visualization of E-cadherin (cyan) localization in Calu-3 cells under no sn control, wt PAO1 sn, Δ*lasB* PAO1 sn, and wt PAO1 sn + compound **3** conditions. Nuclei were counterstained with DAPI (blue). Scale bar, 25 µm. **(F)** TEER and **(G)** FluNa permeability in Arlo cells under identical conditions as Calu-3 cells.

Gene expression analysis revealed distinct, cell type-specific cytokine responses to LasB inhibitors. In Calu-3 cells, treatment with the inhibitors partially reversed LasB-induced transcriptional upregulation of several cytokines, most notably *IL1B*, *TNF*, and *IL1A*, with compound **1** showing the strongest effects (Figure 4A, left). Conversely, Arlo cells exhibited further upregulation of most inflammatory cytokines upon compound treatment in wt PAO1 sn challenged cells (Figure 4A, right). This paradoxical response in Arlo cells may reflect cell type-specific immune reprogramming in which inhibition of the dominant virulence activity of LasB exposes alternative pro-inflammatory signaling cascades. CBA analysis demonstrated significantly reduced levels of IL-6 and TNF by wt PAO1 sn, with partial rescue by LasB inhibitors (Figure 4B, C). Furthermore, in Calu-3 cells, evaluation of CSFs showed compound-mediated downregulation of *CSF2* and partial *CSF3* reduction at the transcriptional level (Figure 4A, left). While CBA revealed partial G-CSF protein rescue, GM-CSF remained undetectable, suggesting that transcriptional suppression may dominate over post-translational degradation for this CSF (Figure 4B). Importantly, treatment with compounds alone or in combination with Δ*lasB* PAO1 sn did not alter cytokine secretion in either cell type, confirming specificity of the observed effects (Figure S10).

Further evaluation of cytokine levels in Calu-3 cells challenged with low-LasB-producing strains (NH57388A muc. and RP73) demonstrated that even minimal LasB quantities are capable of reducing cytokine levels (Figure 4B). This observation is consistent with LasB's proposed role in modulating cytokine stability. Marked cytokine reduction was observed in cells exposed to NH57388A muc. sn (~6 nM LasB), producing low LasB levels. In contrast, cytokine levels in cells treated with RP73 sn, a strain with negligible *lasB* expression (LasB <3 nM), were similar to those seen upon exposure to Δ*lasB* PAO1 sn (Figure 4B). These results support the notion that low-level LasB activity may be sufficient to alter the inflammatory milieu during infection. Further supporting this notion, experiments using pure LasB on Calu-3 cells revealed that concentrations ranging from 100 to 3 nM effectively diminished cytokines levels. Notably, G-CSF, GM-CSF, or TNF-α became undetectable, while low levels of IL-6 persisted following 3 nM LasB treatment. This suggests that LasB efficiently targets a range of cytokines, with IL-6 showing relative resistance at lower concentrations. The ability of LasB to reduce cytokine levels at such low concentrations underscores its potential to influence immune signaling during *P. aeruginosa* infections.[43, 54] These findings are consistent with prior reports implicating LasB in the disruption of host defense pathways, but they also suggest a potential limitation of partial inhibition strategies, as residual LasB activity may still be sufficient to impact key immune mediators.

These results highlight two key challenges: LasB’s extreme proteolytic efficiency necessitates near-complete inhibition to preserve cytokines and cell type-specific responses complicate therapeutic predictions. To address these complexities and identify broader mechanisms underlying LasB-mediated immune evasion, we next interrogated the global transcriptional changes induced by infection and upon treatment.

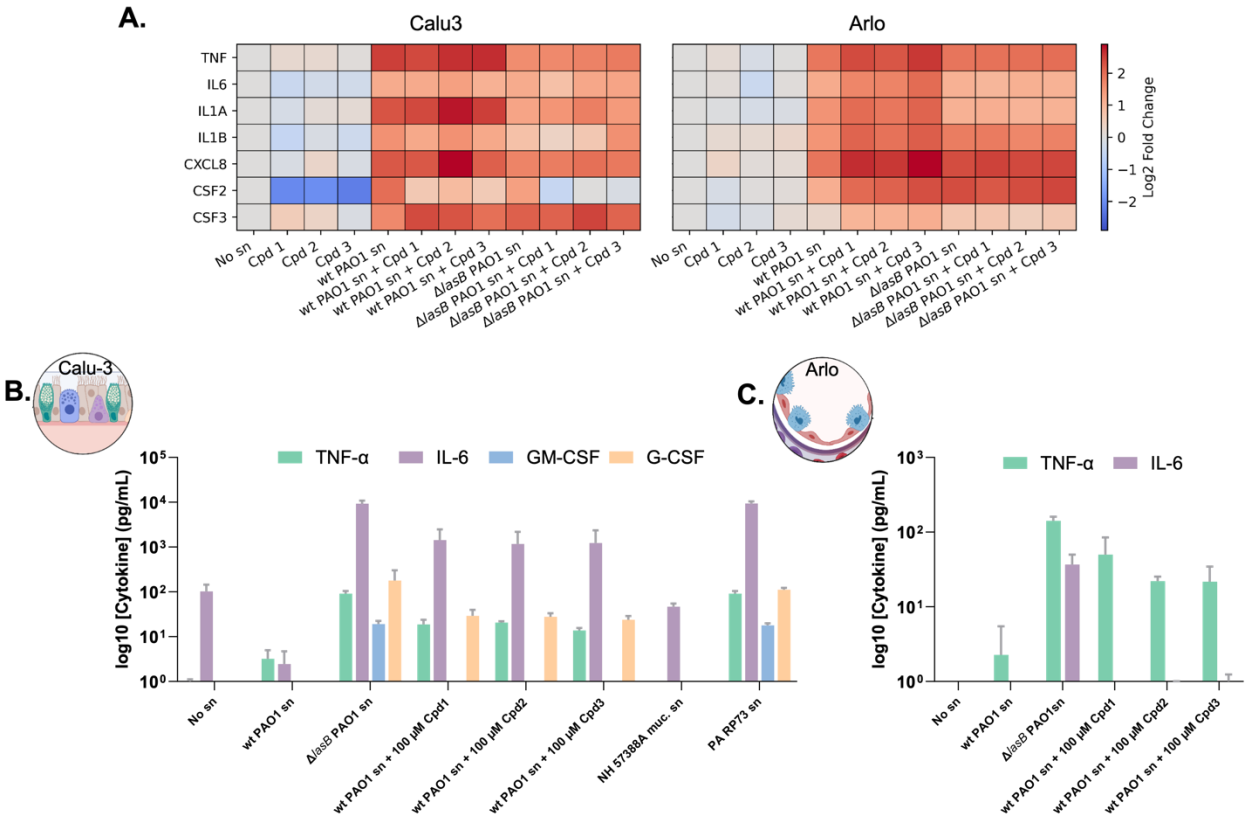

Figure 4: LasB inhibitors differentially modulate cytokine expression and secretion in a cell type-specific manner. (A) Heatmaps depicting $\log_2$ fold change in mRNA expression of inflammatory cytokines and colony stimulating factors (CSFs) in Calu-3 (left) and Arlo (right) cells under indicated treatment conditions. Cells were either healthy (no supernatant (sn)), treated with compounds alone (compounds **1–3**), challenged with wild-type (wt) *Pseudomonas aeruginosa* PAO1 sn, or co-treated with wt PAO1 sn and individual compounds. Additional conditions included Δ*lasB* PAO1 sn alone and in combination with compounds. **(B, C)** Log_{10} concentrations (pg/mL) of secreted cytokines quantified via cytometric bead array (CBA) in Calu-3 **(B)** and Arlo **(C)** cells under the same treatment conditions. Additional conditions in Calu-3 cells include exposure to NH57388A muc. and RP73 sn, representing low- and negligible-LasB-producing clinical isolates, respectively. Cytokine quantification was limited to detectable proteins: TNF-α, IL-6, GM-CSF, and G-CSF in Calu-3 cells; TNF-α and IL-6 in Arlo cells. Data represent mean values from ≥3 independent experiments.

2.3. Transcriptomic Profiling of LasB Effects on Calu-3 Cells

To identify LasB-affected targets and separate them from the global transcriptomic changes induced by *P. aeruginosa* in Calu-3 cells, we conducted RNA sequencing. The cells were exposed to various conditions differing in the presence, absence, and inhibition of LasB: wt PAO1 sn, Δ*lasB* PAO1 sn, wt PAO1 sn with compound treatment, including compound toxicity controls, and off-target controls (compound + Δ*lasB* PAO1 sn). The resulting data were processed using the RNADetector software, differential expression (edgeR) analysis comparing all conditions to wt PAO1 sn-treated samples.[59] This approach allowed us to identify expression patterns most likely dysregulated by LasB activity and evaluate the compound's ability to restore normal expression patterns (Figure 5A, B).

Among the significantly affected pathways in Calu-3 cells following LasB treatment, we identified processes previously associated with *P. aeruginosa* pathomechanisms. Upregulation of lipid

metabolism genes Acyl-CoA synthetase long chain family member 1 and 1-Acylglycerol-3-phosphate O-acyltransferase 2 (*ACSL1*, *AGPAT2*) as well as cell adhesion molecules Claudin-4 and Claudin-10 (*CLDN4/10*) suggests alterations in cell membrane composition and integrity, consistent with *P. aeruginosa*'s known disruption of epithelial barriers.[60–63] Immune modulation was evident through downregulation of 2'-5'-Oligoadenylate Synthetase 2 (*OAS2*) and Tumor Necrosis Factor Superfamily Member 10 (*TNFSF10*) alongside upregulation of Myeloid Differentiation Primary Response 88 (*MYD88*), a key adaptor in innate immune signaling.[64–66] Further analysis revealed that the dysregulation extends to the upregulation of dual-specificity phosphatases (*DUSP*s), which are involved in Mitogen-Activated Protein Kinase (MAPK) signaling regulation, and downregulation of B-Cell Lymphoma 6 (*BCL6*), a transcriptional repressor in immune responses.[67, 68] The altered expression of transcription factors and signaling molecules Transcription Factor 7 (*TCF7*) , Erb-B2 Receptor Tyrosine Kinase 2 (*ERBB2*), and Mitogen-Activated Protein Kinase Kinase Kinase 1 (*MAP3K1*) indicates broad changes in cellular signaling pathways.[69–71] Notably, upregulation of Vasoactive Intestinal Peptide Receptor (*VIPR1*) and Spire-Type Actin Nucleation Factor 2 (*SPIRE2*), involved in actin organization, suggests LasB-induced changes in cellular signaling and cytoskeletal remodeling.[72, 73] The modulation of growth factor-related genes such as Fibroblast Growth Factor Binding Protein 1 (*FGFBP1*), and cytoskeletal components including Actinin Alpha 4 (*ACTN4*) points to LasB's interference with normal growth, differentiation, and structural integrity of the airway epithelium.[74, 75] Additionally, the upregulation of Transmembrane 4 L Six Family Member 1 (*TM4SF1*), involved in cell motility, and Thyroid Hormone Receptor Interactor 6 (*TRIP6*), a focal adhesion protein, further emphasizes the impact of LasB on cell–cell and cell–matrix interactions.[76, 77]

Collectively, these data reveal the multifaceted impact of LasB on airway epithelial cells, disrupting barrier integrity, immune signaling, and cellular architecture — hallmarks of *P. aeruginosa* pathogenesis (Figure 5A, B). However, they also highlight the challenge of identifying specific clinical markers that isolate the effects of LasB within the broader context of *P. aeruginosa* infections. This will be even more complex in in vivo settings with several cell types affected by LasB in different ways.

Building upon our transcriptomic analysis of LasB effects on Calu-3 cells, we further validated our RNA-seq findings in a Calu-3 based in vitro system through qPCR quantification of selected transcripts: *VIPR1*, *DUSP2*, *SPIRE2*, *CLDN4*, *CLDN10*, *FGFBP1*, *LGALS4*, *MYD88*, *TCF7*, *ACTN4*, *TM4SF1*, *TRIP6*, and *BCL6*. This selection encompassed genes involved in diverse cellular processes, including signaling, cytoskeletal organization, cell adhesion, and immune response, providing a comprehensive view of the impact of LasB (Figure 5C). Among the validated transcripts, *FGFBP1*, *VIPR1*, and *DUSP2* exhibited the most pronounced upregulation in response to LasB. Notably, *FGFBP1*, a secreted chaperone that enhances FGF signaling and is implicated in angiogenesis, inflammation, and wound healing, was markedly upregulated. This suggests a possible role in coordinating tissue repair and remodeling in response to *P. aeruginosa*-induced epithelial damage in the airway epithelium. We extended our validation to Arlo cells, where overall gene expression changes across conditions were less pronounced. Nonetheless, we observed a modest upregulation of *DUSP2* and *FGFBP1*, indicating that these genes may also respond to LasB activity in this cell type (Figure 5D).

Importantly, treatment with LasB inhibitors effectively reversed the upregulation of *FGFBP1*, *VIPR1*, and *DUSP2* in Calu-3 cells, with compound **3** showing the strongest efficacy (Figure 5C). This specificity of our inhibitors confirms that the observed gene expression changes are LasB-dependent and highlights the therapeutic potential of targeted LasB inhibition in preserving epithelial function.

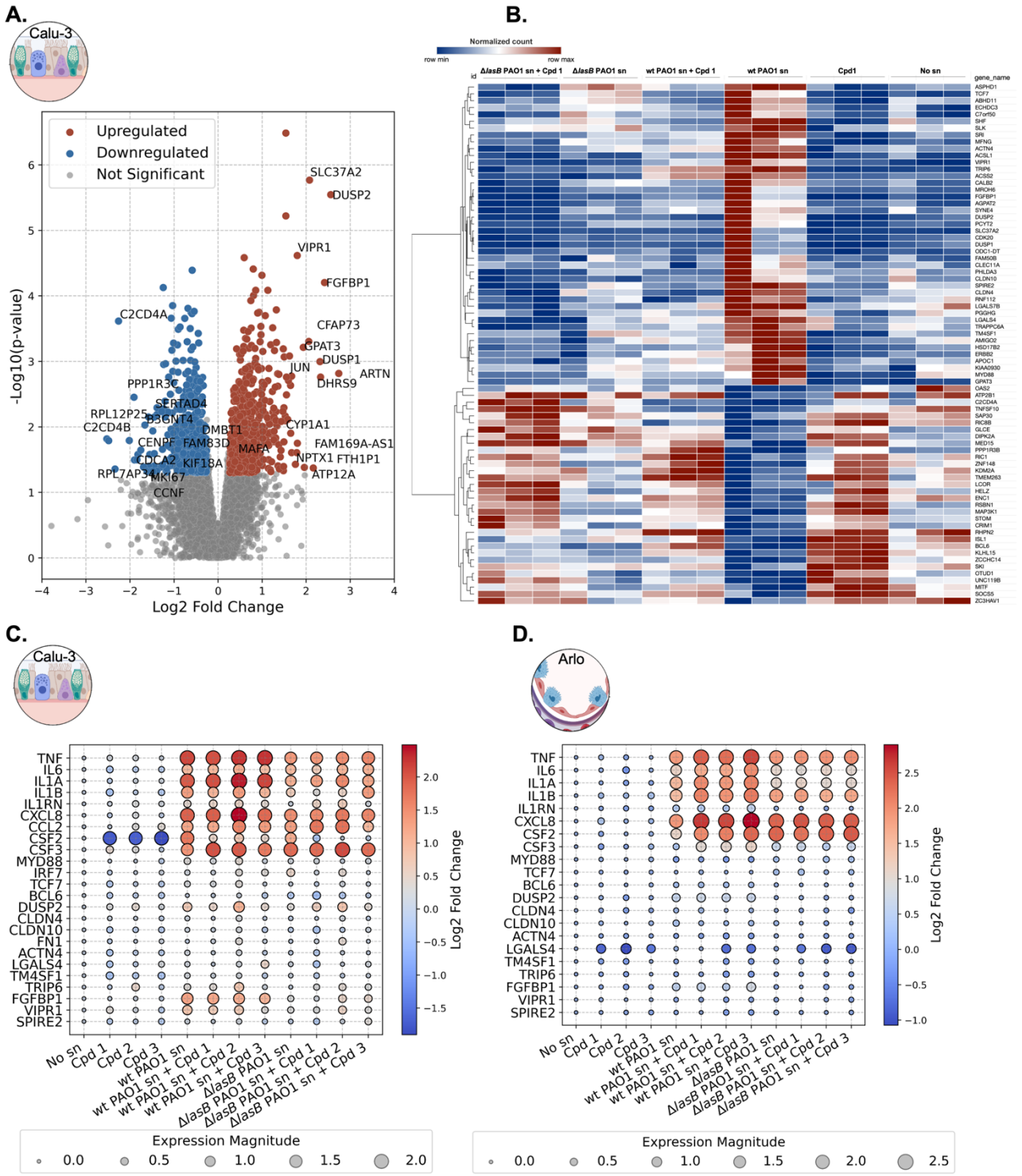

Figure 5: Transcriptomic analysis of LasB-specific effects on lung epithelial cells. (A) Volcano plot of RNA-sequencing data comparing all treatment and control conditions against the wild-type (wt) *Pseudomonas aeruginosa* PAO1 supernatant (sn)-treated Calu-3 cells. Data of the $\log_2$ fold change is plotted against the $-\log_{10}$ p-value. Upregulated genes are shown in red, downregulated genes in blue, and non-significant genes in gray.

(B) Heatmap showing top upregulated and downregulated genes in wt PAO1 sn-treated cells, with gene expression patterns across all tested conditions, including healthy (no sn), compound **1**, and Δ*lasB* PAO1 sn ± compound **1**. Heatmap generated with Morpheus. **(C, D)** Bubble heatmaps of qPCR validation in Calu-3 **(C)** and Arlo **(D)** cells for selected genes, including cytokines and top LasB-regulated genes. Bubble size represents magnitude of fold change, color indicates direction (red = upregulated, blue = downregulated). Gene expression is normalized to healthy controls. Data are from at least three independent experiments.

Comparative Analysis and Insights into LasB-Mediated Barrier Disruption

Since in vitro screening can be strongly influenced by the selected cell type, we compared our results in silico with all publicly available transcriptomic datasets from similar *P. aeruginosa* infection models to place our findings in a broader biological context. FastQ files from experiments with comparable time points and experimental conditions (controls and infected cells) were retrieved using Sequence Read Archive (SRA) tools from the Gene Expression Omnibus (GEO) database — specifically, GSE97036 (6 h, no arsenite) and the normal lung epithelial cell line (NuLi-1) from GSE199424 (8 h) (see Data S1 for used SRA files).[78] These datasets were processed together with the RNA sequencing data from our study using a common pipeline to ensure normalization across all samples (Figure S11). While differences in sequencing depth and library preparation can introduce variability, differential expression analysis revealed consistent expression patterns across models. Notably, *DUSP2* was repeatedly upregulated in both Calu-3 and primary bronchial epithelial cells upon infection. This recurring pattern suggests that *DUSP2*, a key regulator of MAPK signaling, plays a conserved role in the epithelial response to *P. aeruginosa*, likely contributing to inflammation or stress pathway modulation, and is unlikely to represent a cell line–specific artifact.

Additionally, Claudin-4 was identified as a potential target for LasB in bronchial Calu-3 cells. To investigate this further, we visualized junctional protein using CLSM. Imaging revealed accumulation or redistribution of Claudin-4 signal in Calu-3 cells treated with LasB, suggesting altered junctional integrity or protein localization in response to protease activity (Figure 6A). This effect was less apparent in Arlo cells, indicating potential cell type-specific differences or the need for adjusted exposure parameters such as higher LasB concentrations or prolonged incubation (Figure 6B). Moreover, Claudin-4 has previously been implicated as a target of LasB in nasal epithelial cells, further supporting its relevance as a potential proteolytic substrate in our model.[34] Importantly, this junctional disruption was mitigated by our LasB inhibitors, demonstrating their efficacy in preserving Calu-3 epithelial barrier integrity (Figure 6A, S12A). This finding not only validates our transcriptomic analysis but also uncovers a previously unrecognized mechanism by which LasB may compromise bronchial airway epithelial barriers. Furthermore, all inhibitors (compounds **1** – **3**) were applied to Calu-3 and Arlo samples under each treatment condition (no sn, Δ*lasB* PAO1 sn, and wt PAO1 sn) to not only test LasB inhibition but also their potential side effects on Claudin-4 localization (Figure S12). Indeed, CLSM recordings showed that every compound inhibits LasB, which resulted in the preservation of Claudin-4 localization in Calu-3 cells (Figure S12A). Moreover, the compounds themselves have no influence on the expression of the tight junction protein (Figure S12C, D), while also no major impact of the compounds in combination with Δ*lasB* PAO1 sn was observed (Figure S12E, F). This again underlines the specificity of the inhibitors towards reducing damages of LasB to proteins central for cell-cell interaction by keeping the distribution intact for multiple substrates of LasB.

Toward a More Physiologically Relevant Infection Model

To further elucidate the role of LasB in a more physiologically relevant context, we sought to extend our infection model beyond the use of bacterial supernatants. By transitioning to bacterial infections, we aimed to capture the dynamic interactions between living *P. aeruginosa* and host cells, including the real-time production of LasB. This approach would allow us to assess the efficacy of our LasB inhibitors in a more complex and realistic setting, potentially uncovering additional aspects of host-pathogen interactions and the role of LasB in virulence.

In this context, Calu-3 cells were infected with wt or Δ*lasB* PAO1. A clear dose-dependent toxicity of wt PAO1 was observed after challenging the lung cells with a multiplicity of infection (MOI) of 3 to 300 (Figure S13). In contrast, Δ*lasB* PAO1 showed no toxicity at the same MOI range. Interestingly, infection with Δ*lasB* PAO1 led to a slight increase in TEER, potentially indicating the activation of protective epithelial responses. This may reflect enhanced tight junction formation or an upregulated innate immune response in the absence of major virulence factors. Area-under-the-curve (AUC) calculations further emphasized the dose-dependent nature of wt PAO1-induced damage (Figure S13). Additionally, measurements of LDH release at MOIs of 30 and 300 corroborated the absence of significant cell death under these experimental conditions (Figure S14).

We then evaluated the efficacy of our LasB inhibitor **3** (10 µM), in mitigating epithelial barrier disruption during *P. aeruginosa* PAO1 infection at an MOI of 30. This was compared to meropenem treatment at 11.5 ng/mL, a concentration approximately 200-fold lower than the minimum inhibitory concentration (MIC), which was previously determined under similar experimental conditions (2 ± 1 µg/mL in 0.5% LB and 99.5% HBSS). In addition, we assessed the combination of both compounds to examine potential synergistic effects (Figure 6C, D).

Infection with wt PAO1 resulted in a marked reduction of TEER, with values dropping to approximately 20% of healthy control levels after 7 h. Treatment with compound **3** alone offered partial protection, preserving TEER at around 37% of the uninfected control. Meropenem alone, though used at sub-MIC levels and thus not fully bactericidal, was more effective in maintaining epithelial integrity, with TEER levels reaching approximately 77% of the uninfected control. Remarkably, the combination of compound **3** and meropenem demonstrated a pronounced synergistic effect, preserving TEER at approximately 92% of healthy control levels. This synergy likely arises from the complementary mechanisms of action: while meropenem reduces the bacterial load, compound **3** attenuates the virulence activity of LasB, thereby preserving barrier integrity and potentially improving antibiotic penetration. These findings highlight the therapeutic potential of antivirulence strategies when used in conjunction with conventional antibiotics, especially at sub-MIC levels (Figure 6C, D).

Colony-forming unit (CFU) counts provided further insights into bacterial survival and growth (Figure 6E). Treatment with compound **3** alone resulted in a slight, non-significant reduction in the number of CFUs compared to untreated wt PAO1-infected cells. This is consistent with its role as an antivirulence agent rather than a bactericidal compound. In contrast, meropenem significantly reduced bacterial burden, with the most pronounced reduction observed under combination treatment. These results reinforce the potential of pairing LasB inhibitors with conventional antibiotics to enhance bacterial clearance and preserve epithelial barrier function during *P. aeruginosa* infection. The observed synergy suggests that targeting virulence factors such as LasB can enhance antibiotic efficacy, offering

a promising approach, particularly in the context of antibiotic resistance. This strategy may be especially beneficial in immunocompromised patients, where antivirulence treatments alone may be insufficient. By disarming bacterial virulence and preserving host tissue integrity, LasB inhibitors can improve the efficacy of antibiotic therapy.

While our current model does not include immune components, it still offers valuable insights into epithelial responses and LasB-mediated damage. Future studies involving immune cells could help to clarify how antivirulence strategies interact with host defense. Additionally, testing LasB inhibitors alongside other clinically used antibiotics, such as tobramycin or ciprofloxacin, may further elucidate their potential to enhance standard therapies.

Host Response Modulation and Transcriptomic Validation by LasB Inhibition

To assess how LasB inhibition modulates host responses during live *P. aeruginosa* infection, we evaluated a broad panel of inflammatory and transcriptomic markers in Calu-3 cells. These included pro-inflammatory cytokines and colony-stimulating factors as well as key transcriptomic targets identified in earlier analyses: *DUSP2*, *CLDN4*, *FGFBP1*, and *VIPR1* (Figure 6F), thereby providing a comprehensive overview of host transcriptional responses to infection.

Infection with wt PAO1 induced a pronounced upregulation of all measured cytokines and CSFs, consistent with a strong pro-inflammatory response, possibly akin to a cytokine storm. This elevation was noticeably attenuated in Δ*lasB* PAO1 infections, supporting the idea that LasB is a key driver of excessive inflammatory signaling. Remarkably, treatment with compound **3** during wt PAO1 infection substantially reversed this effect. For genes such as *IL6*, *IL1B*, and *CSF3*, expression levels were brought back to levels comparable to those seen in the Δ*lasB* PAO1-infected condition, indicating that compound **3** can mitigate LasB-driven inflammation during bacterial infections.

Within this broader context, *DUSP2* and *FGFBP1* stood out as particularly responsive to LasB activity. In line with our RNA sequencing data (Figure E, G), these genes were strongly upregulated during wt PAO1 infection. However, their expression was significantly lower in Δ*lasB*-infected cells and, importantly, also upon compound **3** treatment. The consistent regulation of *FGFBP1* may point to its involvement in epithelial repair or remodeling, while *DUSP2* — a key regulator of MAPK signaling — likely reflects an activation of stress or inflammatory pathways. The ability of compound **3** to normalize the expression of both genes highlights its potential in restoring host-cell homeostasis and counteracting LasB-induced dysregulation.

Together, these findings establish LasB not only as a critical virulence factor driving inflammation and transcriptional reprograming in host cells but also as a viable therapeutic target. The broad transcriptional normalization observed with compound **3** treatment reinforces the promise of antivirulence strategies in mitigating damage during *P. aeruginosa* infection.

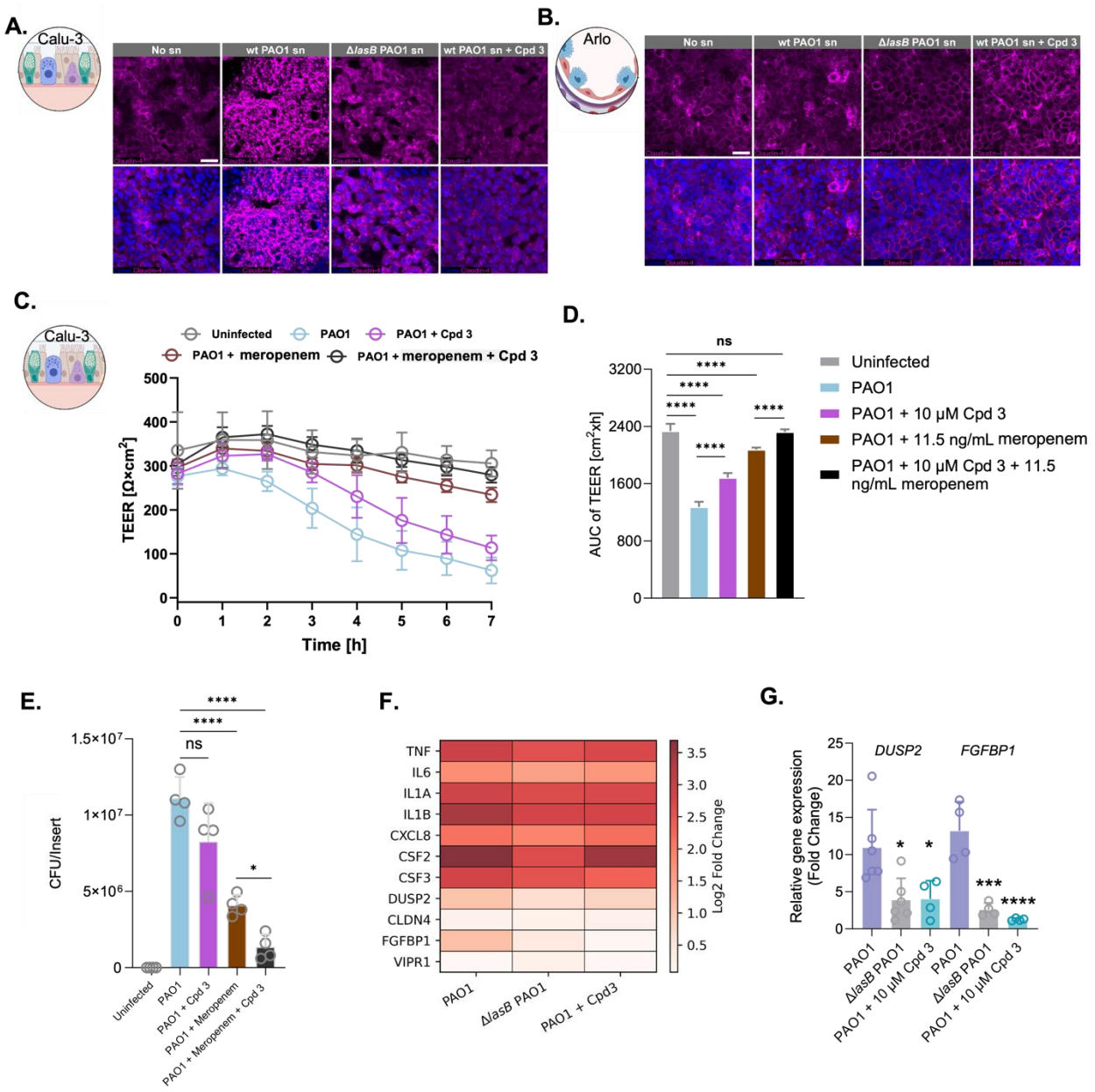

Figure 6: LasB inhibition preserves epithelial integrity and modulates host responses during live *Pseudomonas aeruginosa* infection. (A–B) Confocal laser scanning microscopy (CLSM) images showing Claudin-4 (magenta) localization in Calu-3 **(A)** and Arlo **(B)** cells under different treatment conditions (healthy control, wild type (wt) PAO1 supernatant (sn), Δ*lasB* PAO1 sn, and wt PAO1 sn + compound **3**). Nuclei were counterstained with DAPI (blue). Scale bar: 25 µm. **(C)** Transepithelial electrical resistance (TEER) measurements of Calu-3 monolayers infected with wt or Δ*lasB* PAO1 at multiplicity of infection (MOI) of 30, treated with meropenem (11.5 ng/mL), compound **3** (10 µM), or their combination. **(D)** Area under the curve (AUC) quantification of TEER data from panel C further emphasizing the protective effect of combined treatment. **(E)** Colony-forming unit (CFU) counts from infected Calu-3 cells under corresponding conditions. **(F)** Heatmap showing relative expression of inflammatory cytokines and colony-stimulating factors alongside transcriptomic markers in Calu-3 cells following infection and treatment. **(G)** Relative gene expression (fold change) of DUSP2 and FGFBP1 under the same conditions. Data represent means from n = 3 independent experiments. Statistical analysis was performed using one-way ANOVA followed by Dunnett's multiple comparisons test (****p < 0.0001; ***p < 0.001; **p < 0.01; ns, not significant).

3. Conclusions

This study provides a comprehensive analysis of the multifaceted role of LasB in *P. aeruginosa* pathogenesis, revealing its significant impact on epithelial barrier integrity, immune modulation, and gene expression. Our findings demonstrate LasB-mediated cleavage of E-cadherin, disruption of Claudin-4 integrity, modulation of inflammatory responses, and widespread changes in gene expression, particularly in *FGFBP1* and *DUSP2*. While Claudin-4 has been implicated in other epithelial contexts, including nasal epithelial cells, our findings newly establish its altered localization in bronchial airway epithelia in response to LasB activity, extending its relevance as a potential virulence target in the lower respiratory tract.[34] Furthermore, we demonstrate that LasB reduces the abundance of colony-stimulating factors GM-CSF and G-CSF, thereby providing novel insights into its immune-modulatory functions. These findings are in line with prior in vivo studies that observed a reduction in G-CSF levels as a downstream consequence of LasB activity in murine models.[17] However, our study extends these observations by providing direct evidence that LasB diminishes GM-CSF and G-CSF levels in human bronchial epithelial cells.

The efficacy of our novel LasB inhibitors in mitigating these effects, especially when combined with conventional antibiotics, highlights the potential of antivirulence strategies in combating *P. aeruginosa* infections. The synergistic effect observed between LasB inhibitors and antibiotics in infection models with living bacteria is particularly promising, as it suggests a potential approach to enhance the efficacy of existing treatments while reducing the risk of antimicrobial resistance.[30] This is further supported by recent in vivo studies, which have shown that LasB inhibitors can reduce bacterial burden and improve antibiotic performance in animal models.[11, 30, 58]

Our transcriptomic analysis has uncovered novel targets and pathways affected by LasB, contributing to a deeper understanding of *P. aeruginosa* pathogenesis. These insights may pave the way for new therapeutic strategies and diagnostic biomarkers for tracking disease progression and treatment efficacy. Given the high attrition rate in clinical development, where over 65% of drug candidates fail in phase II trials, rigorous preclinical studies remain essential for identifying promising candidates earlier in development and de-risking potential safety or efficacy issues.[79] Our multifaceted approach, combining functional assays, protein analyses, and transcriptomics, provides a solid foundation for future translational research.

Looking ahead, further investigation into the long-term effects of LasB inhibition on *P. aeruginosa* virulence and host responses is warranted. Additionally, a deeper exploration into the potential of combining LasB inhibitors with other antimicrobials (like phages) or other antivirulence agents, such as those targeting the T3SS or bacterial adhesion and biofilm formation, could lead to more comprehensive treatment strategies.[31, 80] Future studies should also optimize inhibitor delivery, particularly for respiratory applications, and evaluate their performance in more complex and chronic infection models, such as those relevant to cystic fibrosis.

This work not only advances our understanding of *P. aeruginosa* pathogenesis but also demonstrates the potential of targeting virulence factors as a promising approach to combat antibiotic-resistant infections. As we continue to face the growing threat of antimicrobial resistance, innovative strategies will be crucial in developing effective treatments for *P. aeruginosa* and other challenging pathogens.

Acknowledgments

The authors thank A. Boese, T. Bach, S. Amann and J. Jung for excellent technical support. CARB-X funding for this research (ID 05CARB-X0891, for A.K.H. Hirsch) is supported by federal funds from the U.S. Department of Health and Human Services (HHS); Administration for Strategic Preparedness and Response; Biomedical Advanced Research and Development Authority; under agreement number 75A50122C00028, and by awards from Wellcome (WT224842), and Germany's Federal Ministry of Education and Research (BMBF). The content of this manuscript is solely the responsibility of the authors and does not necessarily represent the official views of any CARB-X funders.

Conflict of Interest

The authors declare the following competing financial interest(s): R.S., L.H., A.A., D.Y., J.H. and A.K.H.H. are co-inventors on three international patent applications (WO 2022/043322 A1, WO 2023/166039 A1 and EP24178040.2) that are related to different classes of LasB inhibitors.

Data availability

All data are available in the main text or the Supporting Information. The data that support the findings of this study are available from the corresponding authors upon reasonable request.

References

[1] Bhagirath AY, Li Y, Somayajula D, Dadashi M, Badr S, Duan K. Cystic fibrosis lung environment and Pseudomonas aeruginosa infection. BMC Pulm Med 2016; 16(1): 174 [https://doi.org/10.1186/s12890-016-0339-5][PMID: 27919253]

[2] Moradali MF, Ghods S, Rehm BHA. Pseudomonas aeruginosa Lifestyle: A Paradigm for Adaptation, Survival, and Persistence. Frontiers in cellular and infection microbiology 2017; 7: 39 [https://doi.org/10.3389/fcimb.2017.00039][PMID: 28261568]

[3] Qin S, Xiao W, Zhou C*, et al.* Pseudomonas aeruginosa: pathogenesis, virulence factors, antibiotic resistance, interaction with host, technology advances and emerging therapeutics. Signal Transduct Target Ther 2022; 7(1): 199 [https://doi.org/10.1038/s41392-022-01056-1][PMID: 35752612]

[4] Assefa M, Amare A. Biofilm-Associated Multi-Drug Resistance in Hospital-Acquired Infections: A Review. Infect Drug Resist 2022; 15: 5061–8 [https://doi.org/10.2147/IDR.S379502][PMID: 36068834]

[5] Llor C, Bjerrum L. Antimicrobial resistance: risk associated with antibiotic overuse and initiatives to reduce the problem. Ther Adv Drug Saf 2014; 5(6): 229–41 [https://doi.org/10.1177/2042098614554919][PMID: 25436105]

[6] Calvert MB, Jumde VR, Titz A. Pathoblockers or antivirulence drugs as a new option for the treatment of bacterial infections. Beilstein J Org Chem 2018; 14(1): 2607–17 [https://doi.org/10.3762/bjoc.14.239][PMID: 30410623]

[7] Seth W. Dickey, Gordon Y. C. Cheung, Michael Otto. Different drugs for bad bugs: antivirulence strategies in the age of antibiotic resistance. Nature reviews Drug discovery 2017; 16(7): 457–71.

[8] Moeller AH, Caro-Quintero A, Mjungu D*, et al.* Cospeciation of gut microbiota with hominids. Science 2016; 353(6297): 380–2 [https://doi.org/10.1126/science.aaf7891][PMID: 27463671]

[9] Korotkov KV, Sandkvist M, Hol WGJ. The type II secretion system: biogenesis, molecular architecture and mechanism. Nat Rev Microbiol 2012; 10(5): 336–51 [https://doi.org/10.1038/nrmicro2762][PMID: 22466878]

[10] Everett MJ, Davies DT. Pseudomonas aeruginosa elastase (LasB) as a therapeutic target. Drug Discov Today 2021; 26(9): 2108–23 [https://doi.org/10.1016/j.drudis.2021.02.026][PMID: 33676022]

[11] Everett MJ, Davies DT, Leiris S*, et al.* [Copy] Chemical Optimization of Selective Pseudomonas aeruginosa LasB Elastase Inhibitors and Their Impact on LasB-Mediated Activation of IL-1β in Cellular and Animal Infection Models. ACS Infect Dis 2023; 9(2): 270–82.

[12] Suleman L. Extracellular Bacterial Proteases in Chronic Wounds: A Potential Therapeutic Target? Adv Wound Care (New Rochelle) 2016; 5(10): 455–63 [https://doi.org/10.1089/wound.2015.0673][PMID: 27785379]

[13] Parmely M, Gale A, Clabaugh M, Horvat R, Zhou WW. Proteolytic inactivation of cytokines by Pseudomonas aeruginosa. Infect Immun 1990; 58(9): 3009–14 [https://doi.org/10.1128/iai.58.9.3009-3014.1990][PMID: 2117578]

[14] Ian Alan Holder, Robert Wheeler. Experimental studies of the pathogenesis of infections owing to Pseudomonas aeruginosa: elastase, an IgG protease. Canadian journal of microbiology 1984; 30(9): 1118–24.

[15] Horvat RT, Clabaugh M, Duval-Jobe C, Parmely MJ. Inactivation of human gamma interferon by Pseudomonas aeruginosa proteases: elastase augments the effects of alkaline protease despite the presence of alpha 2-macroglobulin. Infect Immun 1989; 57(6): 1668–74 [https://doi.org/10.1128/iai.57.6.1668-1674.1989][PMID: 2470675]

[16] Matheson NR, Potempa J, Travis J. Interaction of a novel form of Pseudomonas aeruginosa alkaline protease (aeruginolysin) with interleukin-6 and interleukin-8. Biol Chem 2006; 387(7): 911–5 [https://doi.org/10.1515/BC.2006.115][PMID: 16913841]

[17] Cigana C, Castandet J, Sprynski N*, et al.* Pseudomonas aeruginosa Elastase Contributes to the Establishment of Chronic Lung Colonization and Modulates the Immune Response in a Murine Model. Front Microbiol 2020; 11: 620819 [https://doi.org/10.3389/fmicb.2020.620819][PMID: 33510733]

[18] Carlier FM, Fays C de, Pilette C. Epithelial Barrier Dysfunction in Chronic Respiratory Diseases. Front Physiol 2021; 12: 691227 [https://doi.org/10.3389/fphys.2021.691227][PMID: 34248677]

[19] Guillot L, Nathan N, Tabary O*, et al.* Alveolar epithelial cells: master regulators of lung homeostasis. Int J Biochem Cell Biol 2013; 45(11): 2568–73 [https://doi.org/10.1016/j.biocel.2013.08.009][PMID: 23988571]

[20] Martens K, Hellings PW, Steelant B. Calu-3 epithelial cells exhibit different immune and epithelial barrier responses from freshly isolated primary nasal epithelial cells in vitro. Clin Transl Allergy 2018; 8: 40 [https://doi.org/10.1186/s13601-018-0225-8][PMID: 30214714]

[21] Kreft ME, Tratnjek L, Lasič E, Hevir N, Rižner TL, Kristan K. Different Culture Conditions Affect Drug Transporter Gene Expression, Ultrastructure, and Permeability of Primary Human Nasal Epithelial Cells. Pharm Res 2020; 37(9): 170 [https://doi.org/10.1007/s11095-020-02905-w][PMID: 32820417]

[22] Florea BI, Cassara ML, Junginger HE, Borchard G. Drug transport and metabolism characteristics of the human airway epithelial cell line Calu-3. J Control Release 2003; 87(1-3): 131–8 [https://doi.org/10.1016/S0168-3659(02)00356-5][PMID: 12618029]

[23] Carius P, Jungmann A, Bechtel M*, et al.* A Monoclonal Human Alveolar Epithelial Cell Line ("Arlo") with Pronounced Barrier Function for Studying Drug Permeability and Viral Infections. Advanced science 2023; 10(8): e2207301 [https://doi.org/10.1002/advs.202207301][PMID: 36748276]

[24] Carius P, Horstmann JC, Souza Carvalho-Wodarz C de, Lehr C-M. Disease Models: Lung Models for Testing Drugs Against Inflammation and Infection. Handb Exp Pharmacol 2021; 265: 157–86 [https://doi.org/10.1007/164_2020_366][PMID: 33095300]

[25] Li Y, Wang Y, Li C*, et al.* The Role of Elastase in Corneal Epithelial Barrier Dysfunction Caused by Pseudomonas aeruginosa Exoproteins. Invest Ophthalmol Vis Sci 2021; 62(9): 7 [https://doi.org/10.1167/iovs.62.9.7][PMID: 34232259]

[26] Zhu Y, Ge X, Di Xie, Wang S, Chen F, Pan S. Clinical Strains of Pseudomonas aeruginosa Secrete LasB Elastase to Induce Hemorrhagic Diffuse Alveolar Damage in Mice. Journal of inflammation Research 2021; 14: 3767–80 [https://doi.org/10.2147/JIR.S322960][PMID: 34393497]

[27] Andreas M. Kany, Asfandyar Sikandar, Jörg Haupenthal*, et al.* Binding Mode Characterization and Early in Vivo Evaluation of Fragment-Like Thiols as Inhibitors of the Virulence Factor LasB from Pseudomonas aeruginosa. ACS Infect Dis 2018; 4(6): 988–97.

[28] Camberlein V, Jézéquel G, Haupenthal J, Hirsch AKH. The Structures and Binding Modes of Small-Molecule Inhibitors of Pseudomonas aeruginosa Elastase LasB. Antibiotics 2022; 11(8): 1060 [https://doi.org/10.3390/antibiotics11081060][PMID: 36009930]

[29] Kaya C, Walter I, Alhayek A*, et al.* Structure-Based Design of α-Substituted Mercaptoacetamides as Inhibitors of the Virulence Factor LasB from Pseudomonas aeruginosa. ACS Infect Dis 2022; 8(5): 1010–21 [https://doi.org/10.1021/acsinfecdis.1c00628][PMID: 35451824]

[30] Konstantinović J, Kany AM, Alhayek A*, et al.* Inhibitors of the Elastase LasB for the Treatment of Pseudomonas aeruginosa Lung Infections. ACS Cent Sci 2023; 9(12): 2205–15 [https://doi.org/10.1021/acscentsci.3c01102][PMID: 38161367]

[31] Metelkina O, Konstantinović J, Klein A*, et al.* Dual inhibitors of Pseudomonas aeruginosa virulence factors LecA and LasB. Chem Sci 2024; 15(33): 13333–42 [https://doi.org/10.1039/D4SC02703E][PMID: 39183927]

[32] Ghosh N, Dutta M, Singh B, Banerjee R, Bhattacharyya P, Chaudhury K. Transcriptomics, proteomics and metabolomics driven biomarker discovery in COPD: an update. Expert Rev Mol Diagn 2016; 16(8): 897–913 [https://doi.org/10.1080/14737159.2016.1198258][PMID: 27267972]

[33] Yang X, Kui L, Tang M*, et al.* High-Throughput Transcriptome Profiling in Drug and Biomarker Discovery. Front Genet 2020; 11: 19 [https://doi.org/10.3389/fgene.2020.00019][PMID: 32117438]

[34] Nomura K, Obata K, Keira T*, et al.* Pseudomonas aeruginosa elastase causes transient disruption of tight junctions and downregulation of PAR-2 in human nasal epithelial cells. Respiratory research 2014; 15(1): 21 [https://doi.org/10.1186/1465-9921-15-21][PMID: 24548792]

[35] Clark CA, Thomas LK, Azghani AO. Inhibition of protein kinase C attenuates Pseudomonas aeruginosa elastase-induced epithelial barrier disruption. Am J Respir Cell Mol Biol 2011; 45(6): 1263–71 [https://doi.org/10.1165/rcmb.2010-0459OC][PMID: 21757681]

[36] Kuehn A, Kletting S, Souza Carvalho-Wodarz C de*, et al.* Human alveolar epithelial cells expressing tight junctions to model the air-blood barrier. ALTEX 2016; 33(3): 251–60 [https://doi.org/10.14573/altex.1511131][PMID: 26985677]

[37] Michael Buchert, Kursad Turksen, Frédéric Hollande. Methods to Examine Tight Junction Physiology in Cancer Stem Cells: TEER, Paracellular Permeability, and Dilution Potential Measurements. Stem cell reviews and reports 2012; 8: 1030–4.

[38] Balaji Srinivasan, Aditya Reddy Kolli, Mandy Brigitte Esch, Hasan Erbil Abaci, Michael L. Shuler, and James J. Hickman. TEER Measurement Techniques for In Vitro Barrier Model Systems. Journal of laboratory automation; 20(2): 107–26.

[39] Hoffmann N, Rasmussen TB, Jensen PØ*, et al.* Novel mouse model of chronic Pseudomonas aeruginosa lung infection mimicking cystic fibrosis. Infect Immun 2005; 73(4): 2504–14 [https://doi.org/10.1128/IAI.73.4.2504-2514.2005][PMID: 15784597]

[40] Cigana, C., Bianconi, I., Baldan, R., De Simone, M., Riva, C., Sipione, B., … & Bragonzi, A. Staphylococcus aureus Impacts Pseudomonas aeruginosa Chronic Respiratory Disease in Murine Models. The Journal of Infectious Diseases; 217(6): 933–42.

[41] Beaufort N, Corvazier E, Mlanaoindrou S, Bentzmann S de, Pidard D. Disruption of the endothelial barrier by proteases from the bacterial pathogen Pseudomonas aeruginosa: implication of matrilysis and receptor cleavage. PLoS One 2013; 8(9): e75708 [https://doi.org/10.1371/journal.pone.0075708][PMID: 24069438]

[42] Parmely, M. I. C. H. A. E. L., Gale, A. N. D. R. E. W., Clabaugh, M. A. T. T. H. E. W., Horvat, R. E. B. E. C. C. A., & Zhou, W. W. Proteolytic inactivation of cytokines by Pseudomonas aeruginosa. Infect Immun 1990; 58(9): 3009–14.

[43] Saint-Criq, V., Villeret, B., Bastaert, F., Kheir, S., Hatton, A., Cazes, A., Xing, Z., Sermet-Gaudelus, I., Garcia-Verdugo, I., Edelman, A. and Sallenave, J.M. Pseudomonas aeruginosa LasB protease impairs innate immunity in mice and humans by targeting a lung epithelial cystic fibrosis transmembrane regulator–IL-6–antimicrobial–repair pathway. Thorax 2018; 73(1): 49–61.

[44] LaFayette SL, Houle D, Beaudoin T*, et al.* Cystic fibrosis-adapted Pseudomonas aeruginosa quorum sensing lasR mutants cause hyperinflammatory responses. Sci Adv 2015; 1(6) [https://doi.org/10.1126/sciadv.1500199][PMID: 26457326]

[45] Sun J, LaRock DL, Skowronski EA*, et al.* Role of Inflammasome-independent Activation of IL-1β by the Pseudomonas aeruginosa Protease LasB 2020.

[46] Souche A, Vandenesch F, Doléans-Jordheim A, Moreau K. How Staphylococcus aureus and Pseudomonas aeruginosa Hijack the Host Immune Response in the Context of Cystic Fibrosis. Int J Mol Sci 2023; 24(7) [https://doi.org/10.3390/ijms24076609][PMID: 37047579]

[47] Zhu Y, Chidekel A, Shaffer TH. Cultured human airway epithelial cells (calu-3): a model of human respiratory function, structure, and inflammatory responses. Crit Care Res Pract 2010; 2010 [https://doi.org/10.1155/2010/394578][PMID: 20948883]

[48] Whitsett JA, Alenghat T. Respiratory epithelial cells orchestrate pulmonary innate immunity. Nat Immunol 2015; 16(1): 27–35 [https://doi.org/10.1038/ni.3045][PMID: 25521682]

[49] Yoshikawa T, Hill TE, Yoshikawa N*, et al.* Dynamic innate immune responses of human bronchial epithelial cells to severe acute respiratory syndrome-associated coronavirus infection. PLoS One 2010; 5(1): e8729 [https://doi.org/10.1371/journal.pone.0008729][PMID: 20090954]

[50] Yoshikawa T, Hill T, Li K, Peters CJ, Tseng C-TK. Severe acute respiratory syndrome (SARS) coronavirus-induced lung epithelial cytokines exacerbate SARS pathogenesis by modulating intrinsic functions of monocyte-derived macrophages and dendritic cells. J Virol 2009; 83(7): 3039–48 [https://doi.org/10.1128/JVI.01792-08][PMID: 19004938]

[51] Yamamoto K, Ferrari JD, Cao Y*, et al.* Type I alveolar epithelial cells mount innate immune responses during pneumococcal pneumonia. J Immunol 2012; 189(5): 2450–9 [https://doi.org/10.4049/jimmunol.1200634][PMID: 22844121]

[52] Cigana C, Castandet J, Sprynski N*, et al.* Pseudomonas aeruginosa Elastase Contributes to the Establishment of Chronic Lung Colonization and Modulates the Immune Response in a Murine Model. Front Microbiol 2020; 11: 620819 [https://doi.org/10.3389/fmicb.2020.620819][PMID: 33510733]

[53] Hamilton JA, Achuthan A. Colony stimulating factors and myeloid cell biology in health and disease. Trends Immunol 2013; 34(2): 81–9 [https://doi.org/10.1016/j.it.2012.08.006][PMID: 23000011]

[54] Bastaert F, Kheir S, Saint-Criq V*, et al.* Pseudomonas aeruginosa LasB Subverts Alveolar Macrophage Activity by Interfering With Bacterial Killing Through Downregulation of Innate Immune Defense, Reactive Oxygen Species Generation, and Complement Activation. Frontiers in Immunology 2018; 9: 1675 [https://doi.org/10.3389/fimmu.2018.01675][PMID: 30083156]

[55] Kolbe U, Yi B, Poth T, Saunders A, Boutin S, Dalpke AH. Early Cytokine Induction Upon Pseudomonas aeruginosa Infection in Murine Precision Cut Lung Slices Depends on Sensing of Bacterial Viability. Frontiers in Immunology 2020; 11: 598636 [https://doi.org/10.3389/fimmu.2020.598636][PMID: 33250899]

[56] Llanos A, Achard P, Bousquet J*, et al.* Higher levels of Pseudomonas aeruginosa LasB elastase expression are associated with early-stage infection in cystic fibrosis patients. Sci Rep 2023; 13(1): 14208 [https://doi.org/10.1038/s41598-023-41333-9][PMID: 37648735]

[57] Galdino ACM, Viganor L, Castro AA de*, et al.* Disarming Pseudomonas aeruginosa Virulence by the Inhibitory Action of 1,10-Phenanthroline-5,6-Dione-Based Compounds: Elastase B (LasB) as a Chemotherapeutic Target. Front Microbiol 2019; 10: 1701 [https://doi.org/10.3389/fmicb.2019.01701][PMID: 31428062]

[58] Kiefer AF, Schütz C, Englisch CN*, et al.* Dipeptidic Phosphonates: Potent Inhibitors of Pseudomonas aeruginosa Elastase B Showing Efficacy in a Murine Keratitis Model. Adv Sci (Weinh) 2025: e2411807 [https://doi.org/10.1002/advs.202411807][PMID: 39973061]

[59] La Ferlita A, Alaimo S, Di Bella S*, et al.* RNAdetector: a free user-friendly stand-alone and cloud-based system for RNA-Seq data analysis. BMC Bioinformatics 2021; 22(1): 298 [https://doi.org/10.1186/s12859-021-04211-7][PMID: 34082707]

[60] Kato A, Ito M, Sanaki T*, et al.* Acsl1 is essential for skin barrier function through the activation of linoleic acid and biosynthesis of ω-O-acylceramide in mice. Biochim Biophys Acta Mol Cell Biol Lipids 2022; 1867(2): 159085 [https://doi.org/10.1016/j.bbalip.2021.159085][PMID: 34813948]

[61] Ruiz M, Bodhicharla R, Ståhlman M*, et al.* Evolutionarily conserved long-chain Acyl-CoA synthetases regulate membrane composition and fluidity. Elife 2019; 8 [https://doi.org/10.7554/eLife.47733][PMID: 31769755]

[62] Ylermi Soini. Claudins in lung diseases. Respiratory research 2011; 12(70): 1–11.

[63] Golovkine G, Reboud E, Huber P. Pseudomonas aeruginosa Takes a Multi-Target Approach to Achieve Junction Breach. Frontiers in cellular and infection microbiology 2017; 7: 532 [https://doi.org/10.3389/fcimb.2017.00532][PMID: 29379773]

[64] Li L, Zhao H, Chen B*, et al.* Noninvasive Identification of Immune-Related Biomarkers in Hepatocellular Carcinoma. J Oncol 2019; 2019: 2531932 [https://doi.org/10.1155/2019/2531932][PMID: 31531018]

[65] Prasad K, Khatoon F, Rashid S*, et al.* Targeting hub genes and pathways of innate immune response in COVID-19: A network biology perspective. Int J Biol Macromol 2020; 163: 1–8 [https://doi.org/10.1016/j.ijbiomac.2020.06.228][PMID: 32599245]

[66] Deguine J, Barton GM. MyD88: a central player in innate immune signaling. F1000Prime Rep 2014; 6: 97 [https://doi.org/10.12703/P6-97][PMID: 25580251]

[67] Lang R, Raffi FAM. Dual-Specificity Phosphatases in Immunity and Infection: An Update. Int J Mol Sci 2019; 20(11) [https://doi.org/10.3390/ijms20112710][PMID: 31159473]

[68] Huang C, Hatzi K, Melnick A. Lineage-specific functions of Bcl-6 in immunity and inflammation are mediated by distinct biochemical mechanisms. Nat Immunol 2013; 14(4): 380–8 [https://doi.org/10.1038/ni.2543][PMID: 23455674]

[69] Wu JQ, Seay M, Schulz VP*, et al.* Tcf7 is an important regulator of the switch of self-renewal and differentiation in a multipotential hematopoietic cell line. PLoS Genet 2012; 8(3): e1002565 [https://doi.org/10.1371/journal.pgen.1002565][PMID: 22412390]

[70] Ho J, Moyes DL, Tavassoli M, Naglik JR. The Role of ErbB Receptors in Infection. Trends Microbiol 2017; 25(11): 942–52 [https://doi.org/10.1016/j.tim.2017.04.009][PMID: 28522156]

[71] Kyriakis JM, Avruch J. Mammalian mitogen-activated protein kinase signal transduction pathways activated by stress and inflammation. Physiol Rev 2001; 81(2): 807–69 [https://doi.org/10.1152/physrev.2001.81.2.807][PMID: 11274345]

[72] Fu Y, Liu S, Rodrigues RM*, et al.* Activation of VIPR1 suppresses hepatocellular carcinoma progression by regulating arginine and pyrimidine metabolism. Int J Biol Sci 2022; 18(11): 4341–56 [https://doi.org/10.7150/ijbs.71134][PMID: 35864952]

[73] Welz T, Kerkhoff E. The role of SPIRE actin nucleators in cellular transport processes. J Cell Sci 2023; 136(6) [https://doi.org/10.1242/jcs.260743][PMID: 36994763]

[74] Xie B, Tassi E, Swift MR*, et al.* Identification of the fibroblast growth factor (FGF)-interacting domain in a secreted FGF-binding protein by phage display. J Biol Chem 2006; 281(2): 1137–44 [https://doi.org/10.1074/jbc.M510754200][PMID: 16257968]

[75] Fu J, Li L, Yang X*, et al.* Transactivated Epidermal Growth Factor Receptor Recruitment of α-actinin-4 From F-actin Contributes to Invasion of Brain Microvascular Endothelial Cells by Meningitic Escherichia coli. Frontiers in cellular and infection microbiology 2018; 8: 448 [https://doi.org/10.3389/fcimb.2018.00448][PMID: 30687645]

[76] Shih S-C, Zukauskas A, Li D*, et al.* The L6 protein TM4SF1 is critical for endothelial cell function and tumor angiogenesis. Cancer Res 2009; 69(8): 3272–7 [https://doi.org/10.1158/0008-5472.CAN-08-4886][PMID: 19351819]

[77] Lin VTG, Lin F-T. TRIP6: an adaptor protein that regulates cell motility, antiapoptotic signaling and transcriptional activity. Cell Signal 2011; 23(11): 1691–7 [https://doi.org/10.1016/j.cellsig.2011.06.004][PMID: 21689746]

[78] Goodale BC, Rayack EJ, Stanton BA. Arsenic alters transcriptional responses to Pseudomonas aeruginosa infection and decreases antimicrobial defense of human airway epithelial cells. Toxicol Appl Pharmacol 2017; 331: 154–63 [https://doi.org/10.1016/j.taap.2017.06.010][PMID: 28625800]

[79] Wong CH, Siah KW, Lo AW. Estimation of clinical trial success rates and related parameters. Biostatistics 2019; 20(2): 273–86 [https://doi.org/10.1093/biostatistics/kxx069][PMID: 29394327]

[80] Chemani C, Imberty A, Bentzmann S de*, et al.* Role of LecA and LecB lectins in Pseudomonas aeruginosa-induced lung injury and effect of carbohydrate ligands. Infect Immun 2009; 77(5): 2065–75 [https://doi.org/10.1128/IAI.01204-08][PMID: 19237519]

2.1.1 Supporting Information

Material and Methods

Preparation of bacterial culture supernatants

Bacterial culture supernatants were obtained from *Pseudomonas aeruginosa* strain PAO1 (DSM-19880) and its *lasB* knockout variant after overnight growth in lysogeny broth (LB) medium. Cultures were incubated at 37°C with shaking at 180 rpm for approximately 18 to 19 h. Following incubation, the cultures were centrifuged at 5000 rpm for 10 min at 4°C. The supernatants were then filtered through 0.2 µm non-pyrogenic sterile filters. Aliquots were prepared for single-use and stored at -80°C until needed.

Cell cultures

Arlo cells (passage 1–20) were cultured in SAGM™ (Small Airway Epithelial Cell Growth Medium, Lonza) with SingleQuots™ Supplement Pack. The complete medium was additionally supplemented with 1% (v/v) fetal calf serum (FCS, Sigma) and 1% (v/v) penicillin-streptomycin and cells were maintained according to the method described in Carius *et al.*[23] Cells were maintained at 37°C in a humidified 5% CO_2 atmosphere, with medium changes every 2–3 days. Cells were passaged every 7 days: washed twice with PBS (Sigma), detached using 2 mL trypsin-EDTA (0.05%; Gibco) for 8 min, centrifuged at 300 RCF for 4 min, and resuspended in complete SAGM. Flasks were pre-coated for 1 h at 37 °C with 2 mL of 1% (v/v) human fibronectin (1 mg/mL; Corning) and 1% (v/v) bovine collagen type I (3 mg/mL; Sigma) in sterile distilled water. Coating solution was removed immediately before seeding. 0.7×10^6 cells were seeded per flask or used for experiments.

Calu-3 cells were cultured in minimum essential media (MEM, Life Technologies) supplemented with 10% (v/v) FCS, 1% (v/v) penicillin-streptomycin, 1% (v/v) non-essential amino acids solution (NEAA, Life Technologies), and 1% (v/v) sodium pyruvate. To maintain the cells, the culture medium was aspirated, and the cells were washed once with 13 mL phosphate-buffered saline (PBS). Subsequently, 3.5 mL of pre-warmed Trypsin/EDTA was added to the flask, and the cells were incubated at 37°C for 10–20 min, monitoring for detachment. Once detached, the cells were neutralized by adding 6.5 mL fresh medium and gently resuspended by pipetting. The cell suspension was transferred to a 15 mL Falcon tube and centrifuged at 1790 rpm (300 x g) for 5 min at room temperature, followed by aspiration of the supernatant. The cell pellet was resuspended in 5 mL fresh medium, and cell viability was assessed. For routine cultivation, 2.5×10^6 cells were seeded in a new T75 flask with a final volume of 13 mL. Cells were fed every 2-3 days and maintained in a humidified incubator at 37°C with 5% CO_2. All reagents for both cells were prewarmed to 37 °C before use.

Transwell preparation and Transepithelial Electrical Resistance (TEER) experiments

To conduct Transepithelial Electrical Resistance (TEER) measurements under liquid-covered conditions (LCC), Calu-3 and Arlo cells were seeded separately onto 0.33 cm² permeable cell culture inserts (400 nm pore size; Corning, 3470) at a density of 3×10^4 and 3.3×10^4 cells per insert, respectively, allowing 8–10 days for cells to establish tight junctions. Apical inserts received 200 µL of this cell suspension, while the basolateral compartments were filled with 800 µL cell culture medium. To prevent evaporation, outer wells were filled with 800 µL phosphate-buffered saline (PBS), and two wells per plate were designated as blank controls, containing cell culture medium only.

Throughout the culture period, medium changes were performed every 2 to 3 days, with fresh MEM (for Calu-3) or SAGM (for Arlo) medium replacing the old medium in both apical and basolateral compartments. On day 8–10, TEER measurements were initiated. In the first step, TEER measurements were taken for each well in the transwell plate. Before measurement, the electrode was sterilized using 70% isopropanol and then equilibrated in PBS until reaching a TEER value below 20 Ω·cm². The culture medium was then replaced with 200 µL Hanks' balanced salt solution containing $CaCl_2$ and $MgCl_2$ (HBSS, Gibco, Thermo Fisher Scientific Inc.), and cells were incubated at 37°C for 30–60 min. Following incubation, TEER measurements were conducted again using a suitable electrode system and the EVOM 2 with STX2 electrode (WPI). Next, HBSS was removed from the apical and basolateral. Supernatants and compounds of interest were added to the apical side to reach the desired concentrations in a final volume of 200 µL, and the basolateral compartments were filled with 800 µL HBSS. In parallel, several controls were included: blank inserts (without cells) containing only HBSS in both compartments to account for background resistance; a medium control, consisting of inserts with cells exposed to HBSS (including the equivalent DMSO concentration used for compound solubilization), representing the negative control; and a sn control, where cells were treated with wt PAO1 sn alone (without compounds), serving as the positive control for barrier disruption. Plates were incubated at 37°C + 5% CO_2 on a plate shaker at 200 rpm. TEER was recorded at 1 h intervals for up to 7 h. Basolateral and apical medium samples, as well as cell samples, were collected post-measurement for further analysis. The blank-corrected mean values of the data were used for calculations, with the unit area resistance (UAR) calculated as follows:

$$UAR\ [\Omega * cm^2] = \left(\Omega_{monolayer} - \Omega_{blank}\right) * effective\ membrane\ area$$

where the effective membrane area was 0.33 cm². The initial UAR at t=0 was set to 100%, and subsequent changes in transepithelial electrical resistance were calculated relative to this baseline.

Transport experiments and P_{app} calculations

The transport of fluorescein sodium (FluNa) across cellular monolayers was evaluated concurrently with TEER measurements, using hourly sampling. After the cells were incubated with HBSS and a TEER measurement was taken, the apical and basolateral compartments were aspirated, and 176 µL of FluNa (10 µg/mL in HBSS) was added to the apical (donor) compartment of each transwell. Additional 44 µL of specific test solutions was added to each well, while 800 µL of HBSS was added to the basolateral (acceptor) compartment. Immediately after adding these solutions, samples of 20 µL from the apical and 200 µL from the basolateral compartments were taken and transferred to a 96-well plate for measurement of initial concentrations. The transwell plates were then placed on an orbital shaker set to 150 rpm (IKA, Germany) in an incubator at 37°C in a humidified atmosphere with 5% CO_2, and basolateral samples (200 µL) were collected every 60 min over a 7 h period. Each sample removal was followed by replenishing with 200 µL of HBSS. A calibration curve was prepared using a 1:2 dilution of FluNa, and duplicate concentrations (200 µL) were loaded into the first two rows of the plate. At the experiment's conclusion, a final TEER measurement was recorded, and fluorescence was assessed in the 96-well plate with a CLARIOstar plate reader using excitation and emission wavelengths of 488 nm and 530 nm, respectively. The gain was calibrated against the highest concentration in the calibration curve. The apparent permeability (Papp) of FluNa was subsequently calculated based on the following equation:

$$P_{app}\ [cm/s] = \frac{dQ}{dt}\left[\frac{\mu g}{s}\right] \times \frac{1}{A\ [cm^2] \times C_0\ [\frac{\mu g}{mL}]}$$

Sample collection after TEER

At the conclusion of the TEER experiment, samples were collected from the apical and basolateral compartments, along with the cells, for subsequent analyses, including gene expression studies, CBA, E-cadherin protein quantification via western blot, and lactate dehydrogenase (LDH) assay. The supernatant from the apical compartment was centrifuged at 300x g for 4 min at room temperature. Two 60 µL aliquots of the supernatant were then transferred into separate tubes for LDH and CBA analyses. For gene expression studies, cells were first washed with 200 µL of cold PBS, then incubated with 350 µL of buffer RLT (Qiagen) at room temperature for 5 min. Cells were subsequently detached from the surface using a pipette tip, transferred into fresh tubes, and stored at -80°C for future RNA extraction. Cell lysates used for E-cadherin quantification were prepared following the method outlined by Aljohmani *et al*.[81]

LDH quantification

LDH release from each sample was measured relative to the healthy control using the CytoTox 96® Non-Radioactive Cytotoxicity Assay (Promega). All reagents were prepared as per the manufacturer's instructions. A 50 µL portion of the apical samples, previously stored at -80°C, was transferred into a flat-bottom 96-well plate (Thermo Scientific™ Nunc™). An additional 50 µL of substrate mix was then added to each well. The plate was incubated for 30 min at room temperature, and protected from light. Following incubation, 50 µL of stop solution was added to each well, and absorbance was read at 490 nm using the PHERAstar instrument.

Gene expression analysis in Calu-3 and Arlo cells

RNA was extracted from the cells using the RNeasy Micro Kit (Qiagen) following the manufacturer's instructions, with minor adjustments: centrifugation times were extended from 15 seconds to 30 seconds, and RNA was eluted in 11 µL of RNase-free water. RNA purity and concentration (ng/µL) were assessed using the NanoDrop™ 2000 spectrophotometer (Thermo Fisher Scientific). All RNA samples were then reverse transcribed to cDNA using the High-Capacity cDNA Reverse Transcription Kit (Applied Biosystems™). Target genes were quantified via qPCR using the PowerUp™ SYBR™ Green Master Mix (Applied Biosystems™) on the StepOne Plus instrument, in accordance with the manufacturer's guidelines. Data analysis was performed using the ΔΔCt method, with fold changes calculated relative to the healthy control.

Quantification of *lasB* expression in *P. aeruginosa* strains

Overnight cultures of *P. aeruginosa* strains PAO1, Δ*lasB* PAO1, PA NH 57388A muc., and PA RP73 were grown in LB medium. Cultures were adjusted to an OD_{600} of 1, and cell lysates were prepared by adding two volumes of QIAGEN RNAprotect® Bacteria Reagent. After vortexing and resting at room temperature for 5 min, samples were centrifuged at 5000x g for 10 min at room temperature. Pellets were resuspended in 20 µL Proteinase K combined with 200 µL TE buffer (30 mM Tris-Cl, 1 mM EDTA, pH 8.0, 15 mg/mL lysozyme), vortexed every 2 min over a 10-min period. Following this, 700 µL of buffer RLT (QIAGEN RNeasy Plus Kit) was added, and samples were vortexed and centrifuged with the gDNA eliminator spin column at 14000 rpm for 2 min. The flow-through was combined with 700 µL of 99% ethanol for RNA extraction using the QIAGEN RNeasy Plus Kit, with centrifugation times extended to 2 min. RNA was eluted with RNase-free water and treated with Invitrogen™ DNA-free™ DNA Removal Kit to ensure complete removal of genomic DNA.

Concentrations were measured on a NanoDrop 2000 (Thermo Fisher Scientific), and 100 ng of RNA was reverse transcribed using the High-Capacity cDNA Reverse Transcription Kit (Applied Biosystems™).

For qPCR, TaqMan™ Fast Advanced Master Mix (Applied Biosystems™) was used and the absolute quantification was carried out as described in Kiefer, Schütz *et al*.[58] The qPCR was run on a StepOnePlus™ Real-Time PCR System, with thermal cycling conditions as specified in the TaqMan™ protocol. Data were analyzed using the standard curve method, and quantities of *lasB* in copy number per microliter were calculated for each strain.

Cytometric Bead Array (CBA)

Cytokine levels were quantified using a bead-based fluorescence-activated cell sorting (FACS) assay with the CBA method, utilizing Human Soluble Protein Flex Sets specific for IL-6 (558276), TNF (558273), G-CSF (558326), MCP-1 (558287), and IL-1β (558279), along with the Human Soluble Protein Master Buffer Kit (558264), all purchased from BD Biosciences. The assay followed the manufacturer's protocol, with cytokines quantified against their respective standard curves. Bead sorting and analysis were conducted using a BD LSRFortessa™ FACS (BD Biosciences), and data analysis was performed with FCAP Array Version 3.0.1 (BD Biosciences).

Quantification of E-Cadherin *via* Western blot

The procedure was performed as described by Aljohmani *et al*. with a modification in the lysis buffer volume. [81] Briefly, cultured cells were lysed in 50 µL lysis buffer (20 mM Tris·HCl, 150 mM NaCl, 1% Triton X-100, 1 mM EDTA, 1 mM Na_3VO_4, 1 mM PMSF, 10 mM 1,10-phenanthroline monohydrate) supplemented with 1× Complete Inhibitor (Roche Diagnostics Deutschland GmbH, Mannheim, Germany) and incubated at 4°C for 10 min. Cell lysates were centrifuged at 16,000 g for 15 min at 4°C, and the supernatant was used for protein quantification via a commercial Bicinchoninic acid assay (BCA) kit (Thermo Fisher, Karlsruhe, Germany), following the manufacturer's instructions. The subsequent steps, including SDS-PAGE, protein transfer, blocking, antibody incubation, chemiluminescence detection, and densitometric quantification, were performed as detailed in Aljohmani *et al*.

Visualization of E-Cadherin and Claudin-4 *via* Confocal Laser Scanning Microscopy (CLSM)

Arlo and Calu-3 cells were seeded into 24-well transwell inserts and cultured for 10 days under the same conditions used for the TEER experiments. After incubation, the basolateral and apical fluids were aspirated, and both compartments were washed three times with PBS. To fix the cells, 200 µL of 4% paraformaldehyde (Thermo Fisher Scientific Inc., Netherlands) in PBS was added to the apical chambers for 15 min at room temperature. After fixation, the apical chambers were washed three times with PBS. For staining, the transwell inserts were transferred into a new 24-well plate, and the PBS was removed. Both the apical and basolateral chambers were washed twice with HBSS. To permeabilize the cells, a permeabilization buffer consisting of 1% BSA and 0.05% saponin in PBS was added to both chambers, and the cells were incubated at room temperature for 1 h on a shaker plate (MTS 2/4 D S1 Microplate Shaker, IKA, Germany) at 150 rpm. All staining steps were performed in the dark. After the permeabilization step, the buffer was aspirated, and the cells were incubated overnight at 4°C with 200 µL of a primary antibody mixture containing mouse anti-E-Cadherin IgG (1:50, BD Biosciences, USA) and rabbit anti-Claudin-4 IgG (1:100, Invitrogen, USA) in

permeabilization buffer. The following day, the primary antibody solution was removed, and the apical compartments were washed three times with permeabilization buffer, keeping the plate on the shaker plate at 150 rpm for 10 min per wash. Subsequently, 200 µL of secondary antibodies were added to the apical chambers: anti-mouse goat IgG Alexa Fluor 546 (1:500, Invitrogen, USA) and anti-rabbit goat IgG Alexa Fluor 488 (1:1000, Invitrogen, USA), both in permeabilization buffer, and the cells were incubated for 1 h at room temperature. Afterward, the cells were washed three times with permeabilization buffer under the same conditions as before. For the final staining step, the cells were incubated for 30 min at room temperature with 100 µL of 1 µg/mL DAPI (Sigma Aldrich, Switzerland) in PBS. After incubation, the apical chambers were washed three times with PBS under the same conditions. The cell-covered membranes were then mounted onto 24x50 mm microscopy slides (Thermo Fisher Scientific, Netherlands) using Fluorescence Mounting Medium (DAKO Schweiz AG, Switzerland). A cover slip (Carl Roth, Germany) was placed over the membranes, and the samples were wrapped in aluminum foil and left to dry overnight at room temperature.

For imaging, a Leica TC SP8 Confocal Microscope (Leica Microsystems, Wetzlar, Germany) equipped with a 25x water objective (Fluotar VISIR 25x/0.95 WATER) was used. For Calu-3 cell imaging, the argon laser intensity was set to 30%. DAPI was excited at 405 nm with 10% laser intensity, and its emission was detected in the range of 410–501 nm. Alexa Fluor 488, used to detect Claudin-4, was excited at 488 nm with 40% laser intensity, and the emission was detected from 501 to 561 nm. Alexa Fluor 546, used to detect E-Cadherin, was excited at 561 nm with 3% laser intensity, and its emission was detected from 566 to 701 nm. All signals were captured sequentially in three scans to minimize crosstalk, using PMT detectors for DAPI and Alexa Fluor 546 and a HyD detector for Alexa Fluor 488, with a gain of 800 for the PMT detectors and 100 for the HyD detector. For Arlo cell imaging, the argon laser intensity was also set to 30%. DAPI was excited at 405 nm with 30% laser intensity, and its emission was detected in the range of 410–494 nm. Alexa Fluor 488, used to detect Claudin-4, was excited at 488 nm with 70% laser intensity, and its emission was detected from 494 to 564 nm. Alexa Fluor 546, used to detect E-Cadherin, was excited at 561 nm with 6% laser intensity, and its emission was detected from 566 to 701 nm. Signals were captured sequentially in three scans to minimize crosstalk, with PMT detectors for DAPI and Alexa Fluor 546 and a HyD detector for Alexa Fluor 488, with a gain of 800 for the PMT detectors and 100 for the HyD detector. Images were captured at a resolution of 2048 x 2048 with bidirectional X scanning at a scan speed of 100 Hz. Line averaging and frame accumulation of 2 were applied, and a 3x virtual zoom was used for obtaining close-up pictures. Further image editing and compilation was done by using the open-source software ImageJ and GIMP.

RNA Sequencing

Calu-3 cells were exposed to various treatment conditions, including supernatants from wild-type (wt) *P. aeruginosa* (wt PAO1 sn and Δ*lasB* PAO1 sn), 100 µM compound **1** combined with wt PAO1 sn, as well as an HBSS control, an off-target control with compound **1** + Δ*lasB* PAO1 sn, and a compound toxicity control. Following a 7 h incubation, total RNA was extracted using Buffer RLT (Qiagen), and further purified with the Monarch® RNA Cleanup Kit (10 µg capacity, New England Biolabs). RNA integrity and purity were assessed, with all samples showing RNA Integrity Numbers (RIN) greater than 8.

Strand-specific mRNA sequencing was performed. mRNA libraries were prepared using the NEBNext® Ultra™ II Directional RNA Library Prep Kit (NEB #E7765), followed by sequencing on an Illumina NovaSeq 6000 platform using paired-end 50 bp reads (PE50, 2 × 50 bp), yielding approximately 30 million reads per sample and a total flow cell output of 800 million clusters. Raw FASTQ files were analyzed using a standardized pipeline deployed in a Docker container running RNADetector.[59] STAR was employed for alignment, and gene-level quantification was performed using *feature*Counts. Read count matrices were normalized to correct for library size and composition biases using the Bioconductor package edgeR. Pathway enrichment analyses were conducted using the Reactome pathway knowledgebase. The count matrix derived from RNAdetector was modified to only contain identifiers, and the matrix was analyzed using the PADOG analysis method, which includes disease pathways, without any additional normalization. Input matrix and data of the resulting PDF, R-Script and Excel report files are provided in Data S1.

Gene expression profiles were visualized through volcano plots and heatmaps generated in Python (v3.x) using numpy (v2.0.2), pandas (v2.2.3), matplotlib (v3.9.4), and seaborn (v0.13.2). Visualizations were based on a normalized count table and the list of significantly regulated genes identified by RNA-detector (see lists in Data S1). Selected genes showing significant differential expression influenced by LasB activity and its inhibition by compound **1** were further validated by quantitative PCR following the aforementioned protocol.

Calu-3 transwell-based bacterial infection model

Wild type PAO1 and PAO1 Δ*lasB* strains were cultured overnight in LB medium at 37°C with shaking at 180 rpm. The following day, cultures were centrifuged (5000 rpm, 4°C, 10 min), resuspended in fresh LB, and adjusted to an OD_{600} of 0.025. Cultures were then grown to an OD_{600} of approximately 2, centrifuged again, and standardized to an OD_{600} of 1.5. A 1:10 dilution was performed to achieve the desired MOI of 30 for the experiment.

Calu-3 cells were seeded in transwells and grown for 9 days as described above. On the day of the experiment, TEER was measured, and cells were washed with HBSS. After a 30–60 min incubation in HBSS at 37°C + 5% CO_2, TEER was measured again. The apical compartment received 190 µL HBSS with 10 µL of diluted bacterial culture. For compound testing, 1 µL of compound **3** (in DMSO) or meropenem (in PBS) was added, maintaining a final DMSO concentration of 0.5%. The basolateral compartment received 800 µL HBSS. Plates were incubated at 37°C with 5% CO_2, and TEER was measured hourly for 7 h.

To quantify bacterial growth, 10 µL samples were collected from the apical compartment at the start and end of the experiment. These samples were serially diluted, plated on agar, and incubated. Colony-forming units (CFUs) were counted the following day.

Determination of Meropenem Minimum Inhibitory Concentration (MIC) Against *Pseudomonas aeruginosa* PAO1

The antibacterial activity of meropenem was determined in *Pseudomonas aeruginosa* PAO1 (DSM 19880). As a bacteria start OD_{600}, we used 0.03 (optical density of the bacteria at 600 nm) in a total volume of 200 µL in 99.5% HBSS and 0.5% lysogeny broth (LB) medium containing meropenem pre-dissolved in DMSO (maximal DMSO concentration: 1%). Final meropenem concentrations prepared from serial dilutions ranged from 0.0625 to 5 µM. The OD_{600} values were determined directly after

addition of the antibiotic and again after incubation at 37°C for 16 h and 50 rpm in 96 well plates (Sarstedt, Nümbrecht, Germany) using a FLUOstar Omega microplate reader (BMG labtech, Ortenberg, Germany). The given MIC value is a mean of two independent determinations and is defined as the lowest concentration of meropenem that reduced the OD_{600} by ≥ 95%.

Statistical analysis and data visualization

All graphical data are presented as mean ± standard deviation (SD). Statistical comparisons between experimental conditions were performed using Dunnett's one-way ANOVA to determine significant differences. A p-value ≤ 0.05 was considered statistically significant, while p-values > 0.05 were considered non-significant. Graphs were generated using GraphPad Prism (v 9.3.1). Transcriptomic data were analyzed and visualized as heatmaps *via* Python (v3.x).

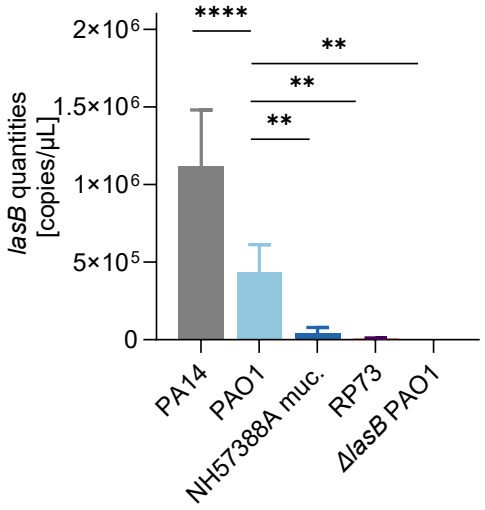

Figure S1: Absolute quantification of *lasB* expression across various *Pseudomonas aeruginosa* strains. *lasB* transcript levels were measured in PAO1, PA14, NH57388A muc., RP73, and Δ*lasB* PAO1 using a standard curve-based absolute quantification approach. PA14 showed the highest expression, followed by PAO1, while NH57388A muc. and RP73 exhibited minimal to undetectable levels. Data represent mean values from three independent experiments (n = 3); error bars indicate standard deviation (SD). Statistical analysis was performed using one-way ANOVA with Dunnett's multiple comparisons test, comparing each strain to PAO1. (****p ≤ 0.0001; **p ≤ 0.01).

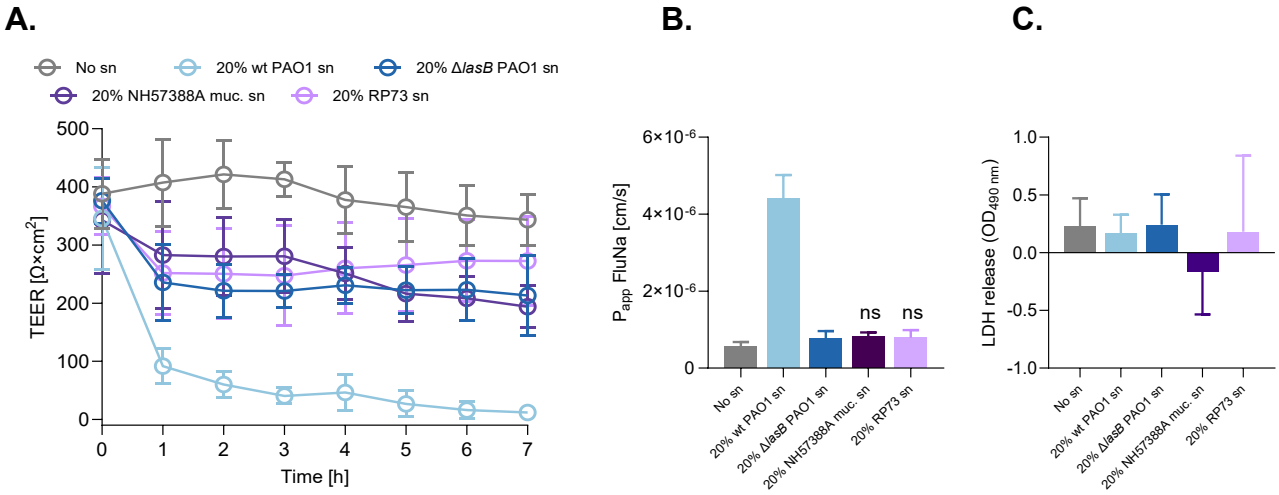

Figure S2: Effect of *Pseudomonas aeruginosa* strains on epithelial barrier integrity. (A) Transepithelial electrical resistance (TEER) and **(B)** fluorescein sodium (FluNa) permeability (P_{app}) measured in Calu-3 cells over a 7-hour period following treatment with 20% (v/v) supernatants (sn) from wild-type (wt) PAO1, Δ*lasB* PAO1, NH57388A muc., and RP73 strains. **(C)** Lactate dehydrogenase (LDH) release assessed at 7 hours to evaluate cytotoxicity. Data represent mean ± standard deviation (n = 3 independent experiments). Statistical analysis was conducted using one-way ANOVA followed by Dunnett's multiple comparisons test, comparing each condition to Δ*lasB* PAO1 sn (****p ≤ 0.0001; ns, not significant).

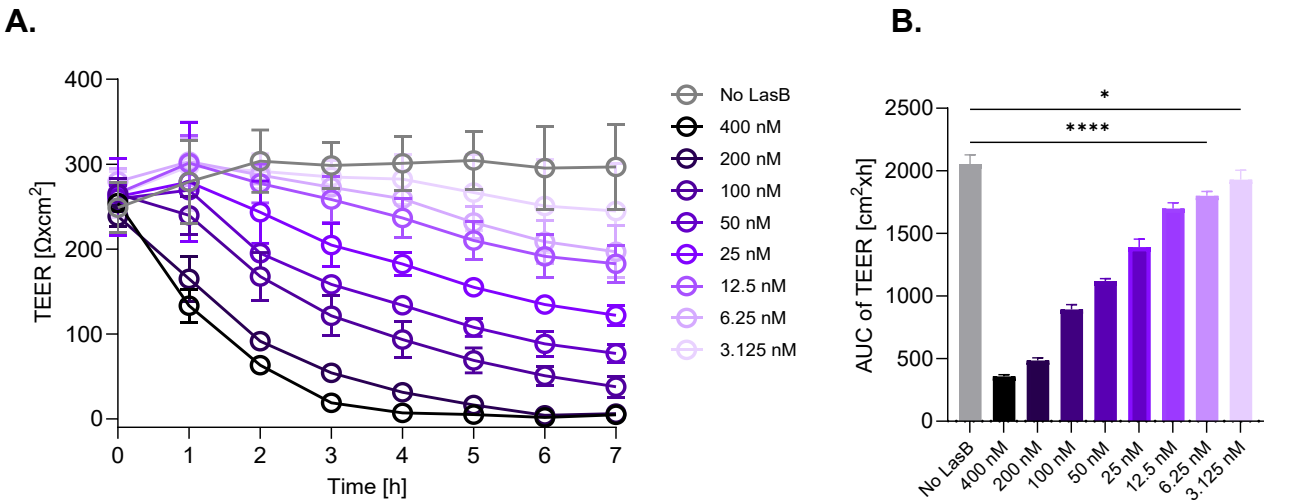

Figure S3: Effect of purified LasB of *Pseudomonas aeruginosa* on Calu-3 epithelial barrier integrity. (A) Transepithelial electrical resistance (TEER) of Calu-3 monolayers following treatment with increasing concentrations of purified LasB protein, monitored over a 7-hour period. **(B)** Area under the curve (AUC) analysis of TEER data quantifies the dose-dependent disruption of barrier function. Data represent mean ± standard deviation (n = 2 independent experiments). Statistical analysis was performed using one-way ANOVA followed by Dunnett's multiple comparisons test against the healthy control (****$p \leq 0.0001$; *$p \leq 0.05$; ns, not significant).

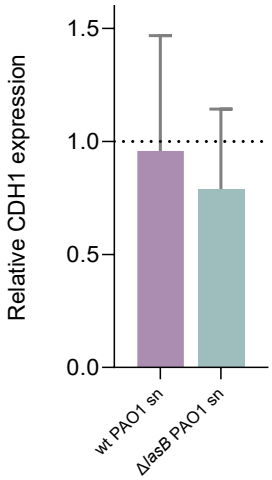

Figure S4: CDH1 gene expression in Calu-3 cells exposed to *Pseudomonas aeruginosa* supernatants. Relative expression of CDH1 in Calu-3 cells following exposure to 20% (v/v) wild-type (wt) PAO1 supernatant (sn) or Δ*lasB* PAO1 sn relative to the unchallenged healthy control.

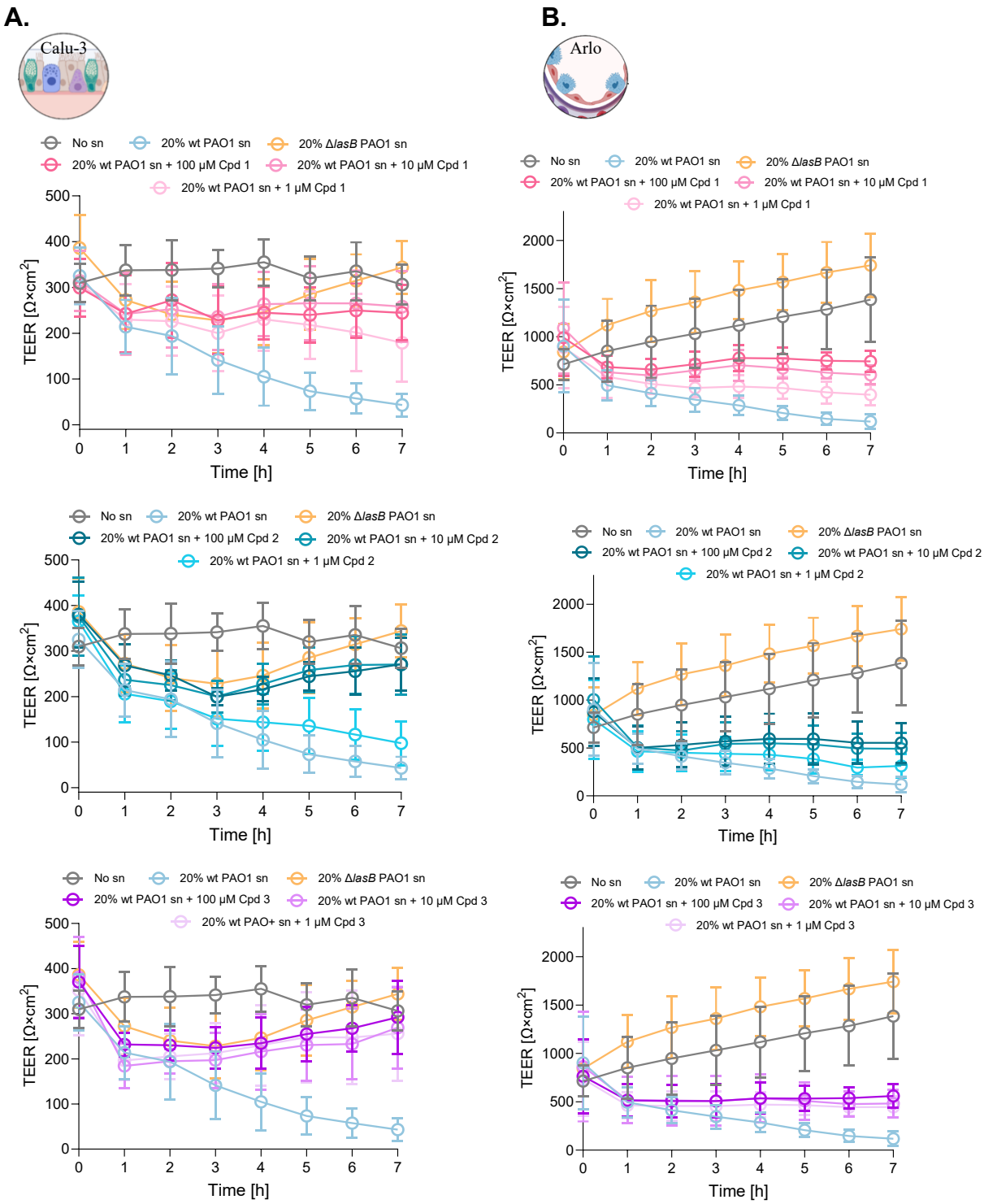

Figure S5: Evaluation of LasB inhibitors in preserving epithelial barrier integrity. Transepithelial electrical resistance (TEER) of **(A)** Calu-3 and **(B)** Arlo cells over 7 hours following exposure to 20% (v/v) wild-type (wt) *Pseudomona aeruginosa* PAO1 supernatant (sn) or Δ*lasB* PAO1 sn, with or without treatment using LasB inhibitors at 1, 10, or 100 µM.. Data represent mean ± standard deviation (n = 3 independent experiments).

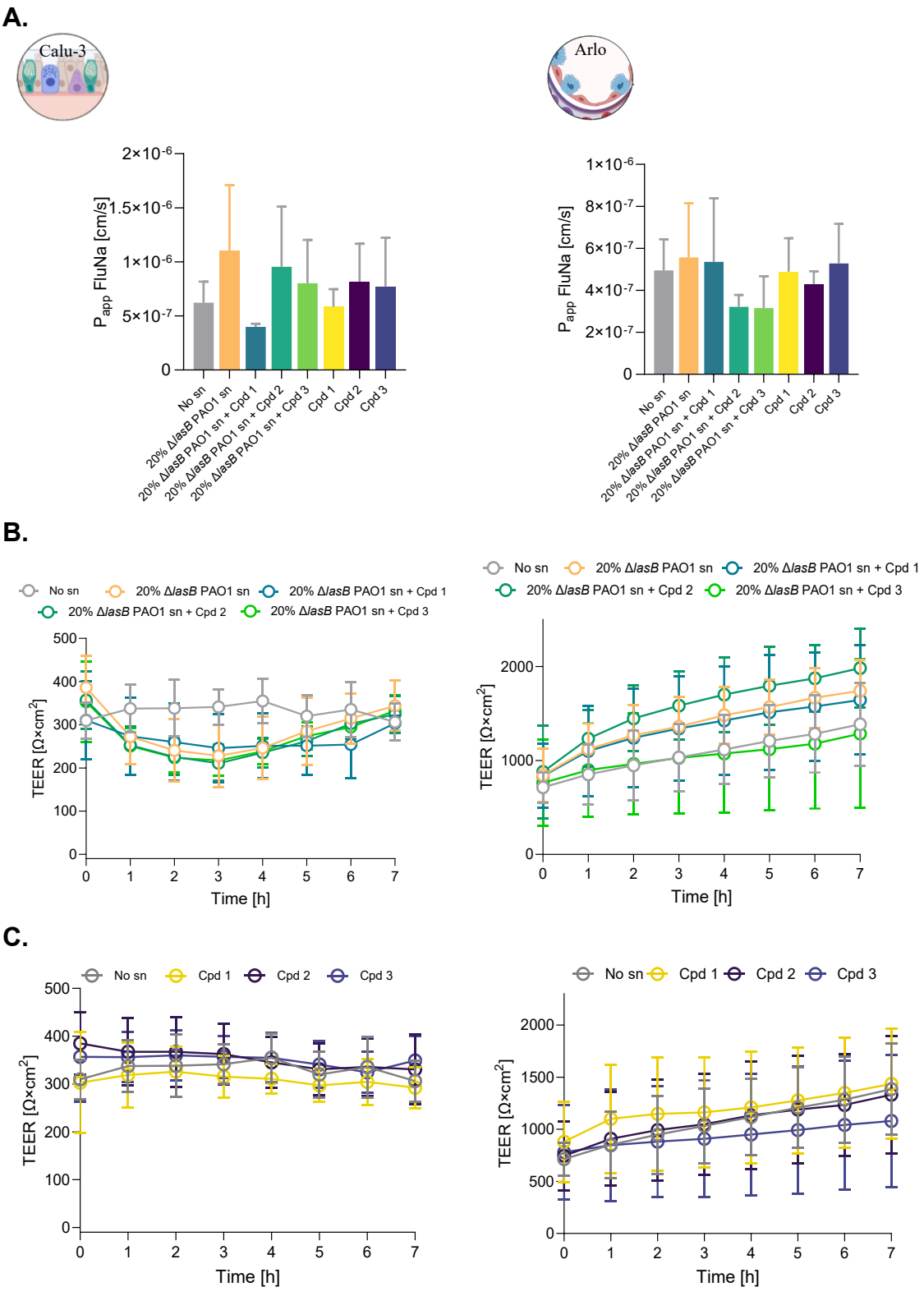

Figure S6: Evaluation of off-target effects and cytotoxicity of LasB inhibitors in Calu-3 and Arlo cells. **(A)** Paracellular permeability (P_{app}) of Calu-3 and Arlo cells following treatment with compounds alone or in combination with Δ*lasB Pseudomonas aeruginosa* PAO1 supernatant (sn). **(B)** Transepithelial electrical resistance (TEER) measurements over 7 hours in both cell lines treated with compounds and Δ*lasB* PAO1 sn to assess potential off-target effects. **(C)** TEER over 7 hours following treatment with compounds alone to evaluate cytotoxicity. Data represent mean ± standard deviation (n = 3 independent experiments). Statistical analysis was

performed using ordinary one-way ANOVA followed by Dunnett's multiple comparisons test, comparing all treatment groups to the healthy control (no sn); no statistically significant differences were observed.

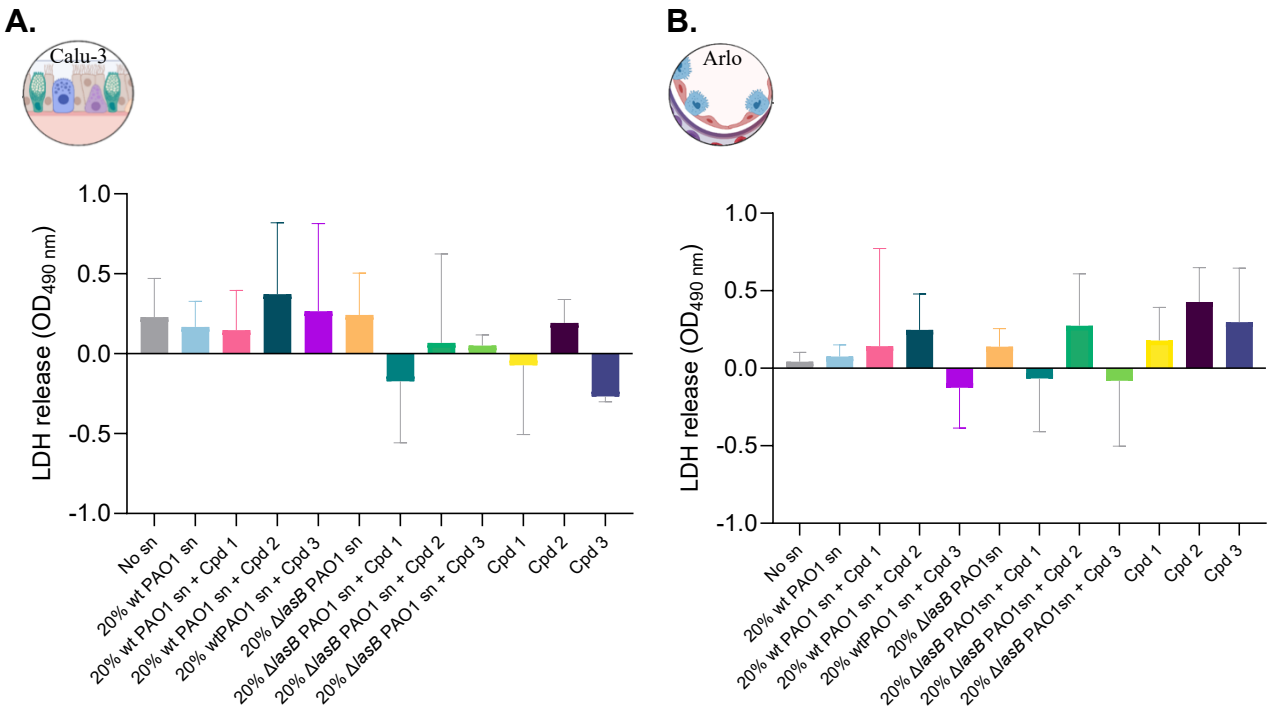

Figure S7: Lactate dehydrogenase (LDH) release in Calu-3 and Arlo cells. LDH release was measured in **(A)** Calu-3 cells and **(B)** Arlo cells under various experimental conditions with, without *Pseudomonas aeruginosa* PAO1 supernatant and with, without compounds.. LDH levels were quantified relative to the healthy control no supernatant (no sn). Data represent mean ± standard deviation (n = 3 independent experiments). Statistical analysis was performed using ordinary one-way ANOVA followed by Dunnett's multiple comparisons test, comparing each treatment group to the healthy control. No statistically significant differences were observed in any experimental condition.

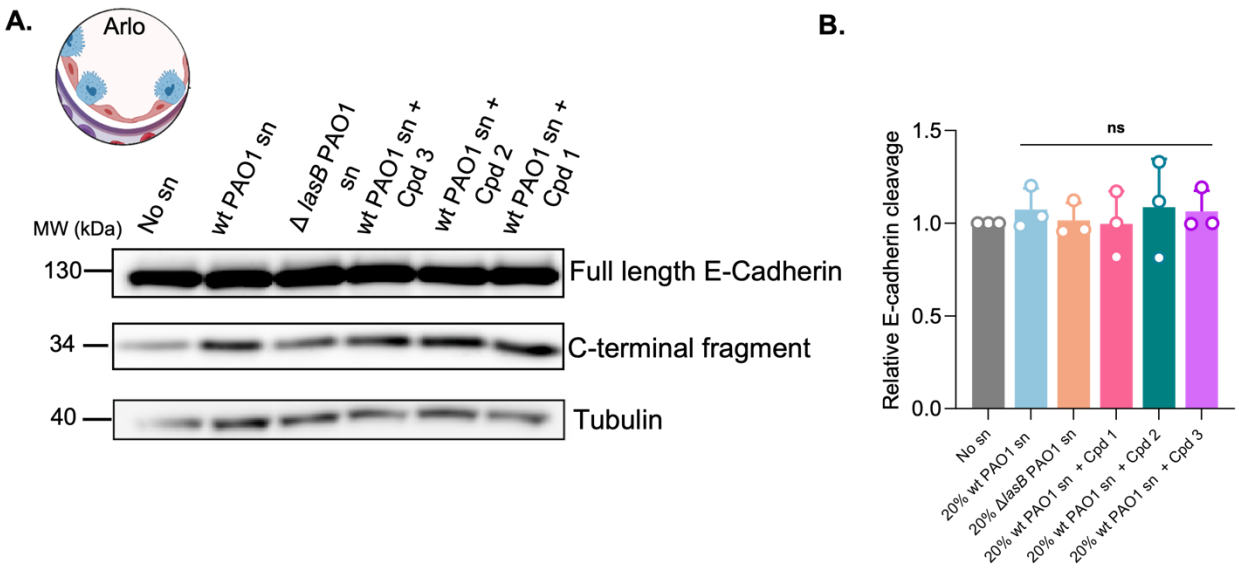

Figure S8: Quantification of E-Cadherin in Arlo cells upon challenge with *Pseudomonas aeruginosa* PAO1 supernatant, with or without inhibitor. (A) Western blot analysis of E-cadherin cleavage in Arlo cells under healthy conditions or following challenge with wild-type (wt) PAO1 supernatant (sn), Δ*lasB* sn, or wt PAO1 sn with 100 µM of LasB inhibitors (**1–3**). Full-length and C-terminal fragment bands are shown, with tubulin as a loading control. **(B)** Relative quantification of E-cadherin cleavage in Calu-3 cells under the same experimental conditions. Data represent mean ± standard deviation (n = 3 independent experiments). Statistical analysis was conducted using one-way ANOVA followed by Dunnett's multiple comparisons test. (ns, not significant).

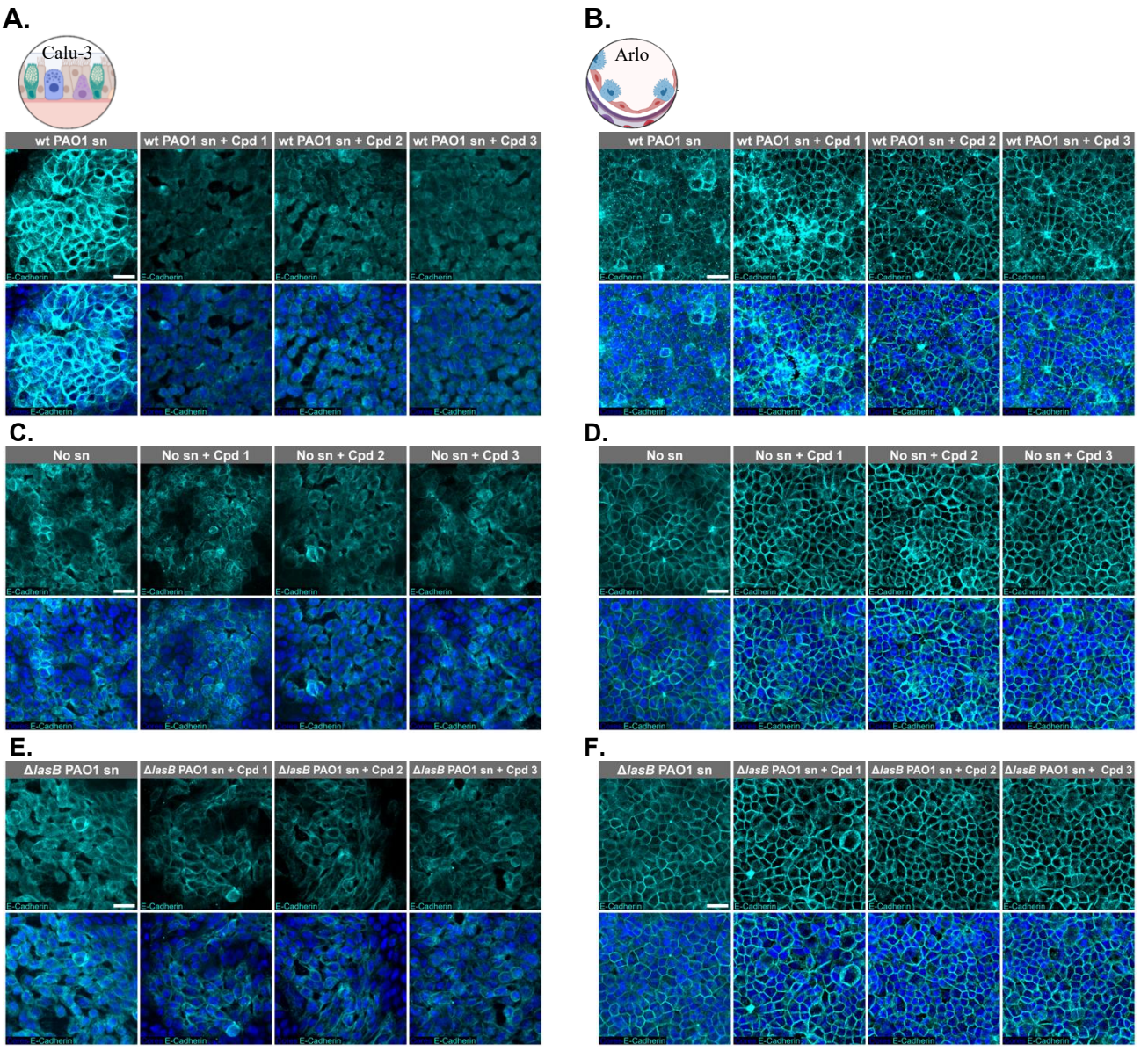

Figure S9: Imaging of E-cadherin (cyan) localization in Calu-3 (left) and Arlo cells (right) under different treatment conditions through confocal laser scanning microscopy (CLSM). **(A)** Cells subjected to 20% (v/v) wild-type (wt) *Pseudomonas aeruginosa* PAO1 supernatant (sn) and visualization of the protective effect of the three different LasB Inhibitors at 100 µM. **(B)** Cytotoxicity tests using no supernatant (no sn) on cells as well as applying each compound at 100 µM. **(C)** Test for off-target side effects through exposure to 20% (v/v) Δ*lasB* sn and treatment with 100 µM of the LasB inhibitors. Nuclei were counterstained with DAPI (blue). The scale bar = 25 µm.

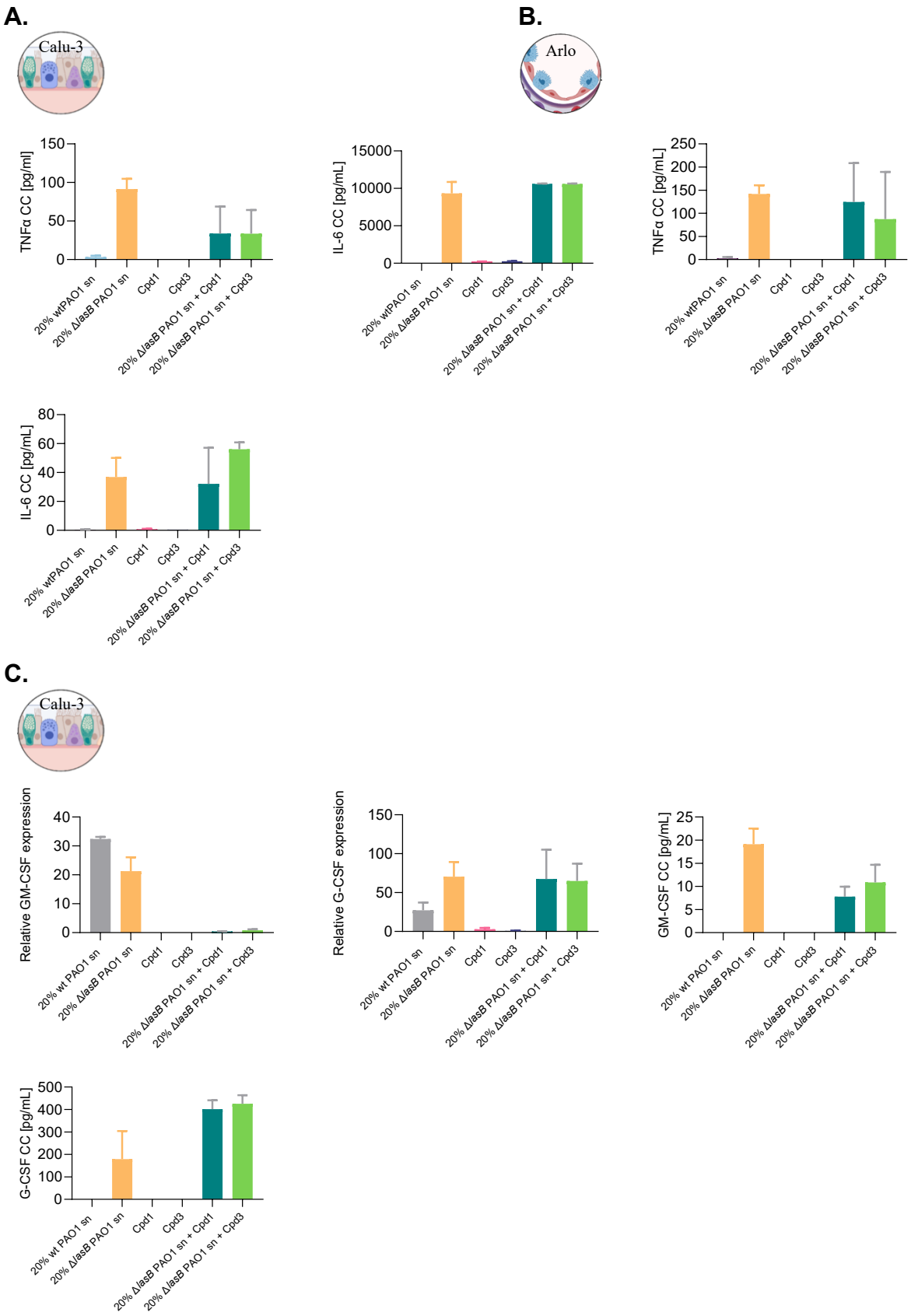

Figure S10: Cytotoxicity, off-target effects, and cytokine profiles of LasB inhibitors. Cytometric bead array (CBA) quantification of TNF-α and IL-6 in **(A)** Calu-3 and **(B)** Arlo cells. **(C)** Expression and protein analysis of colony-stimulating factors under various treatment conditions. All experiments were conducted using 20% (v/v) wild-type (wt) *Pseudomonas aeruginosa* PAO1 supernatant (sn), Δ*lasB* PAO1 sn, inhibitors alone, or

inhibitors combined with Δ*lasB* PAO1 sn. Data represent mean ± standard deviation (n = 3 independent experiments).

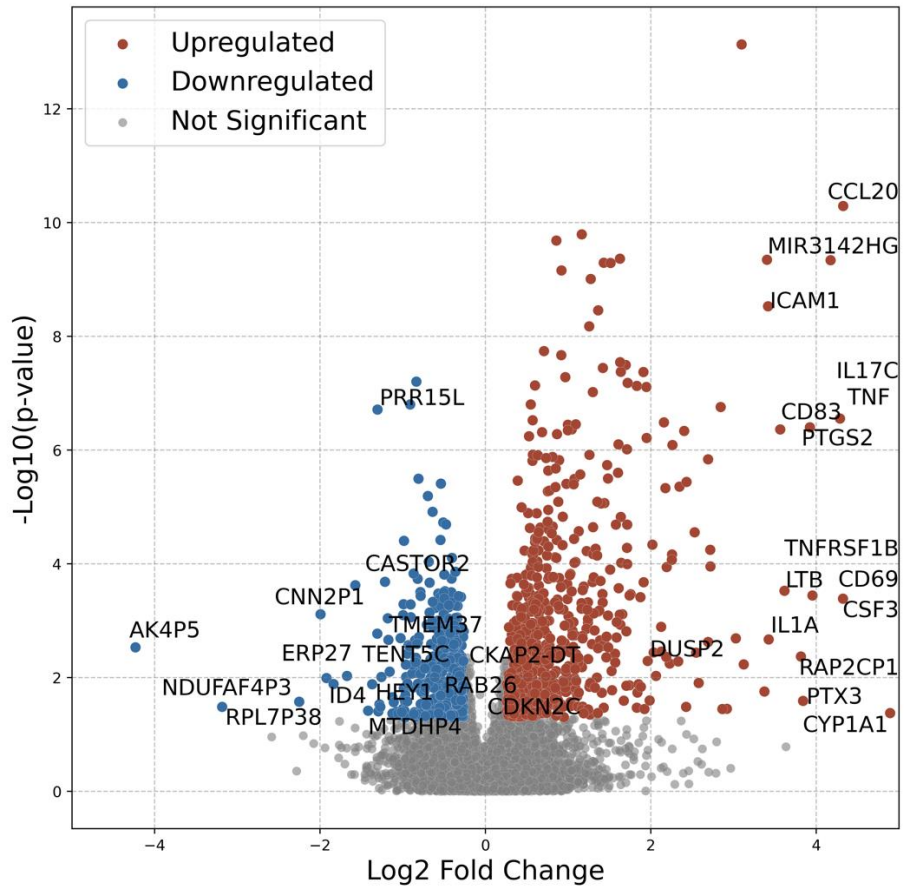

Figure S11: Volcano plot showing the expression of LasB-specific genes — identified in Calu-3 cells exposed to LasB-containing *Pseudomonas aeruginosa* supernatant — in NuLi-1 cells infected with *P. aeruginosa* (GSE199424, 8 h). The plot displays $\log_2$ fold changes versus $-\log_{10}$ adjusted p-values. Commonly downregulated and upregulated genes, including *DUSP2*, are highlighted, indicating conserved transcriptional responses to *P. aeruginosa* across epithelial cell types.

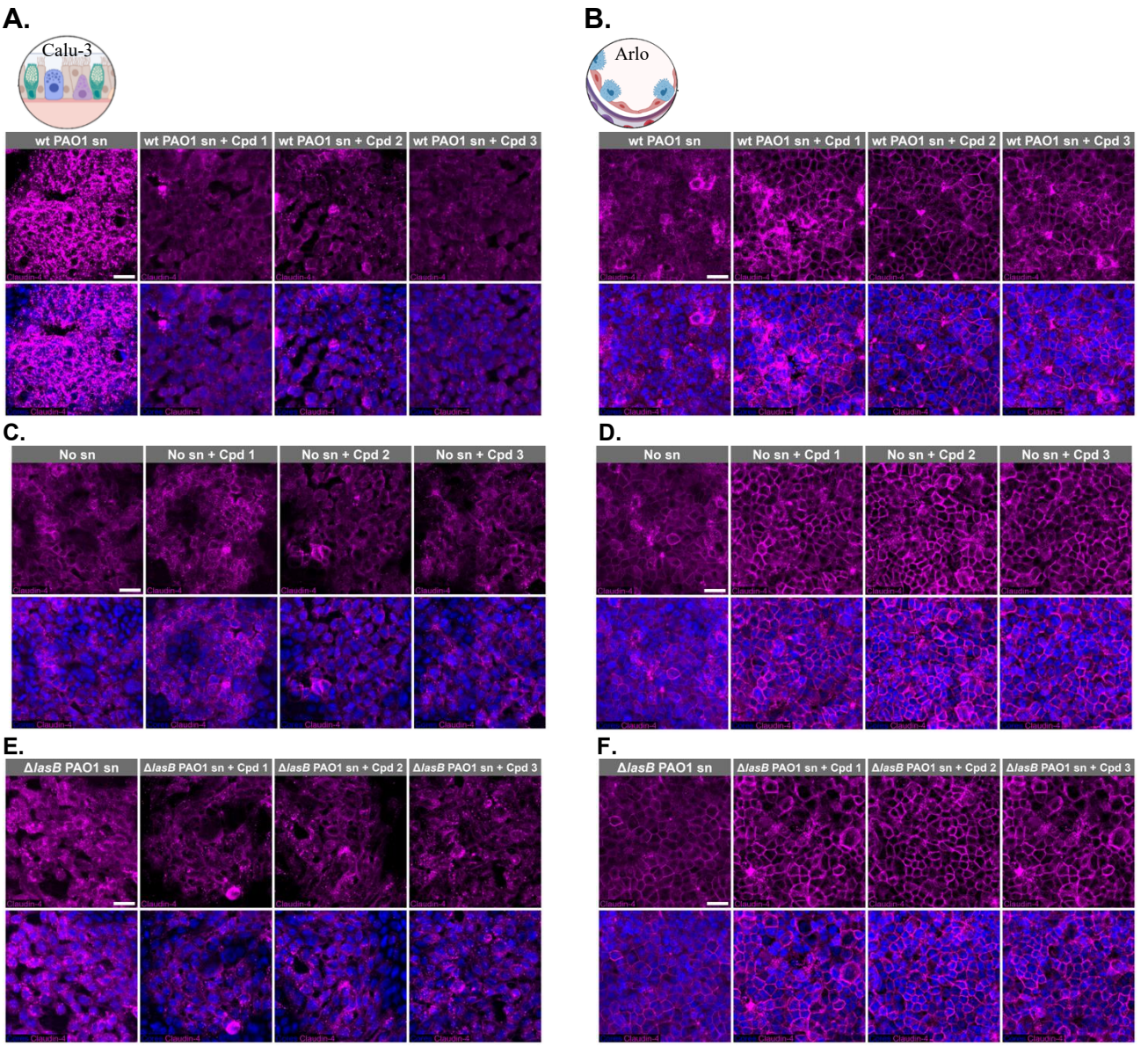

Figure S12: Visualization of Claudin-4 (magenta) localization in Calu-3 (left) and Arlo cells (right) under different treatment conditions through confocal laser scanning microscopy (CLSM). (A) and **(B)** Cells exposed to 20% (v/v) wild-type (wt) *Pseudomonas aeruginosa* PAO1 supernatant (sn), showing the effect of the three different LasB inhibitors at 100 µM. **(C)** and **(D)** Cytotoxicity tests using no sn on cells, as well as applying each compound at 100 µM. **(E)** and **(F)** Test for off-target side effects through exposure to 20% (v/v) Δ*lasB* PAO1 sn and treatment with 100 µM of LasB inhibitors. Nuclei were counterstained with DAPI (blue). Scale bar = 25 µm

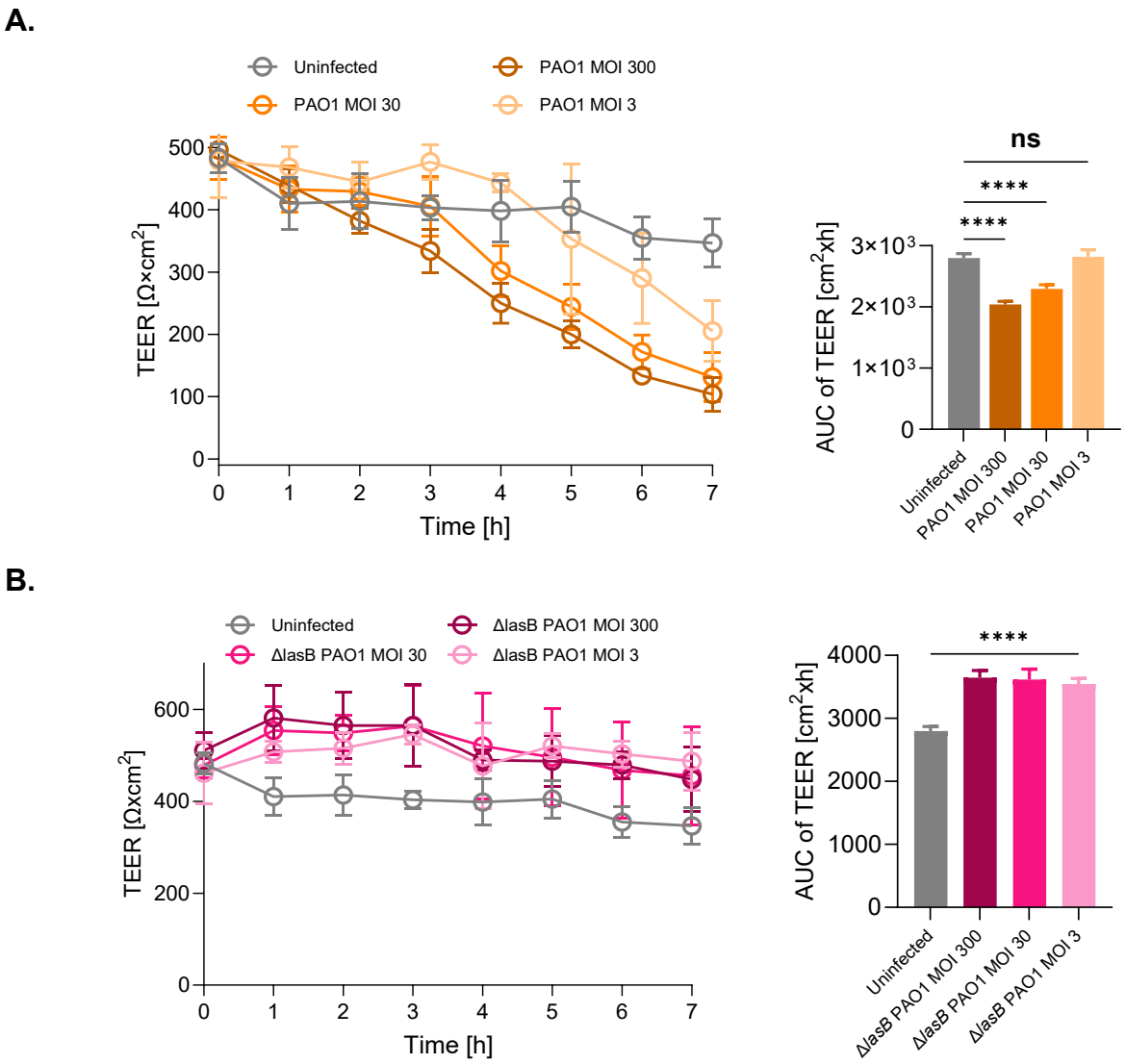

Figure S13: Infection studies of wild-type (wt) and Δ*lasB Pseudomonas aeruginosa* PAO1 on Calu-3 cells. Transepithelial electrical resistance (TEER) of Calu-3 monolayers monitored over 7 hours following infection with **(A)** wt PAO1 and **(B)** Δ*lasB* PAO1 at varying multiplicities of infection (MOIs). Area under the curve (AUC) of TEER data was calculated to assess barrier disruption. Data represent mean ± standard deviation (n = 3 independent experiments). Statistical analysis was performed using ordinary one-way ANOVA followed by Dunnett's multiple comparisons test (****$p \leq 0.0001$; ns, not significant).

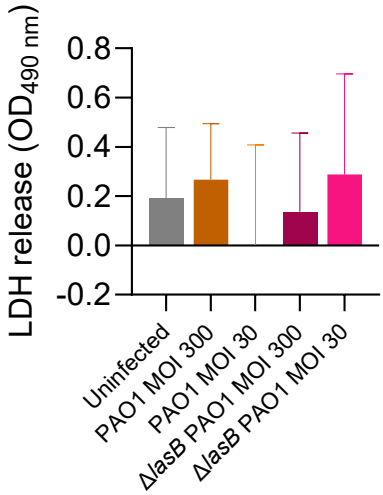

Figure S14: Lactate dehydrogenase (LDH) release in Calu-3 cells upon infection with PAO1. LDH release was measured in Calu-3 cells following infection with wild-type (wt) PAO1 and Δ*lasB* PAO1 at multiplicities of infection (MOI) of 30 and 300. LDH levels were quantified relative to the uninfected control. Data represent mean ± standard deviation (n = 3 independent experiments). Statistical analysis was performed using ordinary one-way ANOVA followed by Dunnett's multiple comparisons test, comparing each group to the uninfected control. No statistically significant differences were observed.

Table S1: Chemical structure of selected compounds for this study.

Compound	Chemical structure
1	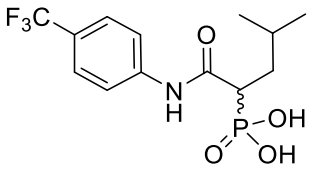
2	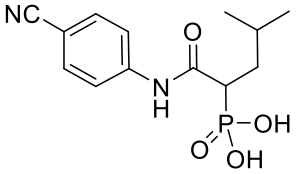
3	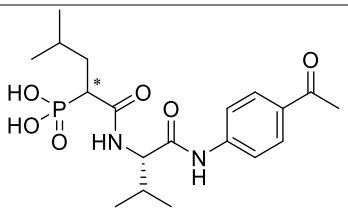

Table S2: List of primers designed for the quantification of cytokine gene expression *via* RT-qPCR.

Gene	Primer	Sequence 5'—3'
POLR2A	Forward	CAGCAAGGTCGTCCTCCCCTGT
	Reverse	GATGCGCAATGGCTTGGTTGAA
GUSB	Forward	CGCCCTGCCTATCTGTATTC
	Reverse	TCCCCACAGGGAGTGTGTAG
IL6	Forward	AGAGGCACTGGCAGAAAACA
	Reverse	TCACCAGGCAAGTCTCCTCA
IL1A	Forward	CAGTGCTGCTGAAGGAGATGC
	Reverse	TGGATGGGCAACTGATGTGAA
IL1B	Forward	TACCCAAAGAAGAAGATGGAA
	Reverse	GAGGTGCTGATGTACCAGTTG
CXCL8	Forward	TCAGAGACAGCAGAGCACAC
	Reverse	CTTGGCAAAACTGCACCTTCA
TNFα	Forward	TAGCCCATGTTGTAGCAAACCC
	Reverse	AGGAGGTTGACCTTGGTCTG
CSF3	Forward	GTCCCACCTTGGACACACTG
	Reverse	TTCCCAGTTCTTCCATCTGCTG
CSF2	Forward	CTGGAGCTGTACAAGCAGGG
	Reverse	CACAGGAAGTTTCCGGGGTT
IL4	Forward	CTGTGCTCCGGCAGTTCTAC
	Reverse	TCACAGGACAGGAATTCAAGC
IL13	Forward	GTCTCAGCTGGGCAGTTTTC
	Reverse	GAACTGTCCCTCGCGAAAAAG
IL37	Forward	TGGGGGTCTCTAAAGGGGAG
	Reverse	CAGCTTCATCAGTTTCTCCTTCTTC
IL1RN	Forward	TGCAAGCCTTCAGAATCTGGG
	Reverse	GAGCATGAGGCTCAATGGGT
TGFB1	Forward	GGAAATTGAGGGCTTTCGCC
	Reverse	CCGGTAGTGAACCCGTTGAT
CCL2	Forward	TCTCGCCTCCAGCATGAAAG
	Reverse	GGCATTGATTGCATCTGGCT
IRF7	Forward	CGGCTGGAAAACCAACTTCC
	Reverse	GCCTGGGCCTTCTCGC

Table S3: List of primers designed for validation of RNA-seq data by RT-qPCR.

Gene	Primer	Sequence 5'—3'
VIPR1	Forward	TTCTCCTCCATTCAAGGCCG
	Reverse	AACTCGCTGCCTTGTCATCC
DUSP2	Forward	TCCTGTCTACGACCAGGGTG
	Reverse	CCACCATCTGGTTGTCCTCC
SPIRE2	Forward	TCTTCTGCAAGAGAGCCGTC
	Reverse	TGGCAGCTGATACCCTCTGA
CLDN4	Forward	TATTGGGGAGGGACGGAAGT
	Reverse	CCTACCCGGAACAGAGGAGA
CLDN10	Forward	TCATACTGTCAGGGCTGTGC
	Reverse	GGCTCCTGCCCATCCAATAA
FGFBP1	Forward	CGTGTGCTCAGAACAAGGTGAA
	Reverse	CACCTGAGCAGCCAGTAGG
MYD88	Forward	CCTCTCTCCAGGTGCCCAT
	Reverse	GTCTTCAGGGCAGGGACAAG
TCF7	Forward	GCGGGACAACTACGGGAAG
	Reverse	ACCGAATGCATTTCTTTTTCCTC
ACTN4	Forward	GGGAAGCCCTGGAGAAAACA
	Reverse	AGGCCCTCAATCTCCTCGAT
TRIP6	Forward	CACCCTGGAGAAATGTGCCA
	Reverse	TGGGGCAAACTTCCTGTGAA
TM4SF1	Forward	ATGCCTCCGAAAACCACCTC
	Reverse	CTGGCAGGAGCATCAGCAG
BCL6	Forward	GCCTGAGAACCTTGACCTCC
	Reverse	AGCCCGTCATGGACCTGTTA

References

[23] Carius P, Jungmann A, Bechtel M*, et al.* A Monoclonal Human Alveolar Epithelial Cell Line ("Arlo") with Pronounced Barrier Function for Studying Drug Permeability and Viral Infections. Advanced science 2023; 10(8): e2207301 [https://doi.org/10.1002/advs.202207301][PMID: 36748276]

[58] Kiefer AF, Schütz C, Englisch CN*, et al.* Dipeptidic Phosphonates: Potent Inhibitors of Pseudomonas aeruginosa Elastase B Showing Efficacy in a Murine Keratitis Model. Adv Sci (Weinh) 2025: e2411807 [https://doi.org/10.1002/advs.202411807][PMID: 39973061]

[81] Aljohmani A, Opitz B, Bischoff M, Yildiz D. Pseudomonas aeruginosa Triggered Exosomal Release of ADAM10 Mediates Proteolytic Cleavage in Trans. Int J Mol Sci 2022; 23(3) [https://doi.org/10.3390/ijms23031259][PMID: 35163191]

2.2 Chapter B

Dipeptidic Phosphonates: Potent Inhibitors of *Pseudomonas aeruginosa* Elastase B Showing Efficacy in a Murine Keratitis Model

Alexander F. Kiefer‡, Christian Schütz‡, Colya N. Englisch, Dominik Kolling, Samira Speicher, Andreas M. Kany, ***Roya Shafiei****, Noran A. Wadood, Ahmad Aljohmani, Niklas Wirschem, Ravindra P. Jumde, Andreas Klein, Asfandyar Sikandar, Yu-Mi Park, Gabriela Krasteva-Christ, Daniela Yildiz, Ahmed S. Abdelsamie, Katharina Rox, Jesko Köhnke, Rolf Müller, Markus Bischoff, Jörg Haupenthal, and Anna K. H. Hirsch.*

‡ these authors contributed equally

Open access article, *Advanced Science* **2024**, 2411807

DOI: 10.1002/advs.202411807

RESEARCH ARTICLE

ADVANCED SCIENCE Open Access

www.advancedscience.com

Dipeptidic Phosphonates: Potent Inhibitors of *Pseudomonas aeruginosa* Elastase B Showing Efficacy in a Murine Keratitis Model

*Alexander F. Kiefer, Christian Schütz, Colya N. Englisch, Dominik Kolling, Samira Speicher, Andreas M. Kany, Roya Shafiei, Noran A. Wadood, Ahmad Aljohmani, Niklas Wirschem, Ravindra P. Jumde, Andreas Klein, Asfandyar Sikandar, Yu-Mi Park, Gabriela Krasteva-Christ, Daniela Yildiz, Ahmed S. Abdelsamie, Katharina Rox, Jesko Köhnke, Rolf Müller, Markus Bischoff, Jörg Haupenthal, and Anna K. H. Hirsch**

The ubiquitous opportunistic pathogen *Pseudomonas aeruginosa* is responsible for severe infections and notoriously known for acquiring antimicrobial resistance. Inhibiting the bacterium's extracellular elastase, LasB – a zinc-dependent protease – presents a promising strategy to mitigate its virulence. Within this medicinal chemistry–driven hit-to-lead optimization campaign, a new series of highly potent dipeptidic phosphonates is designed and synthesized following a structure–based drug-discovery approach. In vitro and in vivo evaluation reveal beneficial pharmacokinetic profiles, excellent selectivity over human off-targets and good tolerability in murine toxicity studies. Ultimately, the scaffold presented herein demonstrates promising in vivo efficacy in a murine *Pseudomonas aeruginosa* keratitis model in combination with the antibiotic meropenem.

1. Introduction

The infectious inflammation of the cornea, known as infectious keratitis, ranks as the fifth leading cause of blindness and visual impairment worldwide.[1,2] Annually, it accounts for more than 1.5 million new cases of monocular blindness, emphasizing its persistent and substantial public-health impact.[3] Among the causes of corneal opacity, microbial keratitis – attributable to bacterial, fungal, and protozoal pathogens – emerges as the predominant etiology of corneal blindness in both developed and low- and middle-income countries.

In addition to *Staphylococcus aureus* and *Streptococcus pneumoniae*, *Pseudomonas*

A. F. Kiefer, C. Schütz, S. Speicher, A. M. Kany, R. Shafiei, N. Wirschem, R. P. Jumde, A. Klein, A. Sikandar, Y.-M. Park, A. S. Abdelsamie, R. Müller, J. Haupenthal, A. K. H. Hirsch
Helmholtz Institute for Pharmaceutical Research Saarland (HIPS)
Campus E8.1, 66123 Saarbrücken, Germany
E-mail: anna.hirsch@helmholtz-hips.de

A. F. Kiefer, C. Schütz, S. Speicher, A. M. Kany, R. Shafiei, N. Wirschem, R. P. Jumde, A. Klein, A. Sikandar, Y.-M. Park, A. S. Abdelsamie, K. Rox, R. Müller, J. Haupenthal, A. K. H. Hirsch
Helmholtz Centre for Infection Research (HZI)
Inhoffenstraße 7, 38124 Braunschweig, Germany

A. F. Kiefer, C. Schütz, S. Speicher, A. M. Kany, R. Shafiei, N. Wirschem, R. P. Jumde, A. Klein, A. Sikandar, Y.-M. Park, A. S. Abdelsamie, K. Rox, R. Müller, J. Haupenthal, A. K. H. Hirsch
German Center for Infection Research (DZIF)
Inhoffenstraße 7, 38124 Braunschweig, Germany

A. F. Kiefer, C. Schütz, S. Speicher, A. M. Kany, R. Shafiei, N. A. Wadood, A. Aljohmani, N. Wirschem, R. P. Jumde, A. Klein, A. Sikandar, Y.-M. Park, G. Krasteva-Christ, D. Yildiz, A. S. Abdelsamie, R. Müller, J. Haupenthal, A. K. H. Hirsch
PharmaScienceHub (PSH)
Campus A2.3, 66123 Saarbrücken, Germany

C. N. Englisch, M. Bischoff
Institute for Medical Microbiology and Hygiene
Saarland University
Kirrbergerstraße 100, 66421 Homburg/Saar, Germany

D. Kolling, J. Köhnke
Institute for Food Chemistry
Callinstraße 5, 30167 Hannover, Germany

R. Shafiei, N. Wirschem, A. Klein, Y.-M. Park, R. Müller, A. K. H. Hirsch
Department of Pharmacy
Saarland University
Campus E8.1, 66123 Saarbrücken, Germany

N. A. Wadood, G. Krasteva-Christ
Institute of Anatomy and Cell Biology
Saarland University
Kirrbergerstraße 100, 66421 Homburg/Saar, Germany

The ORCID identification number(s) for the author(s) of this article can be found under https://doi.org/10.1002/advs.202411807

DOI: 10.1002/advs.202411807

ADVANCED SCIENCE NEWS
www.advancedsciencenews.com

ADVANCED SCIENCE Open Access
www.advancedscience.com

aeruginosa is a primary bacterial pathogen associated with infections in compromised corneas (*Pseudomonas* keratitis).[2,4] Particularly contact lens-associated keratitis is predominantly caused by *P. aeruginosa*.[5–7] Intensive topical antibiotic therapy, utilizing fluoroquinolones (e.g., ciprofloxacin), aminoglycosides (e.g., tobramycin), or β-lactam antibiotics (e.g., meropenem), remains the primary treatment approach.[8,9] Nevertheless, this Gram-negative opportunistic bacterium can rapidly develop antibiotic resistance, making infections extremely difficult to treat effectively.[10,11] Notably, *P. aeruginosa* infections often progress from corneal perforation to severe liquefactive necrosis of the cornea, driven by complex pathogenic mechanisms involving both host and bacterial factors.[12,13] Here, *P. aeruginosa* proteases have been considered to be important virulence factors for invasion in acute ocular infections.[14,15] *P. aeruginosa* secretes different proteases, such as staphylolysin (LasA),[16] aminopeptidase,[17] protease IV,[18] and, importantly, elastase LasB (elastase B, pseudolysin). The most abundant extracellular protease LasB, is a zinc-dependent metalloprotease encoded by *lasB*.[19] LasB can degrade collagen, mucins and other host proteins such as surfactant proteins,[20] cytokines,[21] and immunoglobulins, and can cause other harmful effects on various components of the immune system.[22,23] Immunization with LasB has been demonstrated to confer protection against *Pseudomonas* keratitis in both rabbits and mice.[12,24,25] Additionally, studies have shown that peptidic metal-chelating elastase inhibitors (**1–3**)[26,27,28] can significantly reduce corneal melting in an experimental rabbit model of *Pseudomonas* keratitis (**Figure 1A**).[29] Although effective, advancing this approach to a more sophisticated level by slowing the infection to allow sufficient time for antibiotic treatment to preserve vision remains a significant challenge.

In this study, we describe the systematic hit-to-lead optimization process, which integrated a peptidic backbone with α-substituted phosphonates as a zinc-binding group. This strategy was based on a LasB inhibitor scaffold reported previously by our group that is efficacious after inhalative administration.[30] In this work, we improved the in vitro activity, resulting in highly potent compounds that inhibit LasB with single-digit nanomolar potency. The binding modes of three phosphonic acid-containing dipeptides to LasB were elucidated through X-ray co-crystal structures. Additionally, in vitro profiling was performed to characterize our frontrunners, followed by in vivo toxicity studies. Finally, an in vivo proof-of-concept study demonstrated the efficacy of adjunctive treatment with meropenem in a murine *Pseudomonas* keratitis model.

A. Aljohmani, D. Yildiz
Institute of Experimental and Clinical Pharmacology and Toxicology
PZMS
ZHMB
Saarland University
Kirrbergerstraße 100, 66421 Homburg/Saar, Germany
K. Rox
Department of Chemical Biology
Helmholtz Centre for Infection Research (HZI)
Inhoffenstraße 7, 38124 Braunschweig, Germany
R. Müller, A. K. H. Hirsch
Helmholtz International Lab for Anti-Infectives
Campus E8.1, 66123 Saarbrücken, Germany

2. Results and Discussion

2.1. Structure–Activity Relationship of Phosphonic Acid-Containing Dipeptides

Our group recently reported the design, synthesis, and biological evaluation of small-molecule inhibitors targeting *P. aeruginosa* elastase B.[30,31–34] Optimization of the initial thiol-based hit **4** involved introducing an isobutyl side chain at the α-position and substituting the zinc-binding motif with a phosphonic acid group (1st and 2nd generation). This strategic modification led to the development of phosphonate **5**, which exhibited an 18-fold enhancement in half-maximal inhibitory concentration (IC_{50}) compared to the original hit. Building on these findings, the modifications implemented in the 3rd generation of compounds was based on two main objectives. First, based on the co-crystal structures of previously reported 1st and 2nd generation LasB inhibitors, we expected an improvement exploiting a possible growth vector. Second, considering LasB's intrinsic protease activity, we sought to incorporate structural motifs resembling the peptidic substrate found in compounds such as phosphoramidon and peptide-based metal-chelating elastase inhibitors (Figure 1B).[19]

First, we systematically incorporated amino acid moieties adjacent to the leucine-derived phosphonate, as detailed in **Table 1**. Starting with glycine, we synthesized the dipeptide **7**, which exhibited a significant decrease in activity compared to phosphonate **5**. Conversely, the incorporation of a single methyl group by introducing alanine in **8** led to a remarkable 28-fold increase in activity. Increasing bulkiness in the valine-derived inhibitor **9** was the first compound in the series to achieve a single-digit nanomolar IC_{50} value. The corresponding (*R*)-valine analogue **10** also demonstrated substantial activity, though slightly reduced compared to **9**. Incorporation of the beta-amino acid (*S*)-β-Val in **11** caused a significant decrease in LasB inhibition, likely due to deviations from the natural peptide structure. In contrast, cyclopropylglycine (**12**), cyclobutylglycine (**13**), cyclohexylglycine (**14**) and isoleucine (**15**) derivatives exhibited similar activity to **9**. Notably, replacing leucine with cyclopropyl alanine (**16**) resulted in more than a two-fold increase in activity, potentially due to entropic effects. The introduction of *O*-methyl-protected serine facilitated the separation of diastereomers **(*R*)-18** and **(*S*)-18** via preparative high-performance liquid chromatography (HPLC). The (*R*)-configured diastereomer **(*R*)-18** exhibited twice the potency of **(*S*)-18**, aligning with our recent findings on α-substituted phosphonic acids[30] and mercaptoacetamide[32] derivatives. Peptides containing bulkier residues such as cyclohexyl alanine (**19**) and pyran-4-yl alanine (**20**) resulted in an over 48-fold loss in inhibition, likely due to steric repulsion. Additionally, the incorporation of proline into the backbone (**21**) led to a substantial drop in activity, likely due to significant conformational changes. Introduction of aromatic amino acids such as phenylglycine (**22**), phenylalanine (**23**), 2-pyridyl-alanine (**(*R*)-24**/**(*S*)-24**) and 3-pyridyl-alanine (**(*R*)-25**/**(*S*)-25**) resulted in significantly less potent derivatives. The diastereomeric mixtures of the

ADVANCED SCIENCE NEWS
www.advancedsciencenews.com

ADVANCED SCIENCE Open Access
www.advancedscience.com

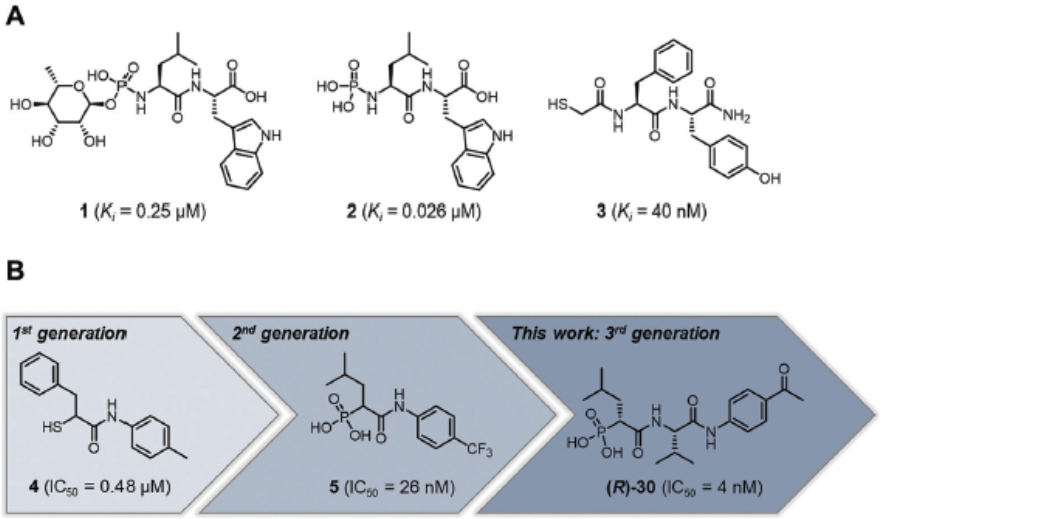

Figure 1. (**A**) Structures of known peptidic LasB inhibitors. Inhibitory constant K_i values for elastase LasB are given in brackets. (**B**) Fragment-to-hit optimization of phosphonate dipeptides via mercaptoacetamide **4** and α-substituted phosphonic acid **5**. Half-maximal inhibitory concentrations (IC_{50}s) are given in brackets.

latter two compounds could be resolved by preparative HPLC, following the same trend as previously described.

With dipeptide **9** in hand, we proceeded to investigate different substitution patterns of the aryl core, incorporating both electron-withdrawing and -donating substituents (**Table 2**). Drawing on our previous research on α-substituted phosphonic acid derivatives, we hypothesized that substitution at the *para*-position would be more favorable for LasB inhibition compared to *ortho* and *meta* positions. To test this hypothesis in the context of the dipeptide class, we first evaluated the mono-chlorine derivatives **27** and **28**. Our results confirmed that single-digit nanomolar potency was attainable only when the substituent was introduced at the *para*-position. The substitution of the chlorine atom with a trifluoromethyl-group in **29** resulted in a slight decrease in inhibitory activity. Notably, the introduction of an acetyl group allowed for the separation of diastereomers via preparative HPLC. The (*R*)-configured diastereomer, **(*R*)-30**, exhibited significantly greater efficacy compared to its (*S*)-configured counterpart, **(*S*)-30**. Furthermore, the activity of **(*R*)-30** was comparable to that of **9**. Modification with electron-donating groups, such as methyl (**32**) or methoxy (**33**), resulted in only a slight reduction in activity. Surprisingly, the incorporation of an isopropoxy substituent (**34**) significantly decreased the activity by a factor of five. Conversely, the introduction of a phenoxy substituent (**35**) restored the activity. The separated imidazoyl-group-containing diastereomers **(*R*)-36** and **(*S*)-36** exhibited a similar trend to the acetyl-containing dipeptides, with the (*R*)-configured inhibitor being more active. Lastly, the incorporation of a bulky morpholino residue (**37**) resulted in a 16-fold decrease in activity compared to **9**.

In conclusion, we successfully identified and optimized a novel dipeptide scaffold, achieving nanomolar activity. We selected the most potent LasB inhibitors, **9**, **30**, **(*R*)-30**, being selected for further in-depth evaluation.

2.2. Co-Crystallization Studies

The dipeptide compounds designed in this study show, for the first time, activity in the single-digit nanomolar range compared to previously published phosphonates.[30] This is probably due to the peptidic valine linker between the isobutyl and benzyl ring decorated with electron-withdrawing groups. To gain further insights into the binding mode of the optimized compounds and explain the increased affinity, we determined the co-crystal structures of compounds **9**, **30**, and **31** (**Figure 2**; Table S1, Supporting Information). Since the dipeptide compounds share the phosphonate zinc-binding group, the *iso*-butyl moiety, and the amide with the compound in a previously published structure (PDB ID 8CC4), key interactions were conserved. These include hydrogen bonds to the side chains of His223, Glu141, and Asn112 and the bidentate hydrogen bond to Arg198 (Figure S1, Supporting Information). However, in contrast to the α-aryl-substituted phosphonates, the peptidic valine linker of the optimized compounds occupies the lipophilic S2' pocket of LasB and engages in a hydrophobic interaction with Leu197 (Figure 2A,C). The increased binding affinity to LasB can be rationalized primarily by the introduction of the additional amide bond of the compound series presented here and the substitution pattern of the adjacent aryl ring. For example, the carbonyl oxygen atom of the keto-group in compound **31** forms additional hydrogen bonds with Arg208 and His224, which results in activity in the low two-digit nanomolar range (Figures S1,S2, Supporting Information). In the co-crystal structure of LasB with **9**, the side chain of Asn112 forms a hydrogen bond with the carbonyl oxygen atom of the dipeptide motif as well as an additional hydrogen bond with the amide nitrogen atom (Figure 2B–D). The extremely efficient bidentate chelation of zinc by the phosphonate, as well as a bidentate hydrogen bond with the side chain of the catalytically active His223 could explain the increased affinity of compound **9**. Compared to the

ADVANCED SCIENCE NEWS
www.advancedsciencenews.com

ADVANCED SCIENCE Open Access
www.advancedscience.com

Table 1. LasB inhibition of α-isobutyl phosphonates with varied amino acids in dipeptide backbone.

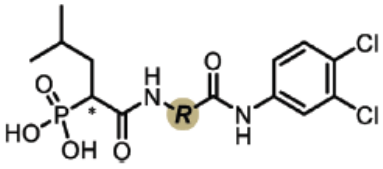

Cmpd	R	IC_{50} [nM]	Cmpd	R	IC_{50} [nM]
7	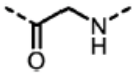	1756 ± 30	(*R*)-**18**	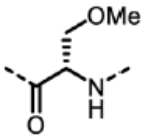	86.7 ± 3.6
8	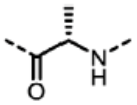	61.7 ± 1.6	(*S*)-**18**		197 ± 5.4
9	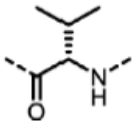	5.1 ± 0.2	**19**	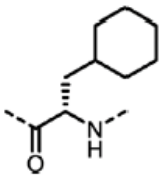	242 ± 21
10	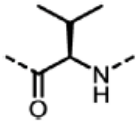	11.3 ± 0.4	**20**	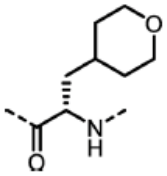	379 ± 8
11	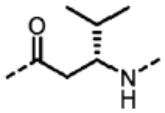	2715 ± 55	**21**	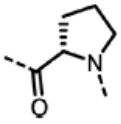	2539 ± 69
12	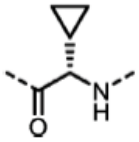	28.8 ± 0.8	**22**	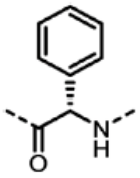	99.6 ± 2.5
13	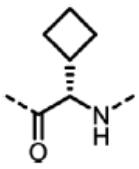	11.9 ± 0.3	**23**	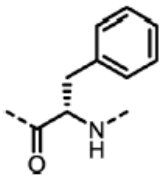	426 ± 48
14	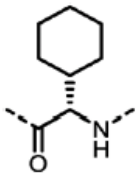	12.4 ± 0.3	(*R*)-**24**	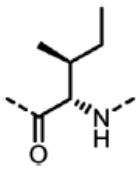	416 ± 23

(*Continued*)

ADVANCED SCIENCE NEWS
www.advancedsciencenews.com

ADVANCED SCIENCE Open Access
www.advancedscience.com

Table 1. (Continued)

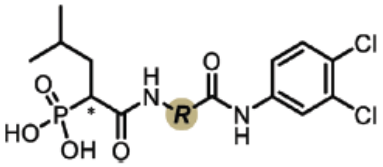

Cmpd	R	IC_{50} [nM]	Cmpd	R	IC_{50} [nM]
15	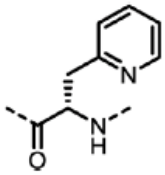	13.1 ±0.5	(*S*)-**24**	1360 ± 50	
16	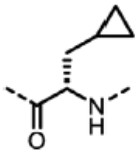	27.1 ± 0.9	(*R*)-**25**	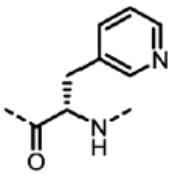	574 ± 16
17	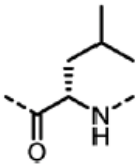	59.4 ± 1.7	(*S*)-**25**		1500 ± 60

other compounds, **30** (and the more active diastereomer **(*R*)-30**) exhibited the most potent in vitro activity. The significant difference in affinity for the two diastereomers of **30** can be explained by the occupancy of the *iso*-butyl moiety in the S1' pocket, which enables a more efficient hydrophobic interaction for **(*R*)-30**.

Extremely striking regarding the binding mode of **30** is the coordination of zinc by the phosphonate oxygen atom: In contrast to the other two compounds (**9** and **31**), the chelation we observed was not bidentate. Instead, only one of the phosphonate oxygen atoms engages the Zn^{2+} cation. This enables the formation of an intramolecular hydrogen bond between a phosphonate oxygen atom and the second amide NH (starting at the phosphonate) (Figure 2D). The change in ligand orientation leads to the disruption of the bidentate hydrogen-bonding interaction between LasB Asn112 and **30**, which appears to be more than compensated for by the intermolecular interaction and resulting compound conformation. The reduction of available conformations for **30** may lead to decreased entropic penalty upon binding to LasB, resulting in a significantly different binding mode compared to **9** and **31** (Figure S3–S6, Supporting Information).

2.3. Pharmacokinetic Studies

Regarding their in vitro absorption–distribution–metabolism–excretion–toxicity (ADMET) properties, frontrunners **9** and **30** as well as additional representative compounds **13**, **14**, **(*R*)-36** have demonstrated the same excellent profile observed with the previously reported monoaryl phosphonates.[30] The tested inhibitors exhibited high solubility, good metabolic and plasma stability (Tables 3 and Figure S2, Supporting Information). For **30**, these properties were validated across multiple species with excellent microsomal and plasma stability in mouse, rat, and minipig fractions (Table S3, Supporting Information). As expected, the high stability could also be confirmed in selected assays for the more active diastereomer **(*R*)-30** (Table S2, Supporting Information). Additionally, we evaluated the Calu-3 permeability of **9** and **30**. As anticipated for these polar structures, both compounds demonstrated low permeability, with values of 0.71 ± 0.24 and 0.86 ± 0.39 × 10^{-6} cm $^{-1}$s, respectively (Figure S7, Supporting Information). These are also expected considering the low lipophilicity, as also characterized by $LogD_{7.4}$. As ADMET data were promising, we conducted a pharmacokinetic study with 30 mg/kg **30** via subcutaneous administration. We observed a good exposure in plasma and also a good exposure in epithelial lining fluid (ELF) and lung tissue. However, ELF exposure was slightly lower compared to plasma with an ELF/plasma ration of ≈0.38. Additionally, the compound distributed well in other tissues (Figure S8, Table S4 and Figure S5, Supporting Information). No accumulation into any tissue investigated that may cause unwanted toxicity was observed.

ADVANCED SCIENCE NEWS
www.advancedsciencenews.com

ADVANCED SCIENCE Open Access
www.advancedscience.com

Table 2. LasB inhibition of α-isobutyl phosphonate containing dipeptides with varied aryl groups.

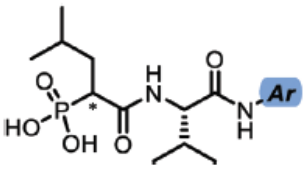

Cmpd	Ar	IC_{50} [nM]	Cmpd	Ar	IC_{50} [nM]
27	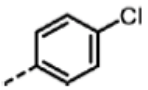	9.0 ± 0.4	**32**	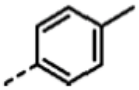	12.9 ± 0.4
28	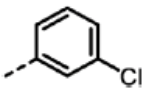	282 ± 13	**33**	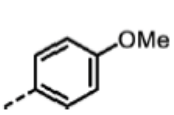	19.9 ± 0.8
29	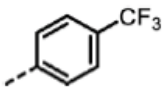	15.2 ± 0.3	**34**	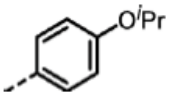	56.7 ± 2.0
30	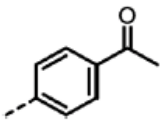	5.0 ± 0.2	**35**	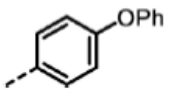	8.0 ± 0.3
(*R*)-30		3.7 ± 0.1	**(*R*)-36**	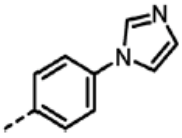	10.9 ± 0.3
(*S*)-30		129 ± 4.0	**(*S*)-36**		417 ± 14
31	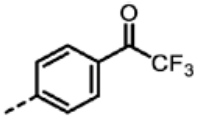	21.7 ± 0.6	**37**	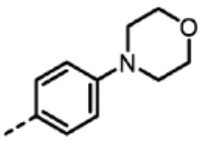	83.7 ± 2.1

Table 3. In vitro ADME results of selected LasB inhibitors. Cl_{int}, intrinsic clearance; $t_{1/2}$, half-life.

Cmpd	Kinetic Solubility PBS pH 7.4 [μM]	Liver S9 Cl_{int} [μL/mg/min]		Plasma $t_{1/2}$ [min]		$LogD_{7.4}$
		Mouse	Human	Mouse	Human	
9	>200	<5.8	<5.8	>150	>150	0.41
30	>200	<5.8	<5.8	>150	>150	−0.58

2.4. Selectivity Toward Human Off-Targets

Next, we investigated the activity of seven selected LasB inhibitors (**9**, **13**, **14**, **30**, **(*R*)-30**, **31**, **(*R*)-36**) against four human zinc-dependent matrix metalloproteinases (MMP) 1–3 and tumor necrosis factor-alpha converting enzyme (TACE, or a disintegrin and metalloprotease 17 (ADAM17)) as human off-targets. All of these targets play crucial roles in physiological processes, hence selectivity over these by our compounds is desirable. Satisfyingly, at a concentration of 100 μM, none of the tested compounds exhibited more than 15% inhibitory activity against these off-targets (Table S6, Supporting Information).

ADVANCED SCIENCE NEWS
www.advancedsciencenews.com

ADVANCED SCIENCE Open Access
www.advancedscience.com

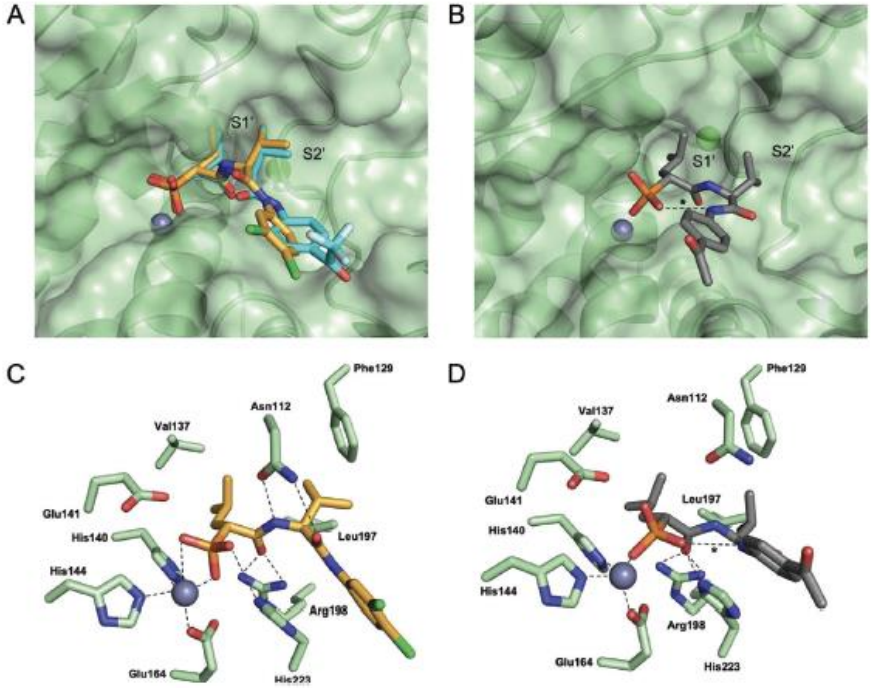

Figure 2. Crystal structure of LasB in complex with **9**, **31** and **30** (PDB codes: 9FQD, 9FQY, 8RIB). (**A**) Superposition and surface representation of the LasB (green) co-crystal structures in complex with **9** (orange) and **31** (cyan). (**B**) Surface representation of LasB (green) in complex with **30** (gray). The intramolecular hydrogen bond is highlighted by an asterisk. (**C**) Schematic 2D representation of interactions between **9** and LasB. The catalytically active Zn^{2+} cation coordinated by His140, His144, Glu164, and the phosphonate is shown as a gray sphere. (**D**) Schematic 2D representation of interactions between **30** and LasB. The aryl ring of **30** is significantly shifted in the co-crystal structure, possibly because of the intramolecular hydrogen bond between a phosphonate oxygen and the second amide nitrogen atom (highlighted by an asterisk). The dimethyl moiety of the valine is rotated by 90° compared to the structure of LasB in complex with derivative **9**.

Moreover, we explored the safety profile of frontrunner **(*R*)-30** in more detail in order to detect additional crucial off-target interactions. For this purpose, we employed the SafetyScreen44 in vitro panel comprising selected binding, inhibition and uptake assays.[35] The panel is a specialized pharmacological profiling tool that tests compounds against 44 key molecular targets, aiming to identify potential safety risks early in drug discovery. At a comparably high concentration of 100 µM (general compound concentration in these assays is 10 µM), **(*R*)-30** displayed inhibition binding to ten targets by >50%, for four of them even by >80% (Figures S9,S10 and Table S7, Supporting Information). The latter comprise off-targets such as the potassium channel hERG (79.4% binding inhibition), the sodium channel (91.1%), the 5-hydroxytryptamin transporter (5-HTT) (84.8%) or cyclooxygenase 1 (COX1) (81.5%) (Table S7, Supporting Information).

It remains to be determined whether this compound also causes functional inhibition. Nonetheless, the overall observation is significant and warrants detailed consideration, particularly when the compound is administered systemically. Specifically, **(*R*)-30** is well-suited for topical administration, such as ocular application. In such cases, it can be assumed that only minimal quantities will enter the bloodstream, thereby minimizing the likelihood of adverse effects. Additionally, this observation seems to be compound-related and not class-specific, as we reported previously on an excellent safety profile for a monoaryl phosphonate derivative, which might be more favorable for systemic administration.[30]

2.5. Toxicity Studies

The seven dipeptides were also tested for cytotoxic effects against HepG2, HEK293, and A549 cell lines. Encouragingly, all LasB inhibitors demonstrated minimal to no impact on human cells (Table S8, Supporting Information). This is in agreement with previous findings on structurally simpler phosphonates.[30] **30** was also tested in a zebrafish embryo toxicity model, which revealed no signs of toxicity up to five days post fertilization at up to 100 µM (Table S9, Supporting Information).

Motivated by these results in cell culture and zebrafish embryos, but with the partial yellow flags in the Safety Screen44 in mind, we conducted a safety study in mice with frontrunner **30**. These experiments were carried out although, as described above, topical application is preferred for the dipeptides. We aimed to generate information about the maximum tolerated dose in a representative species in order to de-risk the scaffold for further development. For the first toxicity study, **30** was applied as a single, subcutaneous dose ranging from 25–400 mg/kg. At all doses up to 400 mg/kg, no clinical signs and no macroscopic findings were observed. **30** only showed a slight effect on food

ADVANCED SCIENCE NEWS
www.advancedsciencenews.com

ADVANCED SCIENCE Open Access
www.advancedscience.com

consumption and on thymus weight with a moderate increase (Tables S10,S11 and S12, Supporting Information). Based on these encouraging results, we performed a repeated–dose follow-up study using an administration scheme with TID intravenous dosing, escalating the total dose to 300 and 600 mg/kg/day, for 3 days. For this study, we further decided to investigate the more active diastereomer **(*R*)-30**. Again, no treatment–related mortality, nor effects on body weight or clinical signs were observed. There was no effect on food uptake either, yet slightly increased weight of the liver, spleen, and testes were found (Tables S13,S14 and S15, Supporting Information). Whether the observed differences in the minor effects on organ weight and food consumption are related to the application of the pure diastereomer versus the mixture in the two studies cannot be clearly assessed at this stage, but might be a possible explanation.

Despite these observations, the effects noted were minimal and occurred only at relatively high doses. For a topical application, as suggested above, significantly lower amounts of compound will enter the system, suggesting a safe application of these LasB inhibitors is possible.

Although we are developing antivirulence agents, which are not supposed to have antibacterial activity but only to reduce the pathogenicity of *P. aeruginosa*, we tested the activity of compounds against *P. aeruginosa* strains PA14 and PA54 and did not observe any effect on bacterial growth at 100 µM (Table S16 and Figure S11, Supporting Information). Furthermore, we did not observe an effect on biofilm formation of PAO1 using a peg lid-based minimum biofilm eradication concentration (MBEC) model (Figure S12, Supporting Information).[36]

2.6. In Vivo Studies in a Murine Keratitis Model

To assess the therapeutic potential of our LasB inhibitors – which exhibit excellent in vitro activities with favorable in vitro ADME, low cytotoxicity and good tolerability – for treating an infection via topical administration, we decided to employ a *Pseudomonas* keratitis model in mice recently established in our group.[37]

As our in vivo model utilizes the *P. aeruginosa* clinical isolate PA54, the expression of *lasB* was verified as initial step. The expression in PA54 was compared to the reference strain PAO1, known for its moderate *lasB* expression, and the high-level *lasB* producer strain PA14, respectively (Table S17 and Figure S13, Supporting Information). These experiments revealed that PA54 is characterized by *lasB* transcript rates under in vitro growth conditions in between the transcript rates produced by PAO1 and PA14, making it suitable for the administration of a LasB inhibitor.

Based on our previous findings on target engagement in a murine pneumonia model in combination with a standard-of-care antibiotic,[30] we applied the dipeptide **(*R*)-30** alone and in combination with the commonly used antibiotic meropenem.[9] The keratitis model was carried out using aged female C57BL/6 mice, as previously published.[37] For infection, $5*10^7$ colony forming units (CFUs) of PA54 were topically administered on denuded, mechanically harmed corneas. Treatments with meropenem, **(*R*)-30**, or meropenem in combination with **(*R*)-30** were performed every 8 h for 72 h (first treatment at 6 h post infection). Each of the in total nine 5 µL-doses contained 1 mg/mL **(*R*)-30** and/or 0.5 mg mL^{-1} meropenem. Sham-treated mice received 5 µL-doses of the vehicle (0.9% saline and 1% DMSO) at the time points indicated above, and uninfected eyes received no treatment.

As a general measure of condition, the change in body weight of the animals was assessed and revealed no systematic changes, which indicates good tolerability in agreement with the previous safety study (Figure S14, Supporting Information). To gain first insights on the impact of our treatments on disease progression, we determined the clinical keratitis scores on a daily basis (**Figure 3A**). While the infected eyes of all sham-treated or only LasB inhibitor-treated mice displayed a severe keratitis at day three post infection (i.e., a median clinical score of 4), this was not the case with the meropenem-treated groups. When treated with the antibiotic alone, already three of the eight meropenem-treated animals showed a decrease in keratitis severity over the study time window (median clinical score of 3 at day three post infection). This effect was more pronounced when meropenem was used in combination with **(*R*)-30** in which 5 out of 8 eyes displayed a clinical score ≤2 at the endpoint, indicating an enhanced healing of the injured tissue (Figure 3A; median clinical score of 2).

When assessing the bacterial loads being present in the infected eyes on day 3 post infection, a comparable pattern emerged. Treatment of the infected eyes with **(*R*)-30** alone had no clear effect on the bacterial loads in the eyes 3 days post infection. Treatment of the infected eyes with meropenem alone reduced the bacterial load in the median by 64-fold, and this effect was even more pronounced in **(*R*)-30** plus meropenem treated eyes (4-log_{10} reduction; Figure 3B). While **(*R*)-30** had minimal impact on the infection process when used alone, these observations suggest that combining the LasB inhibitor with the antibiotic significantly enhanced bacterial infection clearance, surpassing the effectiveness of the antibiotic alone.

To further study the pathophysiological changes beyond LasB inhibition, we investigated the cellular and humoral immune response. Here, we observed a clear impact of the combination treatment on eye neutrophil levels – key-markers of the acute innate immune response – which were significantly reduced when compared to the sham-treatment group (Figure 3C). Notably, when compared to the uninfected controls, eye neutrophil levels were statistically significantly higher in all infection groups, except for the **(*R*)-30** plus meropenem group. For the myeloperoxidase (MPO) levels, significant increase was observed for all infection groups when compared to the non-infected control (Figure 3D). However, when compared to the sham-treated control, all groups that received treatment displayed lowered MPO levels. These findings suggest that the LasB inhibitor, even in the absence of the antibiotic, is likely to alter the release of MPO at the infection site. Further support for an immune-cell modulating activity of **(*R*)-30** was obtained by the determination of the contents of the neutrophil attracting and activating cytokines/chemokines interleukin 1β (IL-1β), keratinocyte chemoattractant (KC), and tumor necrosis factor α (TNFα) in the tissue homogenates (Figure 3E–G). Treatment of the infected eyes with the LasB inhibitor **(*R*)-30** allowed for a significant reduction in IL-1β levels when compared to sham treatment, although not to the levels seen with the meropenem and combination treatment, respectively, which were almost on the level of

ADVANCED SCIENCE NEWS
www.advancedsciencenews.com

ADVANCED SCIENCE Open Access
www.advancedscience.com

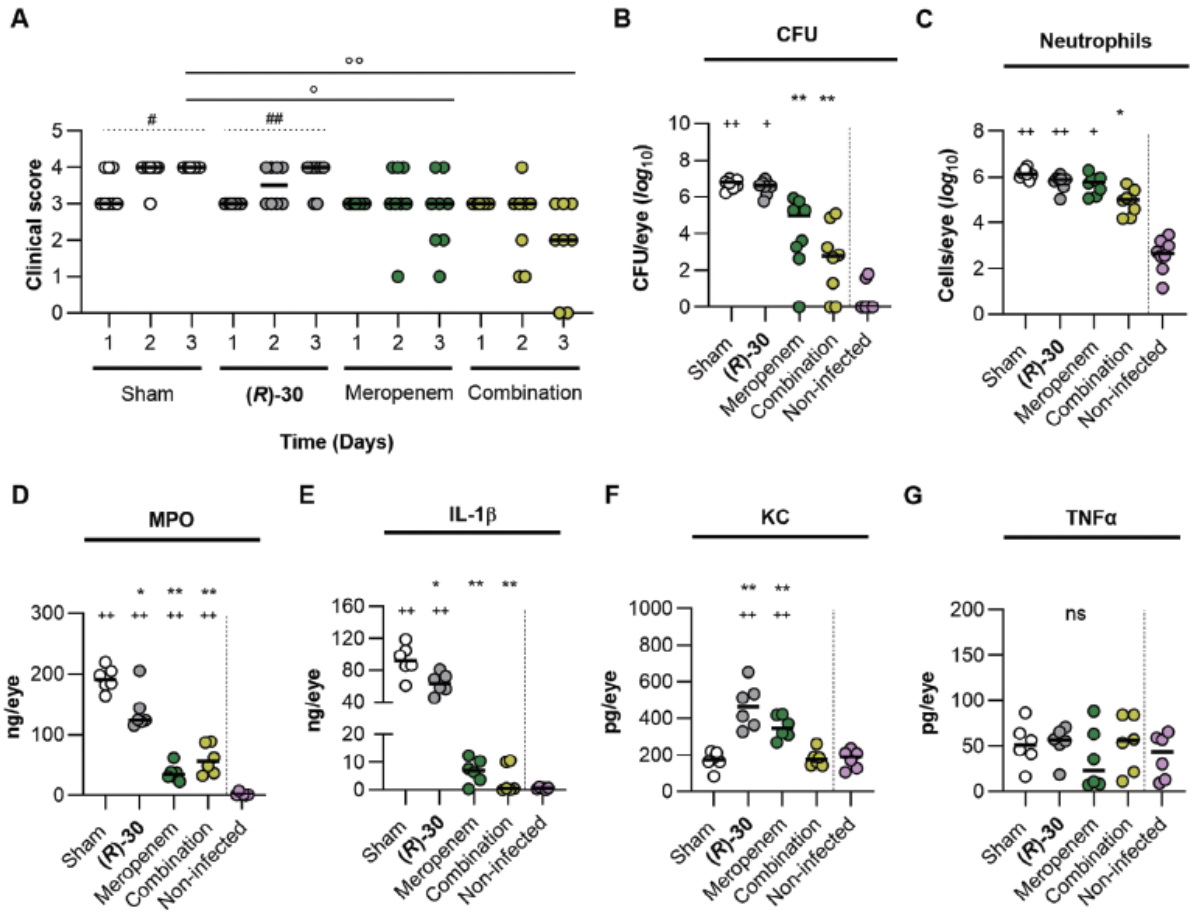

Figure 3. Impact of drug treatment on keratitis development in C57BL/6N mice after infection with strain PA54. (**A**): Evolution of clinical score from day 1 to day 3 (n = 8 per group). (**B**) Determination of bacterial loads in whole-eye homogenates at 3 days post infection (n = 8 per group). (**C**) Neutrophils detected in whole-eye homogenates at 3 days post infection (n = 6 per group). (**D-F**) Myeloperoxidase (MPO, **D**), interleukin-1β (IL-1β, **E**), keratinocyte chemoattractant (KC, **F**), and tumor necrosis factor α (TNFα, **G**) contents in whole eye homogenates obtained from eyes at 3 days post infection (n = 6 per group). Data represent the values of every individual animal (symbols) and the median (horizontal line). ns, not significant; ° or # or + or *, $P < 0.05$; °° or ## or ++ or **, $P < 0.01$. + and *, Brown–Forsythe and Welch ANOVA test with Dunnett's T3 multiple comparison test. +, comparison between the mean of each group with the mean of the non-infected control. *, comparison between the mean of each group with the mean of the sham-treated control. °, Ordinary one-way ANOVA with Dunnett's multiple comparison test. #, RM one-way ANOVA test with Dunnett's multiple comparison test.

this cytokine seen in uninfected eyes (Figure 3E). A different picture emerged for the murine IL-8 homolog KC (Figure 3F). KC levels in the eyes of infected and sham-treated mice as well as in combination therapy-treated mice were found to be on the same level as the KC levels seen in uninfected eyes, while significantly higher amounts of this chemokine were seen in meropenem and LasB inhibitor-treated mice. No clear differences in the contents of TNFα were observed in the eyes of all groups (Figure 3G). We further determined levels of **(*R*)-30** in eye homogenate and serum (Figure S15, Supporting Information) and confirmed exposure of the pathoblocker in the eye, enabling the effects observed here. Serum levels showed that some compound reached the system. Yet, with average levels below 500 nM, compared to the test concentrations (100 µM) in the off-target screening described above, suggesting that a safe ocular administration is achievable. The high levels of KC in eye homogenates of LasB-inhibitor-treated mice are probably explained by efficient inhibition of LasB by **(*R*)-30** in the infected eye tissue, as KC/LasB co-incubation studies confirmed KC to be a substrate for this protease and that the proteolytic activity of LasB on KC is effectively blocked by **(*R*)-30** (Figure S16, Supporting Information).

Altogether, these findings suggest that a LasB inhibitor treatment is able to affect the immune response in infected eye tissue, but without altering the bacterial load and neutrophil content at the infection site. However, a significant impact on the disease development can be reached, when the LasB inhibitor is combined with an antibiotic, leading to noticeable reduction in symptoms of the infection and to a significant reduction in the number of bacteria at the infection site, which is clearly superior to treatment with the antibiotic alone.

3. Conclusions

P. aeruginosa is a priority pathogen responsible for a variety of diseases. In order to tackle this critical and increasingly resistant pathogen, antivirulence approaches have recently gained significant attention. After reporting on a phosphonate-based LasB inhibitor with in vivo activity against lung infections, we have now developed this compound class further, assessing its application for the treatment of bacterial keratitis. In a substrate-inspired approach, a dipeptide backbone was introduced, leading to single-digit nanomolar on-target activity for five LasB inhibitors (**9**, **27**, **30**, (***R***)-**30**, and **35**).

Furthermore, the binding modes of compounds **9**, **30**, and **31** were elucidated using X-ray crystallography, and the influence of the peptidic leucine linker was investigated. Additional interactions with the amino acid side chains of LasB were identified and were mainly responsible for the increased activity of the compounds. In contrast to that, an intramolecular hydrogen bond for the inhibitor was observed in the co-crystal structure of LasB in complex with compound **30**. This presumably freezes a favored conformation, which explains the single-digit nanomolar activity of **30**.

While potential off-target effects were observed at high concentrations in vitro, frontrunner (***R***)-**30** was well-tolerated in vivo. In a murine infection model, it improved the activity of meropenem in the treatment of *Pseudomonas* keratitis, when applied in combination, and altered the immune response in infected eye tissue when applied alone.

Taken together, these findings expand the potential of phosphonate-based LasB inhibitors from the known in vivo proof-of-concept after inhalative administration to the treatment of *Pseudomonas* keratitis, highlighting the versatility of the scaffold in tackling the virulence of this critical pathogen in vivo.

4. Experimental Section

Materials and experimental details are provided in the Supporting Information.

Supporting Information

Supporting Information is available from the Wiley Online Library or from the author.

Acknowledgements

The authors AFK and CS contributed equally. We acknowledge the use of the ESRF beamlines ID30B and ID23-1 and the local contacts for their support. We acknowledge DESY (Hamburg, Germany), a member of the Helmholtz Association HGF, for the provision of experimental facilities. Parts of this research were carried out at PETRA III and we would like to thank Dr. Johanna Hakanpää for assistance in using P11. Beamtime was allocated for proposal Xh-20010236. Furthermore, we like to thank Jeannine Jung, Simone Amann, Tabea Wittmann, Jannine Seelbach, Andrea Ahlers, Kimberley Vivien Sander, Janine Schreiber, Jennifer Wolf, Tabea Trampert, and Pascal Paul for excellent technical support. We are also grateful for the funding by CARB-X (ID 05CARB-X0891). CARB-X funding for this research is supported by federal funds from the U.S. Department of Health and Human Services (HHS); Administration for Strategic Preparedness and Response; Biomedical Advanced Research and Development Authority; under agreement number 75A50122C00028, and by awards from Wellcome (WT224842), and Germany's Federal Ministry of Education and Research (BMBF). The content of this manuscript is solely the responsibility of the authors and does not necessarily represent the official views of any CARB-X funders. We are also grateful for funding by the German Research Foundation (DFG SFB TRR 152 project P22) to G.K-C, and KR4338/1-2 to G.K-C, by the Saarland University and Helmholtz-Institute for Pharmaceutical Research Saarland TANDEM initiative and by the German Center for Infection Research (DZIF, TTU 09.719). TOC graphic was created in BioRender. A.F.K. (2024) BioRender.com/h78×542.

Conflict of Interest

The authors declare the following competing financial interest: A.F.K, C.S., A.M.K, R.P.J, A.S.A, J.H, and A.K.H.H are co-inventors on the international patent application (PCT/EP2021/073381) that incorporates methods outlined in this manuscript. Furthermore, the authors C.S., C.N.E., S.S., A.M.K., R.S., N.A.W., M.B., J.H., and A.K.H.H. are co-inventors on a patent application (EP24178040.2) that was submitted on May 24th, 2024.

Data Availability Statement

The data that support the findings of this study are available from the corresponding author upon reasonable request.

Keywords

elastase B, keratitis, phosphonates, *Pseudomonas aeruginosa*

Received: September 24, 2024
Revised: December 16, 2024
Published online:

[1] M. Cabrera-Aguas, P. Khoo, S. L. Watson, *Clinical Exper Ophthalmology* **2022**, *50*, 543.
[2] L. Ung, P. J. M. Bispo, S. S. Shanbhag, M. S. Gilmore, J. Chodosh, *Survey of ophthalmology* **2019**, *64*, 255.
[3] D. S. J. Ting, C. S. Ho, R. Deshmukh, D. G. Said, H. S. Dua, *Eye (London, England)* **2021**, *35*, 1084.
[4] M. Teweldemedhin, H. Gebreyesus, A. H. Atsbaha, S. W. Asgedom, M. Saravanan, *BMC ophthalmology* **2017**, *17*, 212.
[5] F. Stapleton, T. Naduvilath, L. Keay, C. Radford, J. Dart, K. Edwards, N. Carnt, D. Minassian, B. Holden, *PLoS One* **2017**, *12*, e0181343.
[6] M. Green, A. Apel, F. Stapleton, *Cornea* **2008**, *27*, 22.
[7] Y. Hilliam, S. Kaye, C. Winstanley, *J. Med. Microbiol.* **2020**, *69*, 3.
[8] M. D. Willcox, *Clinical ophthalmology (Auckland, N.Z.)* **2012**, *6*, 919.
[9] C. Elhardt, A. Wolf, C. M. Wertheimer, *J. Ophthalmic Inflammation Infect.* **2023**, *13*, 40.
[10] M. Fernandes, D. Vira, R. Medikonda, N. Kumar, *Graefe's Arch. Clin. Exp. Ophthalmol.* **2016**, *254*, 315.
[11] J. Vazirani, S. Wurity, M. H. Ali, *Ophthalmology* **2015**, *122*, 2110.
[12] J. A. Hobden, *DNA Cell Biol.* **2002**, *21*, 391.
[13] F. R. Burns, C. A. Paterson, R. D. Gray, J. T. Wells, *Antimicrob. Agents Chemother.* **1990**, *34*, 2065.
[14] Y. Li, Y. Wang, C. Li, D. Zhao, Q. Hu, M. Zhou, M. Du, J. Li, P. Wan, *Invest. Ophthalmol. Visual Sci.* **2021**, *62*, 7.
[15] A. S. Kreger, L. D. Gray, *Infect. Immun.* **1978**, *19*, 630.
[16] E. Kessler, M. Safrin, J. C. Olson, D. E. Ohman, *J. Biol. Chem.* **1993**, *268*, 7503.

[17] E. Kessler, *Int. J. Mol. Sci.* **2024**, *25*, 8444.
[18] T.-H. Kim, X.-H. Li, J.-H. Lee, *Microbiology spectrum* **2021**, *9*, e0078221.
[19] M. J. Everett, D. T. Davies, *Drug Discovery Today* **2021**, *26*, 2108.
[20] J. J. Mun, C. Tam, D. Kowbel, S. Hawgood, M. J. Barnett, D. J. Evans, S. M. J. Fleiszig, *Infect. Immun.* **2009**, *77*, 2392.
[21] M. Parmely, A. Gale, M. Clabaugh, R. Horvat, W. W. Zhou, *Infect. Immun.* **1990**, *58*, 3009.
[22] I. Jurado-Martín, M. Sainz-Mejías, S. McClean, *Int. J. Mol. Sci.* **2021**, *22*, 3128.
[23] J. Yang, K.-M. Lee, S. Park, Y. Cho, E. Lee, J.-H. Park, O. S. Shin, J. Son, S. S. Yoon, J.-W. Yu, *Front. Immunol.* **2017**, *8*, 333.
[24] M. E. Marquart, *J. Biomed. Biotechnol.* **2011**, *2011*, 680642.
[25] A. S. Kreger, D. M. Lyerly, L. D. Hazlett, R. S. Berk, *Invest. Ophthalmol. Visual Sci.* **1986**, *27*, 932.
[26] G. R. A. Cathcart, D. Quinn, B. Greer, P. Harriott, J. F. Lynas, B. F. Gilmore, B. Walker, *Antimicrob. Agents Chemother.* **2011**, *55*, 2670.
[27] E. Kessler, M. Israel, N. Landshman, A. Chechick, S. Blumberg, *Infect. Immun.* **1982**, *38*, 716.
[28] L. Poncz, T. A. Gerken, D. G. Dearborn, D. Grobelny, R. E. Galardy, *Biochemistry* **1984**, *23*, 2766.
[29] A. Spierer, E. Kessler, *Curr. Eye Res.* **1984**, *3*, 645.
[30] J. Konstantinović, A. M. Kany, A. Alhayek, A. S. Abdelsamie, A. Sikandar, K. Voos, Y. Yao, A. Andreas, R. Shafiei, B. Loretz, E. Schönauer, R. Bals, H. Brandstetter, R. W. Hartmann, C. Ducho, C.-M. Lehr, C. Beisswenger, R. Müller, K. Rox, J. Haupenthal, A. K. H. Hirsch, *ACS Cent. Sci.* **2023**, *9*, 2205.
[31] J. Konstantinovic, S. Yahiaoui, A. Alhayek, J. Haupenthal, E. Schönauer, A. Andreas, A. M. Kany, R. Müller, J. Koehnke, F. K. Berger, M. Bischoff, R. W. Hartmann, H. Brandstetter, A. K. H. Hirsch, *J. Med. Chem.* **2020**, *63*, 8359.
[32] C. Kaya, I. Walter, S. Yahiaoui, A. Sikandar, A. Alhayek, J. Konstantinovic, A. M. Kany, J. Haupenthal, J. Köhnke, R. W. Hartmann, A. K. H. Hirsch, *Angew. Chem.* **2022**, *61*, e202112295.
[33] C. Kaya, I. Walter, A. Alhayek, R. Shafiei, G. Jézéquel, A. Andreas, J. Konstantinović, E. Schönauer, A. Sikandar, J. Haupenthal, R. Müller, H. Brandstetter, R. W. Hartmann, A. K. H. Hirsch, *ACS Infect. Dis.* **2022**, *8*, 1010.
[34] A. M. Kany, A. Sikandar, J. Haupenthal, S. Yahiaoui, C. K. Maurer, E. Proschak, J. Köhnke, R. W. Hartmann, *ACS Infect. Dis.* **2018**, *4*, 988.
[35] Eurofins, "Safety Screen44 Panel", can be found under https://www.eurofinsdiscovery.com/catalog/safetyscreen44-panel-tw/PP241.
[36] H. Ceri, M. E. Olson, C. Stremick, R. R. Read, D. Morck, A. Buret, *J. Clin. Microbiol.* **1999**, *37*, 1771.
[37] C. N. Englisch, N. A. Wadood, L. Patzold, A. Gallagher, G. Krasteva-Christ, S. L. Becker, M. Bischoff, *Annals Anatomy: Anat. Anz.* **2023**, *249*, 152099.

2.2.1 Supporting information

The supporting information presented here corresponds to the biological portion of Chapter 2.

ADVANCED SCIENCE
Open Access

Supporting Information

for *Adv. Sci.*, DOI 10.1002/advs.202411807

Dipeptidic Phosphonates: Potent Inhibitors of *Pseudomonas aeruginosa* Elastase B Showing Efficacy in a Murine Keratitis Model

*Alexander F. Kiefer, Christian Schütz, Colya N. Englisch, Dominik Kolling, Samira Speicher, Andreas M. Kany, Roya Shafiei, Noran A. Wadood, Ahmad Aljohmani, Niklas Wirschem, Ravindra P. Jumde, Andreas Klein, Asfandyar Sikandar, Yu-Mi Park, Gabriela Krasteva-Christ, Daniela Yildiz, Ahmed S. Abdelsamie, Katharina Rox, Jesko Köhnke, Rolf Müller, Markus Bischoff, Jörg Haupenthal and Anna K. H. Hirsch**

Supporting Information

Dipeptidic Phosphonates: Potent Inhibitors of *Pseudomonas aeruginosa* Elastase B Showing Efficacy in a Murine Keratitis Model

Alexander F. Kiefer[+,a,b,j], Christian Schütz[+,a,b,j], Colya N. Englisch[c], Dominik Kolling[d], Samira Speicher[a,b,j], Andreas M. Kany[a,b,j], Roya Shafiei[a,b,h,j], Noran A. Wadood[e,j], Ahmad Aljohmani[f,j], Niklas Wirschem[a,b,h,j], Ravindra P. Jumde[a,b,j], Andreas Klein[a,b,h,j], Asfandyar Sikandar[a,b,j], Yu-Mi Park[a,b,h,j], Gabriela Krasteva-Christ[e,j], Daniela Yildiz[f,j], Ahmed S. Abdelsamie[a,b,j], Katharina Rox[b,g], Jesko Köhnke[d], Rolf Müller[a,b,h,i,j], Markus Bischoff[c], Jörg Haupenthal[a,b,j] and Anna K. H. Hirsch[*,a,b,h,i,j]

Affiliation(s)

[a] A. F. Kiefer, C. Schütz, S. Speicher, A. M. Kany, R. Shafiei, N. Wirschem, R. P. Jumde, A. Klein, A. Sikandar, Y. Park, A. S. Abdelsamie, R. Müller, J. Haupenthal, A. K. H. Hirsch

Helmholtz Institute for Pharmaceutical Research Saarland (HIPS), Campus E8.1, 66123 Saarbrücken, Germany; Helmholtz Centre for Infection Research (HZI), Inhoffenstraße 7, 38124 Braunschweig, Germany

Email: anna.hirsch@helmholtz-hips.de

[b] A. F. Kiefer, C. Schütz, S. Speicher, A. Kany, R. Shafiei, N. Wirschem, R. P. Jumde, A. Klein, A. Sikandar, Y. Park, A. S. Abdelsamie, K. Rox, R. Müller, J. Haupenthal, A. K. H. Hirsch

German Center for Infection Research (DZIF) Inhoffenstraße 7, 38124 Braunschweig, Germany

[c] C. N. Englisch, M. Bischoff

Institute of Medical Microbiology and Hygiene, Saarland University, Kirrbergerstraße 100, 66421 Homburg/Saar, Germany

[d] D. Kolling, J. Köhnke

Institute for Food Chemistry, Callinstraße 5, 30167 Hannover, Germany

[e] N. A. Wadood, G. Krasteva-Christ

Institute of Anatomy and Cell Biology, Saarland University, Kirrbergerstraße 100, 66421 Homburg/Saar, Germany

[f] A. Aljohmani, D. Yildiz

Institute of Experimental and Clinical Pharmacology and Toxicology, PZMS, ZHMB, Saarland University, Kirrbergerstraße 100, 66421 Homburg/Saar, Germany

[g] K. Rox

Department of Chemical Biology, Helmholtz Centre for Infection Research (HZI), Inhoffenstraße 7, 38124 Braunschweig, Germany

[h] R. Shafiei, N. Wirschem, A. Klein, Y. Park, R. Müller, A. K. H. Hirsch

Department of Pharmacy, Saarland University, Campus E8.1, 66123 Saarbrücken, Germany

[i] R. Müller, A. K. H. Hirsch

Helmholtz International Lab for Anti-Infectives, Campus E8.1, 66123 Saarbrücken, Germany

[j] A. F. Kiefer, C. Schütz, S. Speicher, A. M. Kany, R. Shafiei, N. A. Wadood, A. Aljohmani, N. Wirschem, R. P. Jumde, A. Klein, A. Sikandar, Y. Park, A. S. Abdelsamie, G. Krasteva-Christ, D. Yildiz, R. Müller, J. Haupenthal, A. K. H. Hirsch

PharmaScienceHub (PSH), Campus A2.3, 66123 Saarbrücken, Germany

[+] Authors contributed equally.

3. Biological evaluation

3.1 In vitro inhibition assays

LasB was expressed and purified as described previously.[3] *In vitro* inhibition assays (LasB, MMPs, TACE). All in vitro inhibition assays were performed as described previously.[10] TACE inhibitor screening kits were purchased from Sigma-Aldrich (Saint Louis, MO). MMPs along with the SensoLyte 520 Generic MMP Activity Kit Fluorimetric were purchased from AnaSpec (Fremont, CA, USA). The assays were performed according to the guidelines of the respective manufacturer. Fluorescence signals were measured using a CLARIOstar plate reader (BMG Labtech, Ortenberg, Germany).

3.2 Kinetic solubility

The desired compounds were sequentially diluted in DMSO in a 96-well plate. 1.5 µL of each well were transferred into another 96-well plate and mixed with 148.5 µL of PBS. Plates were shaken for 5 min at 600 rpm at room temperature (r.t.), and the absorbance at 620 nm was measured. Absorbance values were normalized by blank subtraction and plotted using GraphPad Prism 8.4.2 (GraphPad Software, San Diego, CA, USA). Solubility (S) was determined based on the First X value of AUC function using a threshold of 0.005.

3.3 Lipophilicity determination

$LogD_{7.4}$ was analyzed using an HPLC−based method. The UV retention time of reference compounds with known $LogD_{7.4}$ was determined and plotted toward their $LogD_{7.4}$. Linear regression was used to determine the $LogD_{7.4}$ of unknown compounds. Analysis was performed using a Vanquish Flex HPLC system with variable wavelength detector (Thermo Fisher, Dreieich, Germany) with the following conditions: EC150/2 NUCLEODUR C18 Pyramid column, 5 µM (Macherey Nagel, Düren, Germany); eluent A: 50 mM NH4OAc pH 7.4, eluent B: acetonitrile, and flow: 0.6 mL/min. The gradient was set to 0−100% B from 0 to 2.5 min, 100% B from 2.5 to 3.0 min, 100−0% B from 3.0 to 3.2 min, and 0% B from 3.2−5.0.

3.4 Metabolic stability in liver S9 fractions

For the evaluation of combined phase I and phase II metabolic stability, the compound (1 µM) was incubated with 1 mg/mL pooled mouse liver S9 fraction (C57BL/6, Xenotech, Kansas City, USA) or human liver S9 fraction (Corning, USA), 2 mM NADPH, 1 mM UDPGA, 10 mM MgCl2, 5 mM GSH and 0.1 mM PAPS at 37 °C for 120 min. The metabolic stability of testosterone, verapamil and ketoconazole were determined in parallel to confirm the enzymatic activity of

mouse S9 fractions, for human S9 testosterone, diclofenac and propranolol were used. The incubation was stopped after defined time points by precipitation of aliquots of S9 enzymes with 2 volumes of cold acetonitrile containing internal standard (150 nM diphenhydramine). Samples were stored on ice until the end of the incubation and precipitated protein was removed by centrifugation (15 min, 4 °C, 4,000 g). Concentration of the remaining test compound at the different time points was analyzed by HPLC-MS/MS (TSQ Quantum Access MAX, Thermo Fisher, Dreieich, Germany) and used to determine half-life ($t_{1/2}$) and intrinsic clearance (Cl_{int}).

Species profiling was conducted as above using 0.5 mg/mL pooled mouse, rat or minipig liver microsomes (Xenotech, Kansas City, USA) with 2 mM NADPH and 10 mM $MgCl_2$ and testosterone, verapamil and ketoconazole as reference compounds.

3.5 Plasma stability

To determine stability in plasma, the compound (1 µM) was incubated with pooled CD-1 mouse/human/Wistar rat or Göttingen minipig plasma (Neo Biotech, Nanterre, France). Samples were taken by mixing aliquots with 4 volumes of acetonitrile containing internal standard (125 nM diphenhydramine). The plasma stability of procain, propantheline and diltiazem were determined in parallel to confirm the enzymatic activity. Samples were stored on ice until the end of the incubation and precipitated protein was removed by centrifugation (15 min, 4 °C, 4,000 g, two centrifugation steps). Concentration of the remaining test compound at the different time points was analyzed by HPLC-MS/MS (TSQ Quantum Access MAX, Thermo Fisher, Dreieich, Germany) and used to determine half-life ($t_{1/2}$).

Table S2: Additional in vitro ADMET data for selected dipeptides. n.d.: not determined.

Compound	Kinetic Solubility PBS pH 7.4 [µM]	Liver S9 Cl_{int} [µL/mg/min]		Plasma $t_{1/2}$ [min]		$LogD_{7.4}$
		Mouse	Human	Mouse	Human	
13	>200	<5.8	<5.8	>150	>150	–0.58
14	>200	<5.8	<5.8	>150	>150	1.14
(*R*)-30	>200	<5.8	<5.8	>150	>150	n.d.
(*R*)-36	>200	<5.8	<5.8	>150	>150	–0.67

Table S3. Stability of compound 30 in plasma and liver microsomes of the species Wistar rat and Göttingen minipig.

Compound	Mouse	Minipig		Rat	
	Liver Microsomes $t_{1/2}$ [min]	Liver Microsomes $t_{1/2}$ [min]	Plasma $t_{1/2}$ [min]	Liver Microsomes $t_{1/2}$ [min]	Plasma $t_{1/2}$ [min]
30	>120	>120	>240	>120	>240

3.6 Calu-3 Permeability

Compound permeability was assessed in vitro with Calu-3 HTB-55 cell line (ATCC). Cells were cultivated in Minimum Essential Medium supplemented with Earle´s salts, L-glutamine, 10% FCS, 1% non-essential amino acids (NEAA) and 1mM sodium pyruvate. Passages between 35 and 55 were used, medium was changed every 2–3 days. For experiments, cells were harvested using trypsin/EDTA and $1x10^5$ cells seeded on Transwell® inserts 3460. Cells were grown in air-liquid interface beginning day 3 and used for transport studies on day 11–13. Transepithelial/transendothelial electrical resistance (TEER) values exceeded 300 Ω*cm² before beginning transport studies. For experiments, Krebs-Ringer solution was used and cells were accommodated to the buffer for at least 1 h with no decrease in TEER. 200 µL samples were taken in regular intervals from the apical side (time intervals 0, 15, 30, 60, 120, 180, 300 min) and replenished with fresh buffer. TEER was monitored during the experiment, and epithelial barriers were considered compromised if the TEER fell below 300 Ω*cm² during 5 h of experiment duration. A cassette of atenolol, ciprofloxacin and carbamazepine was used as control. Test compounds were applied individually or in cassettes including up to three compounds.

Before analysis, 40 µL of sample was mixed with 80 µL of ice-cold acetonitrile containing internal standard diphenhydramine (150 nM), and the compound concentration was analyzed with HPLC-MS/MS (TSQ Quantum Access MAX, Thermo Fisher, Dreieich, Germany). Samples from the apical compartment taken at the beginning and end of the experiment were diluted 1:10 in KRB + 0.5% DMSO before mixing with acetonitrile.

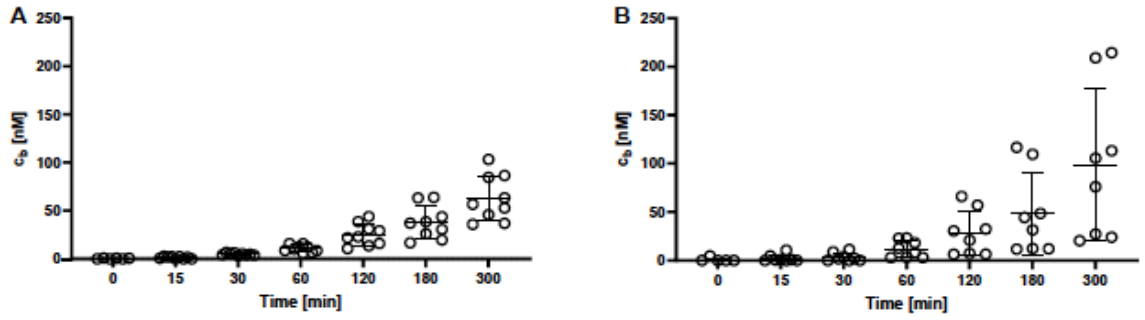

Figure S7: Basolateral concentration of 9 (A) and 30 (B) in the Calu-3 permeability model. Results show individual values, mean and standard deviation of 3 independent measurements with 3 technical replicates each.

3.7 In vivo pharmacokinetic studies

For pharmacokinetic experiments, outbred male CD-1 mice (Charles River, Netherlands), 4 weeks old, were used. The animal studies were conducted in accordance with the recommendations of the European Community (Directive 2010/63/EU, 1st January 2013). All animal procedures were performed in strict accordance with the German regulations of the Society for Laboratory Animal Science (GV-SOLAS) and the European Health Law of the Federation of Laboratory Animal Science Associations (FELASA). Animals were excluded from further analysis if sacrifice was necessary according to the human endpoints established by the ethical board. All experiments were approved by the ethical board of the Niedersächsisches Landesamt für Verbraucherschutz und Lebensmittelsicherheit, Oldenburg, Germany.

30 was subjected to a focused PK study and was administered 30 mg/kg SC. At time points t= 0.25, 0.5, 1, 2, 4, 8 and 24 hours post administration, mice (t = 3 mice per time point) were euthanatized and blood was collected from the heart. For all PK studies, whole blood was collected into Eppendorf tubes coated with 0.5 M EDTA and immediately spun down at 13,000 rpm for 10 min at 4°C. The plasma was transferred into a new Eppendorf tube and then stored at -80°C until analysis. Then, a broncheoalveolar lavage was conducted using isotonic sodium chloride solution for all PK studies. For all PK studies, lung, kidney and liver were aseptically removed and homogenized using a Polytron (Kinematica) in isotonic sodium chloride solution. Organ samples were aliquoted into Eppendorf tubes and stored at -80°C until analysis. Moreover, spontaneous urine was also collected.

All PK plasma samples were analyzed via HPLC-MS/MS using an Agilent 1290 Infinity II HPLC system and coupled to an AB Sciex QTrap6500+ mass spectrometer as described previously.[10] Mass spectrometric conditions can be found in Table S5. First, a calibration curve was prepared by spiking different concentrations of **30** into the respective matrix (mouse

plasma (pooled, from CD-1 mice) for plasma samples, isotonic sodium chloride solution for BALF samples, lung tissue for lung samples, kidney tissue for kidney samples, liver tissue for liver samples and urine for urine samples). Caffeine was used as an internal standard. In addition, quality control samples (QCs) were prepared for **30** with the respective matrix. The following extraction procedure was used: 7.5 µl of a plasma sample (calibration samples, QCs or PK samples) was extracted with 37.5 µl of methanol containing 12.5 ng/ml of caffeine as internal standard for 5 min at 2000 rpm on an Eppendorf MixMate® vortex mixer. 10 µl of a urine sample (calibration samples, QCs or PK samples) was extracted with 40 µl of methanol containing 12.5 ng/ml of caffeine as internal standard for 5 min at 2000 rpm on an Eppendorf MixMate® vortex mixer. Then samples (plasma and urine) were spun down at 13.000 rpm for 5 min. Supernatants were transferred to standard HPLC-glass vials. 50 µl of a BALF / lung tissue / kidney tissue or liver tissue sample (calibration samples, QCs or PK samples) were extracted with 50 µl of methanol and 1 µl caffeine (concentration 1 µg/ml in methanol) for 5 min at 800 rpm on an Eppendorf MixMate® vortex mixer. Then samples (BALF, liver, kidney, lung) were spun down at 4,000 rpm for 40 min at 4°C. Supernatants were transferred to 96well V-bottom plates (Greiner). Urea was used to enable calculation of epithelial lining fluid (ELF) concentrations. Peak areas of each sample and of the corresponding internal standard were analyzed using MultiQuant 3.0 software (AB Sciex). Peak areas of the respective sample were normalized to the internal standard peak area. Peaks of PK samples were quantified using the calibration curve. The accuracy of the calibration curve was determined using QCs independently prepared on different days. PK parameters were determined using a non-compartmental analysis with PKSolver.[11] ELF concentrations were calculated using the following formula (2).[12]

(1) $V\_ELF = V\_BALF \times (Urea\_BALF)/(Urea\_Plasma)$

(2) $c\_ELF = c\_BALF \times V\_BALF/V\_ELF$

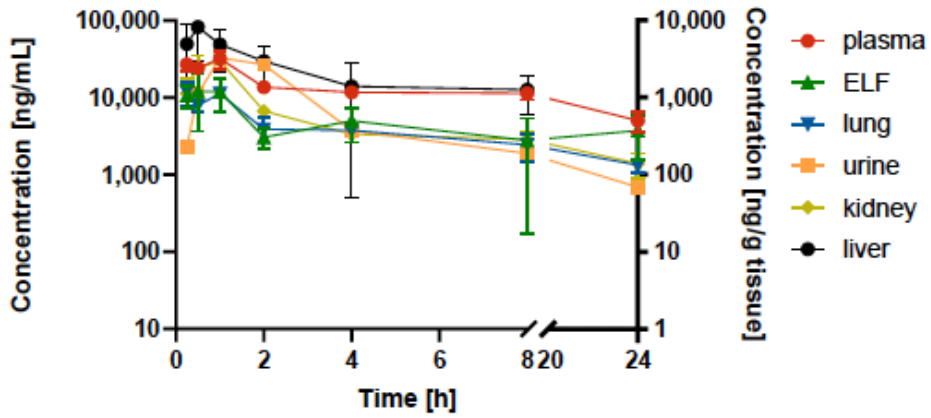

Figure S8: Pharmacokinetic study of 30 applied to mice at 30 mg/kg via subcutaenous administration. Concentrations are given for plasma, epithelial lining fluid (ELF), urine as well as lung, kidney and liver tissue. Corresponding PK parameters are given in Table S7.

Table S4. Plasma pharmacokinetic parameters of 30 after subcutaneous administration to mice (30 mg/kg).

Parameter	Compound 30
$t_{1/2}$ [h]	18.5 ± 11.0
C_{max} [µg/mL]	32.2 ± 8.5
T_{max} [h]	0.75 ± 0.4
AUC_{0-t} [µg/mL*h]	248.9 ± 15.5
MRT [h]	24.6 ± 16.0
Vz/F_obs [L/kg]	1.9 ± 0.6
Cl/F_obs [mL/min/kg]	1.3 ± 0.3

Table S5: Mass spectrometric conditions. Q1 and Q3 masses for caffeine and (*R*)-30 (MS/MS pairs used for quantification are marked with a 'Q')

ID	Q1 Mass [Da]	Q3 Mass [Da]	time [msec]	DP [volts]	CE [volts]	CXP [volts]
Caffeine	195.024	138.000 (Q)	30.0	130.0	25.0	14.0
		110.000	30.0	130.0	31.0	18.0
(*R*)-30	411.125	78.8 (Q)	30.0	–95.0	–82.0	–35.0
		294.9	30.0	–95.0	–40.0	–13.0

3.8 Test against zinc metalloproteases MMP1–3 and TACE (ADAM17), and testing of the Safety Screen44™

We selected a panel of human off-targets, including three human matrix metalloproteases (MMP-1, -2 and -3) and TACE (ADAM-17). These assays were performed as described previously.[3] The TACE inhibitor screening kit was purchased from Sigma-Aldrich (Saint Louis, MO). MMPs along with the SensoLyte 520 Generic MMP Activity Kit Fluorimetric were purchased from AnaSpec (Fremont, CA, USA). The assays were performed according to the guidelines of the respective manufacturer. Fluorescence signals were measured using a CLARIOstar plate reader (BMG Labtech, Ortenberg, Germany).

The off-target Safety Screen44™ was performed by the CRO Eurofins Cerep SA (Celle-L'Evescault, France) according to their protocols.[13]

Table S6: Percent (%) inhibition of three MMPs (1–3) and TACE (ADAM17) in presence of selected LasB inhibitors at 100 µM. Results are means and SD of at least two independent experiments.

Compound	MMP-1 [% inhibition at 100 µM]	MMP-2 [% inhibition at 100 µM]	MMP-3 [% inhibition at 100 µM]	TACE (ADAM17) [% inhibition at 100 µM]
9	13±1	<10	<10	<10
13	<10	<10	<10	<10
14	<10	<10	<10	<10
30	<10	<10	<10	13±4
(*R*)-30	<10	<10	<10	13±2
31	<10	<10	<10	<10
(*R*)-36	<10	<10	<10	<10

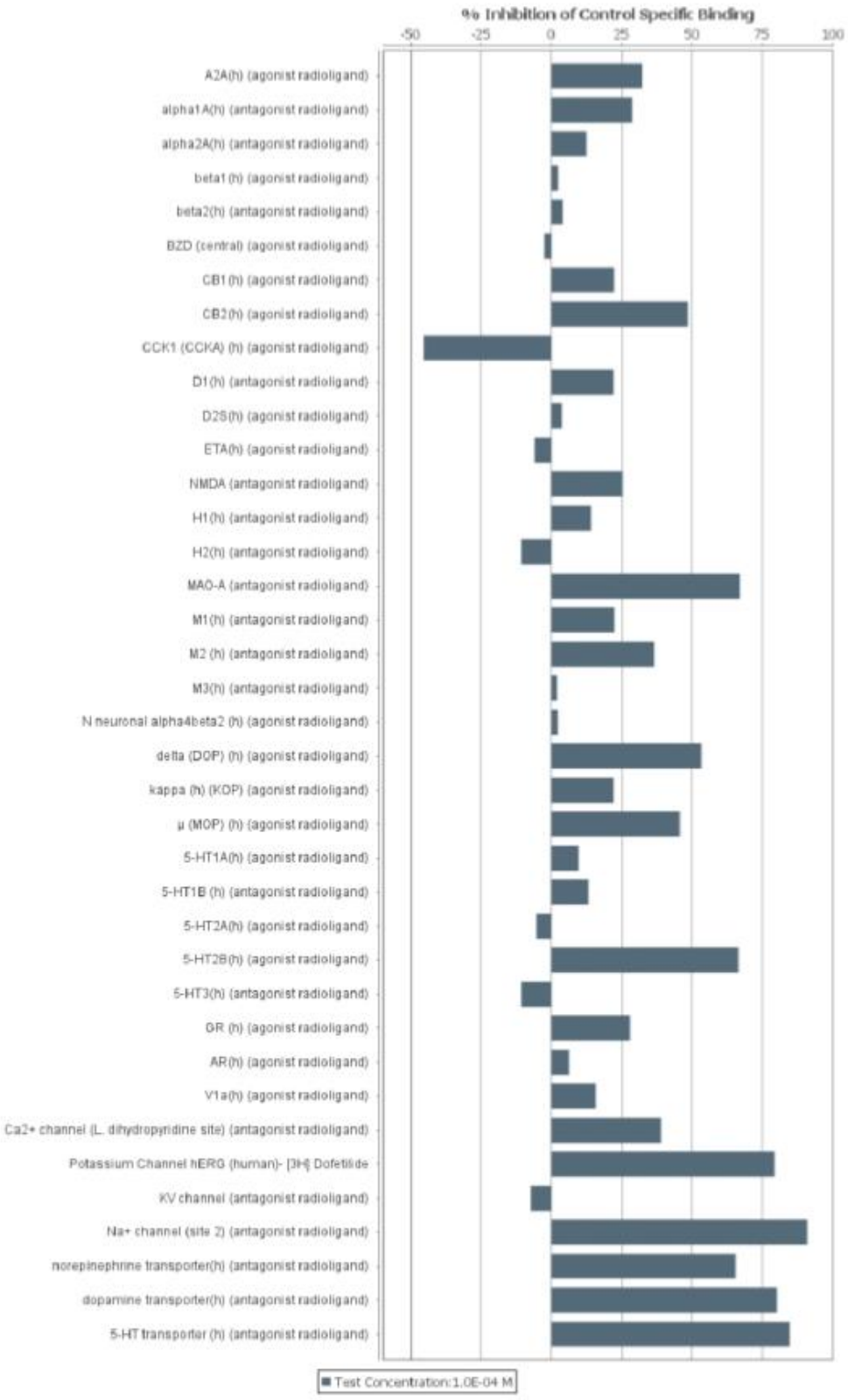

Figure S9. Effect of 100 μM of (*R*)-30 on the binding of the natural ligands of thirty-eight human off-targets. Percent (%) binding inhibition is shown.

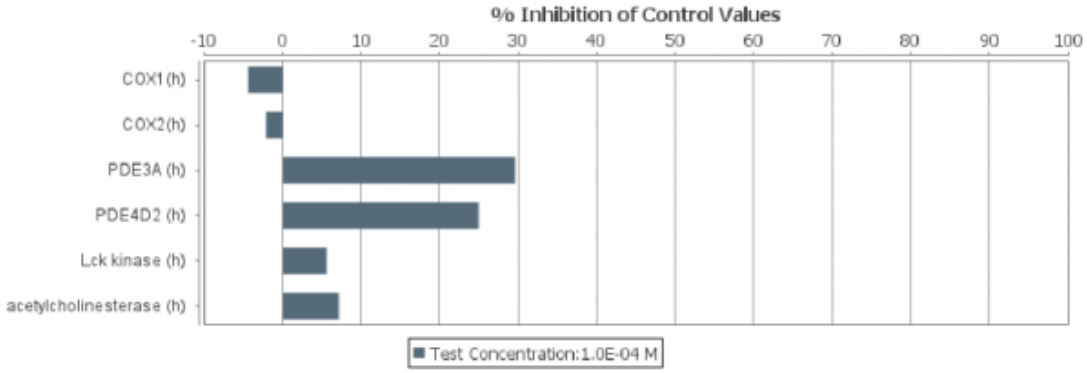

Figure S10. Effect of 100 μM of (*R*)-30 on the enzymatic activity of six human off-targets.

Table S7. Ten human off-targets whose binding to natural ligands was inhibited by >50% by 100 μM of (*R*)-30.

Assay	1.0E-04 M
MAO-A (antagonist radioligand)	66.9%
delta (DOP) *(h)* (agonist radioligand)	53.3%
5-HT_{2B}*(h)* (agonist radioligand)	66.4%
Potassium Channel hERG (human)- [3H] Dofetilide	79.4%
Na^+ channel (site 2) (antagonist radioligand)	91.1%
norepinephrine transporter*(h)* (antagonist radioligand)	65.6%
dopamine transporter*(h)* (antagonist radioligand)	80.3%
5-HT transporter *(h)* (antagonist radioligand)	84.8%
COX1(h)	81.5%
COX2(h)	62.3%

3.9 Cytotoxicity studies

HepG2 (human hepatocellular carcinoma), HEK293 (human embryonal kidney) and A549 (human lung carcinoma) cells ($2x10^5$ cells per well) were seeded in 24-well in flat-bottomed plates. Culturing of cells, incubations and OD measurements were performed as described previously with small modifications.[14] Twenty-four hours after seeding the cells the incubation was started by the addition of compounds in a final DMSO concentration of 1%. The living cell mass was determined after 48 hours in a PHERAstar microplate reader (BMG labtech, Ortenberg, Germany). Two independent measurements were performed for each compound.

Table S8: Percent (%) inhibition of the metabolic activity of three human cell lines HepG2 (hepatocellular carcinoma cells), HEK293 (human embryonic kidney 293 cells) and A549 (lung carcinoma epithelial cells). Results are means and SD of at least two independent experiments.

Compound	HepG2 [% inhibition at 100 µM]	HEK293 [% inhibition at 100 µM]	A549 [% inhibition at 100 µM]
9	<10	<10	<10
13	<10	<10	<10
14	13±0	51±4	<10
30	<10	<10	<10
(*R*)-30	<10	<10	<10
31	<10	19±5	<10
(*R*)-36	<10	11±9	<10

3.10 Evaluation of Zebrafish embryo toxicity

The experiment was performed according to a procedure described in the literature[15] with minor modifications using zebrafish embryos of the AB wild-type line at 1 day post fertilization (dpf). A detailed protocol has been given in our recent publication.[16]

Table S9: Zebrafish embryo toxicity of compound **30**. Starting exposure ar 2 dpf. Ten larvae were tested for each condition. Dpf: days post fertilization.

Compound	Concentration (µM)	Survival rate (%)			Comment
		3 dpf	4 dpf	5 dpf	
30	100	100	100	100	No observations of concern, e.g., no malformed ZF larvae.
	30	100	100	100	No observations of concern, e.g., no malformed ZF larvae.
	10	100	100	100	No observations of concern, e.g., no malformed ZF larvae.
	2	100	100	100	No observations of concern, e.g., no malformed ZF larvae.

3.11 Tolerability study in male CD1 mice

This in vivo experiment was carried out at the CRO Selvita (Zagreb, Croatia). The study was performed in an AAALAC I- approved Facility. The standard study plan relating to this study was reviewed by the Ethics Committee (CARE- Zagreb) as required by International Laws/Regulations and Croatian Low on Animal Welfare ("The Animal Protection Act", Official Gazette, NN 135/06 and NN 37/13) and Animal Welfare Officer. Animals were kept in in solid bottom cages (TECNIPLAST S.p A., Italy, Type III polysulphone cage); 425 mm x 266 mm x 180 mm; 3 animals in each cage. The animals were kept on 4 cm thick layer of corn cob grit,

dust-free bedding (Scobis Due - Mucedola, Italy), with a provision of one paper shelters (Lillico Biotechnology, UK). Animals from each group were housed in 1 cage of 2 animals/cage. Mice were housed in the following ambient conditions: temperature 22 ºC ± 2, with relative humidity 55 % ± 10, 15-20 air changes per hour and 12 hours artificial lighting and 12 hours darkness per day (7 a.m. - 7 p.m.).

The experiments were carried out with male Crl: CD1 (IRC) mice purchased from Charles River, Calco (Milano, Italy). Their age was 7-8 weeks at the start of dosing.

This study was carried out with compounds **30** and **(*R*)-30**. As vehicle we used 10% DMSO, 20% Kolliphor EL and 70% PBS. For both compounds, the dose volume was 5 mL/kg (with the exception of 10 mL/kg for the group with the highest dose of 400 mg/kg of **30**). **30** was administered as a single subcutaneous dose. The used doses were 25 mg/kg, 50 mg/kg, 100 mg/kg, 200 mg/kg and 400 mg/kg. Two mice were used per group. **(*R*)-30** was administered intravenously (IV) (TID, 6h intervals) for 3 days followed by 4 days dose-free. Consequently, the compound was administered at 300 mg/kg/day and 600 mg/kg/day for 3 consecutive days. Here, three mice were used per group.

The observations and examinations that were made, comprise clinical signs, body weight, food consumption, macroscopy at termination and organ weights. Mortality was recorded twice a day, *i.e.* in the morning and at the end of the working day.

Table S10: Body weight (gram) after treatment with **30**.

Group Number		Body Weight (g) Day 1	Body Weight (g) Day 4	Body Weight (g) Day 7	Body Weight (g) Day 8
1 Vehicle	Mean	38.75	38.95	38.90	36.95
(SC)	SD	2.19	2.33	2.26	2.19
	n	2	2	2	2
2	Mean	38.70	38.20	37.75	36.35
25 mg/kg	SD	0.71	0.99	0.49	0.49
	n	2	2	2	2
3	Mean	39.00	39.65	40.10	38.40
50 mg/kg	SD	0.85	1.34	1.56	1.27
	n	2	2	2	2
4	Mean	38.60	39.15	38.95	35.80
100 mg/kg	SD	0.85	0.92	0.92	0.71
	n	2	2	2	2
5	Mean	38.50	39.55	39.35	37.25
200 mg/kg	SD	0.71	0.49	1.91	0.78
	n	2	2	2	2
6	Mean	38.75	39.40	39.35	37.65
400 mg/kg	SD	1.06	1.56	1.63	1.48
	n	2	2	2	2

Table S11: Food consumption after treatment with **30**.

			Days 1 - 7
Group Number	Total Food consumption g-group		g-animal-day
1 Vehicle		Mean	9.16
(SC)	110.0	SD	0.00
		n	2
2		Mean	8.54
25 mg/kg	102.5	SD	0.00
		n	2
3		Mean	7.50
50 mg/kg	90.0	SD	0.00
		n	2
4		Mean	7.30
100 mg/kg	88.0	SD	0.00
		n	2
5		Mean	7.08
200 mg/kg	85.0	SD	0.00
		n	2
6		Mean	6.80
400 mg/kg	82.0	SD	0.00
		n	2

Table S12: Body and organ weights (gram) after treatment with **30**.

Group Number		Final Body Weight (g)	Brain (g)	Heart (g)	Thymus (g)	Liver (g)	Kidneys (g)	Spleen (g)	Testes (g)	Adrenal glands (g)	Epididym. (g)
1 Vehicle	Mean	36.95	0.504	0.200	0.047	1.906	0.714	0.113	0.277	0.021	0.150
(SC)	SD	2.19	0.004	0.028	0.001	0.156	0.082	0.001	0.004	0.001	0.025
	n	2	2	2	2	2	2	2	2	2	2
2	Mean	36.35	0.489	0.193	0.064	1.763	0.652	0.123	0.322	0.018	0.153
25 mg/kg	SD	0.49	0.057	0.004	0.004	0.097	0.037	0.001	0.034	0.001	0.004
	n	2	2	2	2	2	2	2	2	2	2
3	Mean	38.40	0.452	0.179	0.060	1.942	0.655	0.121	0.280	0.020	0.129
50 mg/kg	SD	1.27	0.025	0.012	0.006	0.098	0.025	0.016	0.008	0.002	0.006
	n	2	2	2	2	2	2	2	2	2	2
4	Mean	35.80	0.488	0.175	0.065	1.514	0.554	0.085	0.287	0.022	0.126
100 mg/kg	SD	0.50	0.019	0.006	0.004	0.033	0.050	0.004	0.016	0.001	0.004
	n	2	2	2	2	2	2	2	2	2	2
5	Mean	37.25	0.481	0.193	0.082	2.175	0.607	0.132	0.249	0.020	0.134
200 mg/kg	SD	0.78	0.021	0.003	0.016	0.023	0.029	0.001	0.013	0.004	0.011
	n	2	2	2	2	2	2	2	2	2	2
6	Mean	37.65	0.497	0.204	0.075	2.296	0.688	0.121	0.292	0.026	0.139
400 mg/kg	SD	1.05	0.022	0.011	0.021	0.181	0.088	0.006	0.020	0.000	0.004
	n	2	2	2	2	2	2	2	2	2	2

Table S13: Body weight (gram) after treatment with (*R*)-**30**.

Group Number		Body Weight (g) Day 1	Body Weight (g) Day 2	Body Weight (g) Day 3	Body Weight (g) Day 4	Body Weight (g) Day 5	Body Weight (g) Day 6	Body Weight (g) Day 7
	Mean	36.47	35.37	34.97	34.87	35.40	35.70	35.73
1 Vehicle	SD	2.51	3.36	3.65	3.44	2.99	3.12	3.15
	n	3	3	3	3	3	3	3
	Mean	33.50	34.27	34.27	34.33	34.70	34.97	35.03
4	SD	0.26	0.31	0.06	0.15	0.36	0.49	0.38
300 mg/kg/day	n	3	3	3	3	3	3	3

Group Number		Body Weight (g) Day 1	Body Weight (g) Day 2	Body Weight (g) Day 3	Body Weight (g) Day 4	Body Weight (g) Day 5	Body Weight (g) Day 6	Body Weight (g) Day 7
	Mean	35.20	35.27	34.97	35.30	35.30	35.00	35.50
1 Vehicle	SD	3.20	3.28	3.25	2.93	3.00	3.24	2.74
	n	3	3	3	3	3	3	3
	Mean	36.63	36.27	37.23	37.70	37.17	37.60	37.90
7	SD	1.33	1.07	1.14	1.01	1.56	1.68	1.90
600 mg/kg/day	n	3	3	3	3	3	3	3

Table S14: Food consumption after treatment with (*R*)-30.

Group Number	Total Food consumption g-group		Days 1 - 7 g-animal-day
1 Vehicle	95	Mean	5.28
		SD	0.00
		n	3
4 300 mg/kg/day	101	Mean	5.61
		SD	0.00
		n	3

Group Number	Total Food consumption g-group		Days 1 - 7 g-animal-day
1 Vehicle	81	Mean	4.50
		SD	0.00
		n	3
7 600 mg/kg/day	85	Mean	4.72
		SD	0.00
		n	3

Table S15: Body and organ weights (gram) after treatment with (*R*)-30.

Group Number		Final Body Weight (g)	Brain (g)	Heart (g)	Thymus (g)	Liver (g)	Kidneys (g)	Spleen (g)	Testes (g)	Adrenal glands (g)	Epididym. (g)
1 Vehicle	Mean	35.50	0.505	0.192	0.068	1.858	0.504	0.113	0.226	0.025	0.110
	SD	2.74	0.014	0.036	0.012	0.105	0.095	0.017	0.026	0.006	0.010
	n	3	3	3	3	3	3	3	3	3	3
300 mg/kg/day	Mean	35.03	0.499	0.173	0.067	2.138	0.647	0.136	0.249	0.021	0.125
	SD	0.38	0.025	0.011	0.016	0.054	0.078	0.021	0.027	0.005	0.030
	n	3	3	3	3	3	3	3	3	3	3
600 mg/kg/day	Mean	37.90	0.488	0.183	0.060	2.428	0.559	0.174	0.281	0.022	0.117
	SD	1.90	0.030	0.016	0.017	0.178	0.042	0.022	0.052	0.007	0.015
	n	3	3	3	3	3	3	3	3	3	3

3.12 Antibacterial effects

As start OD_{600} of *Pseudomonas aeruginosa* strain PA14 we used 0.03 in a total volume of 200 µL in lysogeny broth containing the compounds predissolved in DMSO (max. 1%). Final compound concentrations prepared from serial dilutions ranged from 3.125 to 100 µM (double values for each concentration). The ODs were determined after addition of the compounds and again after incubation for 18 h at 37 °C and 200 rpm in 96 well plates (Sarstedt, Nümbrecht, Germany) using a FLUOStar Omega (BMG labtech, Ortenberg, Germany). Given percent (%) inhibition values are means of at least two independent determinations. To obtain the values for a given compound, their ODs were compared to those of DMSO controls. Concerning the

growth curves with *Pseudomonas aeruginosa* strain PA54, a start OD_{600} of 0.03 in a total volume of 200 µL was used. This volume contained 1% of DMSO in all samples. As growth media we used either pure LB medium, or LB supplemented with 10 or 50% of citric acid buffer (pH 7.4, 300 mOsm/L). The OD_{600} was determined every 10 min for 10 or 18 h at either 25 °C or 37 °C, respectively, with permanent shaking in 96 well plates using a FLUOStar Omega.

Table S16: Percent (%) inhibition of the growth of *Pseudomonas aeruginosa* strain PA14 after challenge with 100 µM of seven compounds. Results are means and SD of at least two independent experiments.

Compound	P. aeruginosa PA14 [% inhibition at 100 µM]
9	<10
13	<10
14	<10
30	<10
(*R*)-30	<10
31	<10
(*R*)-36	<10

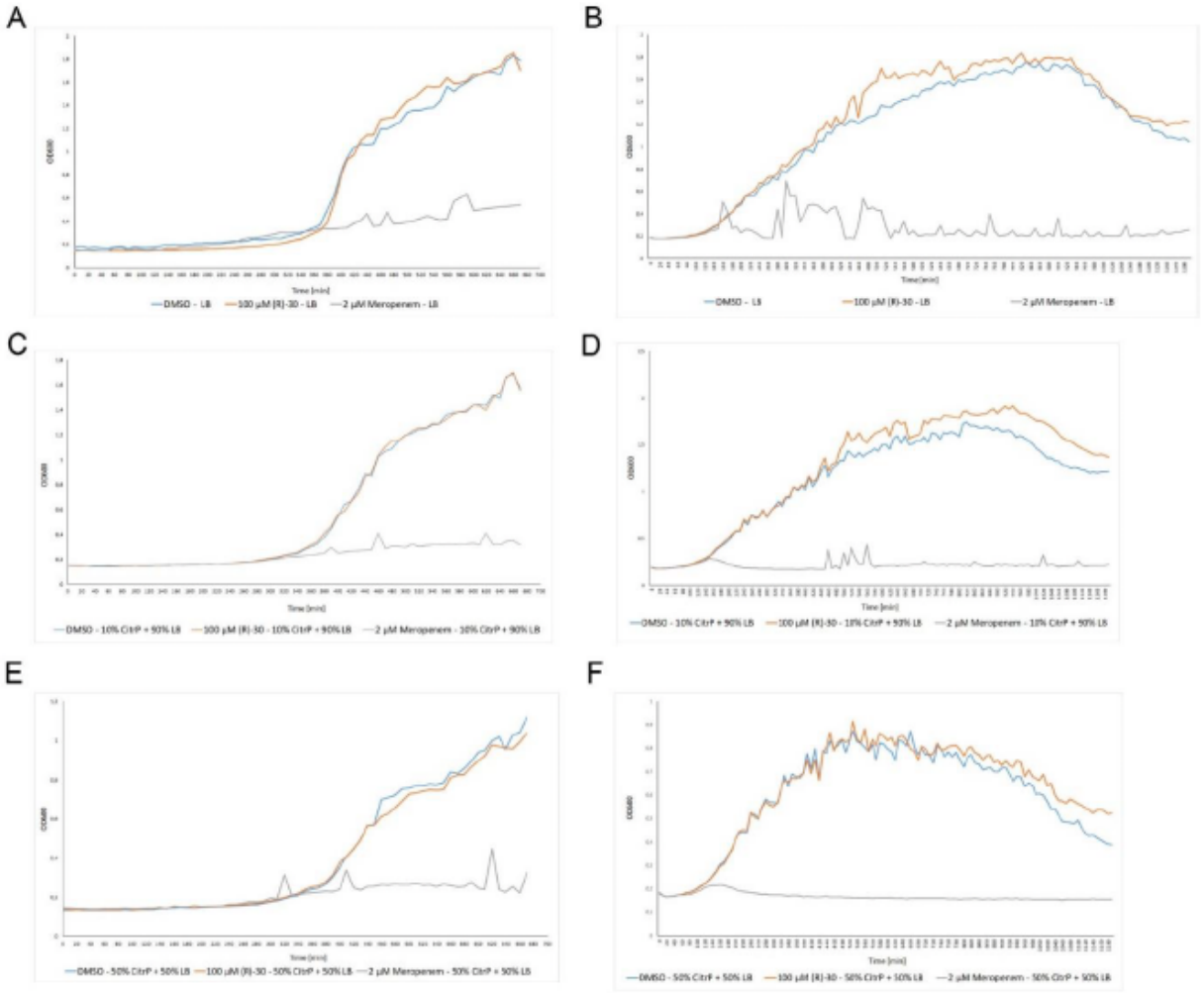

Figure S11: Growth curves of *Pseudomonas aeruginosa* PA54. Bacteria were either treated with DMSO (blue curves), (*R*)-**30** (orange) or meropenem (grey). The cell densities were determined every 10 min after incubation at either 25 °C (A, C, E) or 37 °C (B, D, F). The bacteria were grown in either pure LB medium (A, B), LB medium containing 10% isotonic citric acid buffer (C, D) or LB medium containing 50% isotonic citric acid buffer (E, F).

3.13 Inhibition of biofilm formation

Biofilm formation was determined using a MBEC Assay® Biofilm Inoculator with 96 well base (Innvotech, Edmonton, CA). An overnight culture of PA14 was centrifuged (10 min, 5000 x g). The supernatant including extracellular polymers was removed and the pellet washed with 10 mL of LB medium. Centrifugation was repeated, the supernatant discarded and the pellet resuspended in 5 mL of LB. OD was adjusted to 0.2. The bacteria were further diluted in LB medium, followed by addition of **30** or DMSO control to give OD 0.1, 100 µM **30** and 1% DMSO. 150 µL were added to each well of the 96 well plate. The outer wells were used as blanks containing 150 µL of 1% DMSO in LB. Four replicates per sample were distributed evenly across the plate, with every row containing one replicate of each sample. The well plate was

covered with the peg lid. One layer of parafilm was wrapped around the biofilm inoculator. The inoculator was incubated at 37°C, static for 24 with a beaker of H_2O ensuring humidity.
After 24 h, the plate was removed from the incubator and the peg lid was transferred to a fresh 96 well plate (Nunc U bottom, Thermo Fisher, Dreieich, Germany) containing DMSO or 100 µM **30** in 150 µL 1% DMSO/LB. The inoculator was wrapped with parafilm again and incubated for another 24 h. After that, the peg lid was transferred for 1 min to a 96 well plate containing 200 µL sterile MΩ in each well, followed by another 96 well plate containing 200 µL LB in each well. The system was sealed with parafilm and sonicated for 15 min in an ultrasonic bath with tray. Immediately after sonication, 20 µL were removed from each well using a multi-channel pipette and diluted 1:10 (stepwise, until 10^{-6}). After each dilution step, 10 µL were directly transferred to cetrimide agar plates (spot plating) using fresh pipette tips. Agar plates were incubated for 16 h at 37°C and then used for cell counting. Results are shown in Figure S12.

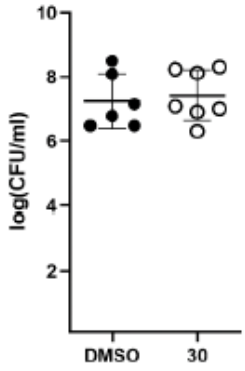

Figure S12: Colony-forming units (CFU) of *P. aeruginosa* PAO1 in biofilms after 48 h growth in presence of 100 µM **30** or DMSO as measured using the Calgary biofilm device.[17] Biofilms were grown for 48 h in presence of DMSO/**30** from the moment of biofilm inoculation. Medium was replaced after 24 h by fresh medium containing DMSO/**30**. Mean ± SD and individual values from 2 independent experiments are displayed.

3.14 In vivo target engagement studies using *Pseudomonas* keratitis model

Evaluation of *lasB* gene expression in *Pseudomonas aeruginosa* strain PA54 through relative and absolute quantification using quantitative polymerase chain reaction (qPCR): Overnight bacterial cultures of *Pseudomonas aeruginosa* strains PA54, PAO1 (DSM 19880) and PA14 (DSM 19882) were prepared in LB medium. The following day, cell lysates were prepared by adding 2 mL of QIAGEN RNAprotect® Bacteria Reagent to 1 mL of culture adjusted to an OD_{600} of 1. These mixtures were vortexed and left at room temperature for 5 min, followed by a 10 min centrifugation at 5000x g at room temperature. The resulting supernatant was removed, and the pellet was re-suspended in 20 µL of Proteinase K previously mixed with 200 µL of TE buffer (containing 30 mM Tris-Cl, 1 mM EDTA, pH 8.0, and 15 mg/mL lysozyme).

This mixture was vortexed for 10 seconds every 2 minutes over a 10-minute period. Subsequently, 700 µL of buffer RLT (provided in the QIAGEN RNeasy Plus Kit) was added to each tube and vigorously vortexed. The flow-through was then transferred to the gDNA eliminator spin column (also provided in the kit) and centrifuged for 2 minutes at 14000 rpm at room temperature. After discarding the column, 700 µL of 99% ethanol was added to the flow-through of each sample.

The next step involved RNA extraction and purification using the QIAGEN RNeasy Plus Kit, with slight modifications to the manufacturer's instructions. Centrifugation times were increased from 15 seconds to 2 minutes, and after eluting the RNA with RNase-free water, samples were treated with the Invitrogen™ DNA-free™ DNA Removal Kit to ensure the complete removal of genomic DNA. For each sample, 8 µL of DNase I buffer was combined with 2 µL of rDNase I, followed by a 25-minute incubation at 37°C. Subsequently, 10 µL of DNase inactivation reagent was added and occasionally mixed for 2 minutes at room temperature. Finally, all samples were centrifuged at 10000x g for 1.5 minutes, and the supernatant containing purified RNA was transferred to a new tube. RNA concentration was measured using a NanoDrop 2000 Spectrophotometer (Thermo Fisher Scientific), and 100 ng of mRNA was used for reverse transcription.

To generate single-stranded cDNA from the purified RNA, the Applied Biosystems™ High-Capacity cDNA Reverse Transcription Kit was employed. The reverse transcription process was conducted according to the manufacturer's instructions, and the final cDNA was used for gene expression analysis. For qPCR, TaqMan™ Fast Advanced Master Mix (Applied Biosystems™) was used, and the qPCR reaction plate was prepared following the manufacturer's instructions, with a final primer concentration of 900 nM and a probe concentration of 250 nM. Primers and Probes specific to *lasB* were designed using Geneious Prime software (Table S16). To ensure there was no contamination and no signal from genomic DNA, a no template control (NTC) and a no reverse transcriptase control (-RT) were included. The gBlocks™ Gene Fragment (Integrated DNA Technologies) for absolute quantification was prepared by adding nuclease-free water to the tube to achieve a concentration of 10 ng/µL, followed by a 20-minute incubation at 50°C. The mixture was then serially diluted by a factor of 5 and amplified alongside the samples using the same primers and probe employed for *lasB* to generate the standard curve. The StepOnePlus™ Real-Time PCR System (Applied Biosystems™) was used for the qPCR run, with thermal cycling conditions according to the TaqMan™ Fast Advanced Master Mix instructions.

The analysis of fold change and copy numbers was conducted through Microsoft Excel, and the data were graphically represented using GraphPad Prism 9.

Table S17: Primers and probes applied in this study (designs were carried out using Geneious Prime bioinformatics software)

Gene	Forward primer	Reverse Primer	Probe	Description
lasB	CATCACCGTCGACATGAACA	AGAAATGCGCGTCGTTCAG	CGCTTCGCCTGCCCGACCAA	*Pseudomonas aeruginosa* Elastase B
rpoS	CTGAACGAACGGGTGACTTC	TCGCTGAGATCGTCATCCTG	ACCGACGATCGCCCCACCGA	RNA polymerase sigma factor RpoS
rho	CAGATCCGGCGCTTCAAC	TCTCCGGACGATCGAAGTTG	GCACGGGCGACACCATCATCGG	Transcription termination factor Rho

Animals: The animal experiments were approved by Saarland University's Animal Welfare Committee (Application number: 17/2021) and conducted in accordance with German and European recommendations and guidelines for the ethical use of animals. The laboratory animals were all C57BL/6N female eight to eleven months old mice. Keeping in specific pathogen-free conditions was provided. Unlimited access to water and show was secured. Temperature was closely maintained around 22 °C and relative air humidity around 50%. Light and darkness alternated at twelve-hour intervals. All laboratory animals were purchased from Charles River GmbH, Sulzfeld, Germany.

P. aeruginosa: The *P. aeruginosa* strain PA54 was employed to induce an experimental bacterial keratitis in the aforementioned C57BL/6N mice. The strain PA54 was isolated from human infections and collected at Saarland University Medical Center's Institute for Medical Microbiology and Hygienics (IMMH) in 2009. According to Magiorakos *et al.*, PA54 can be classified as multidrug-resistant due to its lacking sensibility to the anti-pseudomonal cephalosporins ceftazidime and cefepime, the anti-pseudomonal fluoroquinolones ciprofloxacin and levofloxacin, the phosphoric acid fosfomycin, and the aminoglycoside gentamicin.[18] The minimum inhibitory concentration (MIC) of the reserve antibiotic meropenem (meropenem trihydrate, Sigma) was 1 µg/mL (sensitivity limit = 2 µg/mL). The *exoU*- and *exoT*-positivity of the PA54 strain, foregrounds its keratitogenic potential.

Inoculum: The *P. aeruginosa* strain PA54 is routinely grown overnight on blood agar (TrypticaseTM Soy Agar, 5% sheep blood, BD, Heidelberg, Germany) at 37 °C. To obtain a stationary phase cell inoculum, a freshly grown colony was inoculated in tryptic soy broth (TSB; BD, Heidelberg, Germany) and cultured at 37 °C and 150 rounds per minute (rpm) for 16 h. Then, 2 mL were centrifuged at 13,200 rpm at rt for 2 min, whereupon cells were resuspended in spent medium to an OD_{600} of 10 (~1×10^{10} CFU/mL). Short storage on ice followed, before the infection procedure started.

Infection Procedure: Anesthesia and infection were performed as previously published.[19] Briefly, fentanyl (Hameln Pharma Plus GmbH, Hameln, Germany), midazolam hydrochloride (Midazolam-Hameln, 5 mg/mL, Hameln pharma GmbH, Germany) and medetomidine hydrochloride (Domitor, Orion Corporation, Espoo, Finland) were dissolved in 0.9% NaCl (NaCl 0.9%, Ecotainer 500 mL, B. Braun, Melsungen, Germany), dosed at 0.05 mg/kg, 5 mg/kg and 0.5 mg/kg body weight, respectively, and applied by intraperitoneal injection. Analgesia (Carprofen, 5 mg/kg body weight, Zoetis Deutschland GmbH, Berlin, Germany) was applied subcutaneously. Lacrimation was stopped with 10 µL of a 0.6% acetylcysteine solution (Pharmacy of Saarland University Hospitals, Homburg, Germany). Local analgesia (0.5% proxymetacaine hydrochloride, Proparakain-POS Augentropfen, Ursapharm Arzneimittel GmbH, Saarbrücken, Germany) was eye-dropped and removed after 60 seconds. The blunt side of a scalpel was used to pass five times over the cornea to remove the superficial epithelium. Then, three parallel, vertical, 1–2 mm long scratches were added to the cornea with a PA54-loaded 27-Gauge needle (B. Braun). Afterwards, 5 µL (~5×10^{7} CFU/mL) of the inoculum were pipetted onto the scratched eye and left untouched for 20 min (Preston et al., 1995; Wu et al., 2017). Finally, 1.2 mg/kg body weight naloxone hydrochloride (Naloxon Inresa, 0.4 mg/mL, Inresa Arzneimittel GmbH, Freiburg, Germany), 0.5 mg/kg flumazenil (Flumazenil Inresa 0.5 mg, 0.1 mg/mL, Inresa Arzneimittel GmbH) and 2.5 mg/kg atipamezole hydrochloride (Antisedan, 5 mg/ml, Vetoquinol GmbH, Ismaning, Germany) were dissolved in 0.9% NaCl and injected subcutaneously, awakening the mouse.

Documentation and Treatment: Documentation was performed every 24 h. Keratitis severity was visualized using a stereomicroscope (Leitz ELVAR, Wetzlar, Germany) at 16× magnification combined with a high-resolution microscope digital camera (Seben GmbH, Berlin, Germany) and evaluated using a previously described clinical scoring scheme (Lyu et al., 2020). Briefly, a score of 0 indicates no infiltrates, 1 indicates that less than 50% of the cornea is semitransparent, 2 indicates that more than 50% of the cornea is semitransparent, 3 indicates that less than 50% of the cornea is opaque, 4 indicates that more than 50% of the cornea is opaque, and 5 indicates that either spontaneous corneal perforation or phthisis bulbi

has occurred. The body weight of the mice was measured daily and used as welfare indicator. General condition and behavior were also recorded daily. Treatment was performed every eight hours starting six hours after infection along 72h. Anesthesia was reached using 3% isoflurane inhalation (Isoflurane-Piramal, Piramal Critical Care Deutschland GmbH, Halbergmoss, Germany) under stable oxygen supply (1.0–1.2 L/min). Then a volume of 5 µL of the appropriate substance was applied to the infected eye. A two-minute incubation period followed. The animal was finally reawakened by isoflurane-removal. Four treatment groups were created. The sham treatment group was applied phosphate buffered saline containing 1% DMSO. The meropenem treatment group was applied a 0.9% NaCl solution containing 500 µg meropenem/mL and 1% DMSO. The LasB-inhibitor treatment group was applied a 0.9% NaCl solution containing 1 mg LasB-inhibitor/mL and 1% DMSO. The combination treatment group was applied a 0.9% NaCl solution containing 1 mg LasB-inhibitor/mL, 500 µg meropenem/mL, and 1% DMSO.

Animal Sacrifice: Laboratory animals were sacrificed by intraperitoneal injection of ketamine hydrochloride/xylazine hydrochloride (Ursotamine, 100 mg/mL, Serumwerk Bernburg AG, Germany; Rompun 2%, xylazine, 25 ml, Bayer AG) at a dose of 20 mg/kg body weight three days after infection. The vena cava served was punctured to collect blood. Anticoagulation was achieved by Ca^{2+}-deprivation using a drop of 0.5 M ethylenediaminetetraacetic acid (EDTA). The right and initially infected eye was removed by incising the surrounding skin if necessary.

Eye Homogenization: The removed eyes were homogenized using a POLYTRON PT 1200 E dispenser (Kinematika AG, Lucerne, Switzerland). To avoid bacterial carry-over, the eyes were cleaned with distilled water, 70% ethanol and 0.9% NaCl solution, respectively.

Microbiological Evaluation: Serial dilutions were plated on blood agar for microbiological evaluation of the homogenates. A blood stripe also incubated on blood agar served as a control for potential systemic spread of the pathogen. In both cases, counting was performed after 18h of incubation at 37°C.

Flow Cytometry: The eye homogenates, upon receipt, were sieved using a 70 µm cell filter (Falcon, Corning) to prepare a single cell suspension. Total cell count and cell viability were determined using a NucleoCounter® NC-200™ (Chemomatec, Kaiserslautern, Germany). Single cell suspensions were fixed using 1% paraformaldehyde, centrifuged, and resuspended in FACS buffer (0.1mM EDTA plus 1% fetal bovine serum in PBS). CD16/CD32 antibodies were then added to the samples and incubated at 4 °C for 40 min to block Fc receptors. The surface markers were stained using the following fluorescent dye-conjugated antibodies:

F4/80-PE (clone BM8), CD45- APC (clone 30-F11), CD11b-FITC (clone M1/70), CD11c APC-Cy7 (clone N418), Ly6G PE-Cy7 (1A8-Ly6g), and NK1.1-PerCP-Cy5.5 (clone PK136) (Biolegend, Amsterdam, Netherlands) and incubated at 4 °C for 45 min. The blood samples were first mixed with an ACK-Lysis Buffer (Thermo Fisher Scientific, Braunschweig, Germany) for 20 min. The lysis was terminated in time by adding DPBS. Centrifugation was used to selectively collect the leukocytes. Total cell count estimation and surface marker staining were performed as described above for the eye samples. The BD FACSverse Cell analyzer machine was used for flow cytometry analysis, whereas the resulting data were analyzed using FlowJo Software **(**Version 10.6.2; Becton, Dickinson, and Company (BD), Heidelberg, Germany**).**

Enzyme-linked Immunoadsorption Assay (ELISA): After centrifugation of the homogenates at 2500 g and 4 °C for 10 min, the cell-free suspension was frozen at –70 °C. Quantification of mKC, mTNF-α, mMPO and mIL-1β in the centrifuged homogenate was performed using R&D ELISA kits according to the manufacturer's protocol. Briefly, 96-well microplates were coated with the respective capture antibody and incubated at rt overnight. The following day, the wells were blocked with reagent diluent (1% BSA solution) for 2h, incubated with the samples for 2h, incubated with the detection antibody for 2h and finally incubated with streptavidin-HRP for 20 min. The reaction was started by adding the BM Blue POD substrate solution and stopped after 20 min with 2N H_2SO_4. The absorbance was measured at 450 nm. A serially diluted standard was used in parallel to calculate the concentration of each protein.

Statistical Analysis: Statistical analysis was performed using the GraphPad Prism Software Package (Version 10.0.2). Pairwise comparison for connected and not-connected samples was done with the non-parametric Mann-Whitney *U* test and with the Wilcoxon-signed-rank-test respectively. The non-parametric Friedman test was employed for multiple comparisons for connected samples. The *P*-value was two-sided and considered statistically significant when < 0.05.

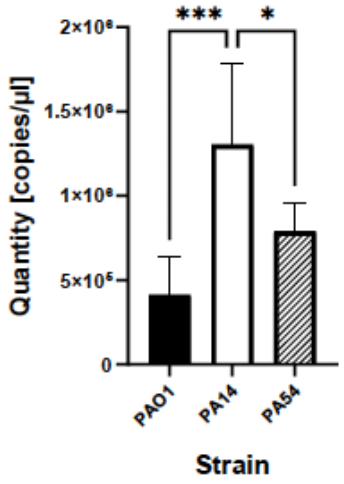

Figure S13: Gene expression analysis of *lasB* in *Pseudomonas aeruginosa* strains PAO1, PA14, and PA54 cultivated in LB medium. Absolute quantification of *lasB* expression in using the standard curve method. These results represent the average of 3 independent experiments ± SD. The ordinary one-way ANOVA was performed, comparing the mean values of PAO1 and PA54 with the highly virulent isolate PA14. (ns = not significant, * = $p \leq 0.05$, *** = $p \leq 0.001$). Data were plotted using GraphPad Prism 9.

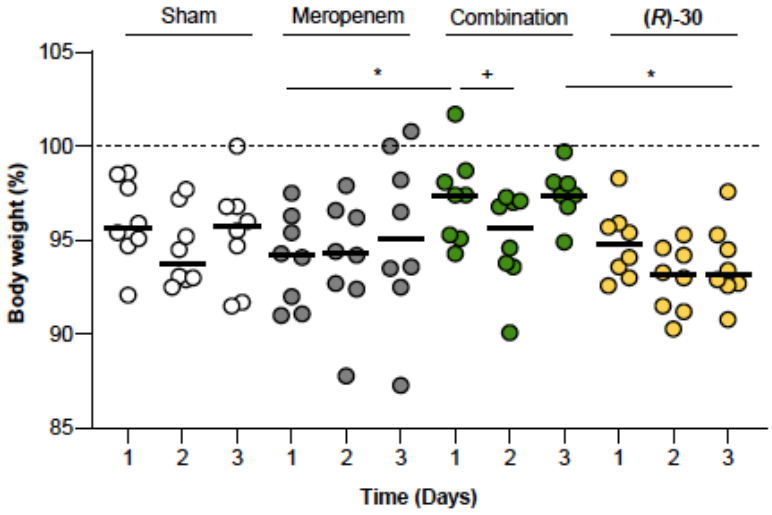

Figure S14: Impact of the PA54 corneal infection and treatment on the body weight over time. Percentages (%) are the percentage of the initial body weight. Aged mice (n = 8 per group) were infected with PA strain PA54 and treated for every 8 h with the treatment indicated for up to 72 h. Data represent the values of every individual animal (symbols) and the median (horizontal line). *, $P < 0.05$ (Mann-Whitney U test between two independent groups) +, $P < 0.05$ (Wilcoxon signed-rank test between different time points within a group).

3.15 Bioanalytical sample preparation of keratitis samples for determination of concentration of (*R*)-30 in eye and serum

All PD serum and eye homogenate samples were analyzed via HPLC-MS/MS using an Agilent 1290 Infinity II HPLC system and coupled to an AB Sciex QTrap6500+ mass spectrometer. First, a calibration curve was prepared by spiking different concentrations of **(*R*)-30** into the respective matrix (mouse serum (pooled, from CD-1 mice) for plasma samples, isotonic sodium chloride solution for eye homogenate samples). Caffeine was used as an internal standard. In addition, quality control samples (QCs) were prepared for **(*R*)-30** with the respective matrix. The following extraction procedure was used: 7.5 µL of a serum sample (calibration samples, QCs or PD samples) was extracted with 37.5 µL of methanol containing 12.5 ng/mL of caffeine as internal standard for 5 min at 2,000 rpm on an Eppendorf MixMate® vortex mixer. Then samples (serum) were spun down at 13,000 rpm for 5 min. Supernatants were transferred to standard HPLC-glass vials. 50 µL of an eye homogenate sample (calibration samples, QCs or PD samples) were extracted with 50 µL of methanol and 1 µL caffeine (concentration 1 µg/mL in methanol) for 5 min at 800 rpm on an Eppendorf MixMate® vortex mixer. Then samples (eye homogenate) were spun down at 4,000 rpm for 40 min at 4 °C. Supernatants were transferred to 96well V-bottom plates (Greiner). HPLC conditions were as follows: column: Agilent Zorbax Eclipse Plus C18, 50x2.1 mm, 1.8 µm; temperature: 30 °C; injection volume: 5 µL; flow rate: 700 µL/min; solvent A: water + 0.1% formic acid; solvent B: acetonitrile + 0.1% formic acid; gradient: 99% A at 0 min and until 1 min, 99% – 0% A from 1.0 min to 2.2 min, 0% A until 4 min. Mass spectrometric conditions were as follows: Scan type: MRM, negative and positive mode; Q1 and Q3 masses for caffeine and **(*R*)-30** can be found in table S5 shown above. Peak areas of each sample and of the corresponding internal standard were analyzed using MultiQuant 3.0 software (AB Sciex). Peak areas of the respective sample were normalized to the internal standard peak area. The MS/MS pairs used for quantification are marked with a 'Q' in the table, the other MS/MS pairs for the respective compound were used for qualification. Peaks of PD samples were quantified using the calibration curve. The accuracy of the calibration curve was determined using QCs independently prepared on different days.

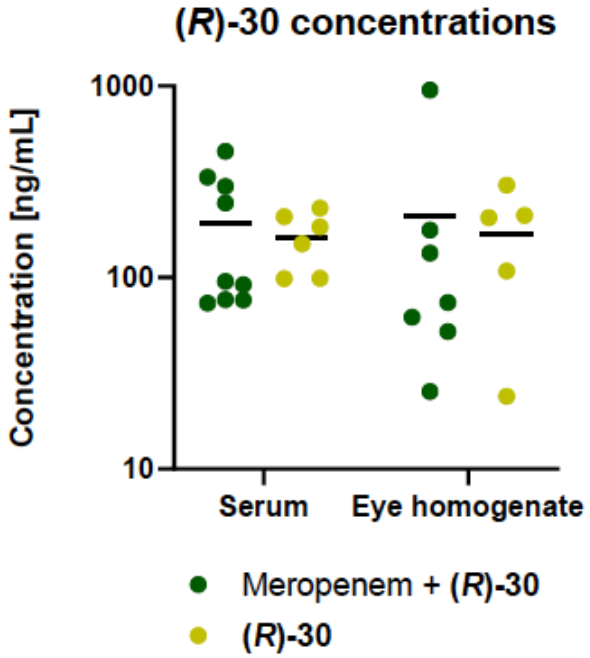

Figure S15: MS-based quantification of (*R*)-30 levels in serum and eye homogenate. Concentrations were determined after single treatment ((R)-30 alone) or after combination with Meropenem.

3.16 LabB-KC studies

To test whether KC might be a substrate for LasB, an ELISA was used to quantify KC levels after co-incubation with LasB. Briefly, 500 pg/ml of the recombinant murine KC standard (R&D part 840327) was incubated for 10 minutes in PBS supplemented with 1% BSA and 0.1% DMSO (vehicle control), LasB (100 nM), **(*R*)-30** (100 µM), or a combination of both. Detection of KC and absorbance measurements were performed as described above (3.11).

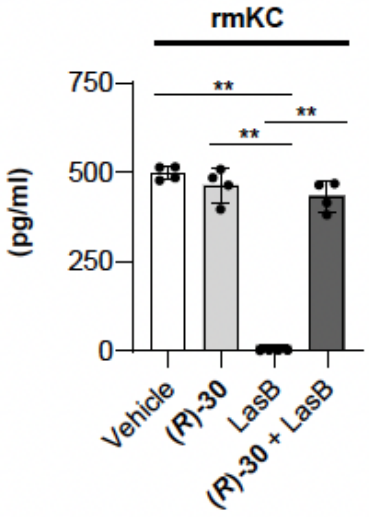

Figure S16: Impact of LasB and **(*R*)-30** on KC stability. 500 pg aliquots of recombinant murine KC (rmKC) were dissolved in PBS supplemented with 1% BSA and 0.1% DMSO and coincubated for 10 min with **(*R*)-30** (100 µM; light grey bar), LasB (100 nM; black bar) or a combination of both (dark grey bar), respectively. rmKC incubated in the solvent (PBS + 1% BSA + 0.1% DMSO) served as vehicle control. Integrity of rmKC was determined by ELISA using anti-mKC antibodies. Data shown represent the mean and SD of four replicates. **, $p < 0.01$ (Brown-Forsythe and Welch ANOVA test with Dunnett's T3 multiple comparison test).

3. Statistical Analysis

Statistics information for Figure 3

Figure	Subfigure	Comparison	Symbol in Figure	Pre-processing	Data presentation	Sample size	Statistical method	Testing level	Post-hoc test	Software
3	A	Identical timepoints between groups: Comparison of the mean of each column with the mean of a control column (Sham-tretament, day 3)	°	no	Individual values and median	8	Ordinary one-way ANOVA	Alpha 0.05; Adjusted P value <0.05	Dunnett's multiple comparison test with a single pooled variance	GraphPad Prism (version 10.3.0)
3	A	Different timepoints within a group: Comparison of the mean of each column with the mean of a control column (day 1)	#	no	Individual values and median	8	RM one-way ANOVA with Geisser-Greenhouse correction	Alpha 0.05; Adjusted P value <0.05	Dunnett's multiple comparison test with individual variances computed for each comparison	GraphPad Prism (version 10.3.0)
3	B	Infected groups: Comparison of the mean of each column with the mean of a control column (Sham-treatment)	*	no	Individual values and median	8	Brown-Forsythe and Welch ANOVA test	Alpha 0.05; Adjusted P value <0.05	Dunnett's T3 multiple comparison test with individual variances computed for each comparison	GraphPad Prism (version 10.3.0)
3	B	All groups: Comparison of the mean of each column with the mean of a control column (Non-infected)	+	no	Individual values and median	8	Brown-Forsythe and Welch ANOVA test	Alpha 0.05; Adjusted P value <0.05	Dunnett's T3 multiple comparison test with individual variances computed for each comparison	GraphPad Prism (version 10.3.0)
3	C	Infected groups: Comparison of the mean of each column with the mean of a control column (Sham-treatment)	*	no	Individual values and median	8	Brown-Forsythe and Welch ANOVA test	Alpha 0.05; Adjusted P value <0.05	Dunnett's T3 multiple comparison test with individual variances computed for each comparison	GraphPad Prism (version 10.3.0)
3	C	All groups: Comparison of the mean of each column with the mean of a control column (Non-infected)	+	no	Individual values and median	8	Brown-Forsythe and Welch ANOVA test	Alpha 0.05; Adjusted P value <0.05	Dunnett's T3 multiple comparison test with individual variances computed for each comparison	GraphPad Prism (version 10.3.0)
3	D	Infected groups: Comparison of the mean of each column with the mean of a control column (Sham-treatment)	*	no	Individual values and median	6	Brown-Forsythe and Welch ANOVA test	Alpha 0.05; Adjusted P value <0.05	Dunnett's T3 multiple comparison test with individual variances computed for each comparison	GraphPad Prism (version 10.3.0)
3	D	All groups: Comparison of the mean of each column with the mean of a control column (Non-infected)	+	no	Individual values and median	6	Brown-Forsythe and Welch ANOVA test	Alpha 0.05; Adjusted P value <0.05	Dunnett's T3 multiple comparison test with individual variances computed for each comparison	GraphPad Prism (version 10.3.0)
3	E	Infected groups: Comparison of the mean of each column with the mean of a control column (Sham-treatment)	*	no	Individual values and median	6	Brown-Forsythe and Welch ANOVA test	Alpha 0.05; Adjusted P value <0.05	Dunnett's T3 multiple comparison test with individual variances computed for each comparison	GraphPad Prism (version 10.3.0)
3	E	All groups: Comparison of the mean of each column with the mean of a control column (Non-infected)	+	no	Individual values and median	6	Brown-Forsythe and Welch ANOVA test	Alpha 0.05; Adjusted P value <0.05	Dunnett's T3 multiple comparison test with individual variances computed for each comparison	GraphPad Prism (version 10.3.0)
3	F	Infected groups: Comparison of the mean of each column with the mean of a control column (sham-treatment)	*	no	Individual values and median	6	Brown-Forsythe and Welch ANOVA test	Alpha 0.05; Adjusted P value <0.05	Dunnett's T3 multiple comparison test with individual variances computed for each comparison	GraphPad Prism (version 10.3.0)
3	F	All groups: Comparison of the mean of each column with the mean of a control column (Non-infected)	+	no	Individual values and median	6	Brown-Forsythe and Welch ANOVA test	Alpha 0.05; Adjusted P value <0.05	Dunnett's T3 multiple comparison test with individual variances computed for each comparison	GraphPad Prism (version 10.3.0)
3	G	Infected groups: Comparison of the mean of each column with the mean of a control column (Sham-treatment)	*	no	Individual values and median	6	Brown-Forsythe and Welch ANOVA test	Alpha 0.05; Adjusted P value <0.05	Dunnett's T3 multiple comparison test with individual variances computed for each comparison	GraphPad Prism (version 10.3.0)
3	G	All groups: Comparison of the mean of each column with the mean of a control column (Non-infected)	+	no	Individual values and median	6	Brown-Forsythe and Welch ANOVA test	Alpha 0.05; Adjusted P value <0.05	Dunnett's T3 multiple comparison test with individual variances computed for each comparison	GraphPad Prism (version 10.3.0)

4. References

[1] E. Badiola, B. Fiser, E. Gómez-Bengoa, A. Mielgo, I. Olaizola, I. Urruzuno, J. M. García, J. M. Odriozola, J. Razkin, M. Oiarbide et al., *Journal of the American Chemical Society* **2014**, *136*, 17869.

[2] P. van der Veken, I. El Sayed, J. Joossens, C. Stevens, K. Augustyns, A. Haemers, *Synthesis* **2005**, *2005*, 634.

[3] A. M. Kany, A. Sikandar, J. Haupenthal, S. Yahiaoui, C. K. Maurer, E. Proschak, J. Köhnke, R. W. Hartmann, *ACS infectious diseases* **2018**, *4*, 988.

[4] D. Kolling, J. Haupenthal, A. K. H. Hirsch, J. Koehnke, *Chembiochem : a European journal of chemical biology* **2023**, *24*, e202300185.

[5] A. Burkhardt, T. Pakendorf, B. Reime, J. Meyer, P. Fischer, N. Stübe, S. Panneerselvam, O. Lorbeer, K. Stachnik, M. Warmer et al., *Eur. Phys. J. Plus* **2016**, *131*, 56.

[6] a) P. Evans, *Acta crystallographica. Section D, Biological crystallography* **2006**, *62*, 72; b) P. R. Evans, *Acta crystallographica. Section D, Biological crystallography* **2011**, *67*, 282; c) A. J. McCoy, R. W. Grosse-Kunstleve, P. D. Adams, M. D. Winn, L. C. Storoni, R. J. Read, *Journal of applied crystallography* **2007**, *40*, 658.

[7] a) A. M. Kany, A. Sikandar, S. Yahiaoui, J. Haupenthal, I. Walter, M. Empting, J. Köhnke, R. W. Hartmann, *ACS chemical biology* **2018**, *13*, 2449; b) M. M. Thayer, K. M. Flaherty, D. B. McKay, *Journal of Biological Chemistry* **1991**, *266*, 2864.

[8] a) P. Emsley, B. Lohkamp, W. G. Scott, K. Cowtan, *Acta crystallographica. Section D, Biological crystallography* **2010**, *66*, 486; b) P. D. Adams, P. V. Afonine, G. Bunkóczi, V. B. Chen, I. W. Davis, N. Echols, J. J. Headd, L.-W. Hung, G. J. Kapral, R. W. Grosse-Kunstleve et al., *Acta crystallographica. Section D, Biological crystallography* **2010**, *66*, 213.

[9] R. A. Laskowski, M. B. Swindells, *Journal of chemical information and modeling* **2011**, *51*, 2778.

[10] J. Konstantinović, A. M. Kany, A. Alhayek, A. S. Abdelsamie, A. Sikandar, K. Voos, Y. Yao, A. Andreas, R. Shafiei, B. Loretz et al., *ACS central science* **2023**, *9*, 2205.

[11] Y. Zhang, M. Huo, J. Zhou, S. Xie, *Computer methods and programs in biomedicine* **2010**, *99*, 306.

[12] S. Kiem, J. J. Schentag, *Antimicrobial agents and chemotherapy* **2008**, *52*, 24.

[13] Eurofins, "Safety Screen44 Panel", can be found under https://www.eurofinsdiscovery.com/catalog/safetyscreen44-panel-tw/PP241.

[14] J. Haupenthal, C. Baehr, S. Zeuzem, A. Piiper, *International journal of cancer* **2007**, *121*, 206.

[15] J. Maes, L. Verlooy, O. E. Buenafe, P. A. M. de Witte, C. V. Esguerra, A. D. Crawford, *PloS one* **2012**, *7*, e43850.

[16] J. Konstantinović, S. Yahiaoui, A. Alhayek, J. Haupenthal, E. Schönauer, A. Andreas, A. M. Kany, R. Müller, J. Koehnke, F. K. Berger et al., *Journal of medicinal chemistry* **2020**, *63*, 8359.

[17] H. Ceri, M. E. Olson, C. Stremick, R. R. Read, D. Morck, A. Buret, *Journal of clinical microbiology* **1999**, *37*, 1771.

[18] A.-P. Magiorakos, A. Srinivasan, R. B. Carey, Y. Carmeli, M. E. Falagas, C. G. Giske, S. Harbarth, J. F. Hindler, G. Kahlmeter, B. Olsson-Liljequist et al., *Clinical microbiology and infection : the official publication of the European Society of Clinical Microbiology and Infectious Diseases* **2012**, *18*, 268.

[19] C. N. Englisch, N. A. Wadood, L. Pätzold, A. Gallagher, G. Krasteva-Christ, S. L. Becker, M. Bischoff, *Annals of anatomy = Anatomischer Anzeiger : official organ of the Anatomische Gesellschaft* **2023**, *249*, 152099.

2.3 Chapter C

Dual inhibitors of *Pseudomonas aeruginosa* virulence factors LecA and LasB

*Olga Metelkina ‡, Jelena Konstantinovi´c ‡, Andreas Klein, **Roya Shafiei**, Mario Fares, Alaa Alhayek, Samir Yahiaoui, Walid A. M. Elgaher, Jörg Haupenthal, Alexander Titz, and Anna K. H. Hirsch.*

‡these authors contributed equally

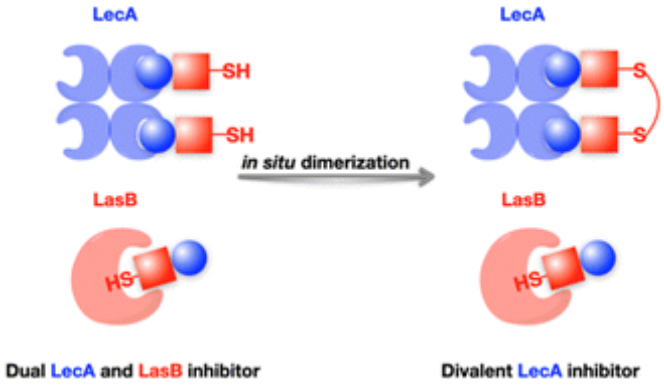

Open access article, *Chemical Science* **2024**, 15, 13333-13342

DOI: 10.1039/D4SC02703E

Chemical Science

ROYAL SOCIETY OF CHEMISTRY

EDGE ARTICLE

View Article Online
View Journal

Cite this: DOI: 10.1039/d4sc02703e

All publication charges for this article have been paid for by the Royal Society of Chemistry

Received 23rd April 2024
Accepted 11th July 2024

DOI: 10.1039/d4sc02703e

rsc.li/chemical-science

Dual inhibitors of *Pseudomonas aeruginosa* virulence factors LecA and LasB†

Olga Metelkina, ‡[abc] Jelena Konstantinović, ‡[a] Andreas Klein,[ad] Roya Shafiei,[ad] Mario Fares,[abc] Alaa Alhayek,[a] Samir Yahiaoui,[a] Walid A. M. Elgaher,[a] Jörg Haupenthal,[a] Alexander Titz *[abc] and Anna K. H. Hirsch *[abd]

Dual inhibitors of two key virulence factors of *Pseudomonas aeruginosa*, the lectin LecA and the protease LasB, open up an opportunity in the current antimicrobial-resistance crisis. A molecular hybridization approach enabled the discovery of potent, selective, and non-toxic thiol-based inhibitors, which simultaneously inhibit these two major extracellular virulence factors and therefore synergistically interfere with virulence. We further demonstrated that the dimerization of these monovalent dual inhibitors under physiological conditions affords divalent inhibitors of LecA with a 200-fold increase in binding affinity. The bifunctional LecA/LasB-blocker **12** showed superiority for the inhibition of virulence mediated by both targets over the individual inhibitors or combinations thereof *in vitro*. Our study sets the stage for a systematic exploration of dual inhibitors as pathoblockers for a more effective treatment of *P. aeruginosa* infections and the concept can certainly be extended to other targets and pathogens.

Introduction

Bacterial resistance to antibiotics is a growing global health problem that urgently requires a solution.[1] Disarming pathogens by targeting bacterial virulence factors has emerged as a new approach to fighting drug-resistant infections.[2–5] Bacterial virulence factors such as toxins, adhesins, invasins, and quorum-sensing molecules play crucial roles in host colonization and infection promotion by suppressing the host immune defense.[6,7] Reducing bacterial virulence *via* the inhibition of these factors also decreases the host's susceptibility to infection and allows the immune system to eliminate bacteria. Moreover, the inhibition of bacterial virulence factors mechanistically reduces the selection pressure for resistant mutants due to the ability of pathoblockers to disarm the pathogens without direct killing.[3,4]

Pseudomonas aeruginosa is a Gram-negative bacterium that is classified as critical on the WHO pathogen priority list and currently, numerous avenues of research are being explored in parallel to identify new therapeutics against this pathogen.[8,9]

Extracellular elastase LasB is a zinc-metalloprotease produced by *P. aeruginosa* and one of its pivotal virulence factors. Its importance for the overall pathogenicity of *P. aeruginosa* has been established and it is considered a valid drug target.[10] The role of LasB in degrading the components of the connective tissue such as elastin and extracellular matrix components (ECMs, *e.g.*, collagen and laminin) facilitates host colonization.[11,12] Besides this, LasB plays an important role in disrupting the host immune system through the degradation of immunoglobulins, cytokines and other immune factors.[13,14] LasB is also known for hydrolyzing blood proteins, such as transferrin and lactoferrin, consequently leading to free-radical-induced cytotoxicity.[15,16] In addition to the host substrates, LasB participates in the processing and activation of other bacterial components (LasA, leucine aminopeptidase, lysine endopeptidase and others), promoting the inflammation process.[17–19]

Another virulence factor, lectin LecA (PA-IL), is an extracellular galactophilic carbohydrate-binding protein expressed by *P. aeruginosa*, which mediates biofilm matrix formation and host colonization.[20,21] It is responsible for bacterial adhesion interacting with the glycocalyx of mammalian cells.[22,23] LecA also attenuates ciliary beating in human airways, preventing mucus clearance and inhibiting the growth of respiratory epithelial cells.[21,24,25] On a molecular level, this lectin was shown to mediate bacterial uptake in a lipid zipper mechanism by binding to host glycolipids presented on its cell surfaces.[26] Additionally, LecA enhances host cellular absorption of another virulence factor, exotoxin A, inducing a pathogenic effect on the intestinal epithelium and it increases the injury of the alveolar capillary barrier.[26,27] It has been demonstrated that the

[a]Helmholtz Institute for Pharmaceutical Research Saarland (HIPS), Helmholtz Centre for Infection Research (HZI), Campus E8.1, 66123 Saarbrücken, Germany. E-mail: alexander.titz@helmholtz-hips.de; anna.hirsch@helmholtz-hips.de

[b]Deutsches Zentrum für Infektionsforschung (DZIF), Standort Hannover – Braunschweig, 38124 Braunschweig, Germany

[c]Department of Chemistry, Saarland University, 66123 Saarbrücken, Germany

[d]Department of Pharmacy, Saarland University, 66123 Saarbrücken, Germany

† Electronic supplementary information (ESI) available. See DOI: https://doi.org/10.1039/d4sc02703e

‡ These authors contributed equally.

inhibition of LecA reduces biofilm formation and the overall virulence of *P. aeruginosa*.[20] Glycomimetics have the potential to act as promising pathoblockers.[28] To increase the efficacy of LecA inhibition and overcome its moderate micromolar affinity to galactosides caused by a shallow binding pocket, multivalent ligands are often utilized.[29–33]

The crucial effects of these two proteins on the infection progress make them validated and attractive therapeutic targets. Simultaneously targeting both LasB and LecA is compelling for multiple reasons. The extracellular co-localization of LasB and LecA overcomes the major hurdle for many therapeutic molecules to penetrate the Gram-negative cell wall. Furthermore, the dual inhibitors can increase drug efficacy in comparison to combination therapy when the two separate therapeutic molecules are applied together.[34] It is expected that a single drug acting on multiple targets possesses more predictable pharmacokinetic and safety profiles, lowers the probability of resistance development and avoids undesirable drug–drug interactions.[34]

In this work, we have chosen established inhibitors of LasB and LecA based on α-isobutyl/benzyl-*N*-aryl-mercaptoacetamide and phenyl β-D-galactoside, respectively, and merged them into one molecule that blocked LecA and LasB with moderate to high potency.[9,35–37,41] In addition, by utilizing the inherently limited chemical stability of thiols and their tendency to form disulfides in an extracellular environment, highly potent divalent LecA-inhibitors were obtained. These disulfides are likely to be formed in the infection setting after saturating LasB *in situ*, yielding highly potent inhibitors of the second virulence factor LecA.

Results and discussion

Design of dual inhibitors

To develop dual inhibitors against *P. aeruginosa* virulence factors LasB and LecA, we selected previously developed thiol-based LasB ligands, which demonstrated high potency but also limited chemical stability due to their tendency to dimerize to disulfides under physiological conditions.[37] It is known that the moderate micromolar potency of galactosides as LecA inhibitors can be significantly improved by utilizing divalent ligands, where two carbohydrate molecules are bridged with a linker to simultaneously bind to two sites in the LecA tetramer.[29,31,33,38] Taking these facts into account, we combined nitrophenyl β-D-thiogalactoside **1** as a LecA inhibitor with the *N*-aryl-mercaptoacetamide-based LasB inhibitors **2** and **3** by merging their aryl moieties into dual inhibitors **11**, **12**, **17**, **18**, **24** and **25** (Fig. 1).[37,39–41] The resulting compounds should be capable of efficiently inhibiting LasB in the initial thiol form, while the dimerization of excess ligand under physiological conditions at the infection site transforms them from moderately monovalent into more potent divalent LecA inhibitors.

Our previously reported crystal structure of thiol **3** in complex with LasB suggested potential for further elongation of the molecule in the direction of the aniline ring (Fig. 2A).[37] At the same time, the co-crystal structure of LecA with **1** showed the opportunity to modify the nitro group in the *para*-position of the phenyl ring without disturbing the crucial interaction of the sugar moiety in the binding pocket (Fig. 2B),[45] which is backed by reported structure–activity relationships.[36,40,42,43] In our hybridized molecules, the thiol group should maintain its crucial coordination to the zinc ion in the active site of LasB, while the galactoside will conserve the calcium(II) chelation with its 3- and 4-hydroxy groups and the T-shaped CH–π interactions between the phenyl aglycon and His50 in the binding site of LecA.[40,44]

Further, we have shown that *N*-arylmercaptoacetamides have moderate redox stability and tend to oxidize to disulfides under physiological conditions.[46] This drawback may offer a significant advantage for the inhibition of LecA, that is, multivalent interactions are among the most efficient ways invented by nature to enhance the lectin–carbohydrate interaction.[47,48] Therefore, we speculated that the designed compounds will first inhibit LasB as thiols, while their excess at the site of infection inevitably dimerizes to give divalent galactosides with an enhancement in LecA binding affinity.

Synthesis of dual LecA/LasB inhibitors

As a first step, we synthesized glycomimetic thiols **11** and **12** in the form of diastereomeric mixtures (Scheme 1A). 4-Nitrothiophenol was glycosylated with β-D-galactose pentaacetate (**4**) using triflic acid as a catalyst to give β-thioglycoside **5** in 66% yield. The reduction of the nitro group to aniline derivative **6** using Pd/C-catalyzed hydrogenation was followed by amide coupling with racemic 2-bromo-4-methylpentanoic acid or 2-bromo-3-phenylpropanoic acid, which afforded compounds **7** and **8** in 86% and 74% yield, respectively. Bromides **7** and **8** were converted into thioacetates **9** and **10** *via* nucleophilic substitution with potassium thioacetate in good yields. The subsequent deprotection under Zemplén conditions with sodium methoxide in methanol furnished thiols **11** and **12** in 43% and 60% yield, respectively.

To investigate whether stereochemistry has an impact on the activity, we synthesized two pairs of diastereomers, utilizing enantiomerically pure starting materials (Scheme 1B). In the case of compounds **17**, **18** and **24**, the corresponding α-bromo carboxylic acids with inverse stereochemistry were used. In the case of **25**, the synthesis started from D-leucine affording (*R*)-2-bromo-4-methylpentanoic acid (**19′**) in quantitative yield, based on the work of Izumiya and Nagamatsu.[49–51] The four derivatives were obtained following the procedures described for the diastereomeric mixtures (Scheme 1).

For the α-benzyl derivatives **17** and **24**, the high degree of diastereomeric purity has been conserved during the three-step reaction cascade, as evidenced by the comparison of the NMR signals corresponding to the anomeric carbon atoms in the ^{13}C NMR spectra of the diastereomeric mixture **11** and the separate diastereomers. Diastereomeric mixture **11** showed two signals at 88.27 and 88.23 ppm, corresponding to the anomeric carbon atoms of the two diastereomers, while **17** and **24** demonstrated one single signal each with a 0.04 ppm difference in chemical shifts (ESI†). The anomeric carbon atom in diastereomeric mixture **12** and in both isomers **18** and **25** appears as a single

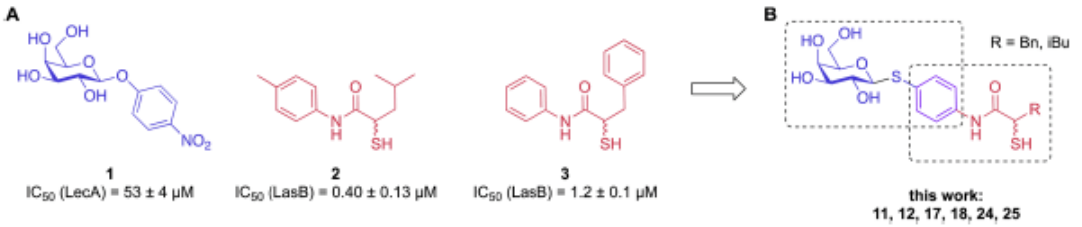

Fig. 1 (A) Reported LecA and LasB inhibitors **1**–**3** and (B) their combination into dual inhibitors.

signal at 88.3 ppm, due to the smaller and/or more flexible isobutyl substituent (ESI†).

The tendency of thiols to form disulfides in an oxidative environment suggests that our monovalent inhibitors will dimerize *in situ* over time, forming structures that can serve as divalent LecA inhibitors with enhanced potency against LecA. Disulfide formation in the presence of *P. aeruginosa* culture supernatant was studied for the two inhibitors **11** and **12** and analyzed by liquid chromatography-mass spectrometry (LC-MS) (Fig. 3B). Disulfides **26** and **27** were synthesized *via* oxidation with H_2O_2 in DMSO/H_2O and used as reference compounds for the stability assay (Fig. 3A). For both, **26** (Bn) and **27** (*i*Bu), we observed two closely eluting substances with identical mass by LC-MS, suggesting that different diastereomers were formed. The separation of those two peaks of the benzylated derivative **26** using preparative HPLC gave **26a** and **26b** (*m*/*z* of 901.28, Fig. S1†).

In the presence of the bacterial culture supernatant of *P. aeruginosa*, the conversion of thiols **11** and **12** into the corresponding disulfides **26** and **27** was monitored at 37 °C and thiol half-lives of 48 min for **11** and 70 min for **12** were determined (Fig. 3B). The kinetics to convert the thiols to the corresponding disulfides allows **11** and **12** to first act as LecA and LasB dual inhibitors and to transform over time into more potent divalent inhibitors of LecA, **26** and **27** (Fig. 3).

Activity against antivirulence targets LecA and LasB

We next evaluated the six synthesized thiol derivatives **11**, **12**, **17**, **18**, **24** and **25** for their inhibitory activity against both LecA and LasB. In addition, we determined the inhibitory activity of disulfides **26** and **27** on LecA but not on LasB as the essential thiol for coordination to the zinc ion is absent, leading to an expected loss in inhibitory activity.

The LasB activity of the thiol derivatives **11**, **12**, **17**, **18**, **24** and **25** was tested using a functional FRET-based *in vitro* proteolysis assay (Fig. 4A). Both α-isobutyl and α-benzyl derivatives demonstrated inhibitory activity against LasB in the same range as the previously observed activities of compounds **2** and **3** (IC_{50} = 0.40 and 1.2 μM, respectively).[37,41] Interestingly, α-benzyl derivative **11** (IC_{50} = 0.30 μM) showed a four-fold improvement in activity compared to **3**. α-Isobutyl derivative **12** (IC_{50} = 0.80 μM) proved to be somewhat less potent than the α-benzyl **11**, and its diastereomer with (*R*)-configuration on the right-hand side of molecule **18** showed a slightly lower IC_{50} of 0.51 μM compared to its (*S*)-isomer (**25**, IC_{50} = 0.77 μM). On the other hand, the (*S*)-isomer **24** (IC_{50} = 0.22 μM) proved to be three-fold more potent compared to the (*R*)-isomer **17** (IC_{50} = 0.73 μM) among the α-benzylated series.

The four thiols **17**, **18**, **24** and **25** as well as three disulfides **26a**, **26b** and **27** were then evaluated for their activity against LecA using a competitive binding assay based on fluorescence polarization (Fig. 4B). The IC_{50} values obtained for LecA inhibition suggested that the addition of the LasB-inhibiting moiety has a positive effect on the affinity towards LecA, decreasing the IC_{50} more than two-fold, from 52.5 μM for **1** to 18.1 μM and 19.8 μM for **11** and **12**, respectively. The substitution of the isobutyl residue with a benzyl group did not affect the affinity of disulfides in the LecA assay (IC_{50} = 4.7 μM and 3.0 μM for **26a** and **26b**, respectively, and IC_{50} = 5.7 μM for **27**), but had an impact

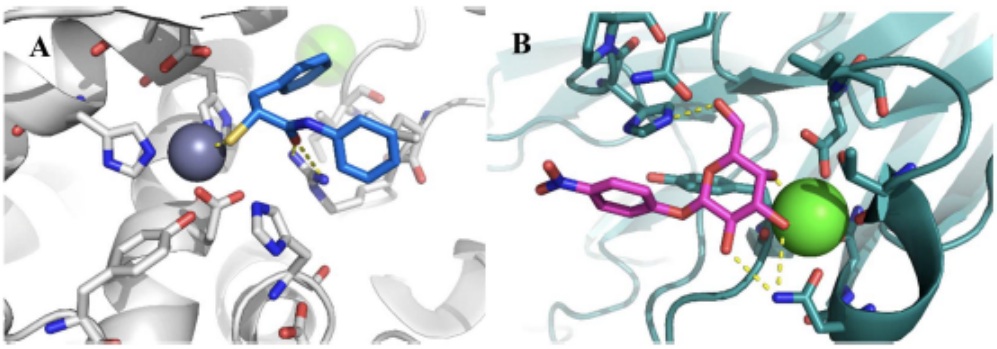

Fig. 2 A) Crystal structure of LasB (gray) in complex with **3** (cyan) (PDB code: 7OC7);[37] (B) crystal structure of LecA (petrol) in complex with **1** (magenta) (PDB code: 3ZYF).[45]

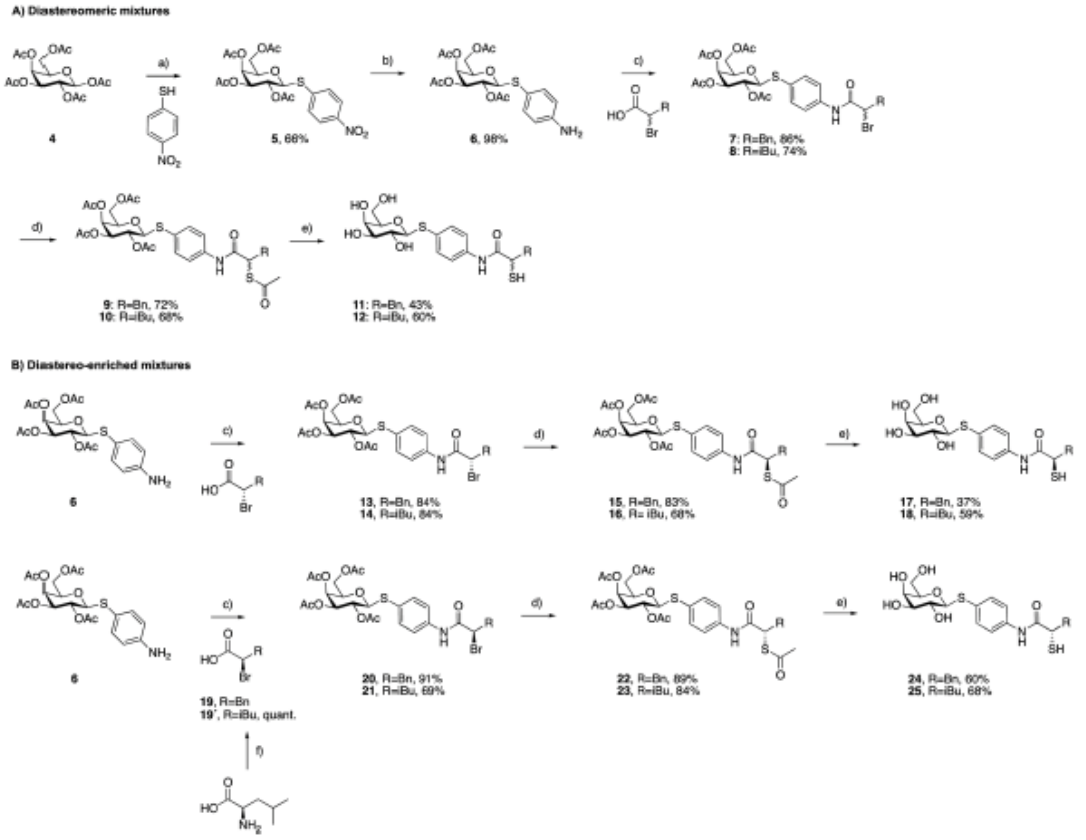

Scheme 1 Synthesis of LecA/LasB dual inhibitors. (a) TfOH, MS 3 Å, DCM, 0 °C, 30 min; (b) H_2, Pd/C, DCM, r.t., 18 h; (c) EDCxHCl, DCM, r.t., 4 h; (d) KSAc, acetone, r.t., 2 h; (e) NaOMe, MeOH, r.t., 45 min; (f) $NaNO_2$, 48% HBr, H_2O, 0 °C to r.t, 3 h.

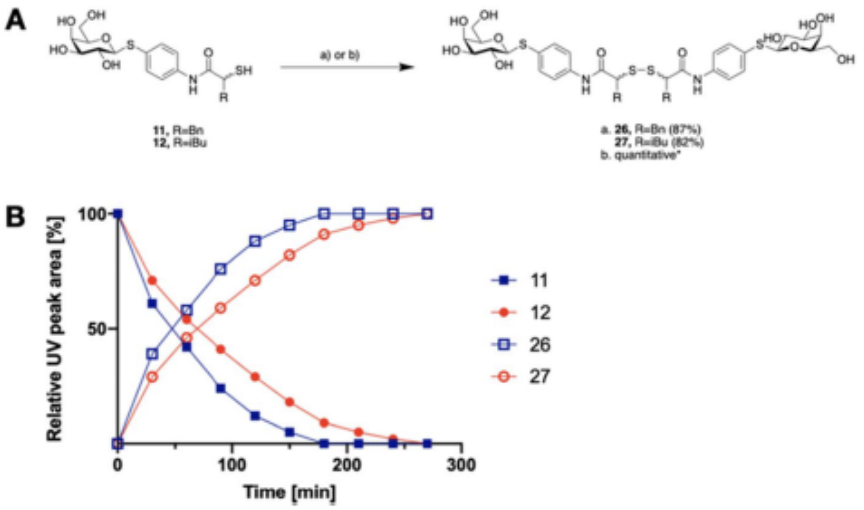

Fig. 3 A) Oxidative dimerization of thiols **11** and **12** into disulfides **26** and **27** using (a) H_2O_2, DMSO/H_2O or (b) *P. aeruginosa* culture supernatant (yield based on LC-MS); (B) dimerization kinetics of thiols **11** or **12** in the presence of *P. aeruginosa* culture supernatant into disulfides **26** or **27** analyzed by LC-MS.

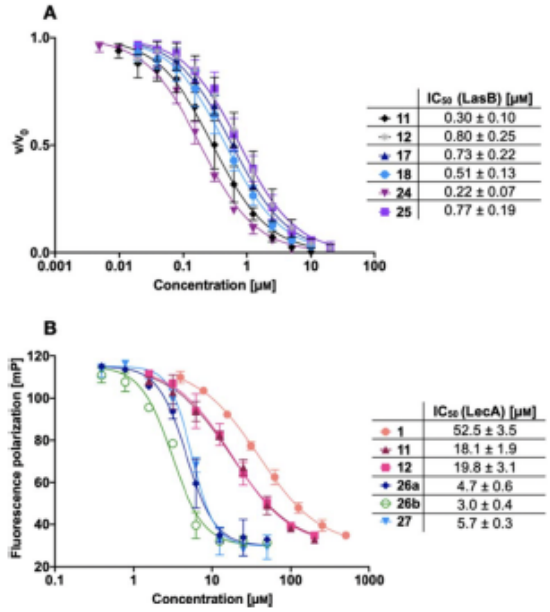

Fig. 4 A) Evaluation of LecA/LasB dual inhibitors by a FRET-based *in vitro* LasB inhibition assay; (B) evaluation of monomeric LecA/LasB inhibitors **11** and **12** and divalent LecA inhibitors **26a**, **26b** and **27** and comparison to the control pNP-Gal (**1**) by a competitive binding assay for LecA based on fluorescence polarization. IC_{50} values were calculated from at least three independent experiments performed in triplicate.

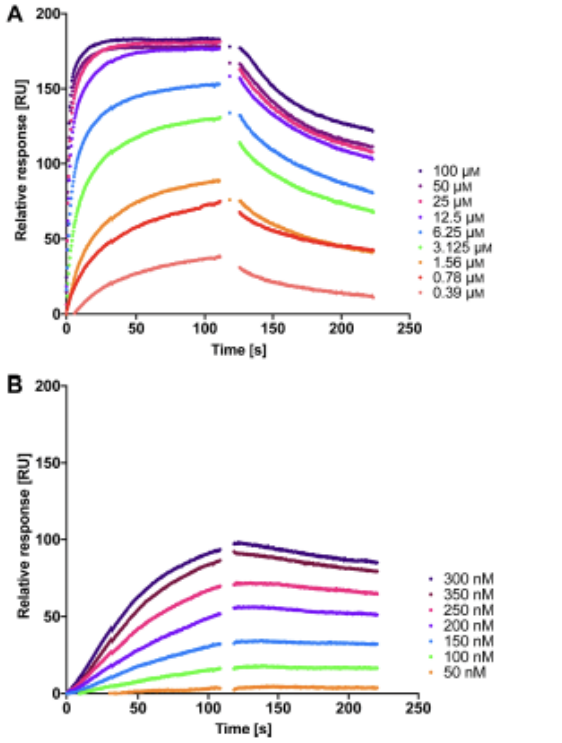

Fig. 5 The interaction of dual inhibitors thiol **17** (A) and disulfide **26a** (B) with LecA studied using SPR.

on the solubility of the corresponding disulfide. While isobutyl disulfide **27** showed a kinetic solubility >600 μM in 10 mm PBS with 2% DMSO at 37 °C, both benzyls **26a** and **26b** had a kinetic solubility of only 300 μM under the same conditions.

In this competitive binding assay, the observed affinity of the divalent LecA-inhibitors **26a**, **26b** and **27** increased more than three-fold compared to the corresponding thiols **11** and **12** (Fig. 4B). Considering the steep Hill slopes >2 of the fitted curves (Fig. 4B), we suspected that both divalent compounds approached the lower limit of the assay as observed before for inhibitors with significantly increased binding strength compared to the fluorescent primary ligand.[31,33]

Therefore, we measured the LecA affinity of thiol derivatives **17**, **18**, **24** and **25** and disulfides **26a**, **26b** and **27** using surface plasmon resonance (SPR) with LecA covalently immobilized on a sensor chip *via* amide coupling (Fig. 5 and Table 1). The data demonstrate a significant increase in the affinity of the divalent compounds for LecA. Based on the fitting of the kinetic binding curves, divalent compounds displayed an up to 200-fold increase in activity (K_D = 7.4 nM and 6.6 nM for **26a** and **26b**, respectively, and K_D = 4.5 nM for **27**) compared to their monovalent thiol analogues (K_D values = 1300 nM, 630 nM, 840 nM and 1000 nM for **17**, **18**, **24** and **25**, respectively), shifting K_D values from the low-micromolar to the single-digit nanomolar range (Fig. 5 and S3†). Thiols **17**, **18**, **24** and **25** reached equilibrium binding within 60 s of interaction with immobilized LecA, followed by their dissociation with moderate off-rates. In contrast, the disulfides demonstrated very slow association rates with an approximately 10-fold increase of k_a compared to the value for **1** (Table 1).[52] Due to the very small off-rates for **26a**, **26b** and **27**, these values have been calculated based on the response at 350 nm of the injected compound and monitoring their dissociation for 30 min (Fig. S2†). The observed very tight binding to immobilized LecA required optimization of the protein surface regeneration procedure. Effective conditions were identified as one injection of 50 mm isopropyl β-D-thiogalactoside in the running buffer, followed by one injection of 20 mm EDTA disodium salt in water. The

Table 1 Kinetic analysis of LecA/LasB inhibitors binding to immobilized LecA using SPR[a]

Compound	k_a [$\times 10^4$ M^{-1} s^{-1}]	k_d [$\times 10^{-4}$ s^{-1}]	K_D [nM]
1	0.40 ± 0.05	1000 ± 330	21 000 ± 4600
17	0.71 ± 0.14	86 ± 20	1300 ± 540
18	1.41 ± 0.47	82 ± 11	630 ± 290
24	0.88 ± 0.23	72 ± 5	840 ± 160
25	0.90 ± 0.31	85 ± 2	1000 ± 590
26a	3.8 ± 0.8	2.8 ± 0.3	7.4 ± 1.4
26b	4.6 ± 0.7	3.0 ± 1.2	6.6 ± 2.4
27	5.2 ± 0.6	2.2 ± 0.3	4.5 ± 0.4

[a] Mean values and standard deviations are from at least three independent experiments.

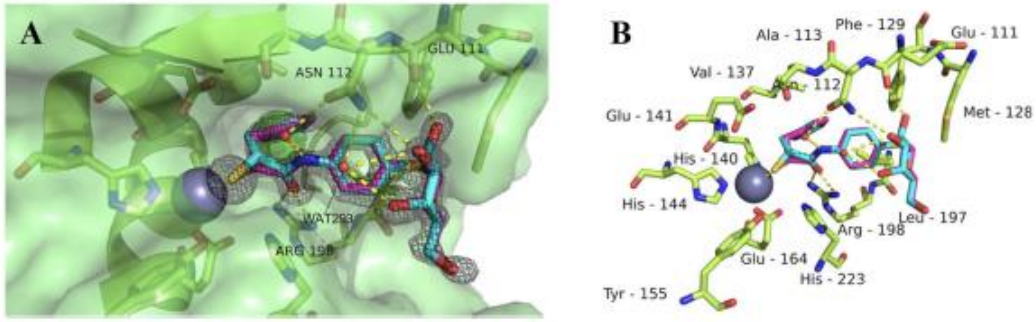

Fig. 6 Crystal structure of **11** in complex with LasB (PDB: 7Z68). (A) Cartoon representation of LasB with a transparent surface (green) and ligated **11** (cyan (*R*), pink (*S*)). The amino acids of LasB forming the binding site are represented as sticks. The gray isomesh represents the polder map of **11** contoured at 3σ. (B) Stick representation of the LasB binding site with bound **11**. Polar interactions between LasB and **11** are highlighted by dashed lines (color code: oxygen = red, nitrogen = blue, sulfur = yellow, and red spheres = water).

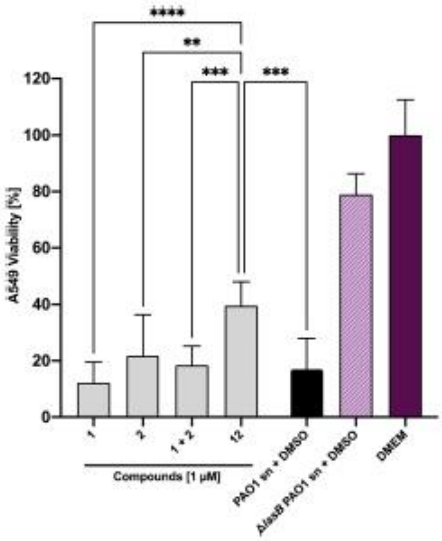

Fig. 7 Inhibition of the LasB-dependent cytotoxicity of *P. aeruginosa* PAO1 culture supernatant on human A549 cells. Effect of PAO1 supernatant in the absence (black bar) or presence (grey) of compounds **1**, **2**, **1** + **2** or **12**. The culture supernatant of the *lasB* knockout mutant (Δ*lasB* PAO1) was applied as a positive control (light purple). The viability of cells that were untreated (DMEM) served as a negative control and are shown in dark violet. The graphs represent the means of three independent experiments ± SD. One-way ANOVA statistical analysis was performed following Dunnett's multiple comparisons test, comparing the mean value of each concentration to the mean value of PAO1 without any treatment with compounds (***$p \leq 0.001$, **$p \leq 0.01$, and *$p \leq 0.05$).

regenerated chip surface was controlled using an injection of **1** to ensure that the activity of LecA was maintained.

Selectivity and toxicity profile of thiols 11 and 12

Given that the novel inhibitors contain a free thiol as a strong zinc binding group, we analyzed the selectivity of the diastereomeric mixtures **11** and **12** on six human matrix metalloproteases (MMPs) as putative off-targets.[53] The data obtained demonstrate selectivity of both compounds for the two intended targets over all six off-targets tested since less than 20% inhibition was observed at 100 µM (Table S1†). Furthermore, we tested the impact of **11** and **12** on bacterial viability to ensure that these compounds are antivirulence agents and not antibiotics. No antimicrobial activity was detected up to 100 µM (Table S2†). Finally, we evaluated the cytotoxicity of compounds **11** and **12** against three human cell lines, HepG2, HEK293, and A549, revealing no detectable cytotoxicity at 100 µM (Table S3†).

Having established the inhibitors' high potency on both antivirulence targets and outstanding toxicity and selectivity properties, we set off to determine the modes of interaction with their targets LecA and LasB at the molecular level. Unfortunately, crystals could not be obtained for LecA with the observable electron density of thiols or the very potent disulfides. The crystal structures of multivalent ligands with multivalent LecA are intrinsically difficult to obtain and only one example has been reported to date, which also displays only incomplete electron density of the ligand.[54]

Co-crystallization of thiol 11 with LasB

To get better insights into the binding mode and to understand the potency of the new inhibitors, we performed co-crystallization experiments with LasB, using the diastereomeric mixture of the α-benzylated analog **11**.

The LasB–**11** complex crystallized in the space group $P12_11$, and crystals diffracted to 1.5 Å resolution (Fig. 6 and Table S4†). The obtained electron density of the ligand in the active site of LasB suggests that the enzyme accommodates both (*R*)- and (*S*)-isomers of compound **11**. These data therefore explain why there is no stronger difference in the activities of the two isomers in the *in vitro* LasB assay ((*R*)-isomer **17** ($IC_{50} = 0.73$ µM) and (*S*)-isomer **24** ($IC_{50} = 0.22$ µM)).

As observed for previous crystal structures of thiols with LasB,[37,46] also here the thiol of **11** displaces the water molecule in the tetrahedral coordination sphere of the zinc ion in the binding site, leading to a sulfur–zinc distance of 2.3 Å. The carbonyl oxygen of **11** forms a hydrogen bond with the side chain of Arg198 (3.1 Å) in the active site, stabilizing the binding of the compound in the core region. The benzyl ring is placed in

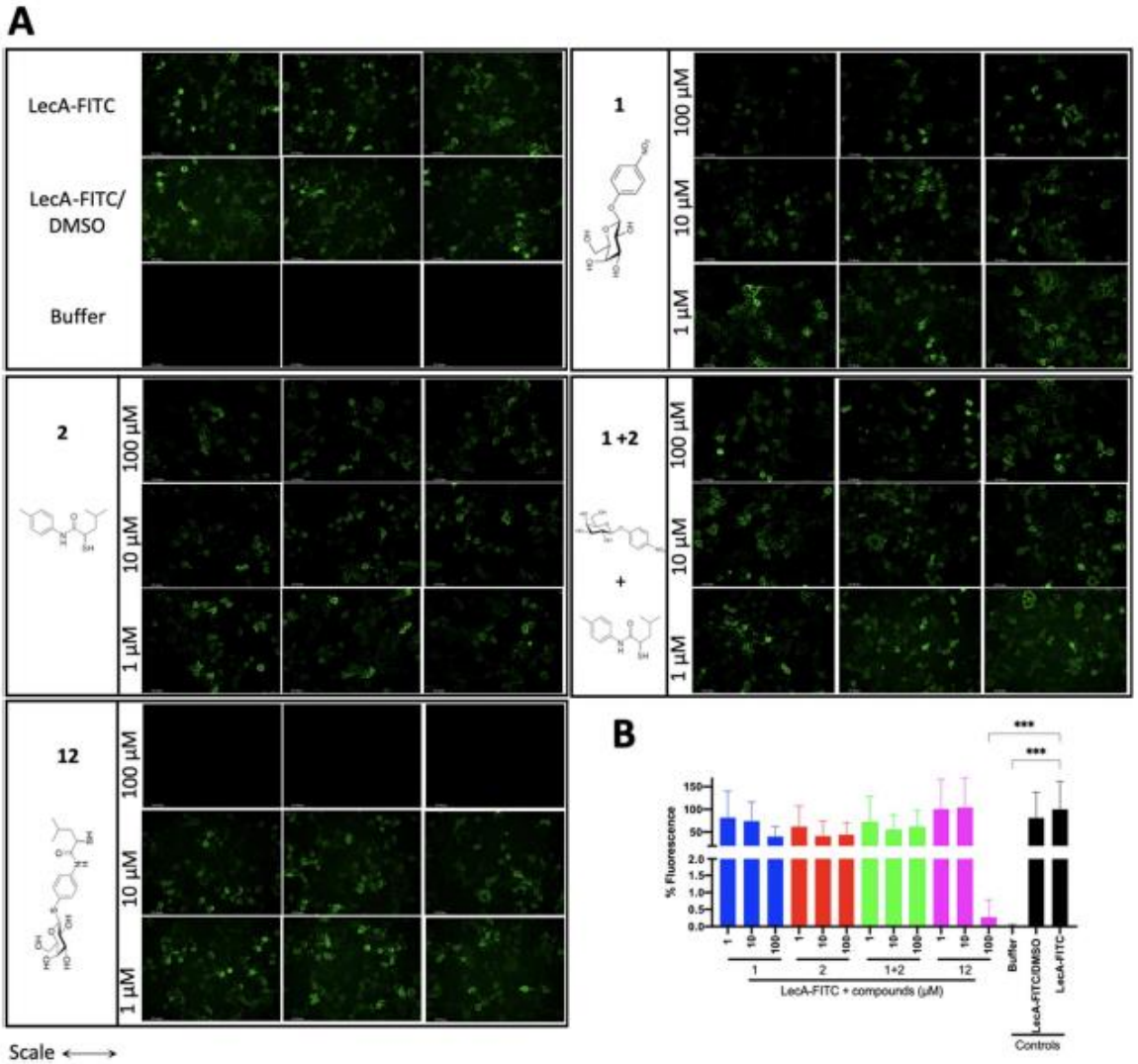

Fig. 8 Analysis of the inhibitory activity of **1**, **2**, a combination of **1** + **2** and **12** on the adhesion of fluorescein-labelled LecA to human A549 cells by fluorescence microscopy. (A) Three representative fluorescence images of one biological replicate of LecA-FITC bound to A549 cells in the presence of the different compounds and under different concentrations (scale bar corresponds to 250 µM). (B) Quantification of mean image fluorescence intensities with the averages and standard deviations for 3 biological replicates ((A), S7A and B†). Intensities are normalized with LecA-FITC in the absence of inhibitors to 100% and in the absence of FITC-LecA to 0%. One-way ANOVA statistical analysis was performed following Dunnett's multiple comparisons test, comparing the mean value of each condition to the mean value of the LecA-FITC positive control (***$p \leq 0.001$, all other data have no statistical significance compared to the LecA-FITC positive control).

the lipophilic S2′ pocket, thereby increasing the binding affinity *via* hydrophobic interactions. The galactose moiety is further stabilized by hydrogen bonds between its 2-hydroxy group (2-OH) and the backbone carbonyl of Glu111, two water-mediated hydrogen bonds *via* the same water (WAT293) between galactose 3-OH and 4-OH and the side chain of Asn112 and a second water-mediated hydrogen bond of 3-OH and the same side chain of Asn112. Thus, the side chain of Asn112 is heavily involved in coordinating through its amide-NH_2 to the ligand's carbohydrate moiety with two water-mediated hydrogen bonds and its amide-oxygen forming a hydrogen bond with the ligand's amide NH. An interesting observation is the unexpected folding of the aglycon, which leads to an intramolecular spatial proximity of hydroxyl 4-OH with its phenyl aglycon. Distances as close as 4.5 Å between 4-OH oxygen and the aryl carbon atom connected to the sulfur indicate attractive intramolecular ROH-π bonding.

In vitro antivirulence evaluation of 1, 2 and 12 on A549 cells

Next, we set out to analyze the ability of the dual inhibitor **12** and the individual treatment or combination of galactoside **1** and thiol **2** to reduce LasB-dependent cytotoxicity from *P. aeruginosa* PAO1 culture supernatant on A549 cells. None of the investigated compounds influenced A549 cell viability at 100

μM in the absence of bacterial culture supernatant (Fig. S4†). When A549 cells were exposed to *P. aeruginosa* PAO1 culture supernatant, both 100 μM and 10 μM of **12** led to an increase in cell viability compared to the combination of the individual LasB (**2**) and LecA (**1**) inhibitors at the corresponding concentrations (Fig. S5†). At 100 μM of **12**, the cytotoxicity of PAO1 culture supernatant reached that of the LasB-deficient strain, which served as the control (Fig. S5†). At 1 μM, only the dual inhibitor **12** had a statistically significant beneficial effect on cell viability, whereas neither **1** nor **2** nor their combination had any effect (Fig. 7 and S5†). These data demonstrate the enhanced potency of the dual inhibitor against the secreted *P. aeruginosa* virulence factors.

Evaluation of the dual inhibitors in LecA adhesion to A549 cells

LecA-mediated cell adhesion is crucial for the initial infection and host-cell invasion of *P. aeruginosa*. Therefore, compounds **1** and **2**, a combination of **1**+**2** and the dual inhibitor **12** were assessed for their ability to inhibit LecA-binding to human A549 cells. 10 μM of LecA-FITC and different concentrations of the respective compounds were incubated at 4 °C for 30 min with confluent A549 cells. After extensive washing, the analysis of the cells *via* fluorescence microscopy revealed that only the dual inhibitor **12** at 100 μM significantly inhibited the binding of LecA-FITC to A549 cells to the background level. No visible fluorescence signal was observed, which was comparable to the negative control of A549 cells in the absence of labeled LecA (Fig. 8). All other compounds and concentrations tested did not show a noticeable reduction in the fluorescence signal compared to the positive control consisting of A549 cells and LecA-FITC (Fig. 8 and S7†). The observation that the dual inhibitor showed high inhibition of LecA cell adhesion, while compounds **1** and **2** alone or in combination failed to do so, further highlights the superiority of **12**.

Conclusions

We report the first dual inhibitors of the major virulence factors LecA and LasB from the WHO priority I pathogen *P. aeruginosa*. Quite remarkably, our dual inhibitors displayed improved inhibitory activity and affinity for both targets down to 220 nM for LasB and 18 μM for LecA, compared to the individual predecessors of 400 nM and 53 μM, respectively. Implied by design, the divalent disulfide derivatives are formed *in situ*, which resulted in a 200-fold increase reaching single-digit nanomolar LecA activity determined using SPR (K_Ds 4.5–7.4 nM). We anticipate that the observed conversion rates of thiols into disulfides in the presence of the bacterial culture supernatant of *P. aeruginosa* are beneficial to ensure the initial saturation of LasB with the thiol and allow the subsequent inhibition of LecA with the potent bivalent disulfides. The crystal structure of the dual inhibitor **11** in complex with LasB confirmed the interaction at the atomic level. To further assess the potential of these merged inhibitors as candidates for therapeutic applications at this early stage, we evaluated their selectivity and toxicity profiles. Importantly, the compounds did not show any inhibition of a panel of six human MMPs as potential off-targets and cytotoxicity was not observed. Finally, we demonstrated a reduction of the cytotoxicity of *P. aeruginosa* culture supernatant by the dual inhibitor **12** on A549 cells *in vitro*, which primarily originates from secreted LasB, as well as an efficient inhibition of LecA adhesion to A549 cells. Both inhibitory effects were observed only for the dual inhibitor **12**, but were absent for single or combination treatments with LecA- or LasB inhibitors **1** and **2**, respectively.

Disarming highly pathogenic *P. aeruginosa* by interfering with its major pathogenicity factors offers a promising new option for therapeutics. Future research will focus on infection models using more complex *in vivo* systems, to support the importance of the presented dual inhibitors and their translation into practical applications.

Experimental section

Experimental details, materials, methods, chemical syntheses and transcripts of ^{1}H and ^{13}C NMR spectra can be found in the ESI.†

Data availability

The datasets supporting this article have been uploaded as part of the ESI.† The crystal structure dataset has been deposited at the Protein Database under code 7Z68, **https://www.rcsb.org/structure/7Z68**.

Author contributions

O. M. and J. K. contributed equally. All authors discussed the results and commented on the manuscript. Design of the study: O. M., J. K., S. Y., A. T., A. K. H. H.; project management A. T., A. K. H. H.; acquisition of funding: A. T., A. K. H. H.; project supervision: A. T., A. K. H. H.; design and chemical synthesis: O. M., J. K., S. Y.; evaluation of oxidative dimerization of thiols by LC-MS: O. M.; evaluation of LasB activity by *in vitro* inhibition assay: J. K.; evaluation of LecA binding by fluorescence polarization assay and SPR: O. M.; cytotoxicity and selectivity profile: J. H.; X-ray: A. K.; *in vitro* antivirulence evaluation: A. A., R. S.; LecA adhesion to A549 cells *in vitro*: R. S., M. F.; writing original draft: O. M., J. K.; writing – review and editing: O. M., J. K., A. T., A. K. H. H., with a contribution of all authors.

Conflicts of interest

The authors declare no competing financial interest.

Acknowledgements

A. T. thanks the European Research Council for funding part of this work (ERC starting grant 716311). A. K. H. H. gratefully acknowledges funding from the European Research Council (ERC starting grant 757913) and the Helmholtz-Association's Initiative and Networking Fund. J. K. acknowledges funding by

the Alexander von Humboldt Foundation. We are indebted to Dr Asfandyar Sikandar and Sebastian Adam (HIPS) for helpful suggestions with structure determination. Furthermore, we are grateful to Dr Joscha Meiers (HIPS), Annabelle Varrot and Anne Imberty (CERMAV) for attempts to crystallize LecA with thiols and disulfides. Dr Anne Imberty is further acknowledged for providing pET25-pail for LecA expression. We thank Nico Dankbar (Xantec) for the invaluable tips for SPR. The authors would like to thank Selina Wolter, Simone Amann, Jeannine Jung and Dennis Jener (HIPS) for technical assistance with LasB *in vitro* inhibition, selectivity and toxicity assays.

References

1 M. Miethke, M. Pieroni, T. Weber, M. Brönstrup, P. Hammann, L. Halby, P. B. Arimondo, P. Glaser, B. Aigle, H. B. Bode, R. Moreira, Y. Li, A. Luzhetskyy, M. H. Medema, J.-L. Pernodet, M. Stadler, J. R. Tormo, O. Genilloud, A. W. Truman, K. J. Weissman, E. Takano, S. Sabatini, E. Stegmann, H. Brötz-Oesterhelt, W. Wohlleben, M. Seemann, M. Empting, A. K. H. Hirsch, B. Loretz, C.-M. Lehr, A. Titz, J. Herrmann, T. Jaeger, S. Alt, T. Hesterkamp, M. Winterhalter, A. Schiefer, K. Pfarr, A. Hoerauf, H. Graz, M. Graz, M. Lindvall, S. Ramurthy, A. Karlén, M. van Dongen, H. Petkovic, A. Keller, F. Peyrane, S. Donadio, L. Fraisse, L. J. V. Piddock, I. H. Gilbert, H. E. Moser and R. Müller, *Nat. Rev. Chem*, 2021, **5**, 726–749.

2 M. Totsika, *Future Med. Chem.*, 2017, **9**, 267–269.

3 M. B. Calvert, V. R. Jumde and A. Titz, *Beilstein J. Org. Chem.*, 2018, **14**, 2607–2617.

4 A. E. Clatworthy, E. Pierson and D. T. Hung, *Nat. Chem. Biol.*, 2007, **3**, 541–548.

5 S. Walesch, J. Birkelbach, G. Jézéquel, F. P. J. Haeckl, J. D. Hegemann, T. Hesterkamp, A. K. H. Hirsch, P. Hammann and R. Müller, *EMBO Rep.*, 2023, **24**, e56033.

6 L. G. Rahme, E. J. Stevens, S. F. Wolfort, J. Shao, R. G. Tompkins and F. M. Ausubel, *Science*, 1995, **268**, 1899–1902.

7 L. Chen, J. Yang, J. Yu, Z. Yao, L. Sun, Y. Shen and Q. Jin, *Nucleic Acids Res.*, 2005, **33**, D325–D328.

8 S. B. Olivia Lawe Davies, *WHO publishes list of bacteria for which new antibiotics are urgently needed*, 2017, **https://www.who.int/news/item/27-02-2017-who-publishes-list-of-bacteria-for-which-new-antibiotics-are-urgently-needed.**

9 S. Wagner, R. Sommer, S. Hinsberger, C. Lu, R. W. Hartmann, M. Empting and A. Titz, *J. Med. Chem.*, 2016, **59**, 5929–5969.

10 M. J. Everett and D. T. Davies, *Drug Discov Today*, 2021, **26**, 2108–2123.

11 C. Wolz, E. Hellstern, M. Haug, D. R. Galloway, M. L. Vasil and G. Döring, *Mol. Microbiol.*, 1991, **5**, 2125–2131.

12 D. Leduc, N. Beaufort, S. de Bentzmann, J.-C. Rousselle, A. Namane, M. Chignard and D. Pidard, *Infect. Immun.*, 2007, **75**, 3848–3858.

13 J. Sun, D. L. LaRock, E. A. Skowronski, J. M. Kimmey, J. Olson, Z. Jiang, A. J. O'Donoghue, V. Nizet and C. N. LaRock, *EBioMedicine*, 2020, **60**, 102984.

14 M. Parmely, A. Gale, M. Clabaugh, R. Horvat and W. W. Zhou, *Infect. Immun.*, 1990, **58**, 3009–3014.

15 B. E. Britigan, M. B. Hayek, B. N. Doebbeling and R. B. J. Fick, *Infect. Immun.*, 1993, **61**, 5049–5055.

16 R. A. Miller, G. T. Rasmussen, C. D. Cox and B. E. Britigan, *Infect. Immun.*, 1996, **64**, 182–188.

17 E. Kessler, M. Safrin, J. K. Gustin and D. E. Ohman, *J. Biol. Chem.*, 1998, **273**, 30225–30231.

18 R. Sarnovsky, J. Rea, M. Makowski, R. Hertle, C. Kelly, A. Antignani, D. V. Pastrana and D. J. Fitzgerald, *J. Biol. Chem.*, 2009, **284**, 10243–10253.

19 J. Oh, X.-H. Li, S.-K. Kim and J.-H. Lee, *Sci. Rep.*, 2017, **7**, 4416.

20 C. Chemani, A. Imberty, S. de Bentzmann, M. Pierre, M. Wimmerova, B. P. Guery and K. Faure, *Infect. Immun.*, 2009, **77**, 11.

21 S. P. Diggle, R. E. Stacey, C. Dodd, M. Cámara, P. Williams and K. Winzer, *Environ. Microbiol*, 2006, **8**, 1095–1104.

22 A. Audfray, A. Varrot and A. Imberty, *C. R. Chim.*, 2013, **16**, 482–490.

23 J. Tiralongo and A. P. Moran, in *Microbial Glycobiology*, ed. O. Holst, P. J. Brennan, M. von Itzstein and A. P. Moran, Academic Press, San Diego, 2010, pp. 549–565.

24 M. Mewe, D. Tielker, R. Schönberg, M. Schachner, K.-E. Jaeger and U. Schumacher, *J. Laryngol. Otol.*, 2005, **119**, 595–599.

25 O. Bajolet-Laudinat, S. Girod-de Bentzmann, J. M. Tournier, C. Madoulet, M. C. Plotkowski, C. Chippaux and E. Puchelle, *Infect. Immun.*, 1994, **62**, 4481–4487.

26 T. Eierhoff, B. Bastian, R. Thuenauer, J. Madl, A. Audfray, S. Aigal, S. Juillot, G. E. Rydell, S. Müller, S. de Bentzmann, A. Imberty, C. Fleck and W. Römer, *Proc. Natl. Acad. Sci. U.S.A.*, 2014, **111**, 12895.

27 R. S. Laughlin, M. W. Musch, C. J. Hollbrook, F. M. Rocha, E. B. Chang and J. C. Alverdy, *Ann. Surg.*, 2000, **232**, 133–142.

28 S. Leusmann, P. Ménová, E. Shanin, A. Titz and C. Rademacher, *Chem. Soc. Rev.*, 2023, **52**, 3663–3740.

29 F. Pertici and R. J. Pieters, *Chem. Commun.*, 2012, **48**, 4008–4010.

30 B. Blanchard, A. Nurisso, E. Hollville, C. Tétaud, J. Wiels, M. Pokorná, M. Wimmerová, A. Varrot and A. Imberty, *J. Mol. Biol.*, 2008, **383**, 837–853.

31 E. Zahorska, S. Kuhaudomlarp, S. Minervini, S. Yousaf, M. Lepsik, T. Kinsinger, A. K. H. Hirsch, A. Imberty and A. Titz, *Chem. Commun.*, 2020, **56**, 8822–8825.

32 M. Bergmann, G. Michaud, R. Visini, X. Jin, E. Gillon, A. Stocker, A. Imberty, T. Darbre and J.-L. Reymond, *Org. Biomol. Chem.*, 2016, **14**, 138–148.

33 E. Zahorska, F. Rosato, K. Stober, S. Kuhaudomlarp, J. Meiers, D. Hauck, D. Reith, E. Gillon, K. Rox, A. Imberty, W. Römer and A. Titz, *Angew. Chem., Int. Ed.*, 2023, **62**, e202215535.

34 A. Anighoro, J. Bajorath and G. Rastelli, *J. Med. Chem.*, 2014, **57**, 7874–7887.

35 C. Kaya, I. Walter, A. Alhayek, R. Shafiei, G. Jézéquel, A. Andreas, J. Konstantinović, E. Schönauer, A. Sikandar,

J. Haupenthal, R. Müller, H. Brandstetter, R. W. Hartmann and A. K. H. Hirsch, *ACS Infect. Dis.*, 2022, **8**, 1010–1021.

36 I. Joachim, S. Rikker, D. Hauck, D. Ponader, S. Boden, R. Sommer, L. Hartmann and A. Titz, *Org. Biomol. Chem.*, 2016, **14**, 7933–7948.

37 C. Kaya, I. Walter, S. Yahiaoui, A. Sikandar, A. Alhayek, J. Konstantinović, A. M. Kany, J. Haupenthal, J. Köhnke, R. W. Hartmann and A. K. H. Hirsch, *Angew Chem. Int. Ed. Engl.*, 2002, **61**(5), e202112295, DOI: 10.1002/anie.202112295.

38 V. Wittmann and R. J. Pieters, *Chem. Soc. Rev.*, 2013, **42**, 4492–4503.

39 F. Casoni, L. Dupin, G. Vergoten, A. Meyer, C. Ligeour, T. Géhin, O. Vidal, E. Souteyrand, J.-J. Vasseur, Y. Chevolot and F. Morvan, *Org. Biomol. Chem.*, 2014, **12**, 9166–9179.

40 R. U. Kadam, D. Garg, J. Schwartz, R. Visini, M. Sattler, A. Stocker, T. Darbre and J.-L. Reymond, *ACS Chem. Biol.*, 2013, **8**, 1925–1930.

41 K. Voos, S. Yahiaoui, J. Konstantinović, E. Schönauer, A. Alhayek, A. Sikandar, K. S. Chaib, T. Ramspoth, K. Rox, J. Haupenthal, J. Köhnke, H. Brandstetter, C. Ducho and A. K. H. Hirsch, *ChemRxiv*, 2022, DOI: 10.26434/chemrxiv-2022-fjrqr.

42 E. Siebs, E. Shanina, S. Kuhaudomlarp, P. da Silva Figueiredo Celestino Gomes, C. Fortin, P. H. Seeberger, D. Rognan, C. Rademacher, A. Imberty and A. Titz, *Chembiochem*, 2022, **23**, e202100563.

43 J. Rodrigue, G. Ganne, B. Blanchard, C. Saucier, D. Giguère, T. C. Shiao, A. Varrot, A. Imberty and R. Roy, *Org. Biomol. Chem.*, 2013, **11**, 6906–6918.

44 V. Camberlein, G. Jézéquel, J. Haupenthal and A. K. H. Hirsch, *Antibiotics*, 2022, **11**(8), 1060, DOI: 10.3390/antibiotics11081060.

45 R. U. Kadam, M. Bergmann, M. Hurley, D. Garg, M. Cacciarini, M. A. Swiderska, C. Nativi, M. Sattler, A. R. Smyth, P. Williams, M. Cámara, A. Stocker, T. Darbre and J.-L. Reymond, *Angew. Chem., Int. Ed.*, 2011, **50**, 10631–10635.

46 A. M. Kany, A. Sikandar, J. Haupenthal, S. Yahiaoui, C. K. Maurer, E. Proschak, J. Köhnke and R. W. Hartmann, *ACS Infect. Dis.*, 2018, **4**, 988–997.

47 L. L. Kiessling, *Bioorg. Med. Chem.*, 2018, **26**, 5229–5238.

48 W. I. Weis and K. Drickamer, *Annu. Rev. Biochem.*, 1996, **65**, 441–473.

49 N. Izumiya and A. Nagamatsu, *Bull. Chem. Soc. Jpn.*, 1952, **25**, 265–267.

50 N. Tka, J. Kraïem and B. B. Hassine, *Synth. Commun.*, 2013, **43**, 735–743.

51 E. R. Samuels and I. F. Sevrioukova, *Tetrahedron Lett.*, 2018, **59**, 1140–1142.

52 O. Metelkina, B. Huck, J. S. O'Connor, M. Koch, A. Manz, C.-M. Lehr and A. Titz, *J. Mater. Chem. B*, 2022, **10**, 537–548.

53 H. Laronha and J. Caldeira, *Cells*, 2020, **9**(5), 1076, DOI: 10.3390/cells9051076.

54 R. Visini, X. Jin, M. Bergmann, G. Michaud, F. Pertici, O. Fu, A. Pukin, T. R. Branson, D. M. E. Thies-Weesie, J. Kemmink, E. Gillon, A. Imberty, A. Stocker, T. Darbre, R. J. Pieters and J.-L. Reymond, *ACS Chem. Biol.*, 2015, **10**, 2455–2462.

2.3.1 Supporting information

Supporting information presented here includes the biological portion of Chapter 3.

Supporting information

Dual inhibitors of *Pseudomonas aeruginosa* virulence factors LasB and LecA

Olga Metelkina[▽a,b,c], Jelena Konstantinović[▽a], Andreas Klein[a,d], Roya Shafiei[a,d], Mario Fares [a,b,c], Alaa Alhayek,[a] Samir Yahiaoui[a], Walid A. M. Elgaher,[a] Jörg Haupenthal[a], Alexander Titz*[a,b,c], Anna K. H. Hirsch*[a,b,d]

[a]Helmholtz Institute for Pharmaceutical Research Saarland (HIPS) – Helmholtz Centre for Infection Research (HZI), 66123 Saarbrücken, Germany

[b]Deutsches Zentrum für Infektionsforschung (DZIF), Standort Hannover-Braunschweig, 38124 Braunschweig, Germany

[c]Saarland University, Department of Chemistry, 66123 Saarbrücken, Germany

[d]Saarland University, Department of Pharmacy, 66123 Saarbrücken, Germany

[▽]These authors contributed equally.

*corresponding authors: anna.hirsch@helmholtz-hips.de, alexander.titz@helmholtz-hips.de

General experimental details.

Commercial chemicals and solvents were used without further purification. Procedures were not optimized regarding yield. Thin layer chromatography (TLC) was performed using TLC Silica gel 60 F_{254} sheets (Merck KGaA, Darmstadt, Germany) and developed under UV light (254 nm) and using a cerium molybdate stain (0.02 M solution of $(NH_4)Ce(SO_4)_4 \cdot 2H_2O$ and $(NH_4)_6Mo_7O_{24} \cdot 4H_2O$ in aqueous 10% H_2SO_4) or a permanganate stain (3 g of $KMnO_4$, 20 g of K_2CO_3 in 5 mL of 5% NaOH and 300 mL of water) with heating. Medium pressure liquid chromatography (MPLC) was performed on a Combiflash Rf200 (Teledyne Isco) system using normal phase silica gel columns (60 Å, 400 mesh particle size, Fluka) or reversed-phase silica gel columns Chromabond Flash C_{18} ec (Macherey-Nagel, Düren, Germany). Preparative high-pressure liquid chromatography (HPLC) was performed on Waters 2545 Binary Gradient Module with a Waters 2489 UV/Vis detector using a RP-18 column (Nucleodur C18 Gravity SB, 5 µm, 250x21 mm from Macherey-Nagel, Germany) and DionexUltiMate 3000 UHPLC+ focused (Thermo Scientific, United States) using a reversed-phase C18 column (Hypersil gold, 5 µm, 250x10 mm from Macherey-Nagel, Germany). Analytical HPLC-MS was performed using: a) Thermo Dionex Ultimate 3000 HPLC (Thermo Scientific, United States) coupled to a Bruker amaZon SL mass spectrometer, with UV detection at 254 nm using a C18 column (Nucleoshell RP18plus, 2.7 µm, 100x2 mm from Macherey-Nagel, Germany) as stationary phase; b) ESI quadrupole MS (MSQ Plus or ISQ EC, Thermo Fisher Scientific, Dreieich, Germany) using C18 column (Hypersil gold, 3 µm, 100x2 mm from Thermo Scientific, United States) and c) Ultimate 3000 HPLC (Thermo Fisher) coupled to a TSQ Quantum Access Max triple quadrupole mass spectrometer (Thermo Fisher) using C18 column (Hypersil gold, 1.9 µm, 100x2 mm from Thermo Scientific, United States). Purity of the final compounds was determined by LC-MS using the UV trace recorded at a wavelength of 254 nm and found to be >95%. High resolution mass spectrometry (HRMS) was performed on an Ultimate 3000 UPLC system coupled to a Q Exactive Focus Orbitrap system with HESI source (Thermo Fisher, Dreieich, Germany). The UPLC was operated with a C18 column (EC 150/2 Nucleodur C18 Pyramid, 3 µm from Macherey-Nagel, Germany). ^{1}H- and ^{13}C-NMR spectra were recorded on a Bruker Avance III 500 UltraShield spectrometer at 500 MHz and 126 MHz, respectively. Chemical shifts (δ) are given in ppm and were calibrated on residual solvent peaks: $CHCl_3$-d_1 (^{1}H-NMR δ = 7.26 ppm, ^{13}C-NMR δ = 77.0 ppm), MeOH-d_4 (^{1}H-NMR δ = 3.31 ppm, ^{13}C -NMR δ = 49.0 ppm), DMSO-d_6 (^{1}H-NMR δ = 2.50 ppm, ^{13}C-NMR δ = 39.51 ppm). Deuterated solvents were purchased from Eurisotop (Saarbrücken, Germany). Multiplicities are specified as s = singlet, bs = broad singlet, d = doublet, dd = doublet of doublets, t = triplet, td = triplet

of doublets, q = quartet, m = multiplet. The spectra were assigned with the help of ^{1}H, ^{1}H-COSY and ^{1}H,^{13}C-HSQC experiments.

Expression and purification of LasB and LecA

LecA was expressed recombinantly using *E. coli* pET25-pail, whereas LasB was isolated from *P. aeruginosa* PA14 culture supernatant as described previously.[1,2]

LecA labeling with fluorescein was performed in analogy to Sommer et al. [3] and Beshr et al.[4] To this end fluorescein isothiocyanate (FITC) was freshly dissolved in carbonate-bicarbonate buffer with pH of 9.3 at a concentration of 3 mg mL^{-1}. Subsequently, 66 µL of this FITC solution was combined with 1.4 mL of LecA at a concentration of 60 µM in carbonate-bicarbonate buffer, pH 9.3. The resulting mixture was then incubated at 25 °C with shaking at 500 rpm for 1 hour. Then, extensive washing with PBS/Ca^{2+} in a 5 kDa molecular weight cutoff centrifugal concentrator was performed to remove excess dye and buffer the labelled protein.

In vitro inhibition assay for LasB

The in vitro inhibition assay was performed as described previously,[2] using purified LasB (final concentration 0.3 nM), the fluorogenic substrate 2-aminobenzoyl-Ala-Gly-Leu-Ala-4-nitrobenzylamide (purchased from Peptides International (Louisville, KY, USA) or Vivitide, LLC (Gardner, MA, USA), final concentration 150 µM)) in assay buffer (50 mM Tris, pH 7.2, 2.5 mM $CaCl_2$, 0.075% Pluronic F-127, 5% DMSO). Fluorescence was measured using a CLARIOstar plate reader (BMG Labtech, Ortenberg, Germany). IC_{50} values were calculated using GraphPad Prism 8 (GraphPad Software, San Diego, CA, USA) from at least three independent experiments performed in duplicate.

Competitive binding assay for LecA

The procedure for the fluorescence polarization-based competitive binding assay for LecA was performed as reported by Joachim et al. with modifications.[1] The assay was performed in TBS/Ca^{2+} buffer (20 mM Tris, 137 mM NaCl, 2.6 mM KCl at pH 7.4 supplemented with 1 mM $CaCl_2$ and contained 5% DMSO). The final protein concentration in the assay was 5 µM for LecA. Fluorescence intensities were recorded on a PheraStar FS plate reader (BMG Labtech GmbH, Germany) and polarization was calculated using MARS Data Analysis (BMG Labtech). IC_{50} values were obtained from a four-parameter curve-fitting procedure. Averages and standard deviations were calculated from at least three independent experiments of technical triplicates each.

Surface plasmon resonance direct LecA binding assay

SPR experiments were performed on a Reichert 2-channel SPR SR7500DC (Reichert Technologies Life Sciences, Buffalo, NY, USA) at 25 °C. For LecA immobilization, the surface of a HC1000M sensor chip (XanTec bioanalytics GmbH, Düsseldorf, Germany) was preequilibrated with borate buffer (1 M NaCl, 0.1 M sodium borate pH 9.0), followed by activation of the polycarboxylate hydrogel with 0.2 M *N*-hydroxysuccinimide (NHS) and 0.4 M 1-ethyl-3-(3-dimethylaminopropyl)carbodiimide hydrochloride (EDC·HCl) in MilliQ water in both channels for 240 s (flow rate 10 µL/min) until the binding response reached 1200 RU. Then, LecA (100 µg/mL) in 10 mM sodium acetate pH 3.6 was injected on the activated chip surface of one channel (injection time 420 s, flow rate 10 µL/min) and 6000 RU of LecA were immobilized. Unreacted NHS esters in both channels were blocked with 1 M ethanolamine hydrochloride in MilliQ water pH 8.5 (injection time 360 s, flow rate 10 µL/min).

Test compound stock solutions were prepared in DMSO (20 mM stocks for monovalent LecA inhibitors, 20 µM stocks for divalent LecA inhibitors) and were subsequently diluted in 10 mM phosphate buffer (pH 7.4, 2.7 mM KCl, 137 mM NaCl, 100 µM $CaCl_2$) to obtain solutions with 2% DMSO.

Monovalent inhibitors **17**, **18**, **24** and **25** were injected for 120 s (flow rate 50 µL/min) at concentrations ranging from 0.39–100 µM. Divalent inhibitors **26a**, **26b** and **27** were injected for 120 s (flow rate 50 µL/min) at concentrations 50–350 nM. The chip surface was regenerated after each inhibitor injection by one injection of 50 mM IPTG in running buffer (10 mM phosphate buffer, pH 7.4, 2.7 mM KCl, 137 mM NaCl, 100 µM $CaCl_2$, 2% DMSO) followed by one injection 20 mM EDTA disodium salt in MilliQ water, and then followed by three injections of the running buffer (injection time 120 s, flow rate 50 µL/min). 100 µM pNP-Gal (**1**) in running buffer was injected before each analyte to monitor and ensure chip regeneration and protein activity.

Affinity/equilibrium analysis was performed for **1** on the same chip. A stock solution of **1** (10 mM in PBS/$CaCl_2$ buffer) was prepared, then diluted to the required concentrations in running buffer and injected at 1.56–400 µM (injection time 60 s, flow rate 50 µL/min) without regeneration steps. Data analysis was performed using TraceDrawer software (Ridgeview Instruments) using a 1:1 binding model to fit the experimental data. Spikes at the end of the injections were removed in TraceDrawer during the data analysis.

Disulfide formation assay

The stability of two thiols **11** and **12** and their ability to form the corresponding disulfides was analyzed by HPLC-MS. Chemically synthesized disulfides **26** and **27** were used as references for the stability assay. 50 mM DMSO stocks of thiols **11** and **12** were diluted 40-fold with *P. aeruginosa* PA14 overnight LB medium culture supernatant (25% v/v, sterile filtered through 0.22 µm filters in 10 mM phosphate buffer, pH 7.4, 2.7 mM KCl, 137 mM NaCl, 100 µM $CaCl_2$) at 37 °C. Samples were drawn over 4.5 hours and analyzed by LC-MS using a RP-18 column 100/2 Nucleoshell RP18plus, 2.7 µm from Macherey-Nagel, Germany (H_2O/MeCN + 0.1% formic acid, 15 – 55% MeCN, retention time (t_R) 5.8 min (**11** or **12**), 6.1 min and 6.3 min (disulfide products **26** or **27**) on a Thermo Dionex Ultimate 3000 HPLC coupled to a Bruker amaZon SL mass spectrometer, with UV detection at 254 nm). Thiol half-lives were determined by analysis of the obtained graphs and values of 80 min for **11** and 46 min for **12** were obtained (Figure 2).

Selectivity and toxicity assays

Human MMPs -1, -2, -3, -7, -8 and -14 along with the SensoLyte 520 Generic MMP Activity Kit*Fluorimetric* were purchased from AnaSpec (Fremont, CA, USA). The inhibition assay was performed according to the guidelines of the manufacturer and as described recently.[5]

Cytotoxicity on human liver (HepG2), kidney (HEK293) and lung (A549) cells were performed using MTT assay and measuring the optical density (OD) photometrically at 570 nm in a FLUOstar Omega plate reader (BMG labtech, Ortenberg, Germany) as described previously.[6]

Antimicrobial activity against *P. aeruginosa* PA14 was tested using ESCMID guidelines and details have been reported previously.[7]

***In vitro* evaluation of 12 and a combination of 1 and 2 using *P. aeruginosa* culture supernatant and A549 cells in a cell viability assay**

The A549 cell line, derived from human lung adenocarcinoma, was grown in Dulbecco's Modified Eagle Medium (DMEM) supplemented with 10% Fetal Bovine Serum (FBS) and 1% penicillin-streptomycin. The cells were cultured following standard protocols for cell maintenance.

To prepare the bacterial culture supernatant, individual flasks containing 15 mL of lysogeny broth (LB) culture medium were inoculated with PAO1 or PAO1 Δ*lasB* strains. Culture flasks were placed on a shaker and incubated at 37 °C and 180 rpm overnight for 18 hours. Following incubation, the bacterial cultures were subjected to centrifugation at 4 °C and 5000 rpm for

10 min, facilitating the separation of bacterial cells from the supernatant. The latter was filtered through a 0.22 µm sterile filter and stored at –80 °C until further use.

In a flat bottom 96-well plate (Corning™ Costar™), each well was seeded with 2.5–3.5*10^3 cells in 100 µL DMEM/FCS and then incubated at a temperature of 37 °C with 5% CO_2 for 24 hours. Then, compounds **12** and **1** combined with **2** in concentrations of 100 µM, 10 µM, and 1 µM were mixed with 10% (v/v) of culture supernatant of *P. aeruginosa* PAO1 (DSM 22644, ATCC 15692) in DMEM/FCS. To minimize the potential negative effect of DMSO, the compound was initially dissolved in 99.9% DMSO, and a final assay concentration of 0.5% DMSO was applied. Additionally, the cells were exposed to 10% (v/v) PAO1 Δ*lasB* culture supernatant to analyze the effect caused by LasB, while DMEM/FCS without any treatment served as a control. The plates were then incubated at 37 °C with 5% CO_2 for 24 hours before conducting the MTT assay.

MTT assay

To assess cell viability, the medium in the well plates was aspirated and a single wash was performed using 100 µL of phosphate buffered saline, pH 7.4 (PBS). A solution of 5 mg MTT (3-(4,5-dimethylthiazol-2-yl)-2,5-diphenyl tetrazolium bromide) per mL PBS was prepared and diluted to a concentration of 10% (v/v) in DMEM/FCS. Subsequently, 100 µL of this MTT solution was added to each well, and the plates were incubated at 37 °C for 3 hours with 5% CO_2. After incubation, the MTT solution was carefully removed, and the formazan crystals were dissolved by adding 150 µL of lysis solution (250 mL DMSO, 25 g SDS, and 1.25 mL AcOH) to each well. The plates were then incubated for an additional 30 min at 37 °C and then, the UV absorbance was measured using a PHERAstar microplate reader. The test samples were read at a wavelength of 550 nm, while the blank was read at 620 nm. At last, the data were statistically analyzed and presented graphically using GraphPad Prism 9 (Figure S4 and S5).

Evaluation of compounds 1, 2 and 12 in inhibiting LecA adhesion to A549 cells via fluorescence microscopy

The A549 cell line were cultured following the protocols for cell maintenance described above. In a flat-bottom cell culture black 96-well plate (Greiner Bio-One, #Cat 655090) each well was seeded with 1*10^4 cells in 100 µL DMEM/FCS and subsequently, incubated overnight at 37 °C with 5% CO_2. On the following day, concentrations of 100 µM, 10 µM, and 1 µM of the compounds **1**, **2**, the combination of **1** and **2**, or **12** were incubated for 30 min at room temperature with 10 µM FITC-labeled LecA. Each test sample comprises 100 µL solution of 10

µM FITC-labeled LecA in DMEM/FCS and varying concentrations of the test compound (ranging from 1 µM to 100 µM). This prepared mixture was then added after 30 min incubation at room temperature to the cell culture wells in duplicate. The compounds were initially dissolved in 99.9% DMSO, and a final assay concentration of 0.5% DMSO was used. Furthermore, the A549 cells were exposed to 10 µM FITC-labeled LecA both with or without DMSO to quantify staining efficacy of LecA on A549 cells and to ensure that DMSO did not have any negative effects. The plate was then incubated at 4 °C for 30 min and wells were washed 5 times with PBS prior to imaging via fluorescence microscopy.

Fluorescence image acquisition, processing, and quantification

Fluorescence images were captured using an inverted fluorescence microscope (Leica DMi8) equipped with a 20x objective (HC PL APO CS2 20x/0.75 IMM UV), an FITC filter cube (EX: 460-500 nm, DC: 505, EM: 512-542 nm) and a monochrome microscope camera (Leica DFC7000 GT). The Leica Application suite X (3.7.4.23463) software navigator was used to image the whole well at one plane. The same image settings were used for imaging all the conditions in each biological replicate.

From each of the three biological replicates, three representative images were selected, each originating from two technical duplicates. Background fluorescence was subtracted using the LasX image processing software with the slider value at 500. Background-subtracted images were then exported as TIFF files, lossless compression, and scale bar were ticked.

The fluorescence signal was quantified with ImageJ by selecting the whole background subtracted image and calculating its mean fluorescence intensity. Data were plotted and statistically analyzed using GraphPad Prism.

X-ray Crystallography of the complex of 11 with LasB.

LasB at a concentration of 3.6 mg/mL was mixed with the diastereomeric mixture of **11** to get a final concentration of 1 mM compound in a 10 mM Tris buffer containing 2 mM $CaCl_2$. Crystal-screens have been set up using the sitting drop method and commercially available PEGs and PEGs II screen solutions (NeXtal Biotechnologies, 6201 Trust Drive Holland, OH 43528). The crystal for the final data set was obtained from the PEG F6 condition, containing 0.2 M potassium nitrate and 20% (w/v) PEG 3350. For data collection, the crystals were cryoprotected with a final concentration of 25% glycerol. Diffraction data were collected at beamline ID30B (ESRF, Grenoble, France) at 100 K and a wavelength of 0.9763 Å. The data was processed using CCP4 Aimless,[8] and the structure was solved by molecular replacement using *P. aeruginosa* LasB (PDB ID 6FZX) without the ligand as a search model in PHASER. The

solution was rebuilt using AutoBuild. Refinement was done with phenix.refine (Phenix version 1.19.2-4158-000)[9] and manually with WinCOOT (0.9.6)[10]. Images were created using PyMOL (2.5.2)[11] (Figure S6).

Table S1. Inhibition of six human matrix metalloproteases (MMPs) in the presence of 100 μM of compounds **11** and **12***.

	Percent inhibition at 100 μM	
	11	**12**
MMP-1	10±5	n.i.
MMP-2	n.i.	19±3
MMP-3	n.i.	n.i.
MMP-7	n.i.	n.i.
MMP-8	n.i.	n.i.
MMP-14	n.i.	19±5

*Means and standard deviations from at least three independent experiments. n.i. = <10% inhibition

Table S2. Antibacterial activity of compounds **11** and **12** against *Pseudomonas aeruginosa* PA14.

	MIC (μM)	
	11	**12**
P. aeruginosa PA14	>100	>100

Table S3. Cytotoxicity of compounds **11** and **12** against HepG2, HEK293, and A549 cell lines*.

	IC_{50} (μM)	
	11	**12**
HepG2	>100	>100
HEK293	>100	>100
A549	>100	>100

*Means from at least three independent experiments

Table S4. Crystal structure of LasB in complex with **11**: Data collection and refinement statistics.

	LasB_11
PDB ID	**7Z68**

*Statistics for the highest-resolution shell are shown in parentheses.

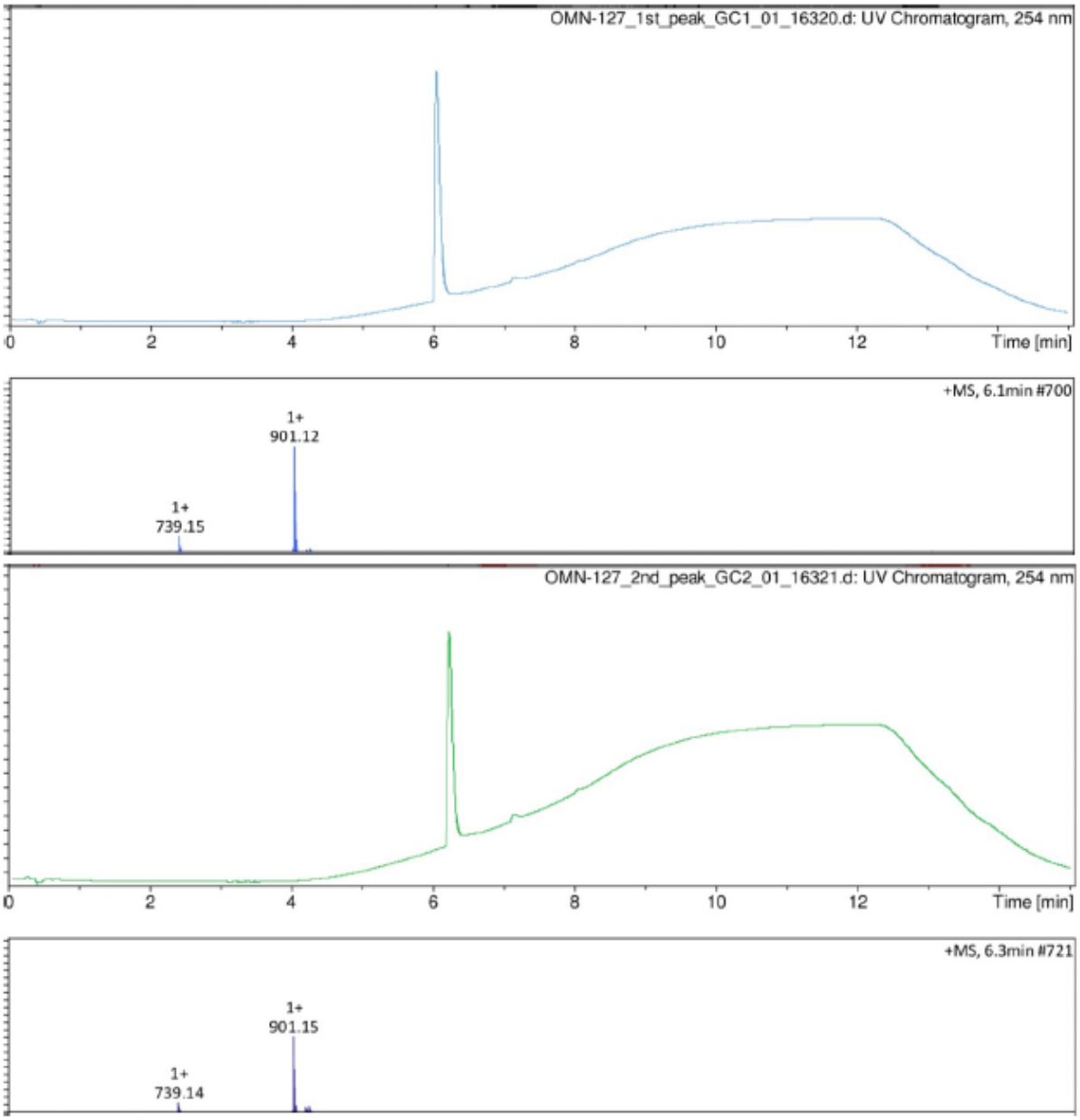

Figure S1. HPLC analysis of compounds **26a** (top) and **26b** (bottom).

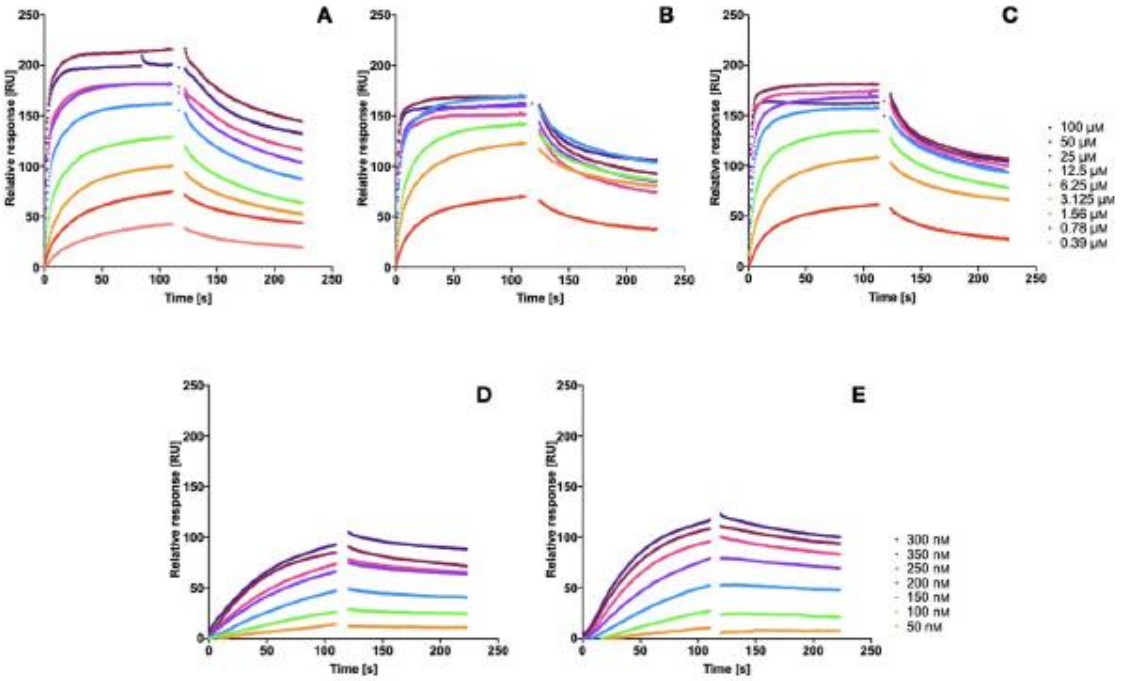

Figure S2. SPR binding curves of the interaction of dual inhibitors A) **24**, B) **18**, C) **25**, D) **27**, E) **26b** with LecA.

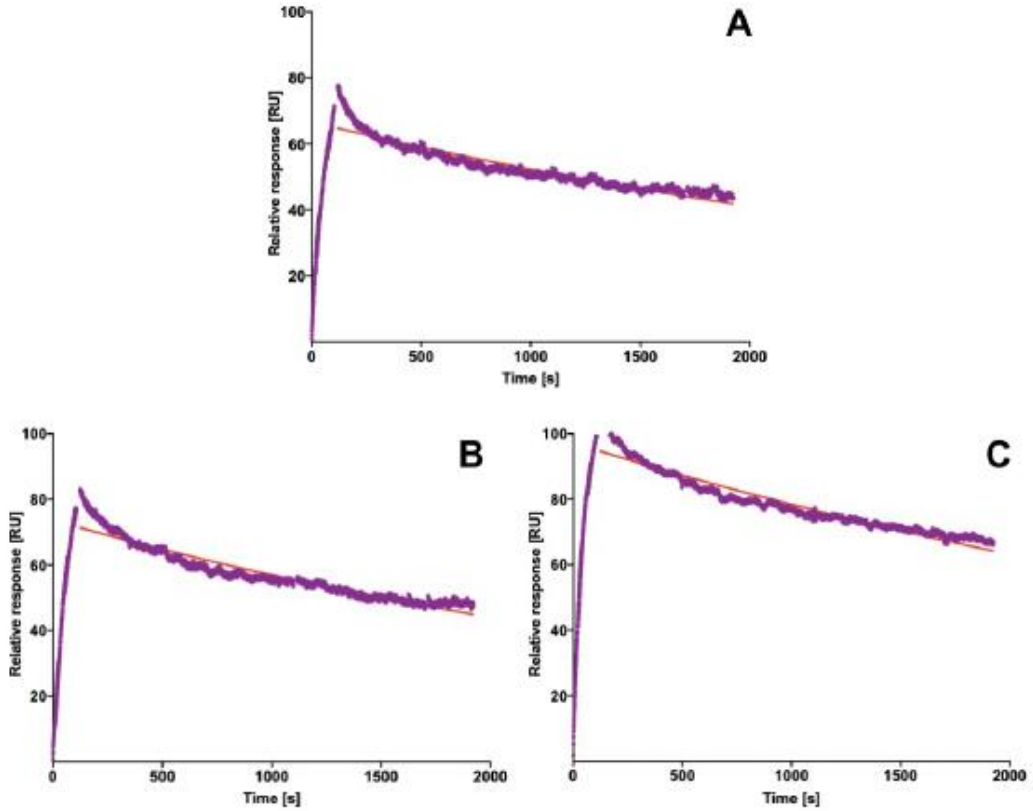

Figure S3. SPR dissociation kinetic analysis of the interaction of divalent LecA inhibitors A) **27**, B) **26a**, and C) **26b** with LecA.

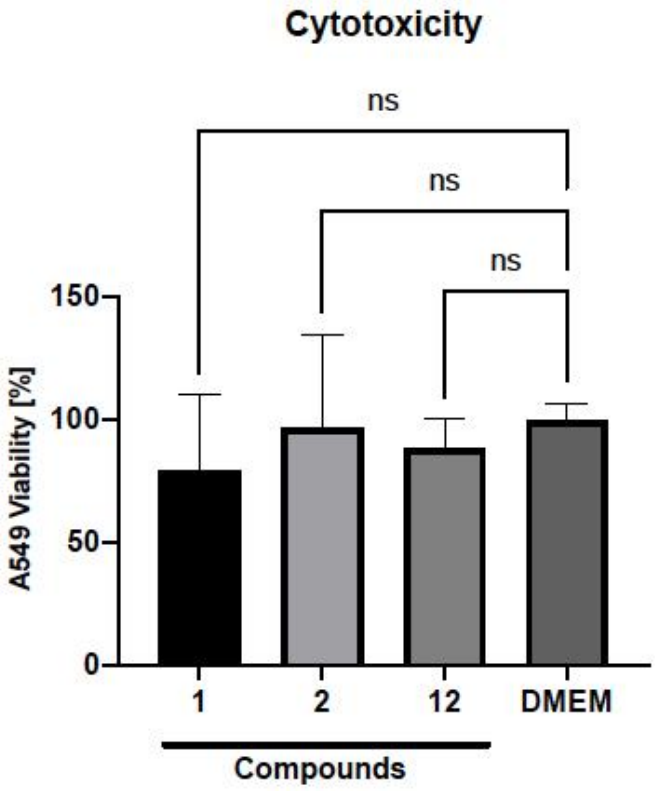

Figure S4. Evaluation of the cytotoxicity of compounds **1**, **2** and **12** at 100 µM. The graphs represent three independent experiments ± SD. One-way ANOVA statistical analysis was performed following Dunnett's multiple comparisons test, comparing the mean value of each concentration to the mean value of DMEM.

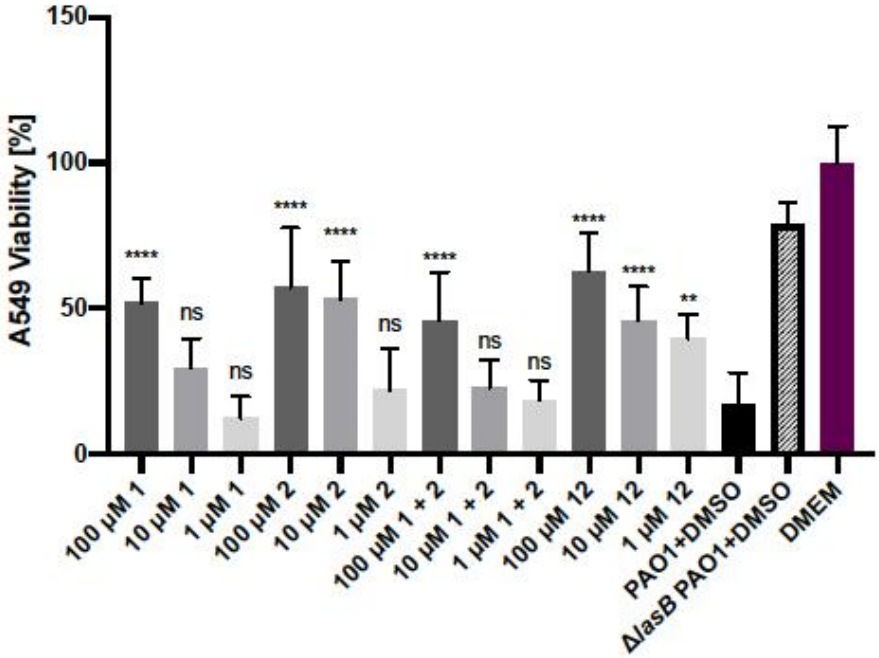

Figure S5. Inhibition of LasB-dependent cytotoxicity: The dose-response inhibitory effect of compounds **1**, **2** the combination of **1** and **2** and compound **12** against 10% (v/v) *P. aeruginosa* PAO1 culture supernatant. The graphs represent three independent experiments ± SD. One-way ANOVA statistical analysis was performed following Dunnett's multiple comparisons test, comparing the mean value of each concentration to the mean value of PAO1 without any treatment with compounds (**** $p \leq 0.0001$, ** $p \leq 0.01$).

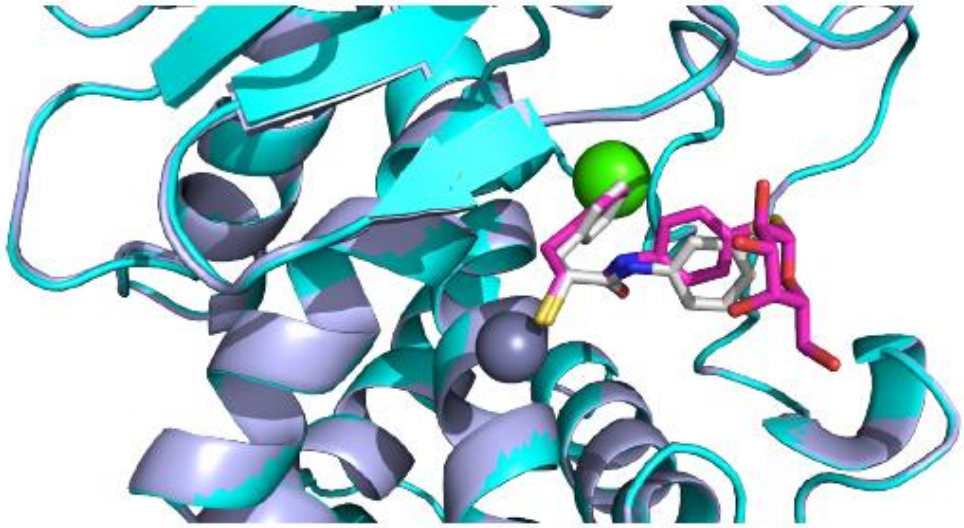

Figure S6. Superposition of the LasB-compound **11** (magenta) and LasB-α-alkyl-*N*-aryl mercaptoacetamide (gray; PDB 7OC7); Zn^{2+} is shown as a gray sphere; Ca^{2+} is shown as a green sphere; the protein structure demonstrates no major deviations between the two complexes

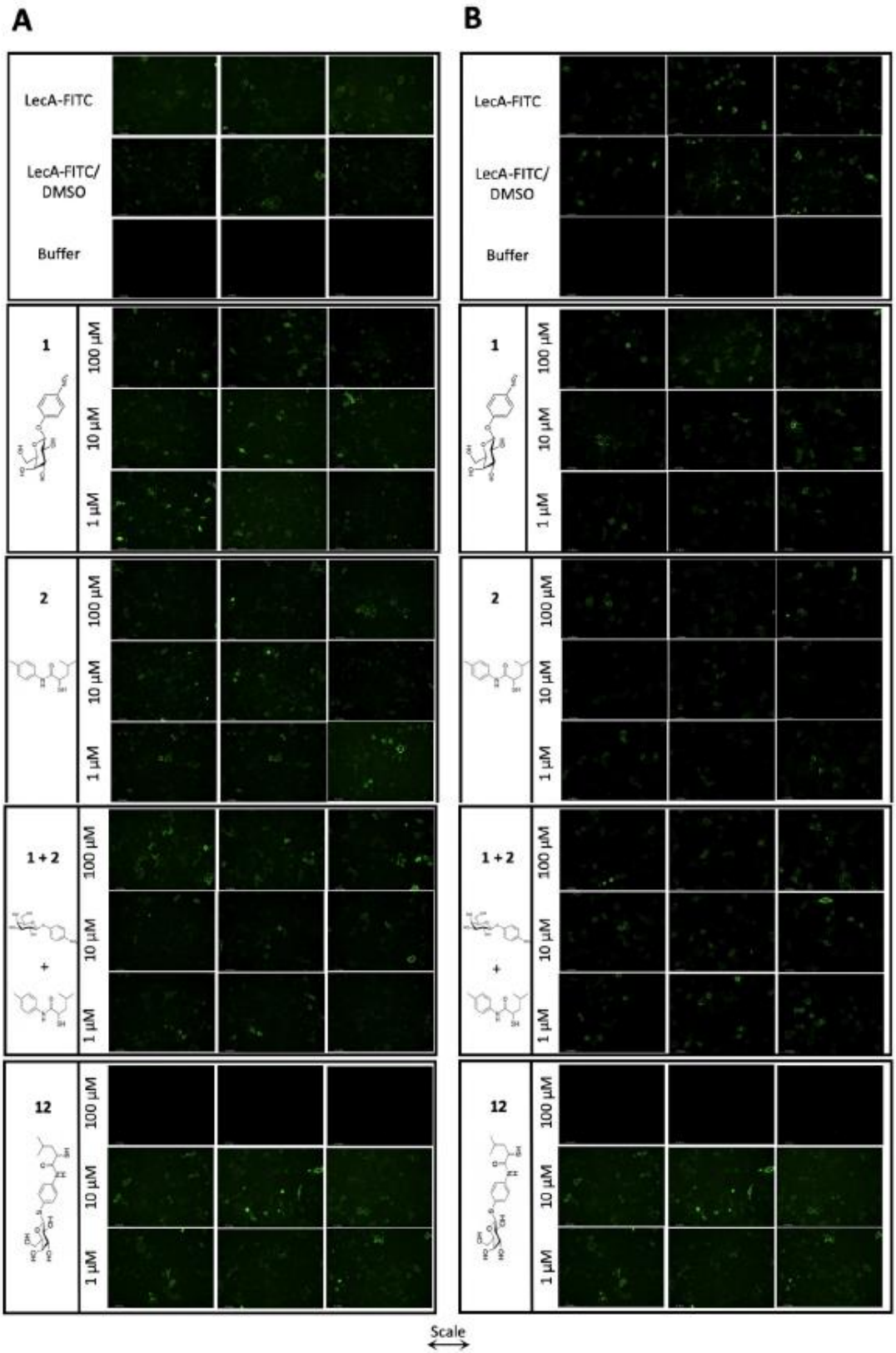

Figure S7. Fluorescence images of LecA-FITC bound to A549 cells in the presence of different concentrations of **1**, **2**, **1+2** and **12** (three representative images from two biological replicates (A, B). Scale bar corresponds to 250 µm

Supporting Information References

1 I. Joachim, S. Rikker, D. Hauck, D. Ponader, S. Boden, R. Sommer, L. Hartmann and A. Titz, *Org. Biomol. Chem.*, 2016, **14**, 7933–7948.
2 A. M. Kany, A. Sikandar, J. Haupenthal, S. Yahiaoui, C. K. Maurer, E. Proschak, J. Köhnke and R. W. Hartmann, *ACS Infect. Dis.*, 2018, **4**, 988–997.
3 R. Sommer, S. Wagner, A. Varrot, C. M. Nycholat, A. Khaledi, S. Häussler, J. C. Paulson, A. Imberty and A. Titz, *Chem. Sci.*, 2016, **7**, 4990–5001.
4 G. Beshr, A. Sikandar, E.-M. Jemiller, N. Klymiuk, D. Hauck, S. Wagner, E. Wolf, J. Koehnke and A. Titz, *Journal of Biological Chemistry*, 2017, **292**, 19935–19951.
5 E. Schönauer, A. M. Kany, J. Haupenthal, K. Hüsecken, I. J. Hoppe, K. Voos, S. Yahiaoui, B. Elsässer, C. Ducho, H. Brandstetter and R. W. Hartmann, *J. Am. Chem. Soc.*, 2017, **139**, 12696–12703.
6 J. Haupenthal, C. Baehr, S. Zeuzem and A. Piiper, *International Journal of Cancer*, 2007, **121**, 206–210.
7 W. A. M. Elgaher, M. Fruth, M. Groh, J. Haupenthal and R. W. Hartmann, *RSC Adv.*, 2014, **4**, 2177–2194.
8 M. D. Winn, C. C. Ballard, K. D. Cowtan, E. J. Dodson, P. Emsley, P. R. Evans, R. M. Keegan, E. B. Krissinel, A. G. W. Leslie, A. McCoy, S. J. McNicholas, G. N. Murshudov, N. S. Pannu, E. A. Potterton, H. R. Powell, R. J. Read, A. Vagin and K. S. Wilson, *Acta Crystallogr D Biol Crystallogr*, 2011, **67**, 235–242.
9 D. Liebschner, P. V. Afonine, M. L. Baker, G. Bunkóczi, V. B. Chen, T. I. Croll, B. Hintze, L. W. Hung, S. Jain, A. J. McCoy, N. W. Moriarty, R. D. Oeffner, B. K. Poon, M. G. Prisant, R. J. Read, J. S. Richardson, D. C. Richardson, M. D. Sammito, O. V. Sobolev, D. H. Stockwell, T. C. Terwilliger, A. G. Urzhumtsev, L. L. Videau, C. J. Williams and P. D. Adams, *Acta Crystallogr D Struct Biol*, 2019, **75**, 861–877.
10 P. Emsley and K. Cowtan, *Acta Crystallogr D Biol Crystallogr*, 2004, **60**, 2126–2132.
11 L. Schrödinger and W. DeLano, PyMOL 2020.
12 R. B. Cohen, S. H. Rutenburg, K.-C. Tsou, M. A. Woodbury and A. M. Seligman, *Journal of Biological Chemistry*, 1952, **195**, 607–614.
13 S. Escopy, Y. Singh and A. V. Demchenko, *Org. Biomol. Chem.*, 2019, **17**, 8379–8383.
14 F. Casoni, L. Dupin, G. Vergoten, A. Meyer, C. Ligeour, T. Géhin, O. Vidal, E. Souteyrand, J.-J. Vasseur, Y. Chevolot and F. Morvan, *Org Biomol Chem*, 2014, **12**, 9166–9179.
15 T. Fujisawa, K. Igeta, S. Odake, Y. Morita, J. Yasuda and T. Morikawa, *Bioorganic & Medicinal Chemistry*, 2002, **10**, 2569–2581.

3 Final Discussion

Pseudomonas aeruginosa is a formidable pathogen in pulmonary infections due to its multifaceted virulence and adaptive resistance mechanisms. This thesis explored one of its key virulence factors, the metalloprotease LasB, across a spectrum of molecular, cellular, and translational contexts, highlighting its pathogenic roles, variability in expression, and the therapeutic potential of antivirulence strategies targeting it.

One of the earliest insights of this work was the significant variability in *lasB* expression among clinical isolates. Using a qPCR-based assay developed for both relative and absolute quantification, we established that even isolates expressing comparatively low levels of *lasB* mRNA can exert detectable biological effects. In particular, exposure to culture supernatants from such strains altered cytokine profiles in lung epithelial models, suggesting that low levels of LasB may still contribute to immune modulation, even in the absence of overt cytotoxicity. Through cytometric bead array (CBA) we observed changes in cytokine levels, supporting a biologically relevant impact of LasB at low expression levels. This underscores the value of precise quantification of *lasB* expression for assessing the virulence potential of clinical isolates.

A second key finding of this work was the cell-type-specific response to LasB. Cells forming tighter epithelial barriers, such as alveolar Arlo cells, exhibited greater resilience, suggesting that tissue architecture and junctional protein density modulate susceptibility to LasB-mediated damage. Mechanistically, LasB was shown to disrupt epithelial integrity by cleaving junctional proteins such as E-cadherin, altering Claudin-4 localization, and interfering with host immune signaling. Interestingly, LasB appeared to exhibit a dual role in immune modulation, both upregulating inflammatory pathways and reducing levels of cytokines such as GM-CSF and G-CSF, potentially through proteolytic degradation.

Transcriptomic analysis played a critical role in expanding the understanding of the systemic effects of LasB. Differential gene expression profiling revealed modulations in key signaling pathways such as MAPK and FGF, and identified novel targets like *FGFBP1* and *DUSP2*. Importantly, *in silico* comparison with primary bronchial epithelial cell datasets showed a strong overlap, suggesting that transwell-based *in vitro* models can yield biologically and translationally relevant insights. These findings further support the utility of such systems for mechanistic discovery and preclinical screening.

From a therapeutic standpoint, multiple strategies were explored to counteract LasB's pathogenic effects. Small-molecule inhibitors of LasB were shown to preserve barrier integrity, restore TEER, and protect junctional proteins. These effects were potentiated when inhibitors were combined with conventional antibiotics, such as meropenem, in infection models. This synergy is particularly promising given the ongoing crisis of AMR and reinforces the concept of antivirulence therapies as antibiotic adjuvants rather than replacements.

The potential of dual-target antivirulence strategies was also evaluated. Compounds designed to inhibit both LasB and LecA showed superior protection compared to single-target controls within their chemical class, underscoring the advantage of addressing multiple virulence mechanisms simultaneously. However, this approach is not without trade-offs. Dual inhibitors

may not match the potency or favorable pharmacokinetic properties of highly optimized single-target agents — such as the dipeptidic phosphonates developed specifically for LasB inhibition — highlighting the need for a balanced strategy tailored to specific clinical contexts.

Despite these promising advances, limitations remain. In many models, full inhibition of LasB activity is required to fully restore host cell function, particularly when protecting cytokine levels. Moreover, while synergy with antibiotics is encouraging, it also means that antivirulence agents alone may not suffice in severe infections. Finally, although several findings were supported by *in vivo* data from studies in mice, species-specific differences remain a critical consideration.

Moving forward, future studies should prioritize evaluating the translational potential of LasB inhibitors using more physiologically complex, human-based models such as lung organoids or organ-on-a-chip platforms. These systems would enable more accurate modeling of host–pathogen interactions and help reduce reliance on animal models, addressing species-specific limitations observed in murine studies. In parallel, co-culture models incorporating immune cells (*e.g.*, macrophages or neutrophils) could offer additional insight into the immunomodulatory effects of LasB, particularly its influence on cytokine dynamics in a more physiologically relevant setting. To deepen mechanistic understanding, advanced proteomics approaches could be employed to directly identify and validate LasB substrates in epithelial and immune contexts, thereby clarifying its role in cytokine modulation and tissue disruption.

In terms of clinical applicability, future research could explore whether long-term exposure to LasB inhibitors results in compensatory changes or resistance mechanisms within *P. aeruginosa* populations. Moreover, combining antivirulence agents with host-directed approaches — such as enhancing epithelial regeneration or modulating immune responses — could amplify therapeutic benefit. Complementing these avenues, the qPCR assay developed in this thesis provides a practical tool for rapid quantification of *lasB* expression in clinical isolates, facilitating virulence profiling and informing personalized treatment strategies.

In conclusion, this thesis provides a comprehensive exploration of LasB as a virulence factor and therapeutic target, combining molecular dissection with pharmacological intervention. It contributes both mechanistic insights and translational tools that help pave the way for next-generation therapies against *P. aeruginosa* and other difficult-to-treat pathogens in the age of AMR.

4 Appendix

Additional Results, Chapter D

Characterization of Collagenolytic Activity and Cytotoxicity of *Clostridium perfringens* Culture Supernatants: Implications for Animal Health and Antivirulence-Based Intervention

Roya Shafiei, *Eva-Maria Schönborn, Sahar Abdollahibiroun, Jörg Haupenthal, Anna K.H. Hirsch.*

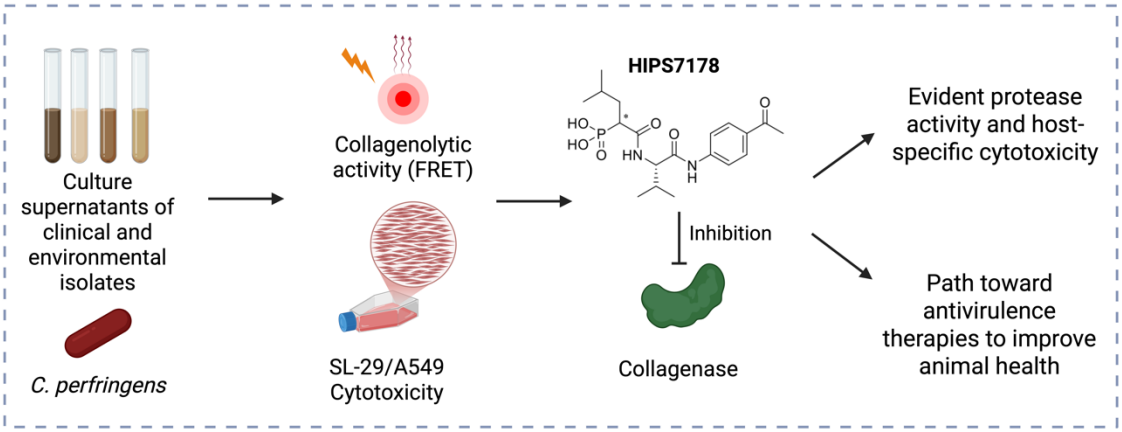

Abstract

Clostridium perfringens is a potent pathogen associated with a range of diseases in humans and animals, partly due to its arsenal of secreted enzymes. Among these, collagenases are hypothesized to play a key role in tissue degradation, but their functional relevance remains undercharacterized. In this study, we evaluated culture supernatants of clinical and environmental *C. perfringens* isolates for collagenase-like activity using fluorogenic substrate assays and examined their cytotoxicity *in vitro*. We observed variable enzymatic profiles across strains, independent of known toxins (NetB, TpeL), and found that even low levels of activity corresponded to marked cytotoxicity in avian SL-29 cells. Attempts to neutralize this activity using small-molecule inhibitors identified one candidate (compound **7178**) with moderate efficacy in enzymatic assays, but limited protective effects in cell-based models. These findings underscore the cytotoxic potential of *C. perfringens* secreted products, support the role of metalloprotease activity, and provide a foundation for developing targeted antivirulence strategies.

Introduction

Clostridium perfringens is a Gram-positive, spore-forming, anaerobic bacterium that causes a wide spectrum of diseases in both humans and animals.[1] In humans, it is associated with conditions such as gas gangrene and food poisoning, while in animals, it is responsible for several economically significant diseases, most notably necrotic enteritis (NE) in poultry.[1,2] This poultry disease alone is estimated to cost the global agricultural industry approximately US$2 billion annually due to its impact on bird health, productivity, and mortality.[2]

The pathogenicity of *C. perfringens* is largely mediated by its production of a diverse arsenal of toxins. Based on the presence of major toxins — including α-toxin, β-toxin, ε-toxin, ι-toxin, enterotoxin, toxin perfringens large (TpeL), and necrotic enteritis toxin B-like (NetB) — the bacterium is classified into five toxinotypes (A to E).[3,4] In addition to these major toxins, *C. perfringens* secretes various extracellular enzymes, notably collagenases, which contribute to tissue degradation and necrosis.[5] These enzymes also support its saprophytic survival during carcass decomposition, as collagen is the most abundant protein in animal tissues.[6] Up to this date, a 120-kDa collagenase encoded by the *colA* gene has been identified and characterized in culture supernatants of multiple strains.[5]

Necrotic enteritis is characterized by severe inflammation and necrosis of the small intestine, with the NetB toxin widely recognized as a key virulence factor.[7–9] However, its role in disease onset remains uncertain. Evidence suggests that NetB may not act during the initial stages of infection, but rather targets deeper layers of the intestinal mucosa.[10] This indicates that other factors likely facilitate early tissue disruption. Among these, collagenases may play a significant role by weakening the mucosal barrier and promoting deeper toxin penetration, thereby amplifying disease severity.[11]

The growing demand for safe poultry products has increased pressure on poultry health management, especially under global restrictions on in-feed antibiotics due to concerns about antimicrobial resistance and drug residues.[12] While low-dose antibiotics were once effective in controlling enteric pathogens and enhancing bird performance, their removal has coincided with a resurgence of *C. perfringens*-associated diseases like NE.[12] Given that this bacterium is a

common inhabitant of the gut and environment, its ability to trigger disease under conditions of dysbiosis or stress presents a persistent challenge to poultry health and industry sustainability.[13]

This study focuses on collagenases and the characterization of collagenolytic activity in culture supernatants (SNs) of various *C. perfringens* strains. We analyzed several clinical and environmental isolates with distinct virulence profiles — some producing NetB or TpeL, while others lacked these key toxins (Table S1). The collagenase activity of each strain was assessed using enzymatic assays to determine their proteolytic potential.

In parallel, we established cell-based cytotoxicity assays, including an MTT viability assay and a Live/Dead staining protocol using SL-29 fibroblasts isolated from a chicken embryo, to evaluate the biological impact of these strains. Notably, we observed that cytotoxicity was significantly higher in animal-derived cells compared to human epithelial cell lines such as A549, suggesting a degree of host specificity in virulence mechanisms. To further assess potential *in vivo* toxicity, we employed the *Galleria mellonella* larvae model, although no overt toxic effects were observed in this system.

Lastly, we tested a series of small-molecule inhibitors originally developed to target collagenase ColH from *Clostridium histolyticum* and the virulence metalloprotease LasB from *Pseudomonas aeruginosa*. These inhibitors were selected due to their known activity against bacterial metalloproteases and the high amino acid sequence similarity between ColH and collagenases found in *C. perfringens*. This allowed us to evaluate their potential cross-species inhibitory activity and explore new avenues for antivirulence strategies.

Together, these experiments provide new insights into the diversity and functional significance of collagenases in *C. perfringens*, laying the groundwork for further investigations into their therapeutic targeting.

Results and Discussion

Evaluation of Collagenolytic Activity and Cytotoxicity of *C. perfringens* Culture Supernatants

The role of collagenases among the extracellular virulence factors of *C. perfringens* remains underexplored, despite their potential contribution to tissue degradation and disease progression. In this study, we evaluated the SNs of 11 clinical and environmental *C. perfringens* isolates (Table S1) for their collagenase-like enzymatic activity and cytotoxic effects *in vitro*.

To establish a reliable readout of enzymatic function, we first screened the SNs of three representative isolates for their capacity to cleave three different fluorogenic peptide substrates (designated A, B, and C). On average, the SNs showed 55%, 95%, and 50% substrate cleavage, respectively (Figure S1). Substrate B consistently yielded the strongest response, and its robust signal across all strains facilitated its selection for subsequent quantification. Notably, these SNs are derived from strains negative for known toxins such as NetB and TpeL, suggesting that the observed proteolytic activity was not dependent on these factors and was more likely attributable to collagenase-like enzymes. Although the substrates used were originally designed for ADAM-10 proteases, the consistent cleavage patterns across isolates support their utility as surrogate markers for general collagenolytic activity under these experimental conditions.

Nonetheless, the lack of collagenase specificity remains a limitation of this assay and requires complementary biochemical validation or genetic manipulation in future studies.

Based on the high cleavage observed with Substrate B, we established a Fluorescence Resonance Energy Transfer (FRET)-based enzymatic assay using this substrate and applied it to all 11 isolates (Figure 1A). The results revealed substantial variability among strains, with isolates **18153, 9239**, and **7381** showing the highest activity. On the other hand, isolates **18207**, **18220**, and **18239** showed considerably lower collagenolytic activity, despite comparable SN concentrations. Importantly, the enzymatic activity did not correlate with the presence or absence of NetB or TpeL, indicating that the collagenolytic potential is an independent trait not linked to these toxins. This suggests that collagenase-like enzymes may serve as additional virulence factors, possibly enabling early host-tissue disruption and facilitating deeper toxin penetration. Overall, these findings highlight the presence of a broadly distributed enzymatic activity that may reflect collagenase or functionally related proteases.

To determine the biological relevance of these enzymatic activities, we next assessed cytotoxic effects of a selection of SNs on epithelial cells. Two cell lines were selected: the human lung adenocarcinoma cell line A549, and the avian fibroblast-derived SL-29 cell line derived from a chicken embryo. Using MTT-based viability assays, we compared responses to SNs from six selected isolates (Figure 1B, S2). Representative data for isolates **7381** and **18239,** which have previously shown high and low enzymatic activity, respectively, are shown in Figure 1B. Across all comparisons, SL-29 cells were more susceptible to cytotoxic effects than A549 cells, even at low SN concentrations of 2.5% v/v, indicating a greater sensitivity of avian-derived cells to *C. perfringens* virulence factors. Importantly, while A549 cells were incubated overnight with SNs, SL-29 cells were only exposed for 8 hours, as longer incubation resulted in complete loss of viability. Furthermore, the cytotoxicity exhibited a concentration-dependent pattern, with a clearer dose-response relationship observed in A549 cells than in SL-29 cells. These findings suggest not only strain-specific differences in virulence but also host-specific susceptibilities that may reflect species barriers or cell-type–dependent sensitivity to extracellular bacterial factors.

To visually confirm these results, we conducted live/dead fluorescence staining of SL-29 cells exposed to SNs from isolate **7381**. The microscopy images corroborated the MTT assay findings, demonstrating substantial cell death at concentrations as low as 1% v/v (Figure 1C). The green/red fluorescence signal clearly distinguished viable from damaged cells, supporting the quantitative findings and illustrating the acute toxicity of this isolate.

To complement the *in vitro* findings, we also tested selected SNs in a model based on *Galleria mellonella* to assess potential systemic toxicity. Larvae were monitored over a period of four to five days post-injection with concentrated SNs. However, no significant lethality was observed compared to control groups. This suggests that the tested SNs lack sufficient virulence to affect this model system or, alternatively, that *G. mellonella* may not be an appropriate surrogate host for studying *C. perfringens* secreted factors in isolation. Future experiments using live bacterial infection or alternative animal models may provide better insights into host–pathogen interactions *in vivo*.

Together, these results demonstrate that *C. perfringens* isolates consistently secrete cytotoxic factors that affect avian and human epithelial cells, and that enzymatic activity — possibly due to collagenases — is widespread and independent of *netB* or *tpeL* expression. Further characterization of these enzymes is necessary to confirm their identity and define their specific contribution to host-cell damage.

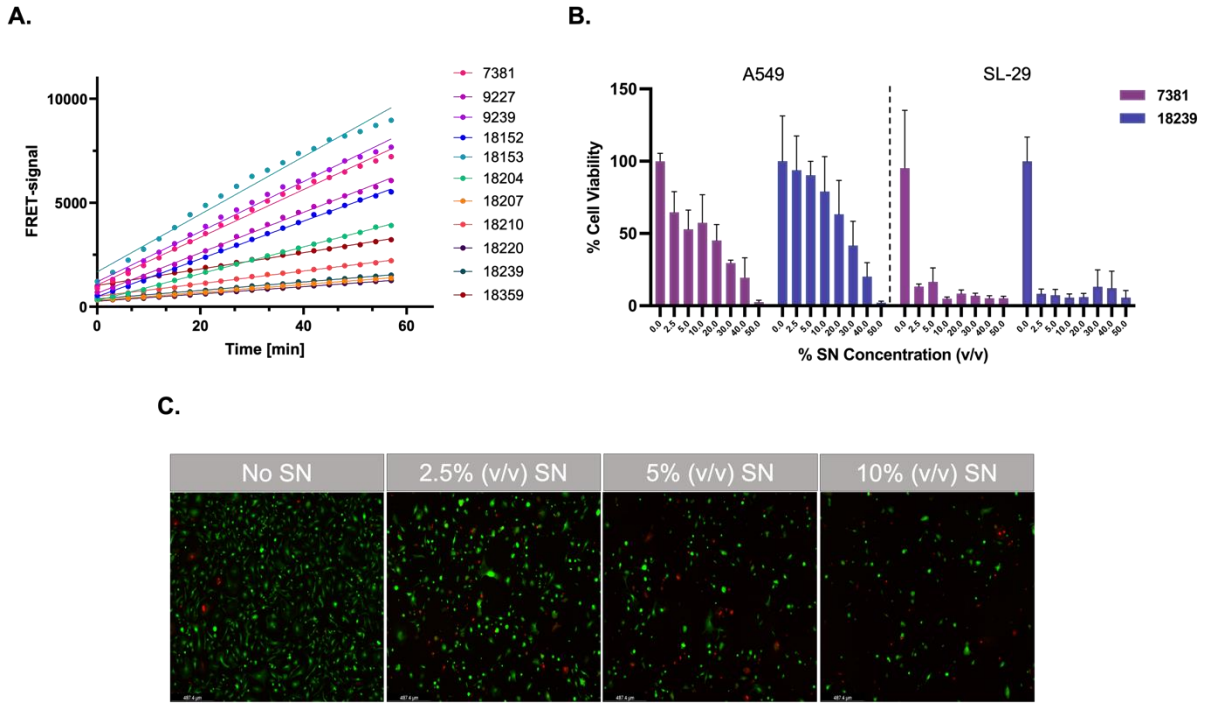

Figure 4: Collagenolytic activity and cytotoxic effects of *Clostridium perfringens* isolates. (A) Fluorescence Resonance Energy Transfer (FRET)-based enzymatic assay showing collagenase-like activity in culture supernatants (SNs) of 11 *C. perfringens* isolates using fluorogenic Substrate B. Relative fluorescence intensity is expressed as a measure of substrate cleavage over time. **(B)** MTT cell viability assay comparing cytotoxic effects of selected SNs on avian SL-29 and human A549 cells. Isolate **7381** (high enzymatic activity) and **18239** (low activity) are shown as representatives. Cell viability is expressed as a percentage relative to untreated controls. **(C)** Live/dead fluorescence microscopy of SL-29 cells upon exposure to SN from isolate **7381**. Green fluorescence indicates live cells (calcein AM), and red fluorescence marks dead cells (EthD-1). Scale bar = 487.5 µm. Graphs were generated using GraphPad Prism 10.

Evaluation of LasB/ColH Inhibitors Against *C. perfringens* Collagenase

To assess the potential of small-molecule inhibitors to block collagenolytic activity in *C. perfringens* SNs, we screened a panel of compounds originally designed to inhibit either *C. histolyticum* collagenase ColH or the *P. aeruginosa* metalloprotease LasB.[14–17] The screening was initially conducted using the established FRET-based enzymatic assay, which offers a simplified and robust platform to detect substrate cleavage. The assay employs a fluorogenic substrate that fluoresces upon proteolytic cleavage, enabling real-time quantification of enzyme activity; inhibitor efficacy is determined by a corresponding decrease in fluorescence, enabling direct assessment of compound efficacy.

Among the tested compounds, four molecules showed inhibition at 100 µM and 200 µM against SNs from three different *C. perfringens* strains (Table S2). As summarized in Table 1, compounds **5797** and **7178** exhibited the most pronounced inhibitory effects. Compound **5797** displayed inhibition ranging from 34% to 42% at 100 µM, but this effect was reduced at 200 µM across all tested strains. This inverse dose-response may be attributable to compound aggregation or off-target effects at higher concentrations, although further investigation is required to elucidate the mechanism.

In contrast, **7178** showed a modest increase in inhibition when tested at 200 µM compared to 100 µM, indicating a more consistent and concentration-dependent activity profile. Based on these findings, compound **7178** was selected for further testing in a more biologically relevant context using SL-29 cells. This cell-based *in vitro* assay allowed us to evaluate not only the enzymatic inhibition but also the protective effect of the compound against *C. perfringens*-induced cytotoxicity.

Table 1: Percent inhibition of collagenolytic activity in *C. perfringens* SNs by selected small-molecule inhibitors at 100 and 200 µM.

Compound	Concentration	%Inhibition ± SD	Target Strains
HIPS5797	100 µM	41.7 ± 7.5	18207, 18359, 9239
	200 µM	2.0 ± 9.8	
HIPS6007	100 µM	14.3 ± 0.6	18207, 18359, 9239
	200 µM	8.3 ± 6.4	
HIPS6044	100 µM	18.7 ± 8.1	18207, 18359, 9239
HIPS7178	100 µM	30.7 ± 9.1	18207, 18359, 9239
	200 µM	39.0 ± 5.3	

To assess the potential of compound **7178** to protect host cells from toxin-induced damage, it was tested in combination with *C. perfringens* SNs in the MTT viability assay using SL-29 avian fibroblasts.

In the first experiment, **7178** was applied at a concentration of 200 µM and pre-incubated for 4 hours with two concentrations of the SN from strain **9227** (1.5% and 2.5% v/v) prior to addition to the cells. To maintain optimal enzyme cofactor availability during this incubation, the reaction mixtures also contained 50 µM $ZnCl_2$ and 50 µM $CaCl_2$, which support metalloprotease activity. As shown in Figure 2A, no improvement in cell viability was observed under either condition, despite the pre-incubation step designed to allow effective target engagement.

To determine whether the lack of protective effect was specific to strain **9227** or influenced by compound concentration, we next evaluated compound **7178** at an elevated dose of 400 µM against SN derived from strain **18204** (Figure 2B). As before, two concentrations of the SN

(1.25% and 2.5% v/v) were tested following a 4-hour pre-incubation with the compound. Despite the increased inhibitor concentration and a different bacterial background, no significant improvement in SL-29 cell viability was detected. Importantly, compound **7178** alone did not induce cytotoxicity at either 200 or 400 µM. Although a minor reduction in viability was observed at the higher dose relative to medium-only controls, this effect was not statistically significant and is unlikely to reflect true toxicity.

Eventhough compound **7178** could not confer protection in a cellular context, its ability to reduce collagenolytic activity by 24–43% in the biochemical FRET-based assay remains a promising finding. The discrepancy between enzymatic inhibition and lack of cellular efficacy suggests that further medicinal-chemistry optimization is likely required. Factors such as cell permeability, metabolic stability, and target engagement in complex biological matrices may influence efficacy and should be addressed in follow-up studies. Nevertheless, compound **7178** represents a potential starting point for the development of targeted collagenase inhibitors in *C. perfringens*.

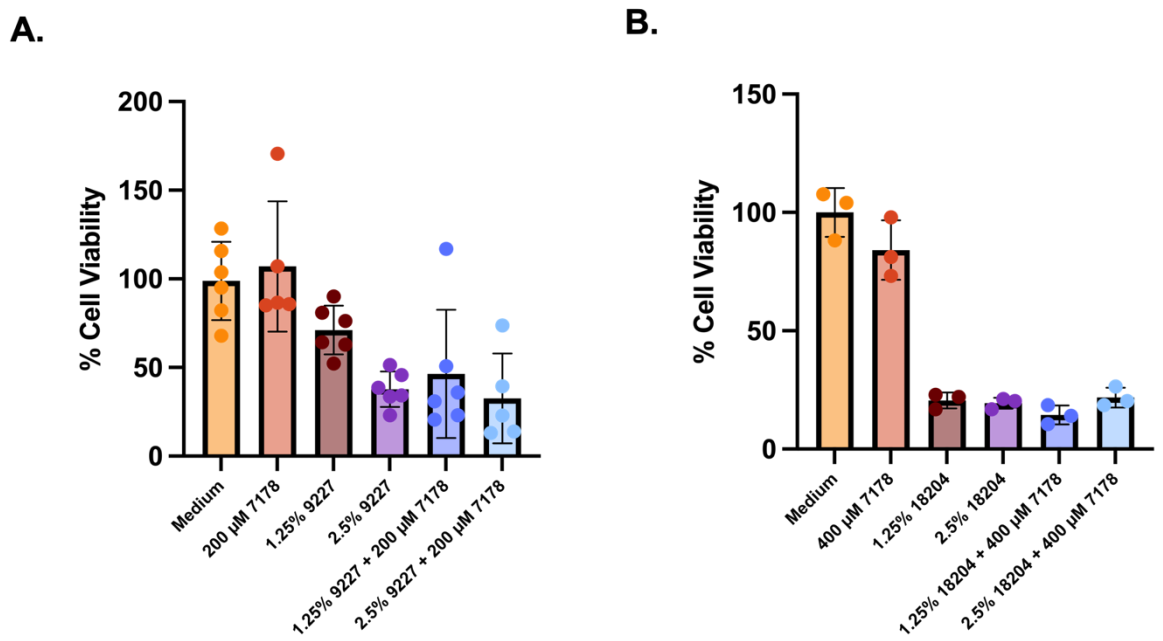

Figure 5: Effect of compound 7178 on SL-29 cell viability in the presence of *Clostridium perfringens* supernatants. (A) SL-29 cells were treated with 1.5% and 2.5% (v/v) supernatant (SN) from strain **9227**, with or without 200 µM **7178** (pre-incubated for 4 h). (B) SL-29 cells were treated with 1.25% and 2.5% (v/v) SN from strain **18204,** with or without 400 µM **7178** (pre-incubated for 4 h). Data represent mean ± SD of technical triplicates. Graphs were generated using GraphPad Prism 10.

Conclusions

This study explored the contribution of collagenase-like activity to the virulence of *C. perfringens*, a pathogen of major relevance to both human and animal health. We characterized the supernatants of 11 isolates for their enzymatic and cytotoxic potential, revealing widespread collagenolytic activity that varied between strains and appeared to be independent of major toxins such as NetB or TpeL.

Interestingly, all culture supernatants, including those from low-activity strains, were highly cytotoxic to avian SL-29 fibroblasts. This suggests that even modest levels of secreted factors are sufficient to compromise these cells, highlighting a pronounced host-specific vulnerability. The cytotoxic effects were less pronounced in human A549 epithelial cells, supporting the idea of selective sensitivity based on cell type or species origin.

To evaluate potential inhibition of collagenase activity, we screened a small panel of compounds previously developed against *C. histolyticum* ColH and *P. aeruginosa* LasB. Compound **7178** showed moderate inhibitory effects *in vitro* using a FRET-based assay, but did not rescue cell viability in the SL-29 model, even at high concentrations. These findings suggest that while inhibition of enzymatic activity is achievable biochemically, further optimization will be necessary for functional cellular protection.

Future research should focus on identifying the specific enzymes responsible for collagenolytic activity through proteomic analysis or targeted mutagenesis. The inhibitors evaluated here may serve as starting points for structure–activity relationship (SAR) studies and medicinal chemistry efforts to improve potency, specificity, and cellular permeability. Moreover, testing live bacterial infections — rather than isolated supernatants — in more representative infection models may provide better insight into the *in vivo* relevance of these virulence factors. Finally, understanding the broader role of collagenases in pathogenesis could inform novel anti-virulence strategies not only in poultry health but also in human medicine, where *C. perfringens* remains an opportunistic threat.

Experimental Section

Preparation of Bacterial Supernatants

A total of 11 *C. perfringens* isolates, provided by Animal Health Innovation (MSD), were used (Table S1). SNs were prepared by the supplier as follows: isolates were cultured overnight on Mueller-Hinton agar plates supplemented with 5% sheep blood at 40 °C. Subsequently, 10–20 well-isolated colonies were transferred into 40 mL Brain Heart Infusion (BHI) broth and incubated for 24 h at 40 °C. Colony-forming units (CFU/mL) were determined for three representative isolates. Cultures were centrifuged at 4000 × g for 10 min at room temperature, and the SNs were sterile-filtered through 0.45 µm Sartorius filters. Sterility was confirmed by plating 100 µL of filtrate on agar and incubating at 40 °C for 24 h. Each filtrate was aliquoted and stored at −20 °C until shipment. For experimental use, aliquots were stored at −80 °C and thawed at room temperature immediately prior to analysis.

FRET-Based Enzymatic Activity Assay of *Clostridium perfringens* Supernatants and Inhibitor Evaluation

To evaluate collagenolytic activity in *C. perfringens* and assess the efficacy of collagenase-targeting inhibitors, a FRET-based enzyme activity assay was employed using SNs. The enzymatic activity assay was performed using a ClarioStar microplate reader (BMG Labtech) at 37 °C. Fluorescence was measured at excitation/emission wavelengths of 485/530 nm. The fluorogenic peptide substrate was dissolved in DMSO to a 10 mM stock concentration.

Assays were conducted in black 384-well plates (Cellstar, Greiner). BHI blanks were included in duplicate and diluted 1:2, mirroring the SN dilutions, to maintain consistent background

levels. Each SN was serially diluted 1:2 in a 96-well V-bottom plate (Greiner). From each dilution step, 20 µL was transferred in duplicate into the 384-well plate. Assay buffer (25 mM Tris, pH 7.2, 10 mM $CaCl_2$) was added (15 µL/well), followed by 15 µL of substrate solution to reach a final substrate concentration of 10 µM. Plates were immediately read in the microplate reader.

To assess inhibitor efficacy, selected small-molecule compounds (developed against *C. histolyticum* ColH and *P. aeruginosa* LasB) were tested at final concentrations of 100 and 200 µM. Compounds were dissolved in 99.9% DMSO and diluted in assay buffer supplemented with 0.075% pluronic acid. For each reaction, 5 µL of the inhibitor solution was mixed with 15 µL substrate and added to wells containing 20 µL of SN. After 15 min incubation at 37 °C, fluorescence was recorded as described above.

Raw fluorescence data were processed in Microsoft Excel and further analyzed and visualized using GraphPad Prism 10. These analyses enabled quantitative comparison of enzymatic activity across isolates and the relative inhibitory effect of test compounds.

Cell Cultures

SL-29 cells, a fibroblast-derived cell line derived from a chicken embryo, were maintained in Dulbecco's Modified Eagle Medium (DMEM) supplemented with 10% fetal bovine serum (FBS), 10% tryptose phosphate broth (TPB), and 1% penicillin-streptomycin (Pen/Strep). Cells were cultured at 37 °C in a humidified incubator with 5% CO_2, and the medium was replaced every 2–3 days. SL-29 cells were passaged upon reaching ≥ 90% confluency using standard trypsinization protocols and routinely seeded at a density of 7.5×10^4 cells/mL.

Human lung epithelial A549 cells were cultured and maintained according to the methods described by Kaya *et al*., using DMEM supplemented with 10% FBS and 1% Pen/Strep under identical incubation conditions.[18]

MTT Cell Viability Assay

Cytotoxic effects of *C. perfringens* SNs on SL-29 and A549 cells were assessed using the MTT assay. SL-29 and A549 cells were seeded at 1×10^5 and 2.5×10^4 cells/well, respectively, in 100 µL of complete medium into the inner wells of sterile, flat-bottom 96-well plates (Greiner), while outer wells were filled with phosphate-buffered saline (PBS) to minimize evaporation. After 24 h of incubation at 37 °C and 5% CO_2 to allow for cell attachment, monolayers were inspected microscopically for confluency.

SNs from selected *C. perfringens* isolates were diluted in culture medium and applied to the cells for 8 h for SL-29 and 24 h for A549 cells, based on prior optimization. Following treatment, wells were washed once with PBS using a multichannel pipette.

Subsequently, 100 µL of MTT solution (prepared from a 5 mg/mL stock in PBS) in complete medium was added per well and incubated for 1 h at 37 °C to allow for formazan formation. The supernatant was then removed, and 150 µL of lysis buffer (DMSO containing 10% SDS and 0.5% acetic acid) was added to dissolve the formazan crystals.

Absorbance was measured at 550 nm with a 620 nm reference using a PHERAstar microplate reader (BMG Labtech). Data were analyzed using Microsoft Excel and visualized with GraphPad Prism 10.

Galleria mellonella in vivo model

To evaluate the virulence of *C. perfringens* secreted factors *in vivo*, a survival assay was conducted using *Galleria mellonella* larvae. This model enables rapid assessment of pathogenic potential through survival analysis. Larvae were selected based on uniform size, bright yellow coloration, and active mobility to ensure consistency and viability across test groups.

Each experimental group consisted of 10 to 15 larvae. The groups included: (1) no injection control, (2) a buffer control injected with sterile PBS, and (3) test groups injected with 10 µL *C. perfringens* SNs. All SNs were previously stored at –80 °C and thawed under sterile conditions prior to use.

Injections were performed using 1 mL syringes fitted with 0.30 × 12 mm needles. Syringes were filled with 10 µL of the designated test sample and mounted onto a microinjector for consistent delivery. Injections were administered into the left hind proleg of each larva to standardize the procedure across all groups.

Following injection, larvae were placed in sterile Petri dishes, covered, and incubated at 37 °C. Survival was monitored twice daily for changes in coloration (melanization) and motility. Larvae were recorded as dead if they showed no response to touch and exhibited complete darkening. At the conclusion of the observation period, survival data were documented and used for Kaplan–Meier survival analysis.

Live/Dead Staining Assay for SL-29 Cells

To assess the cytotoxic effects of *C. perfringens* SNs on SL-29 cells, a Live/Dead staining assay was performed using the Live/Dead Viability/Cytotoxicity Kit (Thermo Fisher). Cells were seeded into sterile 96-well F-bottom plates (Greiner) at a density of 1×10^5 cells/mL in 100 µL per well, as previously established for the MTT assay. The plates were incubated overnight at 37 °C with 5 % CO_2.

On the following day, *C. perfringens* supernatants were thawed at room temperature and diluted in DMEM to final concentrations of 0 %, 2.5 %, 5 %, and 10 %. Each dilution was applied in triplicate (100 µL/well) to the pre-cultured cells, followed by incubation for 3 h under standard conditions.

Shortly before the end of incubation, the Live/Dead staining solution was prepared under sterile conditions by mixing 20 µL Ethidium homodimer-1 (EthD-1, 2 mM) and 5 µL Calcein AM (4 mM) in 10 mL PBS. After supernatant exposure, the cells were washed twice with 100 µL PBS to remove residual compounds, and 100 µL of the staining solution was added to each well.

Plates were incubated for 45 min at room temperature in the dark. Fluorescence imaging was performed using a Leica fluorescence microscope. Calcein AM, indicative of live cells, was excited at 485 ± 10 nm with emission at 530 ± 12.5 nm (fluorescein filter), while EthD-1, marking dead cells, was excited at 530 ± 12.5 nm with emission at 645 ± 20 nm (rhodamine filter). Image acquisition and subsequent analysis were conducted using ImageJ software.

References

1. Rood, J. I. & Cole, S. T. Molecular genetics and pathogenesis of Clostridium perfringens. *Microbiol Rev* 55, 621–648 (1991).
2. Keyburn, A. L., Bannam, T. L., Moore, R. J. & Rood, J. I. NetB, a Pore-Forming Toxin from Necrotic Enteritis Strains of Clostridium perfringens. *Toxins (Basel)* 2, 1913–1927 (2010).
3. Uzal, F. A. *et al.* Towards an Understanding of the Role of Clostridium Perfringens Toxins in Human and Animal Disease. *Future Microbiol* 9, 361–377 (2014).
4. Coursodon, C. F., Glock, R. D., Moore, K. L., Cooper, K. K. & Songer, J. G. TpeL-producing strains of Clostridium perfringens type A are highly virulent for broiler chicks. *Anaerobe* 18, 117–121 (2012).
5. Matsushita, O., Yoshihara, K., Katayama, S., Minami, J. & Okabe, A. Purification and characterization of Clostridium perfringens 120-kilodalton collagenase and nucleotide sequence of the corresponding gene. *J Bacteriol* 176, 149–156 (1994).
6. Hatheway, C. L. Toxigenic clostridia. *Clin Microbiol Rev* 3, 66–98 (1990).
7. Cooper, K. K. & Songer, J. G. Necrotic enteritis in chickens: A paradigm of enteric infection by Clostridium perfringens type A. *Anaerobe* 15, 55–60 (2009).
8. Keyburn, A. L. *et al.* NetB, a New Toxin That Is Associated with Avian Necrotic Enteritis Caused by Clostridium perfringens. *PLoS Pathog* 4, e26 (2008).
9. Olkowski, A. A., Wojnarowicz, C., Chirino-Trejo, M. & Drew, M. D. Responses of broiler chickens orally challenged with Clostridium perfringens isolated from field cases of necrotic enteritis. *Res Vet Sci* 81, 99–108 (2006).
10. Parreira, V. R., Russell, K., Athanasiadou, S. & Prescott, J. F. Comparative transcriptome analysis by RNAseq of necrotic enteritis Clostridium perfringens during in vivo colonization and in vitro conditions. *BMC Microbiol* 16, 186 (2016).
11. Van Damme, L. *et al.* C. perfringens challenge reduces matrix metalloproteinase activity in the jejunal mucosa of Eimeria-infected broiler chickens. *Vet Res* 51, 100 (2020).
12. Lee, K.-W. & Lillehoj, H. S. Role of Clostridium perfringens Necrotic Enteritis B-like Toxin in Disease Pathogenesis. *Vaccines (Basel)* 10, 61 (2021).
13. Blake, D. P. *et al.* Re-calculating the cost of coccidiosis in chickens. *Vet Res* 51, 115 (2020).
14. Kiefer, A. F. *et al.* Dipeptidic Phosphonates: Potent Inhibitors of Pseudomonas aeruginosa Elastase B Showing Efficacy in a Murine Keratitis Model. *Advanced Science* 12, (2025).
15. Voos, K. *et al.* Phosphonate as a Stable Zinc-Binding Group for "Pathoblocker" Inhibitors of Clostridial Collagenase H (ColH). *ChemMedChem* 16, 1257–1267 (2021).

16. Konstantinović, J. *et al.* N-Aryl-3-mercaptosuccinimides as Antivirulence Agents Targeting Pseudomonas aeruginosa Elastase and Clostridium Collagenases. *J Med Chem* 63, 8359–8368 (2020).

17. Schönauer, E. *et al.* Discovery of a Potent Inhibitor Class with High Selectivity toward Clostridial Collagenases. *J Am Chem Soc* 139, 12696–12703 (2017).

18. Kaya, C. *et al.* Structure-Based Design of α-Substituted Mercaptoacetamides as Inhibitors of the Virulence Factor LasB from Pseudomonas aeruginosa. *ACS Infect Dis* 8, 1010–1021 (2022).

Supporting Information

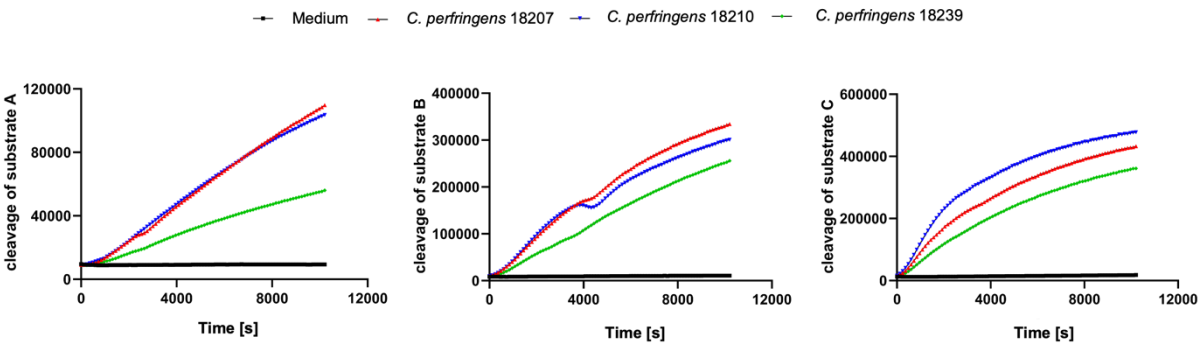

Figure S1: Initial screening of fluorogenic peptide substrates to assess proteolytic activity of representative *Clostridium perfringens* isolates. Three isolates (**18207**, **18210**, and **18239**) were incubated with three different FRET-based peptide substrates (designated A, B, and C) to evaluate their peptidolytic capacity. Substrate B showed the most robust and consistent cleavage across strains and was selected for subsequent collagenase activity assays. Data represent mean substrate cleavage normalized to blank (n = 2 technical replicates). Graphs were generated using GraphPad Prism 10.

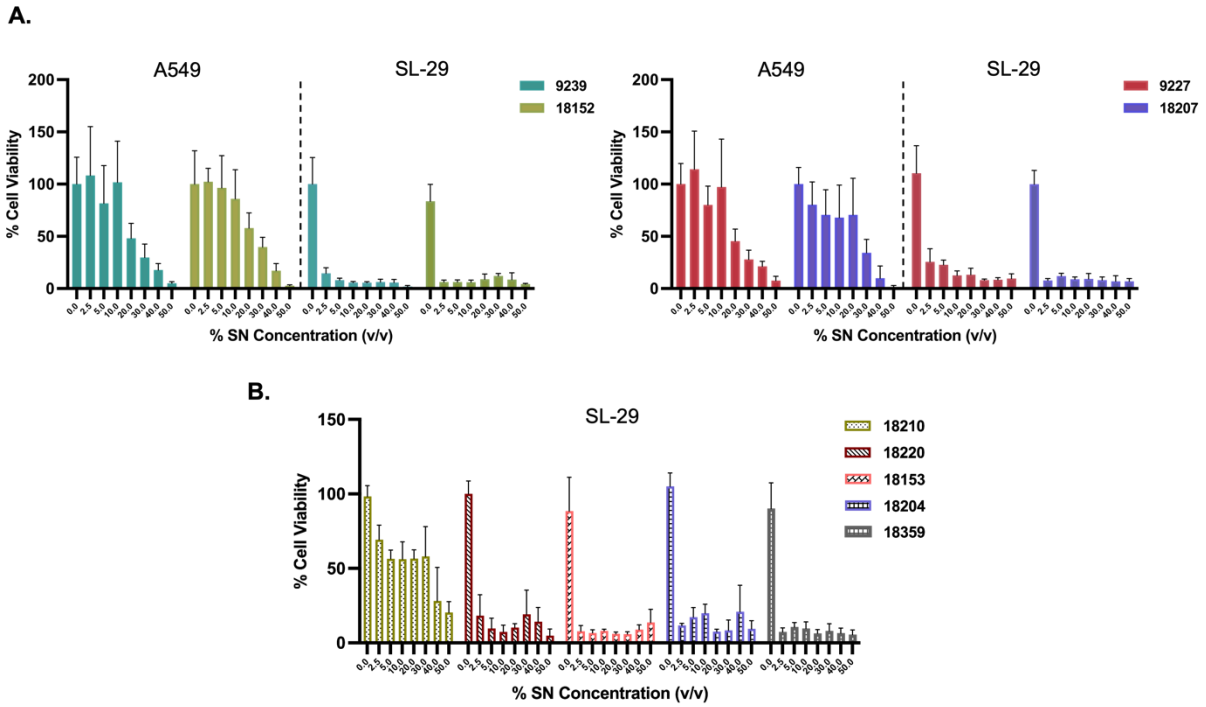

Figure S2: Dose-dependent cytotoxicity of *Clostridium perfringens* supernatants in A549 and SL-29 cells. Cell viability was measured using MTT assays after overnight exposure to increasing concentrations of bacterial supernatant (SN) from selected isolates. SL-29 cells exhibited higher sensitivity to SNs than A549 cells, particularly at lower concentrations. Results are shown as percent viability relative to untreated control (mean ± SD, n = 3). Graphs were generated using GraphPad Prism 10.

Table S1: Characteristics of *C. perfringens* isolates.

ID	Serotype/genes	Pathology
7381	Type A, NetB, TpeL pos	Enteritis
9227	Type A, NetB, TpeL pos	Not known
9239	Type A, NetB, TpeL pos	Not known
18152	Type A, NetB, TpeL pos	Enteritis
18153	Type A, NetB, TpeL pos	Enteritis
18204	Type A, NetB pos, TpeL neg	Enteritis
18207	Type A, NetB pos, TpeL neg	Enteritis
18210	Type A, NetB, TpeL neg	Enteritis
18220	Type A, NetB pos, TpeL neg	Enteritis
18239	Type A, NetB pos, TpeL neg	Enteritis
18259	Type A, NetB pos, TpeL neg	Enteritis

Table S2: Chemical structures of the selected ColH/LasB inhibitors.

Compound	Structure
HIPS5797	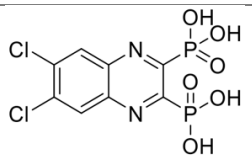
HIPS6007	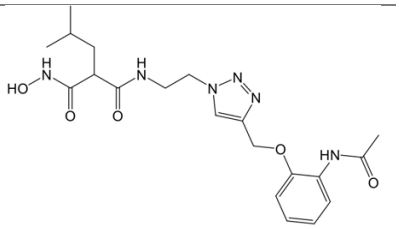
HIPS6044	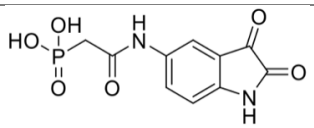
HIPS7178	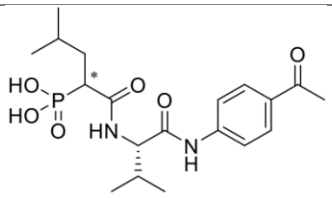

Abbreviations

AMR	Antimicrobial Resistance
MDR	Multidrug Resistance
DNA	Deoxyribonucleic Acid
RNA	Ribonucleic Acid
QS	Quorum Sensing
MMP	Matrix Metalloprotease
LasB	*Pseudomonas aeruginosa* Elastase B
LecA	*Pseudomonas aeruginosa* Lectin A
ColH	*Clostridium histolyticum* Collagenase H
TpeL	Toxin Perfringens Large
NetB	Necrotic Enteritis
WHO	World Health Organization
CF	Cystic Fibrosis
COPD	Chronic Obstructive Pulmonary Disease
ZBG	Zn^{2+}-Binding Group
HAP	Hospital-Acquired Pneumonia
VAP	Ventilator-Associated Pneumonia
T2SS	Type-2 Secretion System
IgG	Immunoglobulin G
IgA	Immunoglobulin A
IL-6	Interleukin-6
IL-8	Interleukin-8
IL-1β	Interleukin-1 beta
TNF	Tumor Necrosis Factor
CSF	Colony-Stimulating Factor
MAPK	Mitogen-Activated Protein Kinase
FGF	Fibroblast Growth Factor
TJs	Tight Junctions
AJs	Adherens Junctions
ZO-1	Zonula Occludens-1
qPCR	Quantitative Polymerase Chain Reaction
mRNA	Messenger RNA

AMP	Antimicrobial Peptide
AAC	Antibody-Antibiotic Conjugate
CRISPR-Cas	Clustered Regularly Interspaced Short Palindromic Repeats and CRISPR-associated proteins
PBP	Penicillin Binding Protein
ESBL	Extended-Spectrum β-Lactamase
mAb	Monoclonal Antibody
MRSA	Methicillin-Resistant *Staphylococcus aureus*
Hib	Haemophilus Influenzae Type b
PCV	Pneumococcal Conjugate Vaccine
MBL	Metallo-β-Lactamase
ADMET	Absorption, Distribution, Metabolism, Excretion, and Toxicity
Calu-3	Human Bronchial Epithelial Cell Line
Arlo	Human Alveolar Epithelial Cell Line
A549	Lung Carcinoma Cell Line
SL-29	Avian Fibroblast-Derived Cells
FRET	Fluorescence Resonance Energy Transfer
SN	Bacterial Culture Supernatant
BHI	Brain Heart Infusion
DMSO	Dimethyl Sulfoxide
DMEM	Dulbecco's Modified Eagle Medium
FBS	Fetal Bovine Serum
TPB	Tryptose Phosphate Broth
Pen/Strep	Penicillin-Streptomycin
PBS	Phosphate-Buffered Saline
CFU	Colony-Forming Units
SAR	Structure-Activity Relationship
FDA	Food and Drug Administration
TEER	Transepithelial Electrical Resistance
GM-CSF	Granulocyte-Macrophage Colony-Stimulating Factor
G-CSF	Granulocyte Colony-Stimulating Factor
DUSP2	Dual Specificity Phosphatase 2
FGFBP1	Fibroblast Growth Factor Binding Protein 1

Publications of the Author Included in This Thesis and Contribution Declaration

Publication A: Kiefer, A.F.‡, Schütz, C.‡, Englisch, C.N., Kolling, D., Speicher, S., Kany, A.M., **Shafiei, R.**, Wadood, N.A., Aljohmani, A., Wirschem, N. and Jumde, R.P., 2024. Dipeptidic Phosphonates: Potent Inhibitors of *Pseudomonas aeruginosa* Elastase B Showing Efficacy in a Murine Keratitis Model. *Adv. Sci*. 2025, 2411807. DOI: 10.1002/advs.202411807

‡ these authors contributed equally

Contribution: The author developed and standardized a gene expression assay for absolute and relative quantification of *lasB* expression levels in clinical *Pseudomonas aeruginosa* isolates. This included full experimental design, data visualization through figure preparation, and authoring critical manuscript components – specifically detailing the methodology and interpreting findings in the results/discussion sections related to this work.

Publication B: Metelkina, O.‡, Konstantinović, J.‡, Klein, A., **Shafiei, R.**, Fares, M., Alhayek, A., Yahiaoui, S., Elgaher, W.A., Haupenthal, J., Titz, A. and Hirsch, A.K., 2024. Dual inhibitors of *Pseudomonas aeruginosa* virulence factors LecA and LasB. *Chem. Sci*., 2024, 15, 13333-13342. DOI: 10.1039/D4SC02703E

‡ these authors contributed equally

Contribution: The author established and conducted the *in vitro* cell-viability assays and LecA-mediated cell-adhesion experiments, followed by fluorescence microscopy imaging. This work included full implementation of protocols, image acquisition, and subsequent quantitative/qualitative analysis. The author also performed detailed data analysis and visualization, and wrote the corresponding methodology and results/discussion sections of the manuscript.

Publications of the Author not Included in This Thesis and Contribution Declaration

Publication C: Alhayek, A., Khan, E.S., Schönauer, E., Däinghaus, T., **Shafiei, R.**, Voos, K., Han, M.K., Ducho, C., Posselt, G., Wessler, S. and Brandstetter, H., 2022. Inhibition of Collagenase Q1 of *Bacillus cereus* as a Novel Antivirulence Strategy for the Treatment of Skin-Wound Infections. *Adv. Therap*. 2022, 5, 2100222. DOI: 10.1002/adtp.202100222

Contribution: The author conducted the *in vitro* cell-viability assay and the *in vivo Galleria mellonella* experiments. Additionally, the author documented the methodologies, interpreted the results, and prepared the accompanying figures for the manuscript.

Publication D: Kaya, C., Walter, I., Alhayek, A., **Shafiei, R.**, Jézéquel, G., Andreas, A., Konstantinović, J., Schönauer, E., Sikandar, A., Haupenthal, J. and Müller, R., 2022. Structure-based design of α-substituted mercaptoacetamides as inhibitors of the virulence factor LasB from *Pseudomonas aeruginosa*. *ACS Infect. Dis*. 2022, 8, 1010−1021. DOI: 10.1021/acsinfecdis.1c00628

Contribution: The author conducted the cell-viability assay and evaluated the efficacy of inhibitors against LasB in *Pseudomonas aeruginosa*. Additionally, the author documented the methodologies, interpreted the results, and prepared the accompanying figures.

Publication E: Konstantinović, J., Kany, A.M., Alhayek, A., Abdelsamie, A.S., Sikandar, A., Voos, K., Yao, Y., Andreas, A., **Shafiei, R.**, Loretz, B. and Schönauer, E., 2023. Inhibitors of the Elastase LasB for the treatment of *Pseudomonas aeruginosa* lung infections. *ACS Cent. Sci*. 2023, 9, 2205−2215. DOI: 10.1021/acscentsci.3c01102

Contribution: The author evaluated the most potent LasB inhibitors using the *in vitro* A549-based MTT assay. Additionally, the author documented the methodologies, interpreted the results, prepared the accompanying figures, and reviewed the manuscript to ensure its accuracy and coherence.

Publication F: Afanasenko, A.M., Wu, X., De Santi, A., Elgaher, W.A., Kany, A.M., **Shafiei, R.**, Schulze, M.S., Schulz, T.F., Haupenthal, J., Hirsch, A.K. and Barta, K., 2024. Clean synthetic strategies to biologically active molecules from lignin: a green path to drug discovery. *Angew. Chem. Int. Ed*. 2024, 63, e202308131. DOI: 10.1002/anie.202308131

Contribution: The author developed and established an *in vivo Galleria mellonella* assay for studying *Streptococcus pneumoniae* infections. This involved systematic evaluation of the most active antibacterial compounds against these bacteria. Additionally, the author documented the methodologies, interpreted the results, prepared the accompanying figures, and reviewed the manuscript.

Manuscripts of the Author Submitted or in Preparation and Contribution Declaration

Manuscript A: **Shafiei, R.‡,** Alhayek, A.‡, Hiller, L., Latta, L., Neu, T., Aljohmani, L., Abdollahibiroun, S., Schönborn, E., Yildiz, D., Schneider-Daum, N., Lehr, C. M., Haupenthal, J., and Hirsch, A.K.H. Exploring the Role of *Pseudomonas aeruginosa* Elastase in Lung Epithelial Barrier Dysfunction: Advancing Towards Antivirulence Therapies (manuscript submitted)

‡ these authors contributed equally

Contribution: The author contributed to conceptualization of the project, designed and executed comprehensive *in vitro* experiments, including transwell-based assays with lung epithelial cells, cellular transport studies, LDH cytotoxicity assay, cytokine quantification via qPCR and FACS CBA, and confocal laser scanning microscopy (CLSM) for junctional protein analysis. Additionally, the author processed RNA sequencing data using Python. The experimental framework was extended to evaluate the efficacy of the most potent LasB inhibitors under identical conditions. All data were processed, analyzed, and visualized by the author, who subsequently prepared publication-quality figures, authored the complete manuscript, and conducted critical revisions of the document in collaboration with the shared first author Alhayek, A.

Manuscript B: Amin, A.‡, Schütz, C.‡, Speicher, S., Jézéquel, G., **Shafiei, R.**, Kolling, D., Abdollahibiroun, S., Kiefer, A., Kany, A. M., Rox, K., Haupenthal, J., Köhnke, J., and Hirsch, A.K.H. Development of amide bioisosteres unravels therapeutic potential of benzimidazole phosphonates as *Pseudomonas aeruginosa* LasB inhibitors (manuscript in preparation)

‡ these authors contributed equally

Contribution: The author evaluated the most potent benzimidazole compounds using an A549 cell-viability assay, an *in vivo Galleria mellonella* infection model, and transwell-based TEER and transport assays with bronchial epithelial cells. She also documented the methodologies and results, prepared the figures, authored the respective methodology and results discussion sections, and reviewed the manuscript.

Manuscript C: Abdelsamie, A.S., Konstantinovič, J., Kany, A. M., Schütz, C., Klein, A., Speicher, S., **Shafiei, R.**, Bouté, M., Park, Y. M., Loretz, B., Müller, R., Sallenave, J. M., Lehr,

C. M., Rox, K., Haupenthal, J., and Hirsch, A. K. H. Multiparameter Optimization of *Pseudomonas aeruginosa* Elastase (LasB) Inhibitors for Systemic Administration (manuscript in preparation)

Contribution: The author conducted an *in vitro* cell-based MTT assay to assess the efficacy of a potent LasB inhibitor and further evaluated this compound's activity against LasB in various *Pseudomonas aeruginosa* clinical isolates using a FRET-based enzyme activity assay. The author analyzed the resulting data, documented the methodologies, interpreted the results, and authored the respective sections of the manuscript. Additionally, the author reviewed the manuscript to ensure its accuracy and coherence.

Manuscript D: Camberlein, V., Alhayek, A., **Shafiei, R.**, Sikandar, A., Kempt, M., Park, Y. M., Konstantinović, J., Rox, K., Kany, A. M., Deprez, B., Müller, R., Haupenthal, J., Deprez-Poulain, R., and Hirsch, A. K. H. Discovery of Selective Nanomolar hydroxamic acid-based inhibitors of LasB by Kinetic Target-Guided Synthesis (manuscript in preparation).

Contribution: The author evaluated the most potent hydroxamic acids using both *in vitro* models based on A549 cells and *in vivo* models utilizing *Galleria mellonella* larvae. The author analyzed the resulting data, documented the methodologies, interpreted the results, and authored the respective sections of the manuscript.

Manuscript E: Jézéquel, G., Kolling, D., **Shafiei, R.**, Konstantinović, J., Kany, A. M., Köhnke, J., Haupenthal, J., and Hirsch, A. K. H. A New Class of Phosphonates Efficiently Target the Virulence Factor Elastase B in *Pseudomonas aeruginosa* (manuscript in preparation).

Contribution: The author evaluated the most potent inhibitors using *in vivo* models with *Galleria mellonella* larvae. The author analyzed the resulting data, documented the methodologies, interpreted the results, and authored the respective sections of the manuscript. Additionally, the author reviewed the manuscript to ensure its accuracy in the final stages.

Conference Contributions

Shafiei, R.; Schütz, C.; Alhayek, A.; Kany, A. M.; Adam, S.; Rox, K.; Haupenthal, J.; and Hirsch, A. K. H.: Biological evaluation of novel phosphonate inhibitors targeting *Pseudomonas aeruginosa* elastase LasB, ESCMID/ASM Conference on Drug Development, Dublin, Ireland, October, 2022 (Poster presentation).

Shafiei, R.; Schütz, C.; Alhayek, A.; Kany, A. M.; Rox, K.; Haupenthal, J.; and Hirsch, A. K. H.: Phosphonate inhibitors targeting *Pseudomonas aeruginosa* elastase LasB demonstrate promising activity in both *in vitro* and *in vivo* studies., 40th Winter School on Proteinases and Their Inhibitors, Tiers, Italy, March, 2023 (Oral presentation).

Shafiei, R.; Konstantinović, J.; Schütz, C.; Alhayek, A.; Kany, A. M.; Rox, K.; Haupenthal, J.; and Hirsch, A. K. H.: Targeting elastase LasB in *Pseudomonas aeruginosa*: A biological study on a new class of phosphonate inhibitors, PhD Assembly for HZI and UdS Doctoral Researchers, Saarbrücken, Germany, May, 2023 (Poster presentation).

Shafiei, R.; Konstantinović, J.; Schütz, C.; Alhayek, A.; Klein, A.; Kany, A. M.; Rox, K.; Haupenthal, J.; and Hirsch, A. K. H.: Targeting elastase LasB in *Pseudomonas aeruginosa*: A biological study on a new class of phosphonate-based inhibitors, Annual Meeting of the DZIF, Hannover, Germany, September, 2023 (Poster presentation).

Shafiei, R.; Alhayek, A.; Haupenthal, J.; and Hirsch, A. K. H.: Biological evaluation of novel pathoblockers targeting bacterial metalloproteinases, Winter School Translational Medicine Explained (TMex) on Translational Research and Medicine Development, Berlin, Germany, November, 2023 (Oral pitch presentation).

Shafiei R.; Jézéquel, G.; Kolling, D.; Camberlein, V.; Schütz, C.; Alhayek, A.; Konstantinović, J.; Kany, A. M.; Yahiaoui, S.; Sikandar, A.; Voulhoux, R.; Rox, K.; Haupenthal, J.; Sallenave, J. M.; Köhnke, J.; and Hirsch, A. K. H.: Development and profiling of *Pseudomonas aeruginosa* LasB inhibitors as novel antivirulence agents, French-German Calls for Projects on Antimicrobial Resistance: Final Review Meeting (BMBF-ANR Meeting), Forsbach, Germany, March, 2024 (Oral presentation).

Shafiei, R.; Alhayek, A.; Konstantinović, J.; Schütz, C.; Latta, L.; Neu, T.; Haupenthal, J.; Lehr, C. M.; and Hirsch, A. K. H.: Exploring the virulence of *Pseudomonas aeruginosa* elastase (LasB): A comprehensive biological study in human lung cell lines, Gordon Research Seminars (GRS), Barga, Italy, June, 2024 (Oral presentation).

Latta, L.; Neu, T.; **Shafiei, R.**; Haupenthal, J.; Schneider-Daum, N.; Hirsch, A. K. H.; and Lehr, C. M.: Use of public transcriptional datasets for validating pulmonary *in vitro* models. The 2024 European Congress on Alternatives to Animal Testing (EUSAAT), Linz, Austria, September, 2024 (Poster presentation).

Acknowledgments

First and foremost, I would like to express my deepest gratitude to my advisors, Prof. Anna K. H. Hirsch and Prof. Claus-Michael Lehr, for giving me the opportunity to pursue my PhD project under their guidance. Their support, encouragement, and trust laid the foundation for this work.

I am also sincerely grateful to Dr. Jörg Haupenthal and Dr. Alaa Alhayek for their dedicated supervision, insightful feedback, and continuous guidance throughout my doctoral journey.

Special thanks go to the LasB team for their collaboration and colleagueship, with particular appreciation to Lukas Hiller for his unwavering support and teamwork. I am equally thankful to my students, Eva-Maria Schönborn and Sahar Abdollahibiroun, for their hard work, scientific contributions, and commitment to the project.

I also extend my thanks to the members of the DDEL team. I would like to especially acknowledge Dr. Lorenz Latta for his guidance and collaboration, as well as Tobias Neu, Clementine Richter, and Dr. Annette Boese for their contributions and the multiple trainings that significantly supported my progress.

I am grateful for the valuable collaboration and input in the LasB project from Dr. Ahmad Aljohmani and Prof. Daniela Yildiz at Universitätsklinikum des Saarlandes, whose expertise enriched this work.

My sincere thanks also go to fellow scientists who generously offered their insights, support, and training throughout this journey: Dr. Yingwen Wu, Dr. Andreas M. Kany, Dr. Joscha Meiers, Mario Fares, and Dr. Carsten Volz.

The technical support provided by the DDOP team was indispensable. I thank Simone Amann, Jeannine Jung, Tabea Wittmann, and Jannine Seelbach for their dedication and for ensuring the lab environment functioned smoothly.

To my colleagues Atanaz Shams, Justine Bassil, Konrad Wagner, Dr. Virgyl Camberlein, and Dr. Christian Schütz—thank you for your friendship, support, and the shared moments that made work not only bearable but often enjoyable.

Finally, I owe my deepest gratitude to my family—my mother, father, and brother. Their unwavering support, love, and belief in me have been the driving force behind everything I have achieved. I am who I am, and where I stand today, because of them. I am also incredibly thankful to all my wonderful friends who stood by me through the highs and lows, offering strength and encouragement throughout this journey.